MARTIN MARIETTA ENERGY SYSTEMS LIBRARIES
3 4456 0285927 1

<1049>
CENTRAL RESEARCH LIBRARY
DOCUMENT COLLECTION
1

ORNL-4330
UC-25 – Metals, Ceramics, and Materials

FUELS AND MATERIALS DEVELOPMENT PROGRAM

QUARTERLY PROGRESS REPORT

FOR PERIOD ENDING JUNE 30, 1968

LIBRARY
REFERENCE COPY

OAK RIDGE NATIONAL LABORATORY
operated by
UNION CARBIDE CORPORATION
for the
U.S. ATOMIC ENERGY COMMISSION

Printed in the United States of America. Available from Clearinghouse for Federal Scientific and Technical Information, National Bureau of Standards, U.S. Department of Commerce, Springfield, Virginia 22151
Price: Printed Copy $3.00; Microfiche $0.65

LEGAL NOTICE

This report was prepared as an account of Government sponsored work. Neither the United States, nor the Commission, nor any person acting on behalf of the Commission:

A. Makes any warranty or representation, expressed or implied, with respect to the accuracy, completeness, or usefulness of the information contained in this report, or that the use of any information, apparatus, method, or process disclosed in this report may not infringe privately owned rights; or

B. Assumes any liabilities with respect to the use of, or for damages resulting from the use of any information, apparatus, method, or process disclosed in this report.

As used in the above, "person acting on behalf of the Commission" includes any employee or contractor of the Commission, or employee of such contractor, to the extent that such employee or contractor of the Commission, or employee of such contractor prepares, disseminates, or provides access to, any information pursuant to his employment or contract with the Commission, or his employment with such contractor.

ORNL-4330

Contract No. W-7405-eng-26

METALS AND CERAMICS DIVISION

FUELS AND MATERIALS DEVELOPMENT PROGRAM QUARTERLY PROGRESS REPORT FOR PERIOD ENDING JUNE 30, 1968

Compiled by

P. Patriarca W. O. Harms

Edited by

D. J. Rucker

NOVEMBER 1968

MARTIN MARIETTA ENERGY SYSTEMS LIBRARIES

3 4456 0285927 1

OAK RIDGE NATIONAL LABORATORY
Oak Ridge, Tennessee
operated by
UNION CARBIDE CORPORATION
U.S. ATOMIC ENERGY COMMISSION

FOREWORD

This quarterly progress report describes research and development on nuclear fuels and materials performed at the Oak Ridge National Laboratory for the U.S. Atomic Energy Commission. With several exceptions, as noted below in the listing of specific programs, the work is sponsored by the Fuels and Materials Branch of the Division of Reactor Development and Technology. Classified aspects of the Nitride Fuels Development activity and work on fuels and materials for isotope heat sources are covered in separate ORNL progress reports.

The report is presented in five parts according to AEC Activity titles provided by the Fuels and Materials Branch, RDT.

Program Title	ORNL Division(s)	Person in Charge	Principal Investigator(s)
	I. Fuels and Claddings		
Sol-Gel Fast Reactor Fuels	Metals and Ceramics Chemical Technology Reactor	P. Patriarca	A. L. Lotts J. L. Scott R. E. Brooksbank
Nitride Fuels Development	Metals and Ceramics Reactor	W. O. Harms	J. L. Scott H. C. McCurdy
Fission-Gas Release and Physical Properties of Fuel Materials During Irradiation	Reactor Chemistry	O. Sisman	R. M. Carroll J. G. Morgan
Zirconium Metallurgy	Metals and Ceramics	C. J. McHargue	P. L. Rittenhouse
	II. Coolants		
Alkali-Metal Corrosion Studies	Metals and Ceramics Reactor	W. O. Harms	J. H. DeVan A. P. Litman R. E. MacPherson

Program Title	ORNL Division(s)	Person in Charge	Principal Investigator(s)
III. Radiation Damage to Structural Materials			
Behavior of Refractory Materials Under Irradiation	Reactor Chemistry	G. M. Watson	G. W. Keilholtz
Fast-Neutron Irradiation Effects on Electrical Insulators*	Reactor Chemistry	G. M. Watson	G. W. Keilholtz
Mechanical Properties Research and LMFBR Cladding and Structural Materials Development**	Metals and Ceramics	C. J. McHargue	J. R. Weir
Radiation Effects in Alloys and Structural Materials	Solid State	D. S. Billington	M. S. Wechsler
IV. Techniques of Fabrication and Testing			
Tungsten Metallurgy	Metals and Ceramics	W. O. Harms	H. Inouye W. R. Martin G. M. Slaughter J. O. Stiegler J. R. Weir
Nondestructive Test Development	Metals and Ceramics	W. O. Harms	R. W. McClung
Joining Research on Nuclear Materials	Metals and Ceramics	G. M. Adamson	G. M. Slaughter
Fuel Element Fabrication Development	Metals and Ceramics	G. M. Adamson	J. V. Cathcart W. R. Martin R. W. McClung
Sintered Aluminum Product Development	Metals and Ceramics	G. M. Adamson	W. R. Martin J. R. Weir

*Sponsored by Reactor Power Systems Branch, Division of Space Nuclear Systems.

**Partially sponsored by Liquid Metals Branch, Division of Reactor Development and Technology.

Program Title	ORNL Division(s)	Person in Charge	Principal Investigator(s)
V. Engineering Properties of Reactor Materials			
Physical and Mechanical Metallurgy of Refractory Alloys	Metals and Ceramics	W. O. Harms	H. Inouye R. W. McClung D. L. McElroy G. M. Slaughter J. R. Weir

CONTENTS

Page

Summary xiii

Part I. Fuels and Claddings

1. Sol-Gel Fast Reactor Fuels 3
   - Plutonium Ceramic Facilities 4
     - Building 4508 Facilities 4
     - Building 3019 Facilities 4
   - Preparation of $(U,Pu)O_2$ Sol-Gel Material 4
   - Development of Fabrication Processes 5
     - Sphere-Pac 6
     - Pelletizing of Sol-Gel $(U,Pu)O_2$ 7
     - Extrusion of Sol-Gel Urania 10
     - Fast Reactor Capsule Fabrication 11
   - Characterization of $(U,Pu)O_2$ Fuels 13
     - Analytical Chemistry 13
     - Hot-Stage Microscopy 14
     - Thermal Conductivity 16
     - Deformation of Sol-Gel Oxide Pellets 17
   - Irradiation Testing of Sol-Gel $(U,Pu)O_2$ 17
     - Uninstrumented Thermal Flux Irradiation Tests 18
     - ORR Instrumented Tests 20
     - Transient Testing of Sol-Gel-Derived $(U,Pu)O_2$ 23
     - Fast Flux Irradiation Tests 24
     - Irradiation Test Calculation 25
2. Nitride Fuels Development 26
   - Synthesis and Fabrication of Uranium Nitride 26
   - Synthesis of Uranium Carbonitride 28
   - Basic Studies on Conversion of Sol-Gel Oxides to Carbonitrides 32
   - Synthesis, Fabrication, and Characterization of Mixed Nitrides 39
   - Purity Control of Glove-Box Atmospheres 40
   - Recirculating Gas System 41

Equipment Modifications 41
Glove Box Pressure-Controllers 42
Study of the Compatibility of UN with Cladding Alloys . . . 42
Studies of Vanadium Carbonitride Solutions 43
Experimental 45
Data and Results 46
Conclusions and Discussion 48
The Hot Hardness of Uranium Carbonitrides 49
Fundamental Research on Uranium Nitride 51
Fuel-Cladding Thermal Conductance Studies 52
3. Fission-Gas Release and Physical Properties of Fuel Materials During Irradiation 54
Effect of Burnup and Burnup Rate on Fission-Gas Release from Single-Crystal UO_2 54
Nonfission Heating During Irradiation 56
Uranium Nitride Experiment 57
4. Zirconium Metallurgy 59
Tubing Fabrication Study 59
Circumferential Texture Variations in Zircaloy Tubing 60
Texture Gradients in Thin-Walled Zircaloy Tubing 61
Deformation and Annealing Textures in Drawn Zircaloy Tubing 62
Texture Development in Single-Crystal Zirconium 62
Deformation of Zirconium at Elevated Temperatures 62
Texture Determination by Optical Methods 63

Part II. Coolants

5. Alkali Metal Corrosion Studies 75
Compatibility of Boiling Potassium with Refractory Alloys 75
Refluxing Capsule Experiments 75
Natural Circulation Loop Tests 84
Forced Circulation Loop Tests 85
Corrosion of Refractory Alloys by Lithium 101
Capsule Tests on Welds of Tantalum-Base Alloys 104

Thermal Convection Loop Tests 110

Forced Circulation Loop Tests 122

Interactions in Refractory Metal—Alkali Metal Systems Containing Oxygen 141

Diffusion of Oxygen in Niobium 141

The Effect of Oxygen on the Compatibility of Tantalum and Potassium 142

Partitioning of Oxygen Between Potassium and Zirconium and Sodium and Zirconium 146

Part III. Radiation Damage to Structural Materials

6. Behavior of Refractory Materials Under Irradiation 151

Irradiation Damage to Nonfissionable Refractory Materials 151

Refractory Metal Carbides 151

Refractory Metal Nitrides 155

Refractory Metal Silicides 157

Effects of Irradiation on LMFBR Fuels 158

7. Fast-Neutron Irradiation Effects on Electrical Insulators . . 159

General Survey of Fast-Neutron Effects on Electrical Insulators 160

Oxides (Al_2O_3, MgO, Si_2ON_2) 162

Specific High-Density Al_2O_3 Commercial Products Considered for Thermionic Insulators 162

Irradiations of Three Types of Al_2O_3 at 600, 800, and 1100°C in the ETR 163

Irradiation of Three Types of Al_2O_3 at 800°C in EBR-II 163

Metal-Clad Al_2O_3 Specimens (ETR) 164

Irradiation of Improved Al_2O_3 164

8. Mechanical Properties Research and LMFBR Cladding and Structural Materials Development 165

Irradiation Damage to Types 316 and Titanium-Modified Type 316 Stainless Steel 165

Results on Standard Types 316 and 316L Stainless Steel 166

Results on Titanium-Modified Types 316 and 316L Stainless Steel 167

Mechanical Properties of Titanium-Modified Type 304 Stainless Steel 171

Electron Microscope Evaluation of Titanium-Modified Type 304L Stainless Steel 174

Drawing of Stainless Steel Tubing 175

The Effect of Cyclotron-Injected Helium on the Creep-Rupture Properties of Type 304 and 0.2% Ti-Modified Type 304L Stainless Steels 176

Electron Microscopy of Irradiated EBR-II Fuel Cladding . . 183

Annealing of Defects 185

Some Effects of Grain Size on the Radiation Damage of Incoloy 800 188

Voids in Vanadium Irradiated in EBR-II 195

Comparison of Laboratory and Commercial Heats of Titanium-Modified Hastelloy N 198

Commercial Melts 198

Laboratory Melts 200

9. Radiation Effects in Alloys and Structural Materials 202

Inhomogeneous Distribution of Tantalum and Tungsten in Zone-Refined Niobium 204

Experimental Procedure 205

Results and Discussion 206

Conclusions 210

The Effect of Interstitial Impurities on Postirradiation Annealing Phenomena in Niobium 210

Experimental Procedures 211

Results 213

Discussion 220

Pseudo Snoek Peak in Niobium 222

Specimen Preparation 222

Experimental Procedures and Results 224

Discussion 228

Radiation Anneal Hardening in Niobium 230

Dislocation Channeling in Neutron-Irradiated Niobium . . . 234

Experimental Details 236

Results 238

Discussion 259

The Temperature Dependence of Radiation Hardening 264

Part IV. Techniques of Fabrication and Testing

10. Tungsten Metallurgy 271

Primary and Secondary Working of Tungsten and Tungsten Alloys 271

Extrusion of Tungsten and Tungsten Alloys 271

Hot-Plug Drawing of Tungsten and Tungsten Alloys . . . 280

Chemical Vapor Deposition of Tungsten Alloys 281

Deposition of Tungsten-Rhenium Sheet for Mechanical Properties Evaluation 281

Investigation of Methods for Producing Fine-Grained Deposits 284

Parametric Studies of the Tungsten-Rhenium Codeposition Process 285

Metallurgical Properties of Tungsten Alloys 286

Long-Time Creep-Rupture Properties of Tungsten Alloys . . . 294

Evaluation of Welds and Brazes in Tungsten Alloys 295

11. Nondestructive Test Development 302

Electromagnetic Studies 302

Ultrasonic Test Methods 305

Optical Visualization of Ultrasound 305

Frequency Analysis 306

Holography 306

12. Joining Research on Nuclear Materials 307

Weldability Studies 307

13. Fuel Element Fabrication Development 310

Irradiation Studies of Dispersion Plates 310

Fuel Plate Fabrication 311

Examination of Arc-Melting Techniques for Preparing UAl_x 311

UAl_x Particle Preparation 311

Determination of Powder Particle-Size Distribution of Research Reactor Fuels 312

The Effect of Fuel Concentration on the Swelling of Fuel-Aluminum Compacts 316

Mechanisms of Swelling in UAl_x-Al Compacts 317

Compressive Strengths of U_3O_8- and UAl_3-Al Composites 320

Effect of Billet Feed Angle on the Curl of Rolled Plate 321

Investigations of Nonuniform Deformation in Simulated Fuel Plates 323

Development of Ductile Dispersion-Strengthened Aluminum 329

Heat-Treatment Studies on Flame-Produced UO_2 Powders 331

Preparation of PuO_2 Powder from PuF_6 by Chemical Vapor Deposition 334

Plate Surface Studies 334

Structure of Anodic Films Formed in Oxalic Acid 335

Effect of the Temperature of the Anodizing Bath 335

Flowing Loop Tests 337

14. Sintered Aluminum Products Development 339

Part V. Engineering Properties of Reactor Materials

15. Physical and Mechanical Metallurgy of Refractory Alloys . . 343

Basic Physical Metallurgy Studies 343

Solubility, Diffusivity, and Permeability of Interstitials in Refractory Metals 343

Interaction of Stress and Vacuum on Properties of Superalloys at Elevated Temperatures 344

Development of Age-Hardening Refractory Alloys 345

Long-Time, High-Temperature Mechanical Properties of Commercial Refractory Alloys 350

Molybdenum Alloys 350

Welding and Brazing Development 352

Brazing Alloy Development 352

Physical Properties of Refractory Materials 355

Physical Properties of Molybdenum 355

Nondestructive Testing 357

Ultrasonic Inspection of Tubing 357

SUMMARY

PART I. FUELS AND CLADDINGS

1. Sol-Gel Fast Reactor Fuels

We continued preparing, developing, and testing sol-gel-derived fuels for fast reactors. Most of the equipment for fabrication and out-of-reactor characterization of plutonium-bearing materials has now been placed into operation. Emphasis during the quarter was on preparing materials and capsules for irradiation testing in the TREAT and in the EBR-II.

We prepared about 3 kg of (U–20% Pu)O_2 for fuel fabrication studies and for irradiation test capsules, but much of this cannot be used in the irradiation test capusles because of various structural imperfections in the microsphere product. In Sphere-Pac development, we completed scoping investigations with ThO_2 microspheres. We set up equipment for packing microspheres of (U,Pu)O_2 in TREAT and EBR-II capsules and initiated preliminary tests using ThO_2 microspheres. We investigated methods of pressing and sintering sol-gel-derived material to fabricate pellets of the proper size with a density of 0.84 ± 0.008 of theoretical for TREAT irradiation tests. It appears that we now have an adequate procedure to meet this specification. After a delay of about one year, we have resumed extrusion development, using UO_2 as a stand-in material for (U,Pu)O_2.

Other fabrication work included preparing a system for filling capsules with sodium and procuring and machining materials for fabrication of various capsules.

The examination of the third uninstrumented capsule in the ETR series was essentially completed. This capsule was irradiated for one ETR cycle with a peak linear heat rating for the central two fuel rods of about 14 kw/ft. The metallographic examination of the fuel rods showed evidence of the evaporation-condensation mechanism of fuel densification, and radial redistribution indicates that the microporosity that was present in the fine UO_2 microspheres before irradiation has disappeared, even in the coolest regions of the fuel rod. Our examination

also revealed the development of porosity in the densified microspheres that are just in contact with the outer edge of the sintered zone. The first instrumented test of mixed oxide Sphere-Pac fuel in the ORR was operated and removed from the ORR during this quarter. The capsule operated within the designed temperature range, and the only difficulty was a period of erratic behavior in the central fuel thermocouple. Our preparations for the transient test program included further reactor physics calculations to investigate various types of thermoneutron filters and additional design work on the TREAT capsule. A proposal for approval in principle for EBR-II irradiation tests of sol-gel fuels was reviewed by the EBR-II Experimental Review Committee. The committee suggested that we modify our schedule to start testing five encapsulated Sphere-Pac test rods in a shared 19-rod subassembly in July or August and plan to do the rest of the proposed testing in unencapsulated rods. We began procurement, inspection, and fabrication of the necessary hardware for the five encapsulated test rods.

2. Nitride Fuels Development

We developed a technique for manufacturing single-phase UCN from mixed UO_2-carbon sols by firing dried gels in nitrogen. More rapid conversion and lower reaction temperatures are possible than from alternate schemes.

Kinetic studies on the conversion of UC_2 microspheres to UCN showed that the reaction is interface controlled instead of diffusion controlled. The reactor kinetics are affected markedly by exposure of the carbide to moist air.

Work was continued on the facility for manufacturing and characterizing mixed (U,Pu)N. Several units are now checked and ready for use.

Measurements of the hot hardness of UN showed that material with low oxygen content is markedly softer than UC between 600 and 1000°C.

Studies of the V-C-N phase diagram showed that active carbon is produced by the reaction of UC with nitrogen and that thermodynamic equilibrium is achieved only in the presence of graphite.

Studies showed that the thermal contact conductance between UN and stainless steel is not very sensitive to the hardness of the stainless steel. Use of a soft metal, such as copper, at the interface markedly improves the contact conductance.

3. Fission-Gas Release and Physical Properties of Fuel Materials During Irradiation

Enriched single-crystal spheres of UO_2 were found to have fractured into small fragments after irradiation to a burnup of 4.6 at. % U. The fracturing process apparently began at a burnup level of about 1.9 at. % U. We think the fracturing is due to concentrations of fission products at internal defects.

A gamma-ray heating experiment was performed but has not yet been evaluated.

Uranium nitride showed a higher fission-gas release than UO_2 at temperatures greater than 800°C. The gas release appears to be by a classical diffusion process with no apparent irradiation trapping.

4. Zirconium Metallurgy

We have now completed much of the proposed experimental fabrication of Zircaloy tubing. Cold drawing experiments are in progress. Texture and property measurements are being made on the finished tubing.

We continued our investigations of circumferential and through-wall texture variations in thin-walled Zircaloy tubing. Several fabrication variables can be directly related to the variations that are found.

We have also seen that, at least in some lots of tubing, alpha-annealing has a much greater effect on the recrystallization texture than has been reported previously.

An optical method of texture approximation for polycrystalline Zircaloy is being developed. This method is based on bireflectance measurements made on polished metallographic sections in plane polarized light.

5. Alkali-Metal Corrosion Studies

Refractory metals and alloys of Nb, Ta, Mo, and W have been tested in boiling potassium at temperatures up to 1400°C for times to 5000 hr, and the cumulative operating time for these systems now exceeds 100,000 hr.

In refluxing capsule experiments, unalloyed niobium was attacked by pure and oxygen-contaminated potassium after 5000 hr at 1200°C while Nb–1% Zr was not. We believe that in the absence of a strong oxide former, such as zirconium, the very high local oxygen concentrations that occur during boiling could have caused this corrosion.

Mass transfer between CVD tungsten inserts and a capsule of tungsten produced by powder metallurgy occurred after 5000 hr at 1240°C. We suspect that impurities in the potassium were responsible.

Two natural circulation–boiling potassium loop tests were completed. Examination of a TZM loop that operated for 4400 hr at 1200°C is in progress. Very small weight changes (< 3 mg/cm^2) were found in the condenser section of an FS-85 loop after 1300 hr at 1200°C.

We have continued analytical examination of the boiling potassium–Nb–1% Zr loop that operated 3000 hr at a maximum temperature of 1095°C. Recent data confirm and describe in detail the transfer of minor amounts of zirconium around the loop. A second boiling potassium loop fabricated of D-43 completed 10,000 hr of operation at a maximum temperature of 1205°C, and the test was terminated for examination. The loop was on-line about 96% of the calendar time since startup. Operational history and difficulties encountered with the NaK secondary circuit, control equipment, and vacuum ion pumps are described.

The effect of oxygen contamination of T-111 and T-222 weld specimens on their corrosion resistance to lithium was determined in 100-hr tests at 750 and 1200°C. No attack of weld or heat-affected zones was observed in samples containing up to 540 ppm O. However, we found attack to a depth of 0.010 in. in the base metal of these samples unless it had been heat-treated for 2 hr at 1300°C after welding. We ascribed this effect to the fact that HfO_2 formed in the weld and heat-affected zone during welding but not in the base metal until the sample was heat-treated at 1300°C.

Analysis of data from Nb–1% Zr loops that operated for 3000 hr at maximum hot-leg temperatures of 1200 and 1300°C indicates a number of differences. Weight losses occurred over two-thirds of the loop length at 1200°C but only over one-third of the length at 1300°C. Zirconium mass transfer accounts for approximately one-half of the weight changes at 1200°C. Although much greater mass transfer of zirconium occurred at 1300°C, it accounted for a smaller fraction of the weight changes, since niobium was the principal element involved.

The diffusivity of zirconium in Nb–1% Zr was determined to be 3.07×10^{-13} cm^2/sec at 1170°C and 6.04×10^{-12} cm^2/sec at 1275°C with an activation energy of 67,500 cal/mole. These data are in good agreement with extrapolations of published data at higher temperatures.

The design, procurement, and fabrication associated with a liquid lithium–forced circulation loop test facility are outlined. Design work and procurement of refractory metal and stainless steel are complete. Fabrication of stainless steel supporting equipment is essentially complete, and welding of T-111 assemblies is in progress.

A study of the niobium-oxygen-potassium system has shown that oxygen migrates from the niobium to the potassium. We calculated the diffusion coefficient of oxygen in niobium to be 3.50×10^{-9} cm^2/sec at 600°C, 2.23×10^{-8} cm^2/sec at 815°C, 4.35×10^{-7} cm^2/sec at 1000°C, and 1.64×10^{-6} cm^2/sec at 1250°C. These results are in good agreement with those found in the literature.

The role played by oxygen in the corrosion of tantalum by potassium is being investigated at 600, 800, and 1000°C. The 600°C results show that oxygen migrates from the tantalum to the potassium – even under the conditions where oxygen has been added to the potassium – and that the amount of oxygen dissolved by the potassium increases with an increase in the oxygen concentration of the potassium.

Studies of the partitioning of oxygen between potassium and zirconium and sodium and zirconium are being conducted in conjunction with our program to develop techniques for analyzing the oxygen concentration of alkali metals. The equilibrium partitioning coefficient (κ°) of oxygen between zirconium and potassium was found to be $\gg 30$ at 815°C.

6. Behavior of Refractory Materials Under Irradiation

Low-temperature (300 to 700°C) irradiations of carbides of refractory metals (Ti, Zr, Ta, Nb, and W) produced an increase in gross volume up to a neutron dose of about 1.5×10^{21} neutrons/cm^2 (> 1 Mev). A shrinkage then occurred at higher doses. A damage model has been proposed to explain this swelling-shrinkage phenomenon. High temperature (1000 to 1100°C) irradiations revealed an in-reactor thermal annealing effect. It was found that neutron doses as large as 4.8×10^{21} neutrons/cm^2 (> 1 Mev) at 1000 to 1100°C produced virtually no gross damage or expansion of lattice parameter. Gross volume expansion was much less than at low-temperatures, and in some cases specimens shrank to less than their preirradiated volumes. The damage model proposed for low-temperature irradiations is being extended to include thermal annealing effects in order to explain the results.

Examinations of refractory metal nitrides and silicides irradiated at high temperature (1000 to 1100°C) are in progress.

Irradiation experiments have been designed for determining the effect of the (n,α) reaction on LMFBR nitride fuels. Depleted fuel specimens are being prepared by the Metals and Ceramics Division for these experiments.

7. Fast-Neutron Irradiation Effects on Electrical Insulators

We are determining the effects of fast neutrons on the properties of electrical insulators considered for use in nuclear-powered thermionic converters. The main effort is on Al_2O_3. Large-grained Al_2O_3 fracture at low temperatures (300 to 600°C) when exposed to neutron doses greater than 3×10^{21} neutrons/cm^2 (> 1 Mev). Results of irradiations at higher temperatures (700 to 1000°C) indicate that in-reactor thermal annealing may extend the useful life of this material as a thermionic insulator. A new series of irradiations of high-density Al_2O_3 ceramics is in progress. Three types of Al_2O_3 commercial products in the form of both solid cylinders and thin-walled cylindrical shells are being irradiated in the ETR at 600, 800, and 1100°C. These specimens are all of small grain size, which should minimize grain boundary separation,

the precursor of gross fracturing in large-grained Al_2O_3. We are also trying to find the effect of dose rate on property changes in these experiments, and we have planned irradiations in the EBR-II to obtain information on neutron energy effects. Metal-clad cylindrical shells of Al_2O_3 will be irradiated in the same facilities to test their resistance to fast neutrons under conditions that may be expected to exist in operating thermionic converters.

8. Mechanical Properties Research and LMFBR Cladding and Structural Materials Developement

Postirradiation creep-rupture testing of types 314 and 316L stainless steel indicates that the properties are dependent upon the irradiation temperature. As the irradiation temperature is increased in the range 550 to 750°C the creep rate and ductility increase. We believe this is due mainly to thermal aging. A few tests on the titanium-modified type 316 stainless steel compositions indicate this alloy to be stronger and more ductile for similar irradiation and testing conditions.

Further postirradiation testing of the large heat of type 304 stainless steel containing 0.2% Ti shows that its resistance to high-temperature embrittlement is improved over standard type 304 stainless steel. A study of the precipitates and precipitation processes in titanium-modified type 304L stainless steel indicates that the size of the small (500-A-diam) precipitates is reasonably stable at 700°C. Some evidence has been obtained that sulfur exists in high concentrations in the titanium-bearing precipitate particles.

Fabrication of the first experimental lots of tubing from both the high- and low-carbon heats of titanium-modified type 304 stainless steel is nearing completion. Our studies indicate that both compositions can be satisfactorily fabricated.

The resistance of the modified type 304L stainless steel to helium embrittlement under creep-rupture testing has been demonstrated. Thus far, we have examined the effects of cyclotron-injected helium to concentrations of 20 ppm.

Driver fuel cladding for EBR-II, annealed after irradiation, shows the annealing behavior of voids strongly dependent on their initial size. Voids with a maximum diameter of 187 A are removed in 1 hr at 700°C, whereas 800°C is required to anneal voids 300 A in diameter.

Incoloy 800 specimens with various carbon and titanium contents and grain sizes have been irradiated at 700°C, and the postirradiation testing of tensile and creep properties is under way. As we expected from our previous experience with stainless steels, there are important effects of titanium and carbon concentration in addition to the expected effects of grain size.

We have recently begun an examination by electron microscopy of unalloyed vanadium irradiated as fuel cladding in EBR-II at 630°C to a fast neutron fluence of 1.7×10^{22} neutrons/cm^2. Voids from 70 to 220 A in diameter were observed in some of the specimens.

The effects of titanium concentration on the postirradiation creep-rupture properties of laboratory heats and small commercial heats of Hastelloy N have been found to be self-consistent.

9. Radiation Effects in Alloys and Structural Materials

Recent progress in the study of radiation damage and radiation hardening in niobium is reported. An investigation of methods for purifying and preparing niobium materials shows that tungsten and tantalum impurities exist in layers after electron-beam zone refining. This investigation used autoradiographic techniques, which are capable of distinguishing between the tungsten and tantalum impurities and yielding, potentially, a quantitative measure of their distributions.

The influence of interstitital impurities, particularly oxygen and carbon, on the response to radiation has been studied by internal friction and resistivity measurements. Previous work showed that oxygen atoms become trapped at defects produced by radiation at about 150°C in neutron-irradiated niobium. The detrapping process upon annealing above about 300°C is described. The internal friction results indicated a more rapid return of oxygen to solid solution than did the resistivity results. Extraneous contributions to the internal friction may be

involved, and there are evidences for a "pseudo Snoek" internal friction peak. Carbon impurities are removed from solid solution between 250 and 300°C in both unirradiated and — to a greater extent — in irradiated niobium containing carbon.

We believe the trapping of interstitial impurities at defects is responsible for radiation-anneal hardening, in which a further increase in strength is observed when irradiated metals are annealed at low temperatures. Evidence for this is presented: a decrease in carbon content caused a corresponding decrease in the magnitude of the radiation-anneal hardening; the hardening due to carbon trapping was consistent with the kinetics of carbon migration; and there was no dislocation channeling (the sweeping away of radiation-produced defect clusters by slip dislocations) in the radiation-annealed niobium. This is consistent with the idea that the defect clusters are stronger barriers to dislocation motion when interstitial impurities are trapped at the defect clusters.

We investigated the phenomenon of dislocation channeling in irradiated niobium in detail by diffraction contrast and stereoscopic transmission electron microscopy. We estimated the strain in the channels from the offset in microstructural features where they were crossed by the channels; the strain corresponded to the passage of several dislocations per atomic plane. We also determined the crystal geometry; in most cases the channel plane was {110}. Possible mechanisms of channeling are discussed.

Finally, some comments concerning the theory of dispersed barrier hardening are given, with particular application to the effect of the barriers on the temperature dependence of yielding.

10. Tungsten Metallurgy

We extruded billets of tungsten and tungsten alloy as primary and duplex extrusions in the form of tube shells, round bars, and sheet bar at 1650 to 1870°C and extrusion ratios of 3.6 to 9.6. We successfully applied the techniques developed for the floating-mandrel extrusion of tungsten-alloy tube shells from 3-in.-diam billets to the production of tube shells 2 1/2 in. in outside diameter and 1 1/4 in. in inside

diameter and tube shells 3 3/8 in. in outside diameter and 2 3/8 in. in inside diameter from 4- and 6-in. diam billets.

In the hot-plug drawing program, we evaluated lubricants and tooling for use at 700 to 1200°C and found that a petroleum-base lubricant was superior to glass lubricants at these temperatures. The dies with zirconia inserts performed well, but we have not solved the problem of breakage of the zirconia-coated drawing plugs. A W–30% Re–30% Mo duplex-extruded tube was reduced 30% in three passes at 1050°C without intermediate anneals.

We developed techniques for the chemical vapor deposition (CVD) of tungsten-rhenium alloy sheet for mechanical properties evaluation. An alloy sheet, nominally W–5% Re, was deposited, yielding about 42 in.^{2} of flat stock with a minimum thickness of 0.045 in. Due to residual stresses, however, most of the material cracked during the grinding of specimens.

We investigated a method for producing fine-grained deposits of tungsten-rhenium alloys by deposition of alternate layers of tungsten and rhenium or the alloy. Annealing 100 hr at 2000°C produced a nearly equiaxed grain structure with a grain size of about 100 μm.

Initial parametric studies of the tungsten-rhenium codeposition process did not confirm a previous thermodynamic analysis that predicted a variation of rhenium content in the gas mixture and deposit with variations in temperature or pressure.

Chemically vapor deposited tungsten rolled to reductions of 40 to 95% at 600 to 1000°C had recrystallization temperatures greater than 1800°C. The material contained 25 ppm F, and observations before annealing and by electron microscopy showed that gas bubbles less than 400 A in diameter and/or fluorine impurity clusters were responsible for retarding recrystallization. Because of its resistance to recrystallization and grain growth, the CVD material has a lower ductile-to-brittle transition temperature (DBTT) than conventionally produced tungsten after annealing at 1400 to 2000°C.

Creep-rupture studies on arc-cast tungsten and tungsten-rhenium alloys at 1650 and 2200°C showed that for 1000-hr rupture lives the creep and rupture strengths decrease in the order W–5% Re, W, W–26% Re, W–25% Re, and W–25% Re–30% Mo.

Successful TIG welding of 1/16-in.-thick unalloyed tungsten sheet required a preheating to at least 150°C. The DBTTs for welds in two different grades of sheet derived by powder metallurgy were about 200°C higher than those for unwelded material, independent of the amount of porosity. The hardness of bead-on-plate welds with W–26% Re filler metal on unalloyed tungsten sheet decreased with aging time and with temperature from 900 to 1600°C.

11. Nondestructive Test Development

We are developing new techniques and equipment for the nondestructive evaluation of materials and components. The major emphasis has been on eddy-current, ultrasonic, penetrating radiation, and holographic methods.

Our analytical work on electromagnetic phenomena has included use of our newly developed closed-form solutions with computer programming to generate numerical solutions to various eddy-current tests. This has included determination of the expected response from discontinuities and the calculation of coil impedance for a coil surrounding a rod with a uniform cladding. Experimental studies are under way to determine the effective field of a small coil.

We have modified our optical system for viewing ultrasonic energy so that it uses parabolic mirrors rather than lenses. This has expanded the field of view and increased sensitivity. The system for frequency analysis has been calibrated for quantitative measurement of amplitude and is now ready for application to actual test problems.

Since we fabricated a detector for measuring laser intensity, we have been able to maintain proper ratios between reference and object beams.

Our holographic studies have included fabricating and using a light meter for adjusting the relative intensities of the reference and object beams. We are studying depth of field for both single- and multiple-beam systems.

12. Joining Research on Nuclear Materials

We are studying the effects of combined phosphorus and sulfur on the hot ductility of heat-affected zones of welds in Inconel 600. Phosphorus contents up to 0.015 wt % did not appreciably affect the zero-ductility temperature; however, high phosphorus does seem to reduce the ductility on heating at elevated temperatures. Also, alloys that contain phosphorus and moderate amounts of sulfur have lower ductilities than the alloys with lower sulfur contents.

13. Fuel Element Fabrication Development

Production of fuel elements for the High Flux Isotope Reactor (HFIR) has continued on schedule at Metals and Controls, Inc. Work on Phase II has been completed, and work under Phase III has been started. Fuel plate yield for this period has been a phenomenal 95.2%. Bond and surface defects continue as the primary causes for rejections.

Technical assistance to the Reactor Development Technology Division on fuel element procurement was continued with the preparation of AF-NETR and ORR specifications and in making technical audits of the fabricators of fuel elements.

We are studying dogboning in simulated fuel plates by using various combinations of 1100, 6061, and X8001 aluminum. Dogboning will occur at both ends of a plate, even when all reduction is in one direction. We conclude that dogboning is observed when the core material is stronger than the frame and cover plate and that the thickness of the cover plate also has a small effect on the amount of dogboning. Dogboning increases fairly constantly with the first few rolling passes until a given thickness has been achieved. We measured large differences between the high-temperature compressive strengths of aluminum-base dispersion compacts containing UAl_3 and those with U_3O_8. The differences increased with increasing fuel concentration and decreased with increasing temperature.

A major problem in preparing UAl_3 powder fuels is the minimizing of the proportion of fines produced during comminution. We have tried a variety of comminuting techniques but have had very little success in reducing the proportion of fines. The measured distribution of particle

sizes during comminution was reproducible but was a function of the method of measurement.

Swelling of UAl_3 is a two-stage process resulting from release of gases and a diffusion-induced transformation. Above a certain fuel concentration, the amount of swelling increases rapidly with increasing fuel concentration. The swelling occurred fairly rapidly and was not highly sensitive to the sizes of fuel particles.

In an effort to obtain on aluminum a corrosion film with improved thermal conductivity, we tested and characterized various anodizing techniques. Oxalic acid showed the most promise. The film characteristics are dependent upon the bath temperature, with lower temperatures appearing to be superior. While the results were somewhat ambiguous, anodized type 6061 aluminum simultaneously exposed to flowing water and a high heat flux suffered only half the corrosion that would be expected of a bare specimen.

With type 1100 aluminum, a linear decrease in density occurred with increasing fast neutron fluence; there was a 1.5% decrease at a fluence level of 1.5×10^{22} neutrons/cm^2. Damage to the hex sheaths of the TRU targets in the HFIR took two forms: numerous voids resulting from the agglomeration of excess vacancies produced from knock-on reactions and a finely dispersed precipitate that we suspect is silicon. Cold work eliminated the voids. We did considerable work to better characterize the as-irradiated material. After anneals from 260 to 480°C, large pores were associated with large inclusions; however, they were absent after a 600°C anneal. A 24-hr anneal at 600°C, which had caused a Swiss-cheese-like porosity in irradiated specimens, produced no porosity in unirradiated material. With unirradiated material, recrystallization was complete at 260°C, where it had not even started with the irradiated material.

14. Sintered Aluminum Product Development

We have concluded our investigation into the influence of processing variables during the fabrication of SAP billets. Our efforts toward developing a ductile SAP alloy will continue. Atomized-aluminum alloys

have been ball-milled and consolidated into billets by the primary billet consolidation process developed at ORNL. These alloy billets have been extruded into rod and are now being evaluated. With this reporting period, the SAP work has been terminated as a separate program. In the future, our reduced efforts on the development of ductile SAP alloys will be part of the Fuel Element Fabrication Program.

15. Physical and Mechanical Metallurgy of Refractory Alloys

We correlated evaporation losses and microstructural characteristics with stress and creep behavior of Haynes alloy No. 25 in vacuum. We found that (1) evaporation losses increased with increasing stress, (2) the amount of Laves phase increased with increasing stress, (3) the rupture life and time to 1% creep were drastically decreased in vacuum, and (4) the creep properties were sensitive to section thickness.

Attempts to calculate the solubility and diffusivity of nitrogen in tungsten from measurements of the degassing rate of nitrogen from tungsten were unsuccessful due to degassing of the vacuum apparatus. The equipment is being modified to minimize this problem.

In studies on age-hardening refractory alloys, we calculated critical temperatures for transformation of high-temperature solid solutions by coherent spinodal decomposition for the Ta-Hf, Nb-Hf, Ta-Zr, and Nb-Zr systems. However, x-ray diffraction studies on quenched and aged specimens indicated that these systems do not undergo spinodal decomposition but precipitate spherical particles that gradually become needlelike with aging time. Plots of hardness versus aging time reveal a minimum between 1000 and 1200°C.

We determined the 1000-hr creep-rupture strengths of the molybdenum alloys TZC, TZM, and Cb-TZM (columbium-modified TZM) from 975 to 1325°C on specimens with various fabrication histories. Certain fabrication sequences were found to have substantially favorable effects on TZM and Cb-TZM. At 980°C, 1000-hr rupture stresses of 90,000 to 100,000 psi were obtained.

We evaluated brazing alloys in the titanium-zirconium-germanium system for joining refractory metals and graphite. Tests indicate the

Ti–46% Zr–8% Ge alloy to be the most attractive for the refractory metals and the Ti–20% Zr–15% Ge alloy the most attractive for graphite.

We measured the electrical resistivity and thermoelectric power of pure molybdenum from 100 to 1700°K and determined the thermal conductivity from 100 to 1250°K. The Lorenz number determined with these data exceeded the Sommerfeld value and was similar to the value determined earlier for tungsten. The lattice contribution to the thermal conductivity was smaller than determined for tungsten.

Ultrasonic equipment was modified to provide strip-chart recordings for permanent records of wall-thickness and eccentricity measurements on refractory alloy tubing.

PART I

FUELS AND CLADDINGS

1. SOL-GEL FAST REACTOR FUELS

A. L. Lotts

Periodic recycling of fuel from fast breeder reactors is necessary to obtain the full economic potential of such reactors operating on the ^{238}U-plutonium cycle. Recycling requires that an irradiated fuel be chemically processed, that the fissile isotopes be reconstituted along with fertile isotopes, and that these isotopes be refabricated into fuel elements. The sol-gel process is ideal for reconstituting fuel from aqueous chemical processing of spent fuel elements. The products of the sol-gel process are, however, structurally different from mixed oxide fuels prepared by other processes. At least the starting fuel forms in refabricated fuel elements containing fuel produced by the sol-gel process will be different in some respects from fuels derived by other routes. Accordingly, the objective of the Sol-Gel Fast Reactor Fuels program is to determine the performance limits of sol-gel-derived $(U,Pu)O_2$ fuel. This will allow us to assess the potential of sol-gel fuels for use in liquid metal-cooled fast breeder reactors and in the Fast Flux Test Facility.

The main task areas of the program are (1) the preparation of $(U,Pu)O_2$ fuel by the sol-gel process, (2) out-of-reactor testing to characterize sol-gel products, (3) the development of fabrication procedures for incorporating mixed oxide fuel into suitable fuel rod components, and (4) the irradiation testing of the fuel. The activities of the program now include (1) preparing a variety of $(U,Pu)O_2$ products; (2) developing procedures for packing $(U,Pu)O_2$ microspheres for making $(U,Pu)O_2$ pellets and for extruding sol-gel-derived clay; and (3) irradiating uninstrumented capsules in the ETR to test Sphere-Pac $(U,Pu)O_2$, irradiating instrumented capsules in the ORR, and designing and constructing experiments and capsules for transient testing and for irradiation experiments in the EBR-II. During the past quarter we have emphasized all of those special tasks necessary for preparing materials and capsules for testing in the TREAT facility and in the EBR-II.

Plutonium Ceramic Facilities

J. D. Sease M. K. Preston W. H. Pechin
R. J. Gray B. C. Leslie

The initial plutonium ceramic facilities for examining and preparing ceramic nuclear fuels that contain alpha-active nuclear materials have been essentially completed, and most of the equipment is operating. Only a few minor tasks remain.

Building 4508 Facilities

The characterization facilities installed in Building 4508 are reported elsewhere.[1]

Building 3019 Facilities

The preoperation and leak checks of the metallography line were completed, and the line was placed in hot operation on June 28, 1968. The large sintering furnace has been installed in laboratory 3 and is undergoing cold check-out. A new safety analysis is being prepared to cover the expanded operations in this building.

Preparation of $(U,Pu)O_2$ Sol-Gel Material

W. T. McDuffee

The sol-gel work reported here, being carried out in the Chemical Technology Division Pilot Plant, Building 3019, is part of a larger program on sol-gel process development and demonstration supported at ORNL.

This quarter 600 g Pu was prepared as aqueous PuO_2 sol for fuel fabrication studies. This material was mixed with UO_2 sol – also prepared for this program – and used to prepare shards for pelletizing studies. Two other lots of PuO_2 sol totaling about 315 g Pu were prepared for mixing with UO_2 sols to yield $(U\text{–}20\%\ Pu)O_2$ microspheres. The first lot (about 150 g Pu) was mixed with the appropriate quantity of

[1]E. S. Bomar *et al.*, pp. 39–40, this report.

natural UO_2 sol and formed into microspheres which, after drying in steam-argon, were calcined to 1200°C in steam-Ar–4% H_2 to greater than 96% of theoretical density and less than 40 ppm C. One-third of this lot of feed material was formed into small microspheres, 65% of which were less than 63 μ; the remainder was formed with an 80% yield of 420- to 595-μ microspheres. There was mild surface cracking in about 20 to 30% of the 420- to 595-μ fraction.

The second lot (about 165 g Pu) of PuO_2 sol was mixed with the appropriate volume of enriched UO_2 sol that had been prepared from 93% enriched uranium containing as impurities 900 ppm fluoride, 500 ppm sulfate, and 500 ppm phosphate. Two-thirds of the enriched mixed sol was formed into 420- to 595-μ microspheres with 41% yield, the loss being largely due to cracked beads and to doublets. The remainder of the feed was formed into fines, 95% of which were less than 63 μ in diameter. All the fired oxide from this lot was greater than 96% of theoretical density, but a significant fraction was badly cracked. In a partly successful effort to minimize cracking, we fired the last fraction of this lot and the smaller (fine) microspheres differently: we held the heating rate to 25°C/hr (instead of 100°C/hr) up to 600°C while maintaining a steam-argon atmosphere over the microsphere bed. Three 4-hr hold periods, at 200, 400, and 600°C, were included. Preliminary metallographic examination of the microspheres indicated that surface cracking was less severe, but the surface was not smooth. This shows the need for better quality control of our feed material.

Development of Fabrication Processes

J. D. Sease

Fast reactors operating at high specific powers will require small-diameter fuel pins with fuel 80 to 90% of theoretical density and a high fissile loading. To satisfy these requirements, we are investigating various fabrication processes for sol-gel-derived $(U,Pu)O_2$ fuels. This quarter, we concentrated on pelletizing and Sphere-Pac fabrication processes and on loading irradiation capsules using these processes.

We began developing extrusion as a means of fabricating sol-gel fuel, using UO_2 sols as a stand-in for mixed $(U,Pu)O_2$ sols. The construction of irradiation capsules for EBR-II and TREAT has begun.

Sphere-Pac (R. B. Fitts, W. L. Moore, A. R. Olsen)

Scoping investigations of the sol-gel Sphere-Pac process were completed this quarter. This technique is now being applied to the loading of $(U,Pu)O_2$ fuels for capsule irradiation testing in TREAT, EBR-II, and ORR facilities. Hardware preparation for this task and final development work on the application of Sphere-Pac to glove box fabrication of long fuel rods are under way.

Studies with ThO_2 Microspheres. — The initial investigation of the sol-gel Sphere-Pac fabrication technique is completed, and we are now studying the glove box loading of long fuel rods. A summary of the principal results of the scoping investigation has been prepared, and a paper has been submitted for oral presentation at the 1968 fall meeting of the American Ceramic Society.

A final point to be resolved was the uniformity of Sphere-Pac fuels formed by the blended bed approach. We have prepared four 10-in.-long by 0.345-in.-diam fuel columns by blending ThO_2 microspheres (4:1-diam ratio) for the coarse, blended bed and infiltrating final spheres. We measured the density variation with a gamma-ray absorption densitometer[2] before and after infiltration of the blended bed. One of the coarse beds was of uniform density (71 ± 1.5% of theoretical density) over the entire fuel length. Two had low-density regions (about 66% of theoretical density) 2 in. long at the bottom. The other exhibited low density at bottom and top. After the infiltration of small spheres, the low-density regions were gone, and the rods were of uniform density (88 ± 1.5% of theoretical density) over the entire length. The density variation in the blended bed before infiltration can probably be eliminated by more sophisticated or better controlled blending techniques. The obliteration of the low-density regions during infiltration is to be

[2]B. E. Foster and S. D. Snyder, Mater. Evaluation, 26(2), 27–32 (1968).

expected since the voids in these areas are larger, thus allowing more efficient packing of the fines.

Since the EBR-II tests will require loading 32-in.-long cladding tubes (13.5-in. fuel column), the loading will be greatly facilitated by holding the fuel rods at the top instead of the bottom, as was done previously. Gripping the rod at the top will permit it to be suspended in a well in the bottom of the glove box and will place the top of the tube within easy reach for filling. We began study of Sphere-Pac under these conditions by loading stainless steel tubes (0.250-in. OD × 0.016-in. wall thickness × 32-in. length) with ThO_2 microspheres, using a coarse fraction of 420 to 500 μ and a fine fraction smaller than 44 μ. The first loadings behaved as expected.

We are now studying the effect of energy input on loading time.

Fabrication of $(U,Pu)O_2$ Fuel Rods. — An existing 6-ft glove box for Sphere-Pac loading the EBR-II fuel rods has been set up in the Building 3019 Plutonium Laboratory and modified by installing a 3-ft well, a variable-angle vibratory unit, and a top pan balance. Cold check-out of this glove-box system with ThO_2 is in progress.

Additional sphere handling equipment was installed in another glove box in Building 3019. This included a pneumatic sphere impactor for breaking cracked micropheres and a shape separator.

Pelletizing of Sol-Gel $(U,Pu)O_2$ (W. L. Moore, R. A. Bradley)

Urania-plutonia pellets with densities of 84.0 ± 0.8 and 91.3 ± 0.9% of theoretical and oxygen-to-metal ratios of 1.980 ± 0.005 are required for transient tests in TREAT and to establish a process that would reproducibly yield pellets of the required density and oxygen-to-metal ratio.

Material Preparation. — The specifications for the TREAT fuel require that the ratio of plutonium to heavy metal (Pu/U+Pu) be 0.20 ± 0.01 and that all of the pellets for the entire TREAT series come from a homogeneous batch of material. We prepared about 2 kg of urania-plutonia powder by blending UO_2 and PuO_2 sols and tray drying the blended sol. It was necessary to blend and tray dry the sol in three batches due to criticality limitations, but the batches were

cross blended to ensure uniformity for the batch of TREAT material. Based on duplicate analyses for uranium and plutonium, the plutonium contents (Pu/U+Pu) of the three batches of tray-dried material were 0.199, 0.200, and 0.200. Due to the excellent agreement between batches, we believe that the cross blending was effective in producing a homogeneous batch of material.

The three batches of dried gel were blended, preground with a mortar and pestle, and then ground in a fluid energy mill.

Pressing and Sintering. — In our previous work we produced 73 to 86% dense pellets from tray-dried urania-plutonia. When we tried to make 84% dense pellets for TREAT, we found that the density was not reproducible; therefore, we have been investigating the effects of process variables on sintered density. The variables that are expected to affect the sintered density are (1) the physicochemical properties of the powder, (e.g., particle size distribution, surface area, crystallite size, particle density, moisture and other volatile content, and oxygen-to-metal ratio); (2) uniaxial forming pressure; and (3) sintering conditions, including heating rate, temperature, time at maximum temperature, and furnace atmosphere.

The physicochemical properties of the powder are determined mainly by the way the sols are formed and tray dried; due to its very high surface area (about 60 m^2/g), however, the powder is very active, and its properties may change from day to day unless it is handled and stored in a dry, inert atmosphere. This was clearly demonstrated when we sieved some tray-dried, jet-milled powder (Batch PuU-TD2) in air. The green densities of pellets pressed from the sieved powder were lower than those of pellets made from the same batch of material before it was sieved. The effect of sieving the powder in air on the relationship between green density and forming pressure is shown in Fig. 1.1. Curve A represents this relationship for Batch PuU-TD2, and curve B is for the same material after it was sieved in air through a 325 mesh screen. Since the weight loss during sintering of the pellets made from the sieved powder was only 7.4% compared to 8.9% for the powder that was not sieved, we believe that sieving the powder removed some of the moisture and thus affected its pressing characteristics. Further evidence of

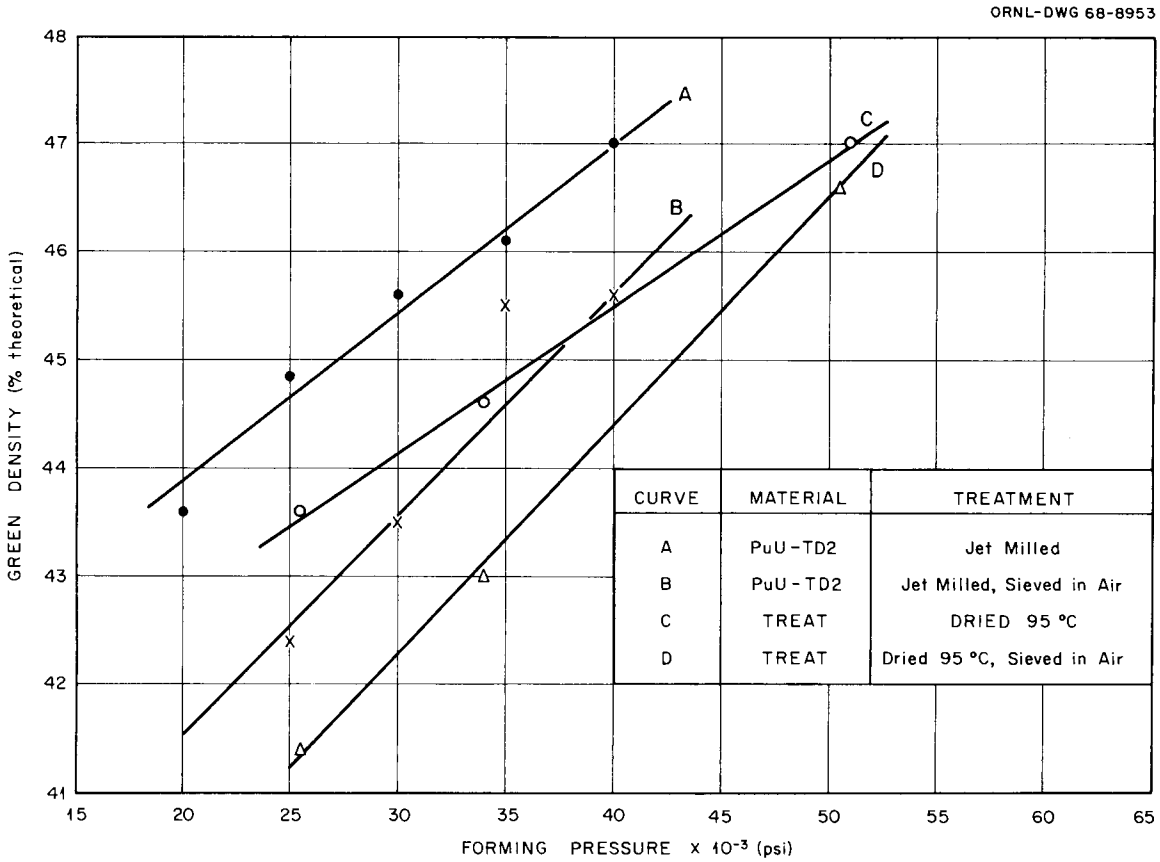

Fig. 1.1. Effect of Powder Treatment and Forming Pressure on the Green Density of Sol-Gel Urania-Plutonia Pellets.

this was the drying cracks present in pellets made from nonsieved powder but not present in those made from sieved powder. Drying the jet-milled powder at 95 °C in flowing argon had about the same effect as screening in air as illustrated by curve C in Fig. 1.1. Curve D shows the effect of screening the dried powder in air on the relationship between green density and forming pressure.

We tried to eliminate the effects of the physicochemical properties of the powder by producing a large, homogeneous batch of urania-plutonia powder for the TREAT pellets. The powder was prepressed at 10,000 psi and granulated to −60 mesh to increase its uniformity. All handling was done in an argon-purged glove box. Three pellets were pressed at 30,000, 35,000, and 40,000 psi from the granulated TREAT powder on six different days. The average green density of the 18 pellets for each pressure is plotted against forming pressure in Fig. 1.2. The maximum

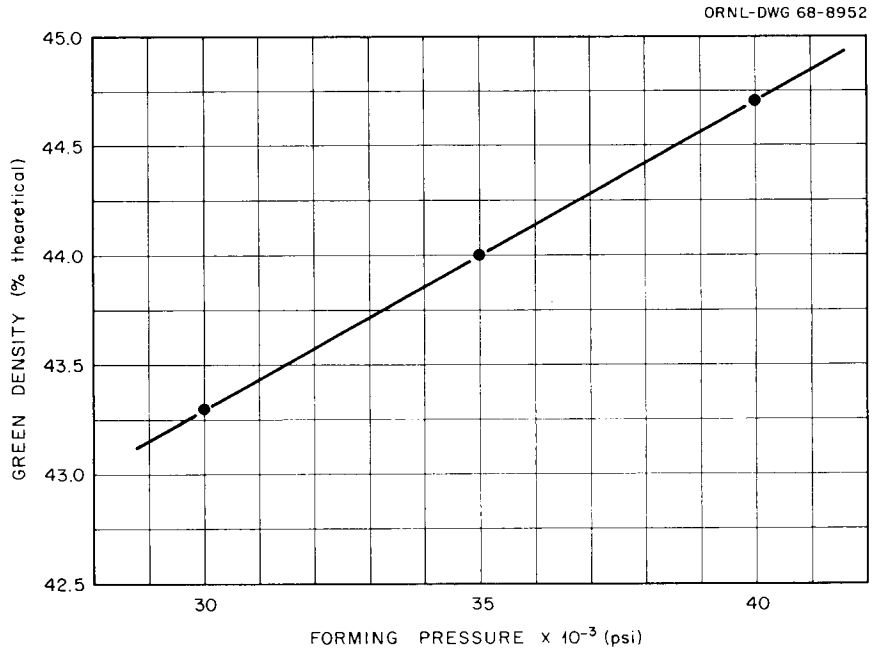

Fig. 1.2. Relationship Between Green Density and Forming Pressure for Granulated Sol-Gel Oxide Material for TREAT Experiments.

deviation from the average value was 0.1%. It appears that this variation will be acceptable for controlling the sintered density.

Pellets have been sintered at 125°C/hr to 1450°C in wet Ar–4% H_2, dry Ar–4% H_2, and CO_2. In each case the atmosphere was changed to dry Ar–4% H_2 at the end of the sintering run to reduce the oxygen-to-metal ratio. Sintered densities appear to be highest after sintering in CO_2 and lowest after sintering in dry Ar–4% H_2. For every sintering run there is a linear relationship between sintered and green density for pellets pressed at 30,000 to 40,000 psi; the reproducibility from run to run, however, is only about ±1%. We believe we can now make the 84.0 ± 0.8% of theoretical density pellets for the TREAT irradiation tests. The oxygen-to-metal ratio of pellets reduced at 1450°C in Ar–4% H_2 for 4 hr is 1.977 ± 0.002 (determined thermogravimetrically).

Extrusion of Sol-Gel Urania (C. R. Reese, R. A. Bradley)

We began an investigation to determine the feasibility of extruding sol-gel-derived urania into cylindrical rods suitable for insertion into LMFBR fuel pins. An extrusion press and other necessary equipment

were installed in an argon-purged box in the Interim Alpha Facility of Building 3019.

We have investigated different techniques of making an extrudable clay from urania-nitrate sol. High-speed centrifuging of nitrate sol in a small laboratory centrifuge produced a clay (approx 4 M) that we thought to be extrudable; when we tried centrifuging the nitrate sol in larger batches (300 ml), however, we were limited by equipment to a speed of 1800 rpm. This slower speed failed to produce a clay after 19 hr of centrifuging. Vacuum filtering the urania-nitrate sol through a fine alumina filter and filter paper failed to produce a residue.

We tried an anion exchange technique in which Dowex-3 anion exchange resin beads (free base form) were mixed with the nitrate sol. Hydroxyl ions on the beads were exchanged for nitrate ions in the sol. This allowed the small UO_2 particles to form agglomerates and create effectively larger particles. Centrifuging this sol at 1800 rpm produced a clay (about 3 M) within 10 hr. Vacuum filtering this anion-exchanged sol through filter paper produced a clay (about 3 M). We believe that the molarity of this clay could be increased by decreasing the rate at which material is fed to the filtering system.

Judging from our previous work with urania and with thoria,[3] we expect chloride-urania sol to yield a clay that is better for extrusion than the nitrate-sol-derived clay. The Chemical Technology Division is producing a chloride-urania sol for our experimentation.

Fast Reactor Capsule Fabrication (J. D. Sease, C. F. Sanders, M. K. Preston)

As part of our fast fuels irradiation program, we are committed to fabricate three types of capsules: (1) EBR-II, (2) TREAT, and (3) ORR. We plan to build completely the EBR-II and the TREAT capsules. We shall fabricate only fueled portions of the ORR capsule.

The EBR-II capsules now have priority, and we hope to have five capsules ready to ship to the EBR-II by the middle of August. The first TREAT capsule is scheduled to be ready around the first of September.

---

[3]R. B. Fitts, J. D. Sease, and A. L. Lotts, Chem. Eng. Progr. Symp. Ser. 63, 28–33 (1967).

Capsule Hardware Procurement. — Essentially all of the material for the EBR-II and TREAT has been received, and fabrication of the various components is beginning. The tubing for the EBR-II fuel rods has been received and inspected. The outer pressure vessel for the TREAT capsule was placed in the shop for fabrication, and various end-plug designs for this capsule are being fabricated for tests of weldability and structural integrity. Proof-test extensometers for the TREAT and EBR-II were fabricated. Weld-test specimens for the EBR-II were fabricated, and weld tests were performed.

Sodium Filling System. — We are fabricating a system for filling the annulus in the TREAT and EBR-II capsules with sodium. The sodium filling system we are building is based on a system being used by the General Electric Company.[4] A schematic of our system is shown in Fig. 1.3. The filling techniques consist of evacuating the capsule and

[4]S. A. Rabin, W. W. Kendall, W. E. Bailey, Short-Term Fast Flux EBR-II Irradiation of PuO_2–UO_2 Fuel Pins, GEAP-5570, pp. 41–45 (October 1965).

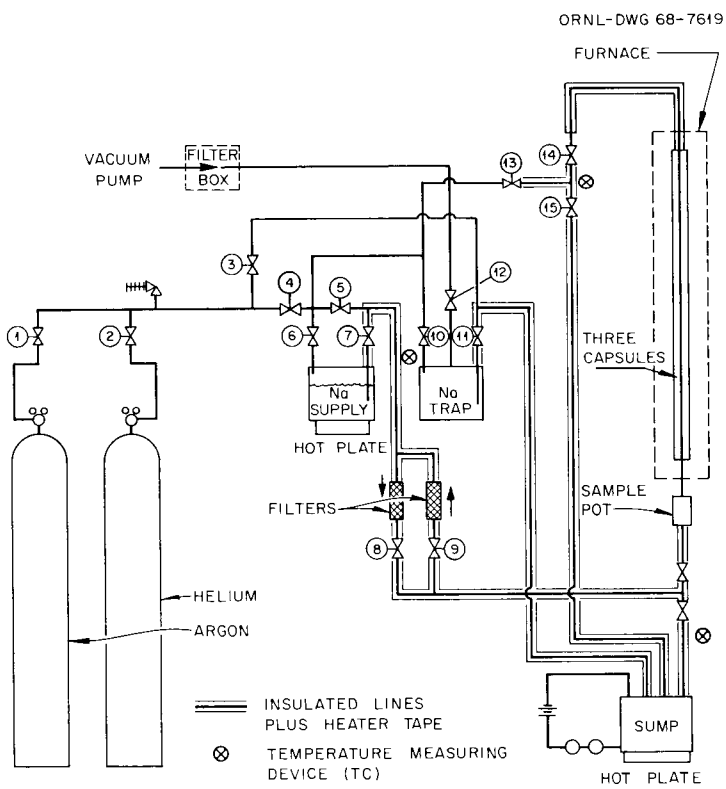

Fig. 1.3. Schematic of the Sodium Fill System

purging the capsule with sodium several times at 565 °C to ensure wetting followed by sodium filling at 175 °C. Bottom cooling will be used to minimize void formation. The system is now about 95% completed.

We plan to inspect the sodium annulus by eddy-current probes and radiography. Standards for the eddy-current inspection have been procured and set up, and the device is being tested.

Characterization of $(U,Pu)O_2$ Fuels

W. H. Pechin

The development of sol-gel fuel fabrication processes requires characterization of the starting materials to control the processing and characterization of the product to determine which properties are important in irradiation behavior. The characterization requires determination of chemical composition and physical properties.

Analytical Chemistry

The Analytical Chemistry Division has designed and built apparatus for measuring gas release from mixed oxide fuels at temperatures up to the melting point of the fuel. This equipment is in the final stage of installation. Data from duplicate determinations of uranium and plutonium by coulometric titration show a 95% confidence interval of ±1.25% for the ratio of uranium to plutonium.

The investigation of both the NITROX and the gravimetric methods for determining the oxygen-to-metal ratio of mixed oxides is continuing. For the NITROX method, the sample is fused in a graphite crucible with platinum and the resulting CO is measured by gas chromatography to determine the oxygen content of the sample. For the gravimetric method, as described by Lyons[5] and subsequently used by NUMEC,[6] the sample is dried in argon at 110 °C and oxidized in air at 750 °C to place all the

---

[5]W. L. Lyon, The Measurement of Oxygen-to-Metal Ratio in Solid Solutions of Uranium and Plutonium Dioxides, GEAP-4271 (May 1963).

[6]Development and Testing of PuO_2 - UO_2 Fast Reactor Fuels Prog. Report January 1, 1967 to March 31, 1967, NUMEC 3524-37.

plutonium in a +4 oxidation state and then reduced in He–6% H_2 at 700°C to bring all the uranium to +4 without reducing the plutonium below +4. At this point the sample is stoichiometric $(U,Pu)O_{2.00}$, and the net weight change indicates the nonstoichiometry of the starting sample. Mathematical comparison of the two methods indicates that the confidence interval for the gravimetric analysis should be about one-tenth of that for the NITROX, and the gravimetric analyses made so far have demonstrated this. The indicated standard deviation with thermogravimetric analyses is 0.001. We are trying to determine the accuracy of the gravimetric analysis by analyzing a sample of known stoichiometric $UO_{2.00}$. Preliminary results with a UO_2 powder have been about 1% low. This low result may have been due to the oxidation of the sample between the time it was removed from the furnace and the time it was weighed, since the equipment in use consists of a furnace and a separate analytical balance. The powdered UO_2 standard is probably more susceptible to this error than the pelletized mixed oxides. For this reason and in view of results of other investigations, we feel that the oxygen-to-metal ratio of 1.98 for the mixed oxide is probably correct.

We are investigating the gravimetric method with a recording thermogravimetric balance. This study will tell us the times and temperatures required for the oxidation and reduction steps with the atmospheres we are using and whether the $UO_{2.00}$ is actually reoxidizing before the final weighing. When a procedure for the gravimetric technique has been standardized, a definitive comparison will be made between NITROX and gravimetric methods.

Hot-Stage Microscopy (Ji Young Chang, C. R. Reese)

A hot-stage microscope has been installed in an alpha-tight glove box so that we can measure the densification rates of various sol-gel $(U,Pu)O_2$ microspheres as a function of temperature. This quarter we have been concerned with achieving leak-tightness in the box, with calibrating instruments, and with developing procedures.

During calibration and check-out, we melted a variety of materials to compare measured with actual temperatures. Our calibration curve is shown in Fig. 1.4. Melting temperatures were determined between 190°C for NH_4NO_3 and 1083°C for gold. Up to about 400°C our measured values

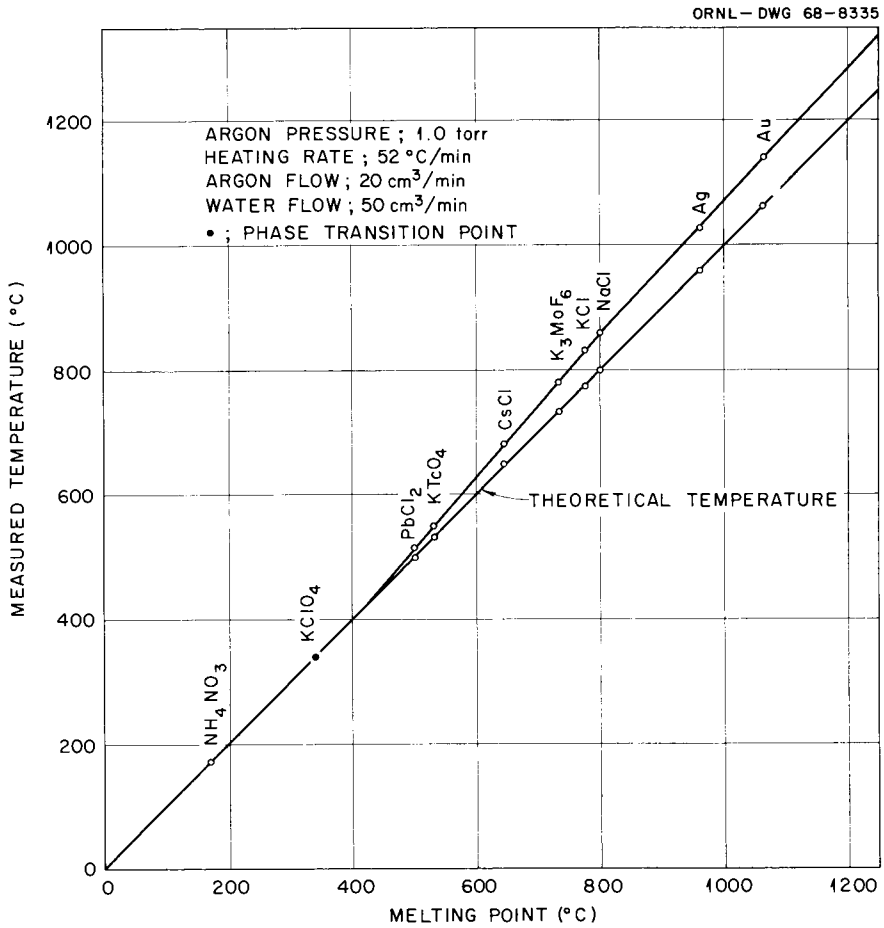

Fig. 1.4. Temperature Calibration Curve for the Hot-Stage Microscope.

compare well with true melting points. At higher temperatures the measured melting point is higher than the true (or theoretical) temperature, probably as a result of the high heating rate (52 °C/min) used.

As a further check on procedure, we determined the melting point of $KMoF_6$ to be 733 ± 4 °C. We also used the facility to study the tetragonal- to cubic-phase transformation of $KTcO_x$. This measurement had to be done in a glove box because of the radioactivity of technetium. Calorimetric measurements[7] on potassium pertechnetate ($KTcO_4$) had shown a heat effect at 480 °C thought to be associated with a change from tetragonal- to cubic-crystal structure. This transformation from an asymmetrical to a symmetrical crystal form should be detectable if the sample is illuminated with polarized light on the hot-stage microscope.

[7]Work completed by R. A. Gilbert and R. H. Busey, Chemistry Division.

However, when we tried this as requested, we found no transformation for the $KTcO_4$, although potassium perchlorate ($KClO_4$), a similar compound, showed a definite color and form change on the hot stage at its phase transition from rhombic to cubic structure at 340°C.

We examined with the hot-stage microscope the dimensional changes that occur when sol-gel urania shards are heated. Two separate runs were made on tray-dried urania particles from the same batch. A urania shard was heated on the microscope stage at a rate of 12°C/min. Photographs were taken at 100°C intervals, and the dimensional changes were measured from the film. Preliminary analysis of the data from both runs on the same material shows a large difference in behavior below 800°C. Both tests showed the UO_2 shards shrinking approximately 8% between 800 and 1160°C. Further analysis of the data will possibly explain the differences below 800°C.

Thermal Conductivity (Peter Spindler)

We tested the components for a radial heat flow apparatus to 1200°K at a pressure of 1 atm Ar. Temperature measurements were made with twelve Pt–10% Rh vs Pt thermocouples after initial tests with Chromel-P vs constantan thermocouples proved unsatisfactory. With Variacs to power the three system heaters, temperature uniformity was better than ±0.2° along the axis of a stand-in specimen. Fluctuations in the 110-volt line current, however, would not permit maintaining this uniformity for more than 20 min, and this is not sufficient to obtain steady-state radial temperatures in radial heat flow specimens. Three electronic recorder-controllers capable of obtaining the needed temperature control have been ordered and will be tested next quarter.

In the meantime, a series of thermal conductivity measurements are being conducted over a broad temperature range on single crystals of LiF (mp 1121°K). The literature contains thermal conductivity values on this material below 80°K only. We have specimens to study the range 80 to 420°K with our absolute longitudinal apparatus and the range 300 to 1050°K with our radial heat flow apparatus. Data in this range should yield valuable guidelines for the effects of infrared transmission and vacancy formation on the thermal conductivity of optically

transparent insulators, and this may be useful in understanding the behavior of nuclear oxides at high temperatures. Initial results show the thermal conductivity of LiF to decrease by nearly a factor of 10 between 80 and 360°K. The thermal resistivity appears to be a linear function of temperature from 200 to 360°K but is nonlinear below 200°K. These results conform to theoretical expectations for phonon conduction in insulators. Our results are in reasonable agreement with the low-temperature results of Berman et al.[8] at 80°K.

Deformation of Sol-Gel Oxide Pellets (C. S. Morgan)

We are studying deformation of polycrystalline UO_2 specimens prepared from sol-gel powder. Specimen preparation involved evaporation of UO_2 sol, grinding, forming, isostatic pressing, and sintering. The sintering — in a hydrogen atmosphere at 1750°C after a slow rate of temperature increase with a two-day hold at 800°C — resulted in specimens 95% of theoretical density. The two-day hold at 800°C was necessary to prevent cracking the specimen. Extensive deformation occurred over the 700 to 1600°C temperature range tested. The specimens usually exhibited a type of yield phenomenon classically associated with metal yielding. The yield stress was above 20,000 psi at 1300°C. A preliminary value of the activation energy of the deformation process, which is thought to be a complex mixture of plastic flow and grain-boundary sliding, is 40 kcal/mole at a stress of 23,300 psi and temperature around 1250°C. These studies are intended to provide a background for deformation studies of sol-gel $(U,Pu)O_2$ specimens.

Irradiation Testing of Sol-Gel $(U,Pu)O_2$

A. R. Olsen

The final evaluation of sol-gel-derived $(U,Pu)O_2$ fuels will be based upon their irradiation performance. The irradiation testing program is concentrating on comparative tests of the fabrication forms:

---

[8] R. Berman, E. L. Foster, and J. M. Ziman, Proc. Roy. Soc. (London) A237, 344–354 (1956).

Sphere-Pac, pellets, and extrusions. The program includes tests in both thermal and fast reactors. The thermal flux irradiations permit the use of instrumented capsules and the achievement of high burnup in relatively short periods of time. These tests will provide information essential to the analysis of the fast flux irradiation tests in which the radial fission-rate distribution and fuel temperature profiles are more typical of anticipated LMFBR operating conditions. The test program also includes transient tests to investigate fuel performance under abnormal operating conditions. The development of mathematical models to predict fuel behavior and computer programs to perform the associated calculations is an integral part of the irradiation test program.

Uninstrumented Thermal Flux Irradiation Tests (A. R. Olsen, J. Komatsu, R. B. Fitts)

A limited number of uninstrumented capsules are being irradiated in the Engineering Test Reactor (ETR). The capsule design permits the simultaneous irradiation of four test rods, each containing a 3-in. fuel column. Two of these capsules are being examined, and two are under irradiation.

The postirradiation examination of capsule 43-112 is essentially complete. This capsule contained three rods with Sphere-Pac (^{238}U–15% Pu)O_2 fuel and one rod with Sphere-Pac UO_2 (20% ^{235}U). This capsule was irradiated for one ETR cycle, about 28 days of effective full power, with a peak linear heat rate for the central two rods of about 14 kw/ft. Although the metallographic examination is incomplete, three interesting phenomena have been noted with both the UO_2 and the $(U,Pu)O_2$ fuels. Figures 1.5 and 1.6 are composite micrographs of transverse sections from the peak burnup regions of the two highest heat-rating rods. With both fuels there is clear metallographic evidence of the evaporation-condensation mode of fuel densification and radial redistribution. Oxide dendrites can be seen growing on the microspheres at the periphery of the sintered zone. Second, the microporosity present in the fine UO_2 microspheres before irradiation has disappeared, even in the coolest regions near the cladding, an indication of

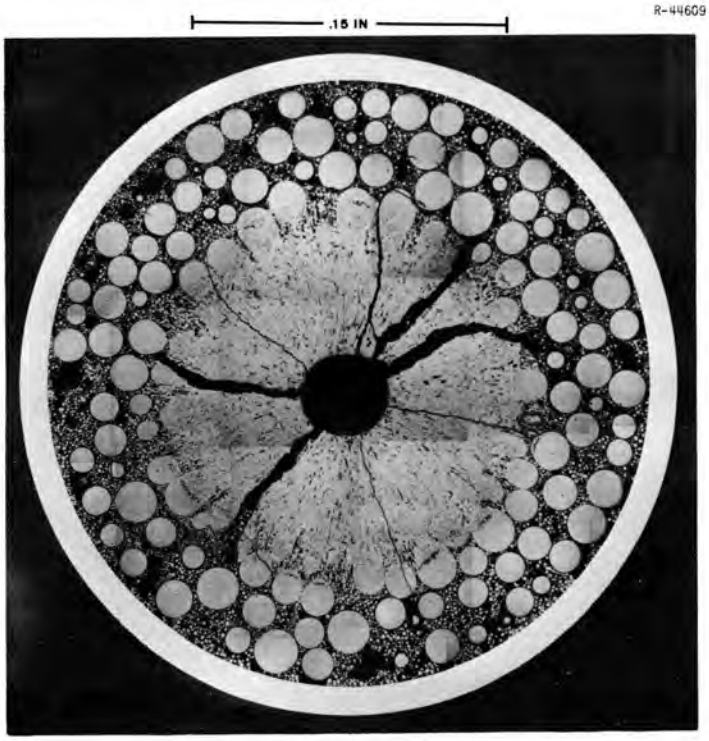

Fig. 1.5. Transverse Section of UO_2 Fuel Rod 2 from ETR Capsule 43-112.

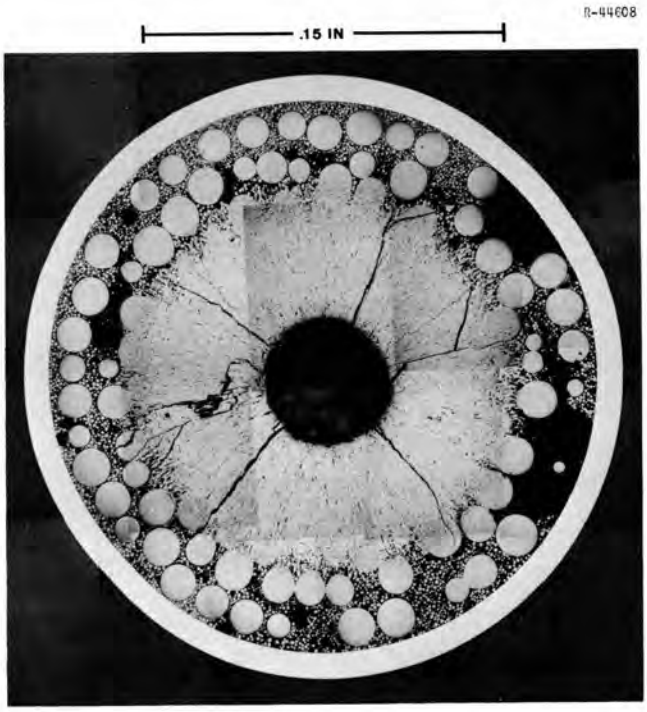

Fig. 1.6. Transverse Section of (^{238}U–15% Pu)O_2 Fuel Rod 3 from ETR Capsule 43-112.

in-reactor sintering. Third, both fuels developed porosity in the densified microspheres that are just in contact with the outer edge of the sintered zone. This indicates a reversal in the fuel movement direction as a result of the high-temperature gradients which result from such contact. Thus, some overriding phenomena such as the Lüdwig-Soret[9] effect may result in localized fuel movement up the temperature gradient. This effect may explain the development of the annular rings seen at the edge of the equiaxed growth region of pelletized $(U,Pu)O_2$ fuels[10] and other oxide fuels.[11]

Capsule 43-103, containing three Sphere-Pac UO_2 fuel rods and one pelletized UO_2 fuel rod, was removed from the reactor this quarter. This capsule was irradiated for four ETR cycles, 126 days of effective full power. The predicted burnup is approximately 4% FIMA. Postirradiation examination has just started.

The two capsules still in the reactor contain three test rods of Sphere-Pac $(^{238}U$–15% $Pu)O_2$ and one of Sphere-Pac UO_2. Capsule 43-113 has achieved about 50% of its target burnup level of 10% FIMA (about 100,000 Mwd/tonne) at a peak linear heat rating of 14 kw/ft. Capsule 43-115 has achieved about 10% of its target burnup level of 5% FIMA at a peak linear heat rate of 16 kw/ft.

ORR Instrumented Tests (R. B. Fitts, V. A. DeCarlo)

Two fuel rods containing 3-in. long fuel columns are irradiated in each capsule. There is a central fuel thermocouple in the top rod, and three thermocouples monitor the cladding on each rod. A calorimeter, formed by four pairs of thermocouples in the outer Zircaloy-2 capsule wall, is located at the midplane of each fuel rod.

---

[9]G. N. Lewis and M. Randall, Thermodynamics and the Free Energy of Substances, 1st ed., p. 184, McGraw-Hill, New York, 1923.

[10]S. A. Rabin, W. W. Kendall, and W. E. Bailey, Short Term Fast Flux EBR-II Irradiation of PuO_2 Fuel Pins, GEAP-5570 (October 1967).

[11]A. R. Olsen, J. W. Ullmann, and E. J. Manthos, Status and Progress Report for Thorium Fuel Cycle Development for Period Ending Dec. 31, 1965, ORNL-4001, pp. 102–112.

Capsule SG-1. — This capsule, containing (U–15% Pu)O_2 Sphere-Pac fuel at 8.8 g/cm^3 smear density, was placed into an ORR poolside facility on April 6, 1968, and operated at selected linear heat generation rates between 5 and 15 kw/ft for about 1200 hr until its scheduled removal on May 26, 1968.

The capsule operated within the design temperature range, and the only operational difficulty was a period of erratic behavior in the central fuel thermocouple. The temperature indicated by this thermocouple was in agreement with design calculations during the first 223 hr of operation, as shown in Table 1.1. Fuel temperatures and reductions

Table 1.1. Measured and Predicted Fuel Central Temperatures for ORR Capsule SG-1

Elapsed Irradiation Time (hr)	Fuel Linear Heat Generation Rate (kw/ft)	Fuel Central Temperature (°C)	
		Measured	Predicted[a]
4	5.8	840	760
55	6.25	880	820
56	8.6	1210	1125
75	8.8	1245	1150
80	9.7	1390	1270
96	9.8	1355	1280
100	11.5	1600	1500[b]
120	11.5	1520	1460[c]
122	12.0	1600	1575[b]
220	12.8	1490	1570[c]
222	14.7	1820	1730[c]
223	14.7	1775	1730[c]

[a]Predicted fuel temperatures based upon pellet fuel with 0.5-mil radial gap and the thermal conductivity given by $k = 0.011 + 1/[T(0.4848 - 0.4465D)]$ (w/cm °C), where D is density in percent of theoretical. Values of D assumed were 80% below 1400°C, 96% theoretical density to 1900°C, and 98% theoretical density above 1900°C. [W. W. Bailey et al., "Thermal Conductivity of Uranium-Plutonium Oxide Fuels," Intern. Symp. Plutonium Fuels Technol., Scottsdale, Ariz., 1967, Nucl. Met. 13, 239–308 (1968)]

[b]Before densification.

[c]After densification.

in temperature due to sintering were close to those expected for a pellet fuel of comparable density. During this period power was raised in five steps to 15 kw/ft. After 3 hr at the high power level and an indicated central temperature of 1800°C the thermocouple emf rose suddenly to 44 Mv, which is above calibration, for about 2 hr. After a period of about 100 hr during which the thermocouple emf varied erratically, principally around 1700 to 1800°C, the temperature indication again became apparently normal. Experiment power and central temperature were maintained below 13 kw/ft and 1400°C, respectively, for the remainder of the exposure.

Postirradiation examination of this capsule is well under way. Fission-gas collection, gamma scanning, flux monitor removal and sectioning, diameter and bow measurements, and sectioning of the fuel rods for metallographic analysis are complete. Preliminary analysis of the gamma scans and dimensional measurements revealed no unusual characteristics. Low magnification examination of the cut surfaces where fuel rods were sectioned for metallography showed extensive fuel sintering and apparent reaction or melting of the molybdenum well of the central thermocouple. Higher magnification examination of polished sections is planned in the near future.

Capsule SG-2. — This capsule is to be of the same design as SG-1 except that the molybdenum thermocouple well will be replaced with W–26% Re; the central fuel thermocouple will be a four-wire rather than a two-wire couple; and the three cladding thermocouples on each fuel element will be located at the midplane of each element. This capsule is scheduled for insertion during the November 15, 1968, ORR shutdown.

Data Analysis. — Analysis of the details of thermal and power history in these experiments is necessary to evaluate small but important variations such as changes in fuel conductivity resulting from in-reactor sintering. Continuous readout is provided for 30 operating parameters. Since these data are collected for periods of 1 to 12 months, a computer program to store and manipulate the data is mandatory for adequate test evaluation. We are preparing such a program with the assistance of the ORNL Mathematics Division. A system to

record these data on computer-compatible magnetic tape is being procured by the ORNL Reactor Division.

Detailed analysis of the calorimeter response over portions of experiment SG-1 reveals an erratic response of the outer couple in each thermocouple pair. This limits the precision of the heat flow measurement. In an effort to reduce this effect, we are investigating the possibility of brazing the calorimeter couples to the calorimeter sleeve or plating the completed assembly.

Transient Testing of Sol-Gel-Derived $(U,Pu)O_2$ (C. M. Cox, J. D. Jenkins)

A new 36-group spectrum-averaged set of neutron cross sections for the TREAT reactor and our experimental capsule were prepared to give more detail in the thermal energy range. Reactor physics calculations to investigate various types of thermal neutron filters have been completed for an 87-cm radius room temperature TREAT core. The results of these calculations, made with the ANISN code,[13] are summarized in Table 1.2. Of the filters considered, cadmium promises to be most effective in reducing the surface-to-center power ratio while maintaining sufficient power to completely melt the specimens. Assuming adiabatic conditions, we have determined the energy required to completely melt the fuel, including the heat of fusion, as 415 cal/g. Using this value and the calculated ratios of specimen power to TREAT power, we calculated the corresponding TREAT pulse energies (tabulated in Table 1.1) Since the present TREAT limit is 1000 Mwsec, it is obviously not practical to consider significantly thicker filters. To determine whether the flattened power distribution has an appreciable effect on the temperature profile, we are performing comparative transient heat transfer calculations to simulate a typical TREAT experiment. In comparing the steady-state radial temperature profiles for the use of no filter and the use of a cadmium filter at 16 kw/ft, we found little difference; the cadmium filter increased the central fuel temperature by about 5%.

---

[12]W. W. Engle, Jr., A User's Manual for ANISN, K-1693 (March 1967).

Table 1.2. Summary of ANISN Calculations for TREAT Reactor Experimental Capsule TR-1[a]

Case	Fuel Surface-to-Center Power Ratio	Average Specimen Power Density TREAT Power ($w\ cm^{-3}\ w^{-1}$)	Minimum TREAT Transient Energy to Melt Specimen (Mwsec)
		$\times 10^{-5}$	
No filter	2.30	9.3	170
0.023 in. boral[b]	1.90	1.9	820
0.010 in. Eu[c]	1.84	2.0	780
0.005 in. Cd	1.80	2.3	680

[a]Fuel composition: $(0.80\%\ U\text{–}0.2\%\ Pu)O_2$. Smear density: $8.96\ g/cm^3$. Cladding: 0.254-in. OD × 0.221-in. ID, type 304 stainless steel.

[b]Assumed natural boron atomic density: $5.124 \times 10^{22}\ cm^{-3}$.

[c]Assumed europium atomic density: $2.07 \times 10^{22}\ cm^{-3}$.

The preliminary design of the basic TREAT capsule has been completed, and drawings are being prepared. Sufficient materials have been procured to construct the first four capsules of the program. If we decide to use the cadmium filter, it will probably be added as a removable, laminated shell on the outside of the capsule.

Fast Flux Irradiation Tests (A. R. Olsen)

Our proposal to operate a 19-rod subassembly in the EBR-II starting in October 1968 was submitted for review and approval-in-principle to the experimental review committee at Argonne National Laboratory. They suggested that we start testing five encapsulated Sphere-Pac test rods in a shared 19-rod subassembly in July or August and plan to do the rest of the proposed testing on unencapsulated rods. The first five rods will provide the necessary proof of performance reliability. We are currently devoting full efforts to procuring, inspecting, and fabricating the necessary hardware for the five encapsulated test rods. We have also contacted Babcock and Wilcox Company personnel to begin coordinating the planning of tests to be conducted in a shared 37-pin subassembly with unencapsulated rods.

Irradiation Test Calculation (C. M. Cox)

The PROFILE program for calculating steady-state radial temperature profiles of long, cylindrical fuel elements is now operational. This program is written in FORTRAN for the CDC 1604 computer and includes two optional thermal conductivity functions — the GE function[14] for $(U,Pu)O_2$ and a more general function of the form

$$k = (A + \frac{B}{T} + CT^3)\ f(P)\ . \qquad (1.1)$$

A, B, and C are constants, and f(P) is a porosity correction factor. The fuel fission density can be fed into the program either as a constant or a variable in space. A three-region densification function has been included as an option with the densities and temperatures corresponding to columnar and equiaxed grains to be specified by the user. A plotter package has also been included.

2. NITRIDE FUELS DEVELOPMENT

W. O. Harms J. L. Scott

The goals of this program are to investigate the properties and behavior of mixed uranium-plutonium nitrides and carbonitrides as LMFBR fuels and through extension of irradiation conditions, to establish the ultimate limitations of UN as a space-nuclear fuel.

For LMFBR applications, our goal is to develop fuel elements that can operate at linear heat ratings up to three times the limit now set for mixed oxides. It is almost certain that the economic benefits of these higher heat ratings will be profound.

The major problems associated with the use of mixed nitrides or carbonitrides as LMFBR fuels are (1) economical synthesis and fabrications, (2) compatibility with candidate cladding alloys, including the effects of fuel burnup, and (3) irradiation behavior.

In dealing with these problems, we place high priority on developing a quantitative description of the thermodynamic properties and pertinent reaction kinetics in the materials systems of interest. This information is applied to the development of fabrication schemes and to the solution of compatibility problems. Promising combinations of fuel and cladding are irradiated under simulated service conditions.

Our work in synthesis, fabrication, and characterization of nitride fuels involves uranium nitride and carbonitride work for space-nuclear and fundamental studies and preparative work for mixed uranium, plutonium nitride, and carbonitrides. For clarity, these two areas are described separately, though our experience with one guides our strategy on the other. Work on UN for space applications is described in classified monthly reports.

Synthesis and Fabrication of Uranium Nitride

R. A. Potter

We are continuing with the synthesis of UN powder and the fabrication of specimens for irradiation tests and physical property measurements.

During the report period, we prepared 25 right cylinders 0.30 in. in outside diameter by 0.10 in. in inside diameter by 0.30 in. in height. The specimens were cold-pressed at 50 tsi around a mandrel and sintered at 2300°C at 1 atm N_2 to 95% of theoretical density. We were unable to prepare 97% dense specimens for hot-hardness measurements, but seven disks about 0.75 in. diam by 0.25 in. high that we were able to press and sinter to a density of 94.5% of theoretical may be used for these measurements. We also prepared 0.5 kg of UN powder, 25 right solid cylindrical pellets of UN containing UO_2 in the grain boundaries, and 48 right solid cylinders of single-phase UN.

While preparing the specimens noted above we made an interesting observation concerning the reaction of UN powder with pressed UN specimens. The UN powder bed on which the samples rested during sintering adhered to the pellets, and light grinding was necessary to remove it. Microscopic examination of the specimens before grinding showed that a transport of material between powder and solid had occurred and that grain boundaries actually crossed the interface as shown in Fig. 2.1.

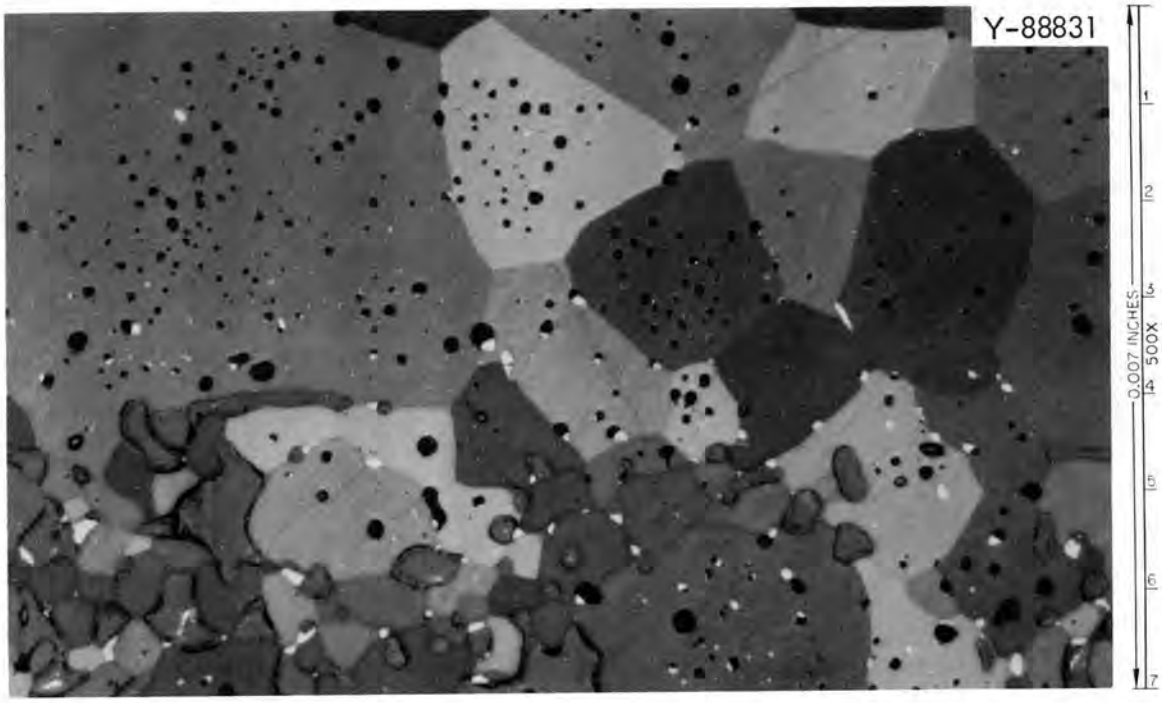

Fig. 2.1. Uranium Nitride Sintered in Contact with UN Powder at 2300°C in 1 atm N_2.

Recently, we have directed some effort toward preparing micropellets. Our interest is in a cylindrical specimen about 0.040 in. in outside diameter by 0.020 in. in inside diameter by 0.250 in. in length. Initial efforts to prepare such a piece by the electrodischarge machinery (EDM) method indicated that with some refinements in technique it will be feasible.

Synthesis of Uranium Carbonitride

J. M. Leitnaker R. L. Beatty K. Notz
K. E. Spear T. B. Lindemer

Our basic studies have shown that producing a UN contaminated with UC will be easier than producing pure UN and very likely just as useful. Thus, we have been investigating practical ways for making carbonitride, drawing on the basic kinetics studies of Lindemer[1] for guidance when possible. We start with UO_2 sol, because this is a likely type of feed material for an aqueous recycle plant. To this sol we add carbon sol in the proper proportions to produce the desired end composition. The mixed sol is gelled, dried, and calcined in nitrogen to produce the final product. The primary advantage of our process is the fine particle sizes which result in rapid reaction rates at relatively low temperatures. Under favorable circumstances, reaction is complete in 15 min at 1500°C. Under less ideal conditions, the reaction may require 30 min in nitrogen at 1700°C followed by another 30 min in argon.

The reaction between the oxide and carbon and nitrogen is sensitive to a number of factors not yet completely understood. First, we find an apparent dependence on amount of carbon in the UO_2: a carbon-to-uranium ratio of 10 results in a considerably faster conversion rate than does a ratio of 2.5. Samples that are fully oxidized, that is, samples in which the uranium is in the U_3O_8 valence, appear to have a

[1]R. B. Lindemer, "Kinetics of the UO_2-C Reaction" and "Kinetics of the UC_2-N_2 Reaction," Metals and Ceramics Div. Ann. Progr. Rept. June 30, 1968, ORNL-4370, Chap. 18.

tendency to sinter, for UO_2 is strongly evident after the usual heat treatment in nitrogen. On the other hand, samples in which the uranium is nearer to UO_2 react to form nitride more completely, and little or no UO_2 is present in the final product. This may be related to the greater tendency of U_3O_8 relative to UO_2 to sinter during firing, or it may be related to the availability of carbon. One might think the carbon availability is reduced by the greater oxygen content of the U_3O_8.

Temperature has a strong effect on the reaction rate. If oxygen content is taken as a measure of completion, then at 1300°C 5.06% O remained after 30 min, whereas the same heat treatment at 1400°C yielded a product with 1.18% O. At the higher temperatures, a 5 min heat treatment produced an oxygen level of 5.15%.

The surface activity of the synthesized product can be a problem. We established conclusively that brief (< 10 min) exposure of reacted material to air at room temperature under certain conditions would result in a weight increase of 2 to 3%, presumably mostly oxygen. This increase could be eliminated by coating the particles with an impervious carbon layer after the reaction experiment but while the sample was still in the furnace. The coating, while protecting the sample from the air, also protects it seemingly from the dissolution methods for oxygen, nitrogen, and free carbon. Thus we quite often get erratic results in the analyses, and samples do not add up to 100%. A picture of a reacted and coated shard is shown in Fig. 2.2.

If after conversion samples are heated in argon, some sintering takes place which we deduce decreases reactivity with air, since oxygen contents of about 0.2% can be obtained. Thus, we are not certain what our analyses for oxygen and nitrogen mean in relation to the quantities we wish to measure.

Metallograph studies have revealed some interesting structures but have not been able to differentiate between various compounds in the reacted shards. For example, Fig. 2.2 shows a sample that has been coated with carbon, which is clearly visible around the outside of each shard. The x ray of the sample reveals comparable quantities of UO_2 and U_2N_3, but metallographically the sample appears to be single phase. In contrast, a difference in appearance between uncoated samples shown

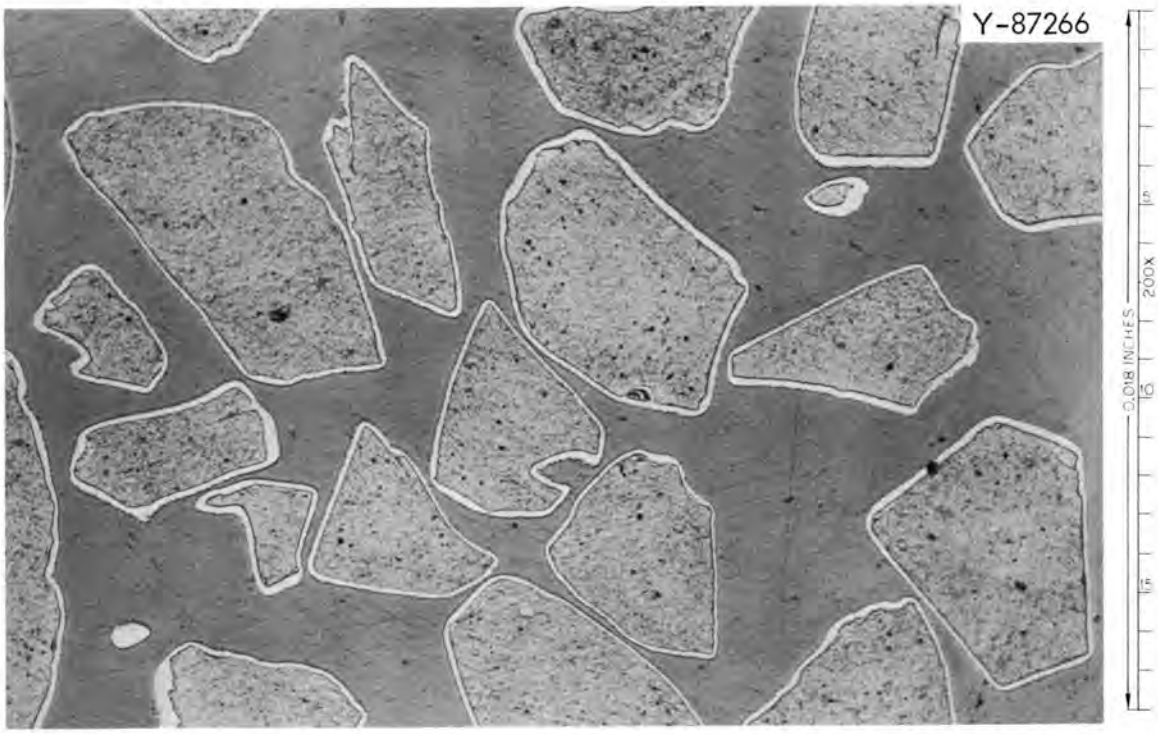

Fig. 2.2. Example of Reacted and Carbon-Coated UO_2 Plus Carbon Sol-Gel Shards. X-ray evidence clearly showed two phases that are not revealed by metallography.

in Figs. 2.3 and 2.4 is quite clear. In the sample shown in Fig. 2.2 two phases (UO_2 and U_2N_3) are indicated by x-ray analysis. One is tempted to ascribe the outside, lighter area in Fig. 2.3 to U_2N_3, perhaps, while the remainder must be, by elimination, the UO_2. However, in Fig. 2.4 only one phase, U_2N_3, is visible by x ray, while the outside layer has enlarged considerably. (The sample of Fig. 2.4 has been heated longer than that of Fig. 2.3 but was otherwise the same.) Tentatively, we ascribe the difference in appearance to either sintering or a change in composition of the U_2N_3 phase.

We have started another series of experiments to determine the effect of particle size and amount of carbon added, time, temperature, shard size, and sintering atmosphere on the rate of conversion and the sintered density of pellets. Results are not yet available.

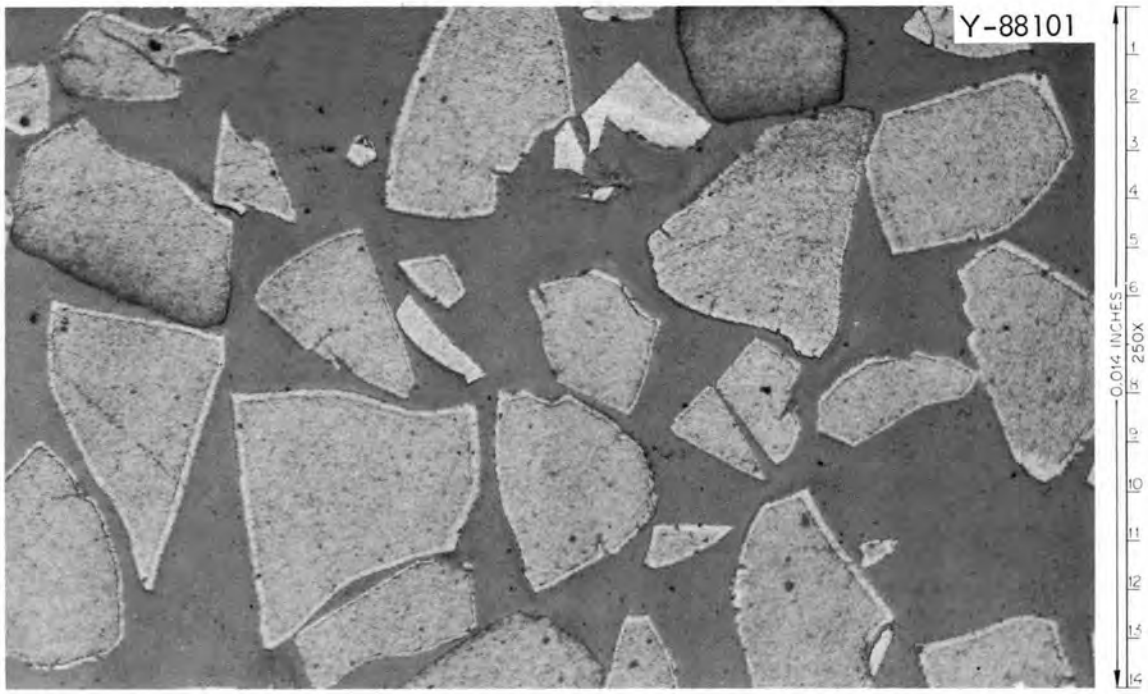

Fig. 2.3. Two Phases Shown by X Ray are Apparently Confirmed by Metallography in UO_2-Carbon Sol-Gel Shards Heated in Nitrogen.

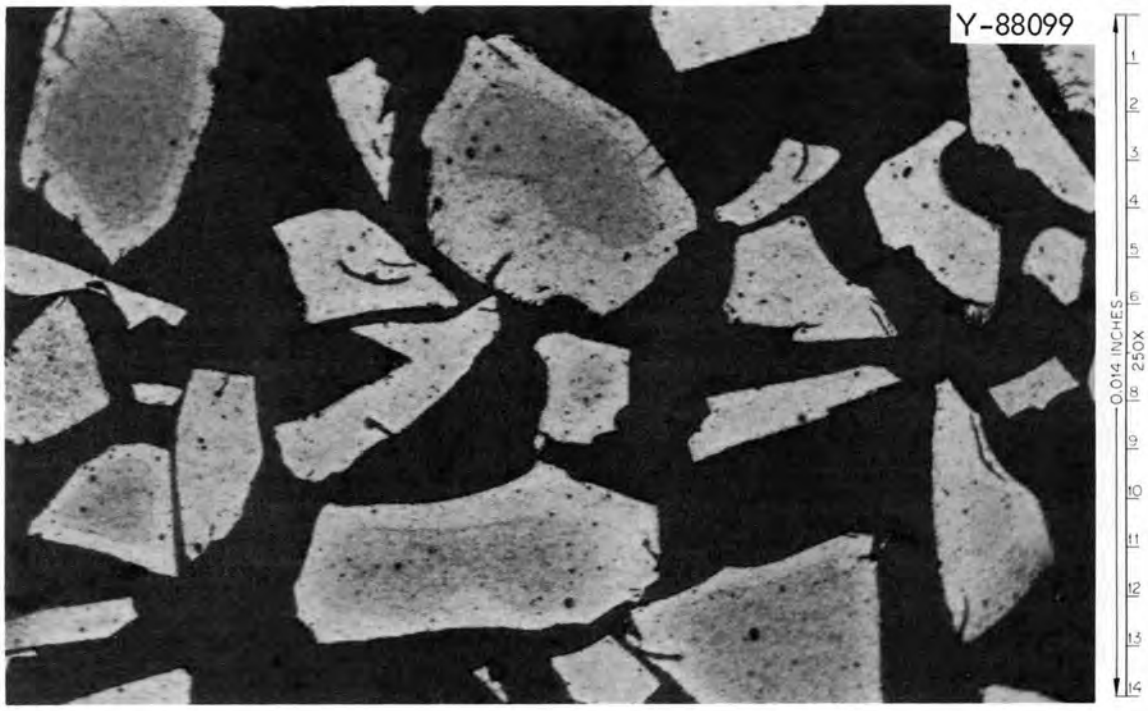

Fig. 2.4. Two Phases Shown by Metallography Are Not Seen in X-Ray Patterns. (Compare with Fig. 2.3; heating conditions were the same except the sample in Fig. 2.4 was heated 6 times longer.)

Basic Studies on Conversion of Sol-Gel Oxides to Carbonitrides

T. B. Lindemer

We are studying the reaction of nitrogen and "UC_2" (nominal dicarbide) to produce U(C,N). In addition to the usual time and temperature parameters, the literature also revealed[2] that the nitrogen pressure, the free carbon in the carbide, and the "age" or reactivity of the carbide were important in the reaction of nitrogen with uranium monocarbide. This quarter we have investigated the effects of several of these parameters on the reaction rate at 1600°C.

We determined the reaction rates from models in the literature for reactions in spheres.[3] Our UC_2 was provided in the form of microspheres of initial radius, r_o, ≈500 μm. After reaction for a given time, a uniform layer of products formed on the outside of the sphere, leaving a spherical UC_2 core of radius r. If the conversion were controlled by a reaction at the gas-solid outer surface, the rate equation

$$1 - \left(\frac{r}{r_o}\right)^3 = \frac{3\,k_s t}{r_o} \qquad (2.1)$$

would be followed. If diffusion through the U(C,N) were rate-limiting, the equation

$$\frac{1}{3} - \left(\frac{r}{r_o}\right)^2 \left(1 - \frac{2}{3}\,\frac{r}{r_o}\right) = \frac{k_D t}{r_o^{\,2}} \qquad (2.2)$$

---

[2]L. A. Hanson, J. Nucl. Mater. 19, 12–18 (1966).

[3]For example, see S. Yagi and D. Kunii, "Studies on Combustion of Carbon Particles in Flames and Fluidized Beds," pp. 231–244 in Fifth Symposium on Combustion, Reinhold Publishing Corporation, New York, 1955.

would be obeyed, while if the reaction at the $U(C,N)$–UC_2 interface controls, the relation

$$1 - \frac{r}{r_o} = \frac{k_I t}{r_o} \tag{2.3}$$

would be used. These equations have appeared in the literature many times and are easily derived. In each experiment we withdraw eight samples from the fluidized bed at equal time intervals, with the final sample having an estimated r/r_o ratio of about 0.3; that is, the reaction is about 97% complete. Average values of r and r_o are obtained from 25 particles in each of the eight samples by quantitative metallographic methods and are used in the plot of the left-hand side of the equations above versus time. The plot is linear for the one rate-controlling process, and from this plot we obtained a value of the reaction-rate constant, k, by least-squares techniques.

The aging effect was studied first, since Hanson demonstrated its importance to the reaction of uranium carbide with nitrogen. This effect manifested itself in a reaction rate that increased by an order of magnitude or more with increasing exposure of newly made UC to moist air at room temperature. Therefore, unless one established the age of the material, analysis of the reaction rates of a set of experiments was nearly impossible. It was also suggested that the aging was associated with the presence of hydrogen. From this we concluded that pretreatment of the carbide might remove these impurities to a given level and thus permit us to hold the aging effect constant so that the other parameters could be investigated. Our efforts to counteract aging consisted of the following:

1. pretreatment at 1600°C in argon in the fluidized bed followed by reaction with nitrogen, all at 380 torr,
2. pretreatment at 1600°C and 10^{-5} torr for either 24 or 76 hr in a bed of spectrographic graphite powder, all held in a tungsten crucible.

In the latter case, the material was cooled to ambient, transferred to a fluidized bed at 1600°C, and reacted with nitrogen. We compared these experiments with ones in which UC_2 received no pretreatment and found that data from all the experiments plotted linearly with the last equation; that is, control appeared to occur at the $U(C,N)-UC_2$ interface. The rate constants obtained by fitting a least-squares line to each set of data are shown in Table 2.1. The reaction-rate constant for the as-received material, about 60% greater than that for the pretreated materials, indicated that an aging effect is present in the UC_2. These experiments also indicated that the simple, 30-min argon pretreatment would bring the UC_2 to a reproducible aging level. We are making additional studies to determine if the UC_2 can be aged further to increase the reaction rate.

Table 2.1. Study of Aging Effects on the Reaction of Uranium Carbide with Nitrogen at 1600°C

Specimen Number	Pretreatment	Reaction Rate Constant ($cm^3\ cm^{-2}\ sec^{-1}$)	Time to Convert 500-μm Spheres (hr)
		$\times 10^8$	
A5163-62	None	11.97	58
A5163-150	None	10.79	64
A5163-84	30 min in argon (380 torr) at 1600°C in fluidized bed	7.793	89
A5163-103	24 hr in vacuum (10^{-5} torr) at 1600°C; cooled to ambient	5.968	116
A5163-129	76 hr in vacuum (10^{-5} torr) at 1600°C; cooled to ambient	7.860	88

We also investigated the effect of nitrogen pressure on the reaction rate for as-received UC_2. One would expect the possible pressure dependence of the reaction-rate constant to follow the expression $k = k_o P_{N_2}^n$ at a given temperature; for example, Hanson found $n = 0.75$ in his study. In addition to the experiments on as-received UC_2 at a nitrogen pressure of 380 torr, another was performed at 180 torr. Both reactions followed the interface-controlled models, with the higher pressure giving a rate only 6% higher than that at the lower pressure. Therefore the exponent, n, was equal to 0.08. From this we tentatively concluded that the reaction rate was independent of pressure in this pressure range, that is, $n = 0$. We will, however, perform other experiments at lower pressures and with "de-aged" material to substantiate this conclusion.

The effect of free carbon in the starting UC_2 material was also qualitatively demonstrated. Chemical analysis of the as-received UC_2 indicated that it was $UC_{1.86}$ with a free-carbon content of 0.22 wt %. This free carbon is observed metallographically in both as-received UC_2 and pretreated UC_2 as small carbon platelets occurring as bright areas under polarized light, as is shown in Fig. 2.5. A typical microstructure observed after reacting this material with nitrogen at 380 torr is shown in Fig. 2.6. This sample was reacted for 1920 min at 1600°C. The dark outer layer is the carbon produced by the conversion reaction; it has diffused to the surface of the microsphere and precipitated there. Additional carbon has precipitated internally in both the gray U(C,N) layer and in the UC_2 core; this carbon apparently precipitated on the free carbon that was originally in the starting UC_2. This effect was generally observed in as-received and pretreated UC_2 at both 1500 and 1600°C.

Occasionally, however, we found a particle that had no internal free carbon. The reaction in this instance was quite different and is demonstrated in Fig. 2.7 for a particle from the same sample as that shown in Fig. 2.6. As can be seen, no internally precipitated carbon is present, apparently because no free carbon was available initially to act as a nucleus for precipitation of the carbon produced by the reaction. It can also be seen that the conversion was not as advanced

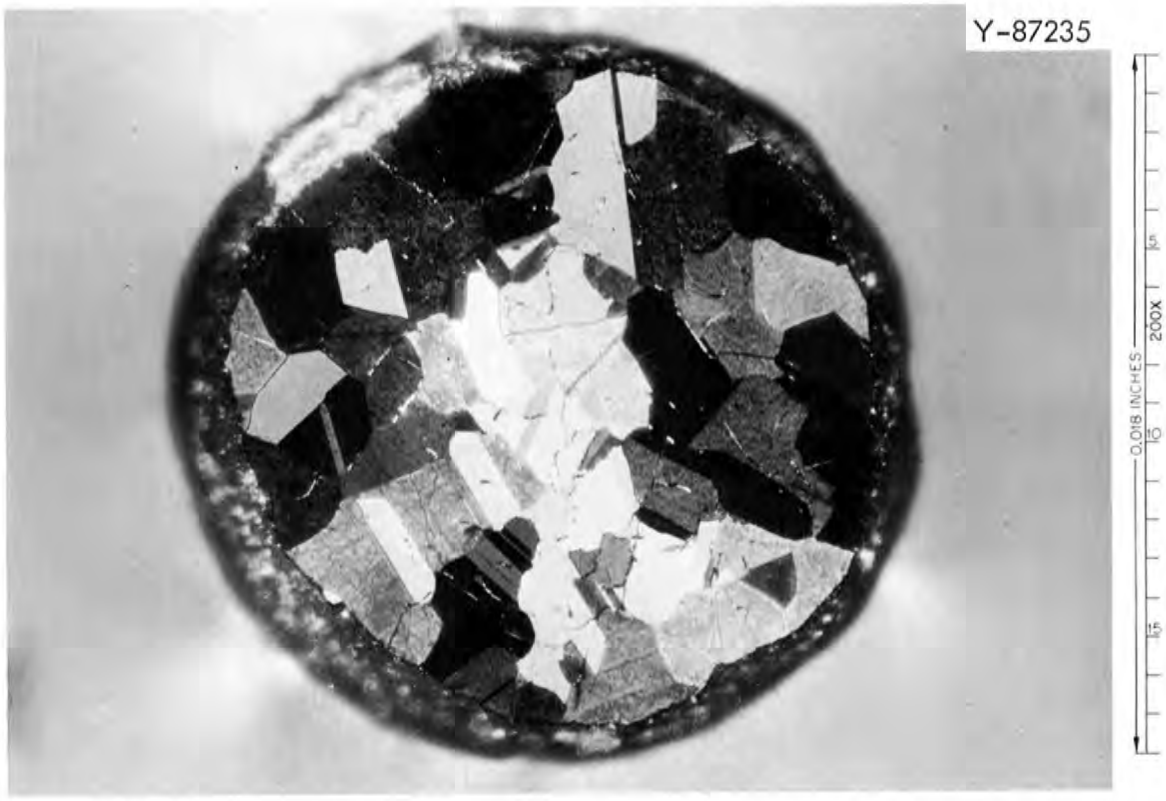

Fig. 2.5. Nominal Uranium Dicarbide Containing 0.22 wt % Free Carbon Evident as Narrow Bright Streaks. Etched in 1:1:1 HNO_3–HAc–H_2O, polarized light.

as that in Fig. 2.6; this was always true of these particles. These particles occurred too infrequently, however, for us to determine which of the three models described above fitted the r/r_o data obtained from the particles.

We performed a few experiments in which we reacted de-aged UC_2 in a N_2–4.14% H_2 mixture at 1600°C. The nitrogen partial pressure was 380 torr, resulting in a hydrogen pressure of 16 torr. This treatment stripped the carbon product from the surface, as is shown in Fig. 2.8. The results of the kinetic studies of this reaction were inconclusive; more work is needed to determine whether the presence of hydrogen affects the reaction rate.

The investigation of this system has clarified the effects of several different experimental parameters, as described above. The behavior of the system is also very reproducible, which implies that

Fig. 2.6. A Typical Microstructure Obtained from the Reaction of Nitrogen with UC_2 Containing Free Carbon at either 1500 or 1600°C. Outer layer and internal particles are carbon, the inner core is UC_2, and the remainder is U(C,N). This specimen was reacted at 1600°C for 1920 min with P_{N_2} = 380 torr. Etched in 1:1:1 HNO_3–HAc–H_2O, bright field.

we will be able to determine with considerable accuracy some of the basic parameters of the reaction, including the activation energy for the reaction. We also expect to be able to find the rate-controlling mechanism for some of the reactions.

These initial results already permit the design of a possible method for producing carbon-free U(C,N) from a uranium dioxide-carbon sol gel. The latter would first be reacted to give fully dense, carbon-free UC_2. This material would be converted with nitrogen to produce U(C,N) free of internal free carbon, as shown in Fig. 2.7; this, in turn, would be reacted with a hydrogen-nitrogen mixture to strip the carbon that diffused to the surface. The advantages of this process lie in the possibility of producing a fully dense U(C,N) of very low

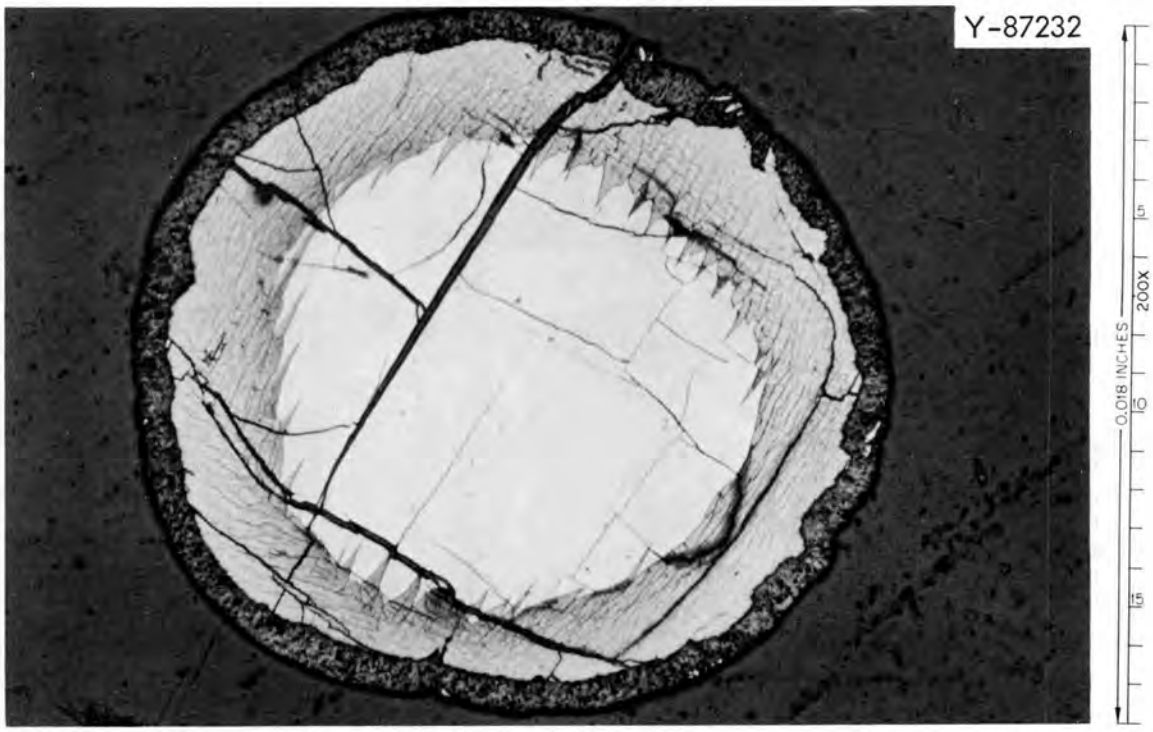

Fig. 2.7. A Typical Result Obtained from the Reaction of Nitrogen with UC_2 Free of Free Carbon. This particle was included in the same sample as the particle shown in Fig. 2.6. Etched in 1:1:1 HNO_3–HAc–H_2O bright field. Reduced 20% of original.

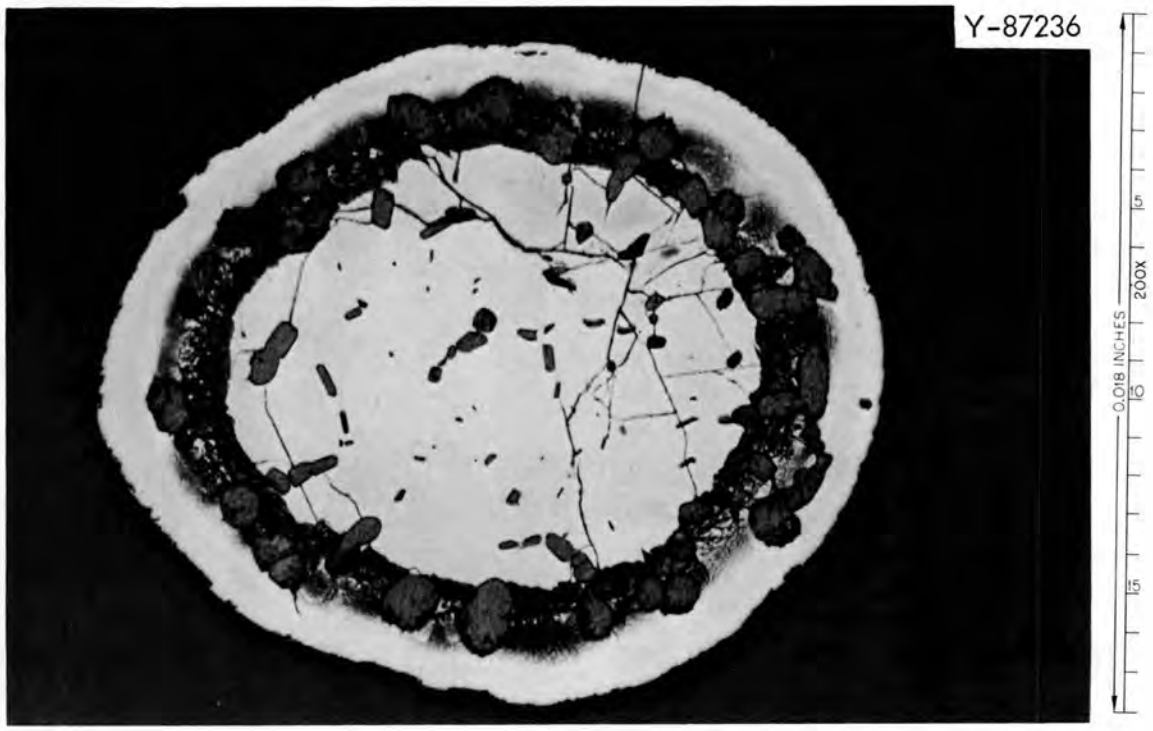

Fig. 2.8. A Typical Microstructure Obtained from the Reaction at 1600°C for 720 min of a N_2–4.14% H_2 mixture with UC_2 Containing Free Carbon. Etched in 1:1:1 HNO_3–HAc–H_2O, bright field.

oxygen content, since UC_2 has an extremely low solubility for oxygen. The disadvantage of the process is the long time required, approximately 0.4 hr/μ of diameter at 1600°C.

Synthesis, Fabrication, and Characterization of Mixed Nitrides

E. S. Bomar Ji Young Chang
J.D.L. Harrison[4] J. M. Leitnaker

The design of our facility for synthesis, fabrication, and characterization of mixed (U,Pu)N was described previously.[5] Most of the equipment is now operational and has been checked out, and final checking of the argon atmosphere boxes for leaks is nearly complete. The high-temperature tungsten furnace for sintering cold-pressed samples that is being built by the Richard D. Brew Company is about 50% complete; delivery is expected in August.

The hot press and its auxiliary equipment were installed during this period. The furnace is now equipped with automatic readout of both thermocouple temperature and the signal from a differential transformer that will provide pellet compaction data. The furnace operated satisfactorily to 2000°C while compacting a specimen of Al_2O_3. The hot press is now ready for work with plutonium-bearing materials.

Leak checking the box containing the synthesis and sintering furnaces disclosed defects in hard-solder joints where the furnace vacuum lines penetrate the box. We redesigned this penetration to provide a weld closure and can now proceed with a leak check on the box. We expect no further difficulty.

During cold check-out, we found a defect in the power supply for the x-ray tube. We corrected the difficulty, and a factory representative aligned the diffractometer. The powder camera has not yet been

---

[4]On loan from Atomic Energy Research Establishment, Harwell, England.

[5]E. S. Bomar *et al.*, "Synthesis and Fabrication of $(U,Pu)N_6$," and "Characterization of Mixed Nitrides," *Metals and Ceramics Div. Ann. Progr. Rept. June 30, 1968*, ORNL-4370, Chap. 18.

mounted in the box, but this will be done when we change the fixed x-ray tube holder for an adjustable one, as the representative recommended. This change will make adjustments after the box is put into service much easier.

The fabrication of the facility for vapor pressure measurement is now under way. As the design of this equipment evolved, some changes in the box to contain the apparatus became necessary. The drawings are being modified accordingly. Several pieces of hardware have been procured: the microbalance, the tungsten-mesh furnace, the residual-gas analyzer, and parts of the high-vacuum system.

Using calcium oxalate as a reference, we checked the thermogravimetric analysis equipment for satisfactory operation and recording of time-weight change data. It is now ready for use. The successive removal of water, carbon monoxide, and carbon dioxide provides information on performance over a range of temperatures. The plotted results were within 2% of that reported for this compound by the instrument manufacturer.

The hot-stage microscope is now operational. The equipment performed very well in every respect including programming of heating and cooling cycles, recording of a time-temperature trace, and photographing the object on the hot stage at temperatures up to 1300°C. We added automatic protection against either flooding of the glove box due to a failure in the cooling-water line or inadvertent pressurizing of the box with the purge gas supplied to the hot stage.

Purity Control of Glove-Box Atmospheres

J.D.L. Harrison[4]

A mobile console for measuring oxygen and water contents and estimating nitrogen, hydrogen, and other volatile impurities in argon has been designed and constructed. The useful ranges are roughly from 2 to 1000 ppm by volume for oxygen and water, 50 to 2500 ppm by volume for nitrogen, and up to 10,000 ppm by volume for hydrogen. We have already used the unit to check the leak tightness of glove boxes in the

Interim Plutonium Facility and will routinely use it to monitor the purity of these box atmospheres with respect to oxygen, water, and flammable vapors.

The console contains three instruments. The instruments used for measuring oxygen (Engelhard Industries Mark II Hersch Cell) and water (Beckman Instrument Company Moisture Analyzer) will measure these impurities in gases other than argon; the purity meter for the discharge tube (Colston Electric Company, Bristol, England) will function only with argon or helium as the carrier gas but will respond to a wide range of impurities in these gases. The electrical outputs from each of the three instruments can be switched to the strip-chart recorder mounted at the top of the console. Six sampling ports are mounted on the front control panel. A rotary sampling valve can connect any of the six ports to the manifold that feeds the instruments. One of these ports can be connected to a small cylinder of high-purity argon mounted on the console, a useful feature when the instruments are being checked or calibrated.

The operation manual for the unit is being written.

Recirculating Gas System

E. S. Bomar J.D.L. Harrison[5]

We have adjusted the instruments and control valves of the recirculating gas system for optimum performance and have measured and recorded for reference the operating characteristics of the system.

Equipment Modifications

Three modifications were necessary. We installed an alpha-activity sampling point in the exhaust line downstream from the blowers; installed a modified 3-in. "Maxitrol" pressure control valve in parallel with the manual air-inlet bleed valve to reduce the full-flow to no-flow pressure variation in the main off-gas servo control valve; and rearranged the compressed air supply to the controller so that the full output pressure could be transmitted to the off-gas servo control valve.

The system will now cope with steady gas-flow valves between 0.5 and about 140 cfm while maintaining a line pressure between −4.0 and −3.0 in. water gage.

Glove Box Pressure-Controllers

Each glove box is equipped with a 2-in. diaphragm pressure-control valve that maintains the box pressure at −1 1/2 in. water gage irrespective of fluctuations in the rate of gas flow through the box or the off-gas line pressure.

After very limited use, two of these valves became much less responsive and failed to keep the glove-box pressure within the prescribed limits. Examination and experiment revealed that the cause of the trouble was mild scuffing of the rubber valve seat by the aluminum mushroom valve. This created a high coefficient of friction between the two and the consequent need for abnormally high forces to close the valve. Lubricating the seat with talc restored the original performance of the units immediately. A test rig that cycled a valve four times a minute let us measure the lifetime of the lubricated seatings. This lifetime proved to be about 70×10^3 cycles before unacceptable sticking occurred again. This is equivalent to a working life of not more than 1000 hr or 200 working days.

A Teflon-sprayed aluminum mushroom galled the unlubricated rubber within 18×10^3 cycles. We are now installing a Teflon seat in place of the rubber seat and will test it soon.

Study of the Compatibility of UN with Cladding Alloys

J.D.L. Harrison[4]

The object of this work is to observe the out-of-reactor interaction between nitrides of nominal compositions UN; $U(N_{0.95}C_{0.05})$; $U(N_{0.95}O_{0.05})$; $U(N_{0.90}C_{0.05}O_{0.05})$ with types 316L, 304L, and ORNL-modified 304 stainless steel, and with V–5% Ti–15% Cr. Due to the limited availability of nitride specimens I will only be able to run the

first and third of these compositions at 1000°C for 100 and 500 hr before I return to Harwell.

Capsules containing the first nitride composition in contact with each of the metals have been assembled and await electron-beam welding. The flat nitride specimens have been metallographically polished on top and bottom surfaces. The metal disks, which alternate with the nitride specimens, have been ground flat and polished on one face only so that the effect of surface finish on any interaction will be tested.

The degreased components were assembled in air. They were handled only with clean rubber gloves and tweezers in order to lessen the amount of impurity.

Capsules containing the third composition will be assembled shortly.

Studies of Vanadium Carbonitride Solutions

K. E. Spear J. M. Leitnaker

A knowledge of the high-temperature chemistry of systems involving U, Pu, V, N, and C is of great importance for understanding interactions of LMFBR nitride and carbonitride fuels with vanadium alloys. In this section, investigations of the properties of the carbon-rich portion of the cubic vanadium carbonitride solid solution are summarized. This particular study is part of a continuing program for investigating the chemical and thermodynamic properties of nitride and carbonitride systems of interest for the LMFBR program. Systems that have been reported previously that involve the five elements listed above are UN (refs. 6,7), PuN (refs. 8,9), UC (refs. 7,10–12) UCN (refs. 13,14), and UVN (ref. 15).

---

[6]H. Inouye and J. M. Leitnaker, J. Am. Ceram. Soc. 51(1), 6–9 (1968).

[7]T. G. Godfrey, J. A. Wooley, and J. M. Leitnaker, Thermodynamic Functions of Nuclear Materials: UC, UC_2, UO_2, ThO_2, and UN, ORNL-TM-1596 (Rev. December 1966).

The lattice parameters of V(C,N) solutions in equilibrium with carbon and nitrogen gas have been determined for a nitrogen pressure of 600 torr and temperatures from 1200 to 1600°C. The equilibrium reaction studied may be written as

$$VC\ [\text{in } V(C,N)] + 1/2\ N_2(600\ \text{torr}) = VN\ [\text{in } V(C,N)] + C(s)\ . \quad (2.4)$$

Similar investigations at nitrogen pressures of 50, 100, and 300 torr are under way and will be reported later.

Our results indicate that vanadium monocarbide reacts with nitrogen reversibly to produce V(C,N) solutions and carbon in a form more active than graphite. Leitnaker[13] found similar results in studies of uranium carbonitrides. Reactions of vanadium nitride with spectroscopic-grade graphite were also found to be reversible in that carbonitride solutions synthesized from these starting materials appeared to react with nitrogen to precipitate graphite, rather than carbon in a more active form plus a more nitrogen-rich V(C,N) solution.

---

[8]K. E. Spear and J. M. Leitnaker, Review and Analysis of Phase Behavior and Thermodynamic Properties of the Plutonium Nitrogen System, ORNL-TM-2106 (March 1968).

[9]K. E. Spear and J. M. Leitnaker, "A Consistent Set of Thermodynamic Values for Plutonium Mononitride," accepted for publication in the Journal of the American Ceramic Society.

[10]J. M. Leitnaker and T. G. Godfrey, J. Nucl. Mater. 21, 175–189 (1967).

[11]J. M. Leitnaker and T. G. Godfrey, J. Chem. Eng. Data 11(2), 392–394 (1966).

[12]J. M. Leitnaker and K. E. Spear, "The High-Temperature Enthalpy of UC_2," submitted for publication to The British Ceramic Society.

[13]J. M. Leitnaker, "The Ideality of the UC-UN Solid Solution," pp. 317–330 in Thermodynamics of Nuclear Materials, 1967, International Atomic Energy Agency, Vienna, 1968.

[14]J. M. Leitnaker, R. A. Potter, K. E. Spear, and W. R. Laing, "The Lattice Parameter of U(C,N) as a Function of Composition," submitted for publication to the Journal of the American Ceramic Society.

[15]K. E. Spear and J. M. Leitnaker, "Thermodynamic Compatibility of Vanadium with Nitride Fuels," Metals and Ceramics Div. Ann. Progr. Rept. June 30, 1968, ORNL-4370, Chap. 18.

Experimental

Four types of double-crucible experiments were performed with an annealing apparatus[13] and a graphite crucible containing two isolated chambers:

1. Fresh (VN + C) samples were heated in both halves of the double crucible.

2. Fresh (VN + C) and (VC + C) samples were heated at the same time.

3. Fresh (VC + C) and previously heated (VN + C) samples were heated at a temperature lower than that used in the previous (VN + C) treatment.

4. A previously heated (VN + C) and (VC + C) sample pair was reheated at a higher, lower, or the same temperature as that used in the previous heating.

Type 1 experiments were performed to ensure that the temperature differences between the top and bottom halves of the crucible were negligible. Type 2 experiments were for approaching equilibrium from two directions in the same experiment. Types 3 and 4 were for approaching equilibrium from the same direction with two samples from different starting materials.

Each sample either gained or lost nitrogen with heating at 600 torr N_2, depending upon the history of the sample. Fresh (VC + C) samples always gained nitrogen, and fresh (VN + C) samples gave off nitrogen. A (VC + C) sample equilibrated first at one temperature, T_1, and then in another experiment at a higher temperature, T_2, gained nitrogen in the first experiment and then lost part of it in the second one. If the order of the two heatings had been reversed, nitrogen would have been added in both cases. For (VN + C) equilibrated first at T_1 and then at T_2, nitrogen was lost in both heatings; if the order of the two experiments had been reversed, nitrogen would have been lost in the first heating and then part of it regained in the second heating at the lower temperature.

The (VN + C) samples were mixtures of vanadium nitride and outgassed spectroscopic-grade graphite with a weight ratio of 4. The

(VC + C) samples were arc-melted vanadium carbide with excess carbon (80 wt % V, 20 wt % C) and were heated as −325 mesh powders.

The N/(N+C) atomic ratios of the V(C,N) solutions studied are known only from our lattice parameter values and the a_o versus N/(N+C) data of Brauer and Schnell.[16] These ratios for our solutions ranged from about 0.05 to 0.3. Oxygen analyses performed on three V(C,N) samples originating from (VC + C) gave values of 0.013, 0.019, and 0.020 wt %; those performed on two carbonitrides originating from (VN + C) gave values of 0.030 and 0.049 wt %.

Data and Results

Three experiments heated at about 1300, 1400, and 1500°C, were performed with identical (VN + C) samples in both halves of the double crucible. The lattice parameter and mass-change results for these three pairs of samples indicate that the top and bottom halves of the crucible are experimentally identical within the limits of our measurements of these properties. These results are listed in Table 2.2.

In the type 2 experiments, the residue from the (VC + C) starting material always had a larger lattice parameter than that from (VC + C). Since VC has a larger lattice parameter than VN [4.1686 A (ref. 16) and 4.1398 A (ref. 17)], one might suppose that the kinetics for adding nitrogen to VC or carbon to VN were just slow. But samples heated for different times at the same temperature gave the same results. Also, the results of experiments of types 3 and 4 show that such an explanation is not correct. Even when nitrogen was either being added to or subtracted from both samples, the sample originating from (VC + C) still had a larger lattice parameter than that originating from (VN + C).

Table 2.3 summarizes the present lattice parameter results for carbon-rich solutions of V(C,N) as a function of temperature and starting material for a nitrogen pressure of 600 torr. The differences between the lattice parameters, Δa_o, of samples originating from vanadium

---

[16] G. Brauer and W. D. Schnell, J. Less-Common Metals 7, 23–30 (1964).

[17] G. Brauer and W. D. Schnell, J. Less-Common Metals 6, 326–332 (1964).

Table 2.2. Experiments Having Identical Starting Materials in Both Halves of the Double Crucible

Sample Number[a]	Time (hr)	Temperature (°C)	Nitrogen Pressure (torr)	Lattice Parameter[b] (A)	Change in Mass[c] (%)
A4825-92	42.6	1299	599.7	4.1581 ± 0.0005	−14.85
A4825-93				4.1576 ± 0.0003	−14.85
A4825-90	17.0	1397	614.2	4.1613 ± 0.0007	−15.76
A4825-91				4.1616 ± 0.0002	−15.79
A4825-78	17.8	1492	600.0	4.1635 ± 0.0002	−16.42
A4825-79				4.1637 ± 0.0002	−16.42

[a]All samples were taken from the same (A4825-72) four-to-one mixture of vanadium nitride and spectroscopic grade graphite. The even numbered sample of a pair was in the top and the odd numbered one in the bottom of the double crucible.

[b]The given error limit is twice the computed standard deviation.

[c]The percent change in mass refers to the sample and is that caused by the loss of nitrogen from the mixture of vanadium nitride plus graphite.

nitride plus graphite and those originating from (VC + C) are also given. The estimated error limits in the parameters take into account the number of experimental results at each temperature, the spread in these results, the small differences in temperatures and pressures for the similar experiments, and the uncertainties — taken as twice the computed standard deviation — in each measured parameter.

The error limits on the differences in the last column of Table 2.3 were estimated from the variations in Δa_o's for individual experiments, not from the spread in the lattice parameters for different experiments of the same nominal temperature and pressure. While one expects small temperature or pressure difference between experiments, this should not affect Δa_o, because both (VN + C) and (VC + C) were heated at the same time in a double crucible in a given experiment.

Table 2.3. The Lattice Parameter of the Carbon-Rich V(C,N) Solution as a Function of Temperature and Starting Materials for a Nitrogen Pressure of 600 Torr

Temperature (°C)	Lattice Parameters of Solutions of V(C,N)[a] Original Starting Materials		
	(VN + graphite)[b]	(VC + graphite)[b]	Δa_o [c]
			$\times 10^4$
1200	4.1535 ± 0.0004	4.1550 ± 0.0005	15 ± 3
1300	4.1576 ± 0.0005	4.1587 ± 0.0004	11 ± 4
1400	4.1618 ± 0.0007	4.1629 ± 0.0007	11 ± 3
1500	4.1636 ± 0.0003	4.1646 ± 0.0004	10 ± 4
1600	4.1648 ± 0.0005	4.1655 ± 0.0005	7 ± 5

[a]The uncertainties in the lattice parameters were estimated as described in the text.

[b]These values are an average of the results obtained at each respective temperature.

[c]The error limits on these differences in the two lattice parameters were estimated as described in the text.

Conclusions and Discussion

We think the difference in lattice parameters for (VN ± C) and (VC + C) samples heated at identical temperatures and pressures exists because active carbon is formed as a product in the reaction of VC with nitrogen to form the carbonitride solution. This carbon is active with respect to the spectroscopic-grade graphite used in the (VN + C) mixtures. At the temperatures and times used in these experiments, this active carbon does not appear to graphitize.

Another interesting result is the apparent "memory" of the samples. In samples heated first at T_2 and then later at a lower temperature, T_1, the V(C,N) solution formed at T_2 reacts with nitrogen at T_1 to form a solution richer in nitrogen and rejects carbon. This carbon must "remember" whether it originated from the vanadium carbide or the spectroscopic-grade graphite in the (VN + C) mixtures since the lattice

parameter results for these T_2 (first)-T_1 (second) type experiments are the same as for the other types of experiments at T_1. The rejected carbon apparently precipitates on preexisting graphite crystals if it originated from a (VN + C) mixture.

The formation of active carbon has been observed previously. Leitnaker[18] obtained a difference of about 500 cal/mole between the enthalpy of carbon formed from the reaction of UC with nitrogen at 1500°C and the enthalpy of graphite. In combustion experiments on pyrolytic graphites, Lewis, Frisch, and Margrave[19] measured a difference of 220 ± 50 cal/mole in samples annealed respectively at 2200 and 3600°C. Browning and Emmett[20] made equilibrium measurements in the system C-CH_4-H_2 and found that carbon obtained from the decomposition of Fe_3C was kinetically stable, but had a free energy about 300 cal/mole more positive than graphite. Therefore, the explanation we give for our experimental observations is not unprecedented.

The Hot Hardness of Uranium Carbonitrides

J.D.L. Harrison[21]

Measurement of the hot hardness of compositions between UN and UC at temperatures up to 1200°C will provide some indication of the way high-temperature strength and creep vary with composition and will assist in the selection of the most appropriate compositions for measurements of creep during irradiation.

The diamond pyramid hardness of a 94.5% dense specimen, 0.7 in. diam × 0.3 in. thick, was measured between 25 and 1200°C with the aid of a diamond indenter with 1.54 kg load. Chemical analysis of

---

[18] J. M. Leitnaker, "The Ideality of the UC-UN Solid Solution," pp. 317–330 in Thermodynamics of Nuclear Materials, 1967, International Atomic Energy Agency, Vienna, 1968.

[19] D. C. Lewis, M. A. Frisch, and J. L. Margrave, Carbon 2, 431–432 (1965).

[20] L. C. Browning and P. H. Emmett, J. Am. Chem. Soc. 73, 581–583 (1951).

[21] On loan from Atomic Energy Research Establishment, Harwell, England.

the specimen is not yet complete. Ceramographic examination of the material before indentation showed that it had an equiaxed structure of about 35-μ grain diameter with most of the 2- to 5-μ porosity distributed uniformly in the grains. There were isolated clusters, about 120 μ in diameter, of grain-boundary porosity and smaller grains in which the local density appeared to be little more than 60%. No UO_2 was visible.

Two or three indentations were recorded at each temperature listed below, and each hardness value listed represents one such indentation:

Temperature, °C	DPH, kg/mm^2
25	423 433
353	270 219 268
477	238 214 236
674	187 182
759	135 141 149
857	103 89
894	69 80.4 85.3
935	67.3 67.3
983	55.9 57.4 57.9
1061	39.1 40.3 41.6
1160	30.6 31.0 29.7
1225	29.7 27.3 28.8

The room-temperature hardness is the same as that reported by Godfrey and Hallerman,[22] who used a 2-kg load and a sapphire indenter. At temperatures up to 700°C, the two sets of results are in reasonable agreement; above this, our work indicates both lower hardness values and a greater dependence of hardness on temperature. A comparison of the present results with hot-hardness measurements of sintered UC made at Atomics International[23] and Harwell[24] indicates that sintered UN may be significantly softer than sintered UC at all temperatures. The "knee" in the log (hardness) versus temperature graph appears to occur at about 600°C for UN as compared to 800°C, or above, for UC. We will very soon do further work with a higher density specimen of UN and arc-cast UC. In the meantime, the present results should be regarded as provisional only.

It has not been possible to make suitable high-density specimens of UC-UN solid solutions. Hot-hardness measurements on these compositions will therefore have to be delayed until a fabrication process has been developed.

Fundamental Research on Uranium Nitride

W. Fulkerson

Preliminary band structure calculations have been made, and a number of property measurements on UN are completed or are in progress.[25] These include low-temperature specific heat (1.3 to 4.6°K), thermal conductivity (77 to 400°K), Seebeck coefficient (6 to 400°K), electrical resistivity (4.2 to 400°K), velocity of sound (300°K), self diffusion of ^{233}U (1400 to 2100°K), and compressive creep (1400 to 1800°K).

---

[22] T. G. Godfrey and G. Hallerman, Metals and Ceramics Div. Ann. Progr. Rept. June 30, 1965, ORNL-3870, p. 167.

[23] Atomics International, Annual Technical Progress Report, AEC Unclassified Programs, Fiscal Year 1964, NAA-SR-9999, Section I-B, p. 55.

[24] H. J. Hedger, U.K. Atomic Energy Research Establishment, Harwell, England, private communication.

[25] W. Fulkerson, "Fundamental Ceramics Research," Metals and Ceramics Div. Ann. Progr. Rept. June 30, 1968, ORNL-4370, Chap. 7.

Fuel-Cladding Thermal Conductance Studies

R. K. Williams T. E. Banks D. L. McElroy

The object of this study is to improve the permissible power generation rating of fuel elements by decreasing the thermal contact resistance associated with the fuel-cladding interface. Emphasis is placed on nitride and carbide fuels, which have relatively high thermal conductivities. The details of the experimental technique have been described,[26] and a summary of the conditions and results of the tests is presented in Table 2.4.

All data that have been collected fit the relationship $R_c = A\sigma^n$, where R_c is the thermal contact resistance in deg cm^2 w^{-1}, σ is the compressive stress in psi, and A and n are materials constants. The results show that the contact resistance for stainless steel—UN interfaces is not very sensitive to the hardness of the stainless steel and that the value of this property can be reduced significantly by using a material that is soft or has a high thermal conductivity, or both.

---

[26]R. K. Williams *et al.*, "Fuel-Cladding Thermal Conductance," Metals and Ceramics Div. Ann. Progr. Rept. June 30, 1968, ORNL-4370, Chap. 18.

Table 2.4. Conditions and Results of Thermal Contact Resistance Measurements in Vacuum at 50°C

Contacting Materials[a]	Hardness[b] (DPH)	RMS Surface Roughness (μin.)	Thermal Conductivity ($w\ cm^{-1}\ deg^{-1}$)	Contact Resistance, R_c, at Compressive Stress[c] of 1000 psi ($deg\ cm^2\ w^{-1}$)	Materials Constants[c]	
					A	n
Copper	50	14–15	4.0	0.17	550	−1.17
T-1 tool steel	835	3–4	0.16			
Type 302 stainless steel[d]	340	3–4	0.1	1.16	1156	−1.00
T-1 tool steel	835	3–4	0.14			
Type 302 stainless steel[e]	415	5	0.1	2.16	620	−0.82
UN	525	6–8	0.14			
Type 302 stainless steel[d]	340	3–4	0.1	2.29	1510	−0.94
UN	525	6–8	0.14			
Type 302 stainless steel[f]	166	5	0.1	1.71	750	−0.88
UN	525	6–8	0.14			

[a]First material listed in given couple was in form of thin foil and second was in form of bulk specimen.

[b]Load for foils: 50 g. Load for bulk specimens: 1 kg.

[c]From relationship $R_c = A\sigma^n$, where σ is the compressive stress in pounds per square inch.

[d]Mill designation: half hard.

[e]Mill designation: full hard.

[f]Mill designation: annealed.

3. FISSION-GAS RELEASE AND PHYSICAL PROPERTIES OF FUEL MATERIALS DURING IRRADIATION

R. M. Carroll R. B. Perez
G. M. Watson J. G. Morgan
O. Sisman

The purpose of this work is to measure the parameters that control the release of fission gas from highly characterized nuclear fuels. These parameters are evaluated in terms of a generalized model to predict release from operating fuel materials. Thermal diffusivity is measured in-reactor in analogous experiments.

Effect of Burnup and Burnup Rate on Fission-Gas Release from Single-Crystal UO_2

A 48%-enriched single crystal of UO_2 was sliced into cubes which were then ground into 997-μ-diam spheres. We placed 36 of these spheres into a tungsten holder so that they formed a hollow cylinder 12 spheres in circumference and 3 spheres deep. It was necessary to use small specimens to prevent thermal-stress cracking, and at least 36 spheres were required to give sufficient fuel volume for meaningful temperature measurements. These specimens released so much fission gas that we were unable to operate above 1300°C because of the radioactivity limitations of the experiment.

During the early portion of the irradiation, we observed that at high fission densities, or burnup rates, the fission-gas release was accelerated. Using these results, along with our previous data and some from the literature, we obtained a relation between fractional gas release and fission density.[1] During this time, that is, to a burnup of 1.9 at. % U, the rate of gas release did not increase with burnup.

Above 1.9 at. % U burnup, the rate of gas release increased as shown in Fig. 3.1. (The reduction in release rate at the start of irradiation is typical for this kind of experiment.) Low-temperature

[1]R. M. Carroll, O. Sisman, and R. B. Perez, Nucl. Sci. Eng. 32(3), 430 (1968).

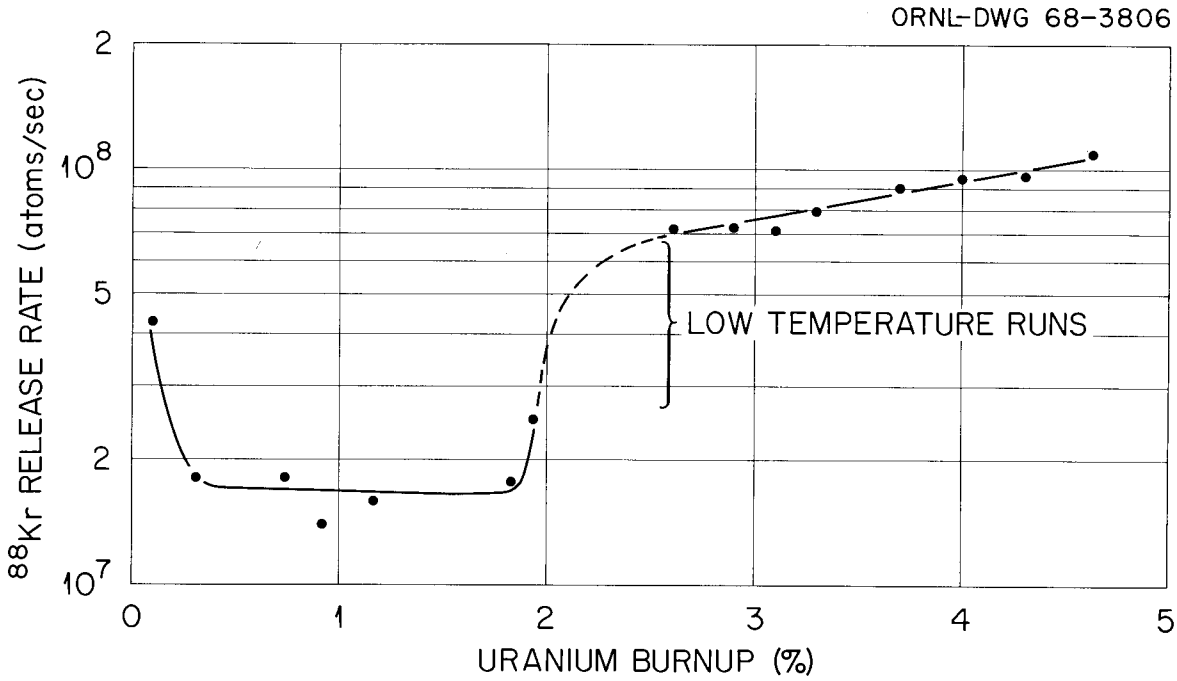

Fig. 3.1. Krypton-88 Release from Single-Crystal UO_2 Normalized to 820°C and 1.5×10^{14} Fissions cm^{-3} sec^{-1} as a Function of Burnup (at. % U).

runs at around 2 at. % U burnup were characterized by small, spontaneous bursts of gas. We had seen such bursts in previous tests when UO_2 was irradiated at temperatures above 1600°C, but never at lower temperatures. We speculated that the single-crystal specimens were becoming strained enough by fission-product accumulation to develop small cracks, causing bursts of gas; the steady-state rate of gas release would, in that case, be increased because of the larger surface area of the cracked specimen. This hypothesis appears to have been correct, for upon opening the capsule after irradiation we saw that the specimens had degenerated into powder.

The steady increase in release rate shown in Fig. 3.1 was likely caused by the continual subdividing of the specimen as fission products accumulated along small defects and generated enough stress to break the crystal particles. This effect was undoubtedly enhanced because the small, single-crystal specimens had only a few internal defects to store the generated fission products, thus concentrating them at a few places.

Nonfission Heating During Irradiation

In making measurements of thermal diffusivity during irradiation, we must know the heat generation within the fuel specimen. We can calculate the fission heating very well by measuring the neutron flux, but the amount of gamma-ray heating is unknown. We had hoped that the gamma-ray heating could be neglected in comparison to the fission heating, but our thermal conductivity measurements indicated that the power production within the fuel was significantly greater than could be accounted for by fission power alone. Therefore we conducted an experiment to measure the nonfission heating within the specimens.

The apparatus consisted of a standard specimen capsule containing a brass holder which in turn supported a slug of pure copper suspended on needle points. Chromel-P vs Alumel thermocouples were pressed into holes drilled into the copper slug and the brass holder.

Two different experimental methods were used. One method was to change the rate of air cooling on the outside of the capsule so that the entire system experienced a temperature increase. The other method was to move the specimen further into the reactor very quickly to cause a temperature increase by the increase in nuclear heating. In both cases, the time-temperature changes of the copper slug and the surrounding brass holder were measured with a data logger, and the information was placed on punched tape.

The time-temperature response for the copper slug and the brass holder were fed into a computer program. A good fit of the time-temperature behavior was given by

$$T(t) = A_o - A_1 e^{-rt} , \qquad (3.1)$$

where T is temperature in degrees centigrade, t is time, A_o and A_1 are constants depending on the properties of the sample and thermal shield, and r is an inverse relaxation time. The computer fit gives values of the parameters A_o, A_1, and r. We are now comparing the parameters obtained from the copper slug to those of the surrounding brass holder

to obtain nonnuclear heating values at different positions in the reactor. The two methods will allow a cross-check on the values obtained.

During the nonnuclear heating measurements, a mixture of argon and helium was passed through the capsule. This allowed an accurate measurement of the thermal neutron flux over the entire period of the experiment.

Uranium Nitride Experiment

A capsule containing three bushings of 19.8%-enriched UN is being irradiated in the ORR C-1 facility. The bushings are stacked to form a hollow cylinder 0.895 in. in length, 0.255 in. in OD, and 0.103 in. in ID and are held in place by an Al_2O_3 holder. The UN bushings, furnished by the ORNL Metals and Ceramics Division, have the characteristics listed in Table 3.1.

Table 3.1. Properties of 19.8%-Enriched UN Bushings for Fission-Gas Release and Thermal Diffusivity Measurements

Specimen Number	Density		Weight (g)	Diameter		Length (in.)
	(g/cm^3)	Percent of Theoretical		Outside	Inside	
				(in.)		
1	13.60	95.0	2.8324	0.2549	0.103	0.2971
2	13.56	94.7	2.8099	0.2557	0.103	0.2990
3	13.53	94.5	2.8777	0.3561	0.103	0.2986

The main purpose in using a relatively massive specimen is to obtain thermal conductivity data during irradiation. Data are being obtained, but values will not be calculated until the nonnuclear heating experiment described above has been evaluated.

Data for the release of fission gas from UN are still being accumulated, but the burnup level at this writing is less than 0.1 at. % U. A summary of the results and some tentative interpretations are presented below.

Below 700°C, the rate of fission-gas release is independent of temperature. The rate varies as the square of the flux, which indicates that gas release below 700°C is by surface knockout and that the specimen surface is not saturated with gas. This is unlike the UO_2 specimens, which showed a direct dependence between neutron flux and knockout release. At burnup rates of 2.7 to 5×10^{12} fissions cm^{-3} sec^{-1} the knockout release is about the same as for UO_2, but at higher burnup rates the knockout release from the UN is greater because of the flux-square dependency.

During the low-temperature runs there was an abrupt increase in gas-release rate that must have been caused by a crack in one of the bushings. This seems strange, for the thermal stresses were low and burnup was insignificant.

At temperatures above 700°C, the rate of fission-gas release from UN is an exponential function of temperature, the same as is true of UO_2. In contrast to UO_2, however, the fractional release rate (release rate-to-birth rate, R/B) for UN does not change with burnup rate. The initial results indicate that the fission-gas release occurs by a classical diffusion process with little trapping by defects produced by irradiation. The activation energy of the gas release is 35 kcal/mole between 800 and 1200°C.

At about 800°C the gas release was about the same from UN as from UO_2. But as the temperature increased, the gas release from UN became much larger than that from UO_2. Extrapolating the data to 1400°C, we predict that the fractional release from UN will be an order of magnitude higher than that from a UO_2 specimen at the same levels of burnup rate, because the temperature dependence of the gas release is lower in UO_2

4. ZIRCONIUM METALLURGY

P. L. Rittenhouse

Several zirconium-base alloys are used in nuclear power reactors for fuel cladding, fuel channels, and pressure tubes. It is our aim to demonstate that, by controlling the crystallographic texture in these materials, we can substantially increase the allowable design stress. This, in turn, will permit the use of lighter sections, reduce the mass of nonfissionable material in the reactor core, and result in more economic nuclear power.

Tubing Fabrication Study

T. M. Nilsson P. L. Rittenhouse
D. O. Hobson E. J. Tenckhoff

The anisotropy of mechanical properties of zirconium alloys is highly texture sensitive, and it is desirable, therefore, to control the texture of products fabricated from those materials. We have undertaken a study of the fabrication of zirconium alloy tubing to (1) show in detail how fabrication events affect texture, (2) allow control of texture in the finished product, and (3) demonstrate the most economical and efficient method of tube production.

As a first step in our study we machined extrusion billets from 4-in.-diam forged Zircaloy-4. These billets were extruded (790°C with molten neutral salt as a lubricant) at ORNL to produce about 75 ft of 1.5-in.-OD by 1-in.-ID tube stock. Sixty feet of these tubes were shipped to Wah Chang Corporation, Albany, Oregon, for tube reduction (rocking).

During this quarter the tube reductions were performed. Before reduction, the annealed tubes were pickled in a nitric-fluoric acid solution. Immediately after pickling, the tubes were conversion-coated in a sodium-phosphate solution. The inside of the tubes was lubricated with an oil-base lubricant (G. Whitfield Richards 31-S). During the rocking step, the outside of the tubes was bathed with the 31-S

lubricant diluted in a 3:1 ratio with water. After the reduction the tubes were again pickled and then annealed in vacuum at 730°C for 2 hr.

An ORNL observer was present during all tube reductions to ensure that the fabrication schedules were followed as closely as possible and that samples were taken from the reduced tubes after each reduction. The detailed sampling will permit us to follow texture development in these tubes very closely. For each die and mandrel combination, the normal sampling was supplemented with at least one piece of tapered section containing some unreduced tube, the partially reduced section, and some completely reduced tube.

The tubes are being shipped to ORNL; when we receive them, we will begin measuring texture and mechanical properties. Also, we will start cold drawing to final size the tubes rocked to intermediate sizes.

Circumferential Texture Variations in Zircaloy Tubing

D. O. Hobson P. L. Rittenhouse

The x-ray texture device, which is capable of both rotating and translating the tubing so that the x-ray scan covers the surface of the tube and thus produces a plot of the variation in circumferential pole density of a specified crystallographic plane, has been modified to produce a more versatile instrument. The device is now capable of tilting the tubing about an axis perpendicular to the plane containing the incident and reflected x-ray beams. This allows circumferential pole density determinations to be made on planes whose poles lie at angles of up to 15° on each side of the perpendicular to the tube surface toward the axial direction. Absorption factor corrections can easily be made as a function of tubing tilt. A computer program has been written[1] that will read intensity data from a punched tape obtained from the counting circuitry and will draw a radial pole figure.

---

[1]G. R. Love, group leader, Metallurgy of Superconducting Materials, private communication.

This device will be used to evaluate the texture uniformity of the Zircaloy tubing fabricated as discussed in this report. Inhomogeneous textures are introduced into Zircaloy tubing during fabrication.[2] This inhomogeneity results in nonuniform strain behavior that can invalidate accepted design criteria. We hope to be able to trace the formation of this inhomogeneity in tubing. Once we are sure of the source of the inhomogeneity, we can take steps to eliminate it.

A description of the design and use of the device for producing circumferential pole figures has been written for publication.

Texture Gradients in Thin-Walled Zircaloy Tubing

E. J. Tenckhoff P. L. Rittenhouse

Fifteen lots of Zircaloy tubing with different processing histories were examined by x-ray diffraction.

We found marked differences in the development of texture that depended on whether wall reduction or diameter reduction was predominant during fabrication. Predominant wall reduction results in a texture with relatively little spread of the basal poles from the radial direction toward the tangential direction. Across the wall thickness — going from the outer to the inner surface — the spread increases from 0 to 25°. In the tubes with major diameter reduction, the spread is rather constant at 45°.

It is also interesting to note that with wall reductions the intensity of the basal poles decreases from the outer to the inner surface. The opposite is true for diameter reduction.

Similarly, there are differences in the textures resulting from ball swaging, cold drawing, and tube reducing. These experiments are still in progress. We will try to develop further information by examining specimens taken from an earlier step of fabrication.

---

[2]D. O. Hobson and P. L. Rittenhouse, to be published in Transactions of the Metallurgy Society of the AIME.

Deformation and Annealing Textures in Drawn Zircaloy Tubing

E. J. Tenckhoff P. L. Rittenhouse

The deformation texture of zirconium alloy sheet and tubing found in the literature can be described as (0001) ± 0 to 40° ND to TD, $\langle 10\bar{1}0 \rangle$ where ND is the sheet normal direction or tube radius and TD is the sheet transverse direction or tube tangent. The annealing texture is generally believed to be the same except for a 30° rotation of the basal plane about its pole. This exchanges the positions of the $\langle 10\bar{1}0 \rangle$ and $\langle 11\bar{2}0 \rangle$ directions; that is, (0001) ± 0 to 40° ND to TD, $\langle 11\bar{2}0 \rangle$.

While we were examining texture gradients in thin-walled Zircaloy tubing we found that there may also be a change in the position of the basal poles back toward the radial direction. The results, at least of two lots of tubing, show a larger influence of the α-annealing treatment on the recrystallization texture than has been believed until now. Experiments are still in progress.

Texture Development in Single-Crystal Zirconium

D. O. Hobson

We are presently examining the interactions of the various deformation systems with each other, as influenced by the stress resolved by the Schmid factors, to try to trace the transition from one deformation system to another. This is part of a continuing effort to understand texture formation in hexagonal materials.

Deformation of Zirconium at Elevated Temperatures

E. J. Tenckhoff

Since zirconium is rolled at elevated temperatures, we are studying its deformation at temperatures up to 800°C. During this quarter the design of the deformation device was completed, and parts of the apparatus were machined. The electro-discharge machine (EDM) was modified to machine the specimens required. The growing of large zirconium single

crystals by electron-beam zoning was also started. A comparison of different cutting methods for the single crystals shows that the gross shape of the shearing cube can be cut with the EDM. This method, however, is not desirable for machining the very small gage section, since it produces a distorted surface layer. We will try an acid saw method for this purpose.

Texture Determination by Optical Methods

L. T. Larson[3]

An optical method for estimating the degree of preferred orientation in fine-grained polycrystalline specimens of zirconium alloys would be valuable in scoping experiments and in quality control of mill products. Certain optical properties (reflectivity values and bireflectance) of zirconium alloys can be used to determine the orientation of single crystals or individual grains.[4] Reflectivity measurements on specimens with as many as several hundred grains in the microscope field of view will be an integration of the reflectivities of each grain. At any one azimuth on the microscope stage, a completely random specimen will have as many grains at their position of maximum reflectivity as it has grains at positions of minimum reflectivity. Positions of all degrees of reflectivity will be equally represented, and the reflectivity will be unchanged during a 360° rotation of the specimen. Similar results are obtained in two other cases: the first is when all of the basal poles of the grains are perpendicular to the section, and the second is when the basal poles lie in the plane of the section but are uniformly disposed in a radial manner. These three possibilities can be separated by visual microscopic examination using the sensitive tint plate. In addition, the percentage of reflectivity will be different for the three.

---

[3]Consultant, Department of Geology, University of Tennessee.

[4]L. T. Larson and M. L. Picklesimer, Trans. Met. Soc. AIME 236, 1104–1106 (1966).

At the other extreme is a specimen in which the basal poles of all of the grains are aligned parallel to one another and lie in the plane of the examined section. Rotation through 360° will give a reflectivity curve with two maxima and two minima (as a prism plane of a single crystal).

We cut 18 sections from six schedules of annealed Zircaloy plate. For each schedule, one polished section from each of the fabrication directions (rolling, transverse, and normal) was prepared and keyed so that it could be placed on the microscope stage with a known fabrication direction at a given stage azimuth. Reflectivity curves were obtained from five different areas on each polished section. The reflectivity curve amplitudes (aggregate bireflectance) for each grouping of five areas were summed and averaged. Using the known reflectivity differences of standards (germanium and silicon) that we ran sequentially with the Zircaloy specimens, we converted the units of bireflectance to percent bireflectance. X-ray pole figures of the basal pole distribution in each specimen are being prepared. Since the general texture pattern is what we desire, only peak positions and relative peak heights are of interest.

Reflectivities and bireflectance have been determined for all of the sections. Table 4.1 summarizes these data. Basal pole figures have been made for the transverse and rolling sections of schedule 9 and for all three of the sections of schedule 18. These are shown in Figs. 4.1 and 4.2.

The bireflectance values for schedule 9 are highest in the transverse section but are nearly that high in the rolling section. No bireflectance was found for the normal section. These data indicate that schedule 9 is highly textured and has a very high concentration of basal poles perpendicular to the normal section. The high and nearly identical bireflectance values for the rolling and transverse sections suggest that these sections contain approximately equally high concentrations of prism or near prism planes and that the basal poles are parallel to the normal direction.

Table 4.1. Bireflectance Values of Polycrystalline Zircaloy

Schedule	Average Aggregate Bireflectance, %		
	Section[a]		
	Transverse	Normal	Rolling
9	3.3	0	3.1
10	2.7	1.3	1.3[b]
11	1.8	1.4	0.9
17	2.0	1.1	1.0
18	1.9	2.6	0.7
62	0.8	1.1	1.3

[a]Sections cut perpendicularly to indicated fabrication directions.

[b]Data questionable because of instrumental problems.

The basal pole plot of section 9R (schedule 9 rolling section) is shown in Fig. 4.1(a). This pole figure clearly shows a large number of basal poles in the normal direction and a slight spread toward the rolling and transverse directions. The pole figure of section 9T, Fig. 4.1(b), also shows the high concentration of basal poles in the normal direction.

Schedule 18 illustrates a different kind of texture. Microscopic examination of section 18R with the sensitive tint plate suggests that there are a very large number of grains with their basal poles in or near the plane of the section. Furthermore, the reflectivity values for 18R are somewhat higher relative to the germanium standard than are several of the other rolling sections. Interpretation based on bireflectance data alone would be incorrect.

The correct interpretation, substantiated by the pole figures shown in Fig. 4.2, is that the rolling section has a high concentration of prism planes lying in the plane of the section and that the basal poles are nearly symmetrically disposed about the 45° positions within the rolling section [Fig. 4.2(a)]. This distribution has the same

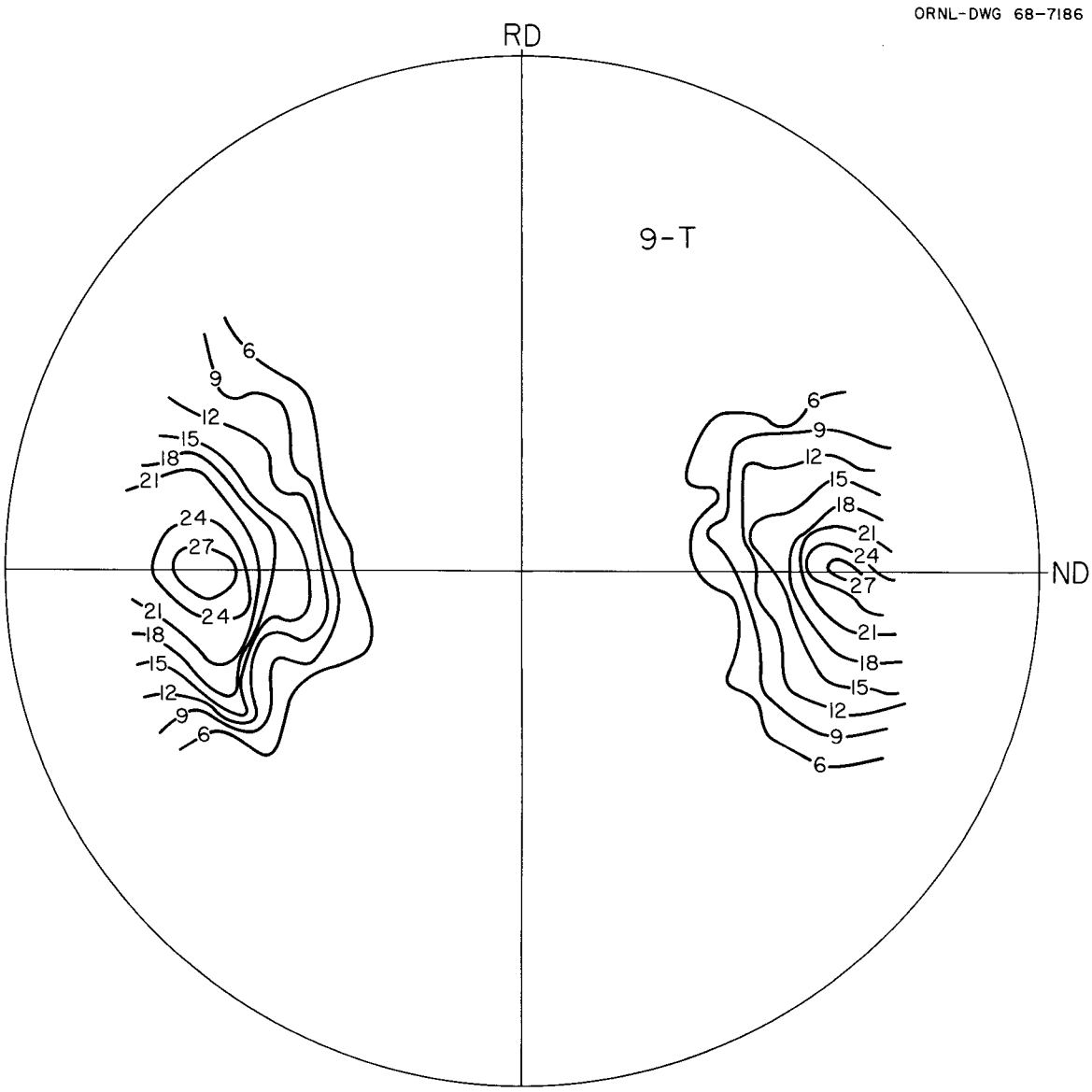

Fig. 4.1. Basal Pole Figures for Schedule 9 Zircaloy. (a) Rolling section. (Continued).

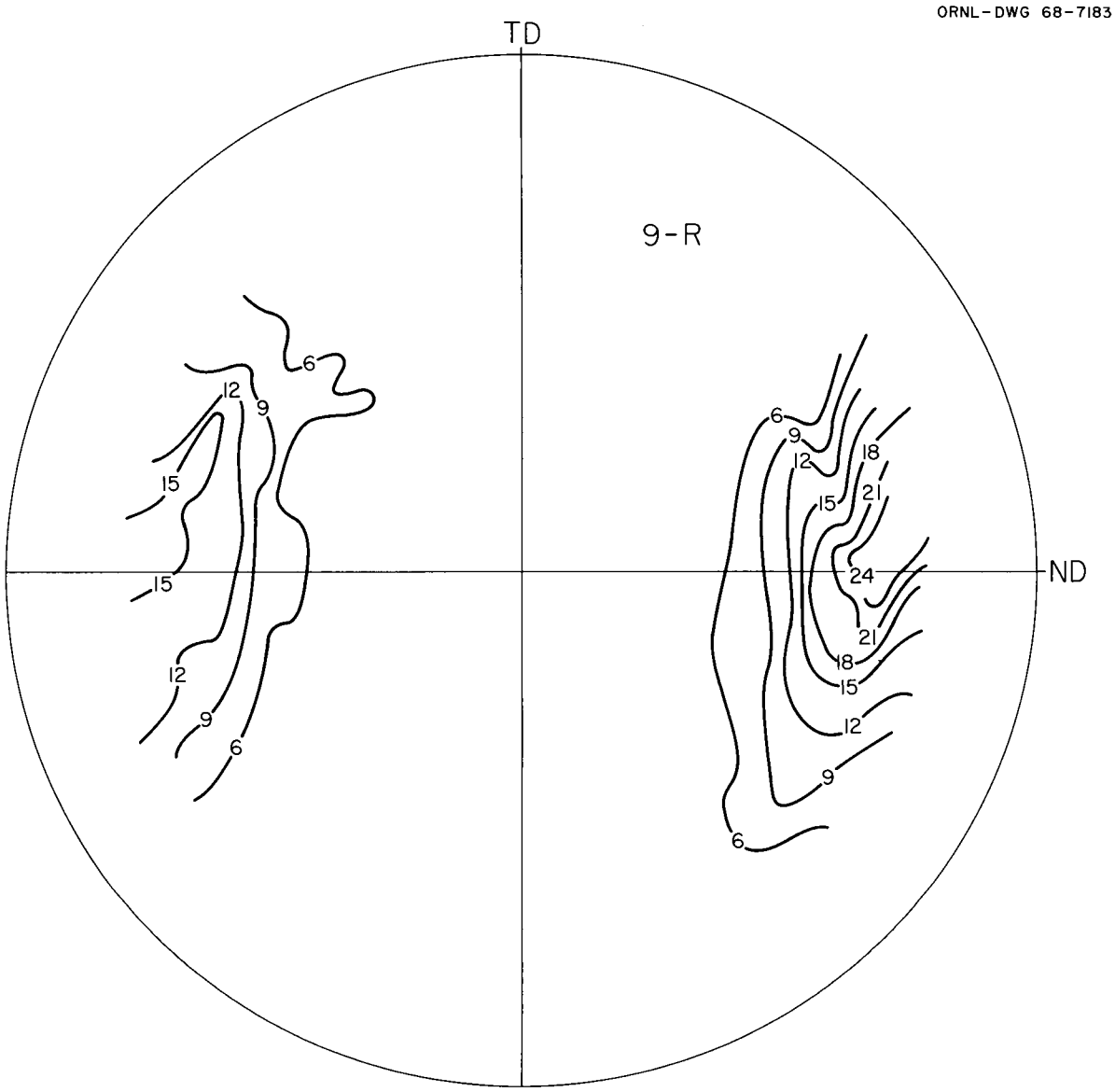

Fig. 4.1 (continued). (b) Transverse section.

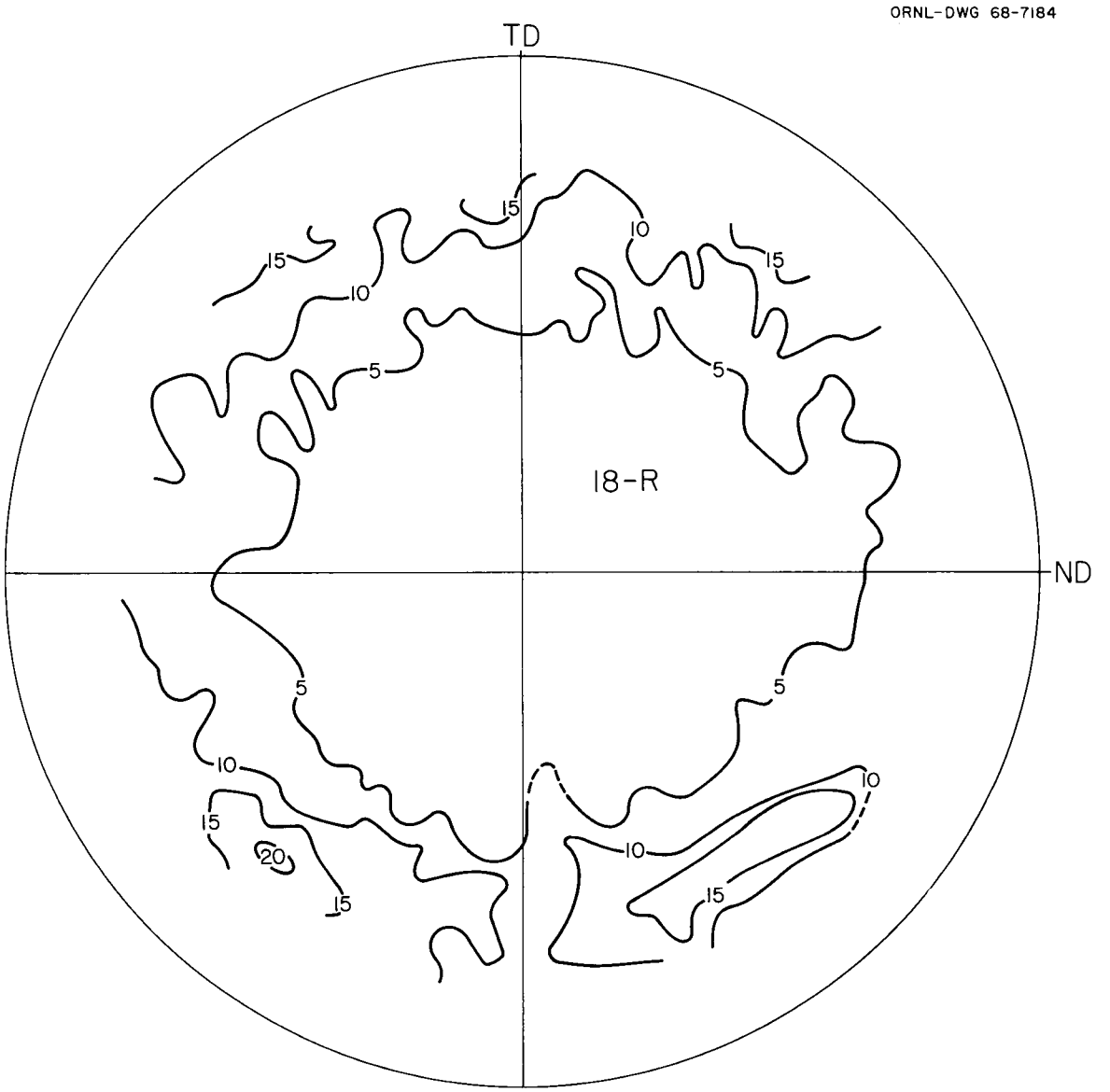

Fig. 4.2. Basal Pole Figures for Schedule 18 Zircaloy. (a) Rolling section. (Continued).

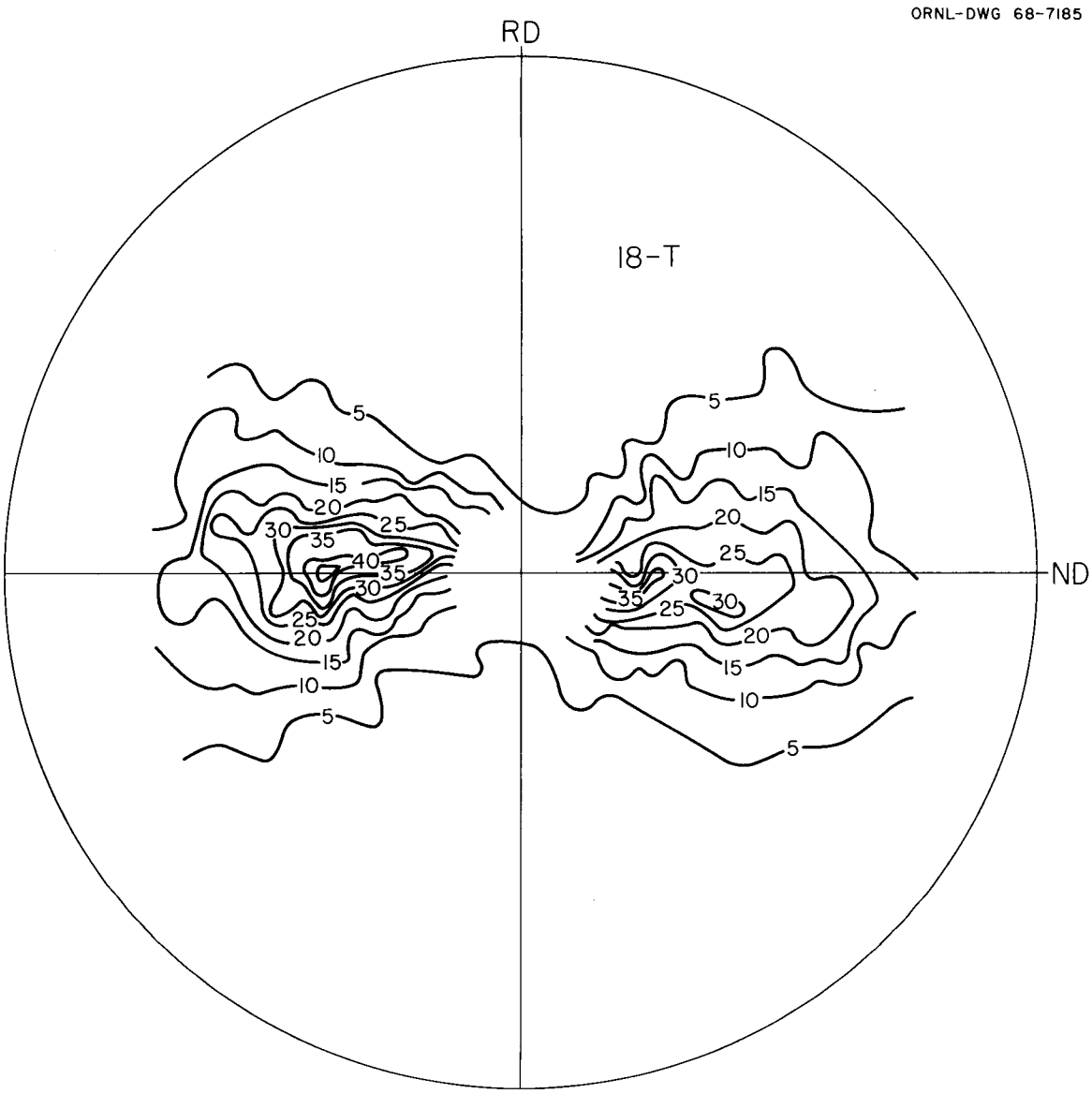

Fig. 4.2 (continued). (b) Transverse section.

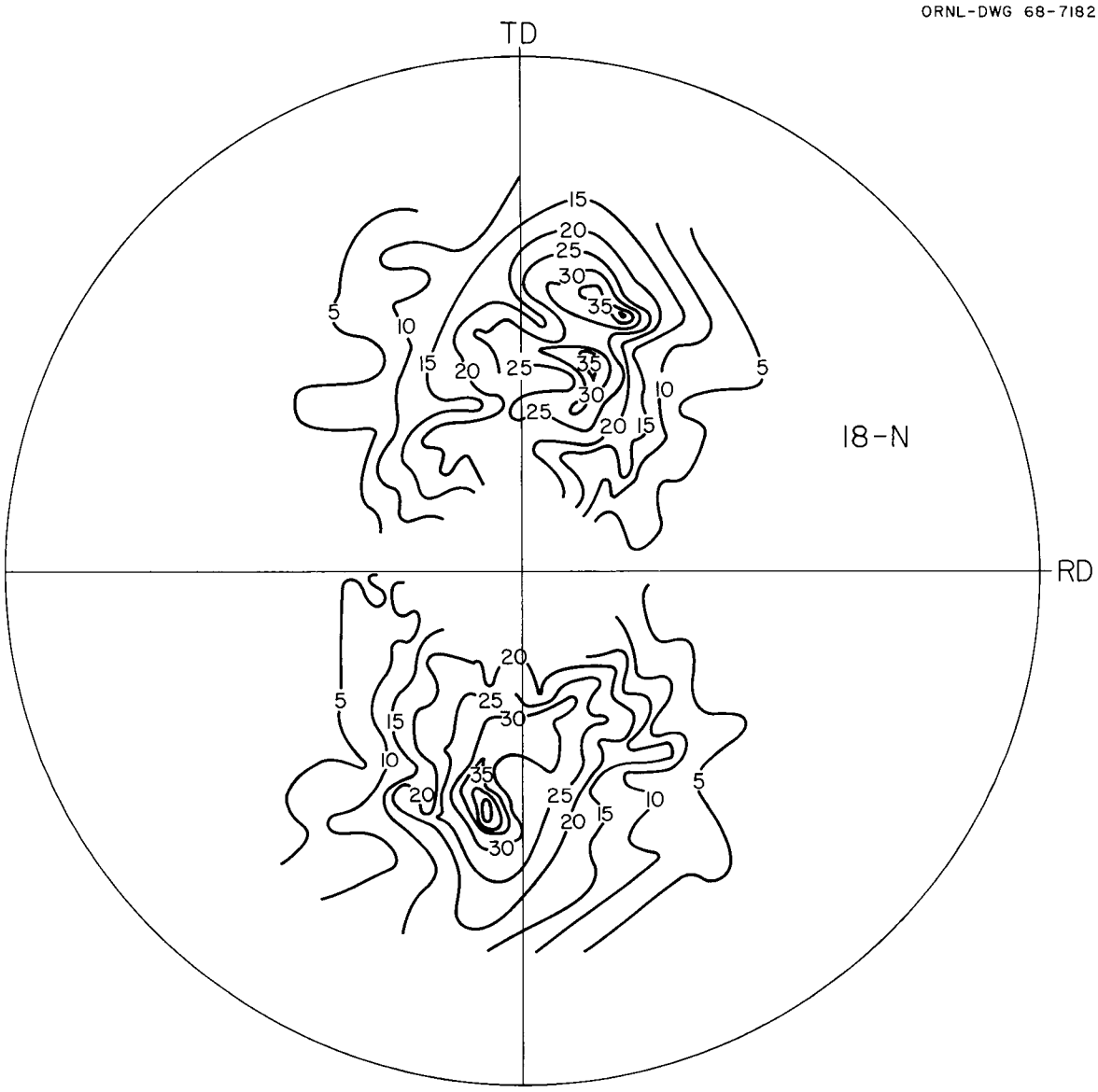

Fig. 4.2 (continued). (c) Normal section.

effect as would one with half of the grains in a position of maximum reflectivity and half with minimum reflectivity. The integrated reflectance of the section is, therefore, about the same throughout the 360° of stage rotation. The basal pole figures for the transverse and normal sections [Fig. 4.2(b) and 4.2(c)] show that the grains are disposed with their basal poles more nearly in the plane of the normal section than the transverse section. This gives higher bireflectance values for the normal section than the transverse section and substantiates the data for schedule 18 in Table 4.1.

The bireflectance data for schedule 11 suggest an interpretation similar to that for schedule 18. Schedule 11, however, has a lower degree of preferred orientation. The optical data for schedule 17 indicate that the grains displayed in the transverse section are, in aggregate, oriented with prism faces near the plane of the section. The bireflectance values for the normal and rolling sections, while nearly the same, result from different phenomena. In the normal section we are observing grains in which the aggregate orientation is perhaps as much as 30° from the basal and in which the basal poles are preferentially spread toward the transverse direction. The explanation of the rolling section bireflectance value is similar to that given for sections 18R and 11R.

The data discussed above indicate that bireflectance measurements in plane polarized light can provide a useful and meaningful approximation of the degree of preferred orientation in polycrystalline Zircaloy. The method should be equally applicable to other nonisometric metals and alloys. More work should be done to establish the precision of the method. More importantly, we need bireflectance measurements on specimens in which we can observe two or three grains within the microscope field of view. This should prove the concept that the sinusoidal shape and amplitude of the reflectivity curves accurately represent the integrated bireflectance of all of the grains present in the section.

PART II

COOLANTS

5. ALKALI METAL CORROSION STUDIES

W. O. Harms R. E. MacPherson

Auxiliary electrical or ion-propulsion requirements for space vehicles necessitate power plants of high efficiency that will operate at high temperatures. For these applications, nuclear power systems have been proposed in which alkali metals are used to transfer heat, drive a turbogenerator, and lubricate rotating components. Accordingly, we are investigating the corrosion properties of candidate alkali metals, primarily lithium and potassium, under conditions of interest for space applications. Because of the relatively high temperatures (> 1000°C), the investigation is concerned largely with refractory metal container materials. We intend both to examine the chemical and metallurgical effects on structural materials produced by alkali metals and to demonstrate engineering-scale construction and operation of refractory alloy—liquid metal loop systems.

Compatibility of Boiling Potassium with Refractory Alloys

J. H. DeVan A. P. Litman W. R. Huntley

Potassium is of principal interest as a working fluid in space nuclear power systems. This program is designed to yield data on the corrosion and erosion of potential container materials by boiling and condensing potassium and potassium vapor.

Refluxing Capsule Experiments (J. R. DiStefano)

We are conducting refluxing capsule experiments as part of a program to evaluate the compatibility of refractory metals with boiling alkali metals. The capsules are tested individually at 1100 to 1400°C for times up to 5000 hr using the test system shown in Fig. 5.1. Materials under investigation include alloys based on Nb, Ta, Mo, and W.

Table 5.1 summarizes the conditions and results of tests most recently completed and those still in progress. The cumulative operating time for refractory metal—boiling potassium systems now exceeds 100,000 hr.

ORNL-LR-DWG 75699R

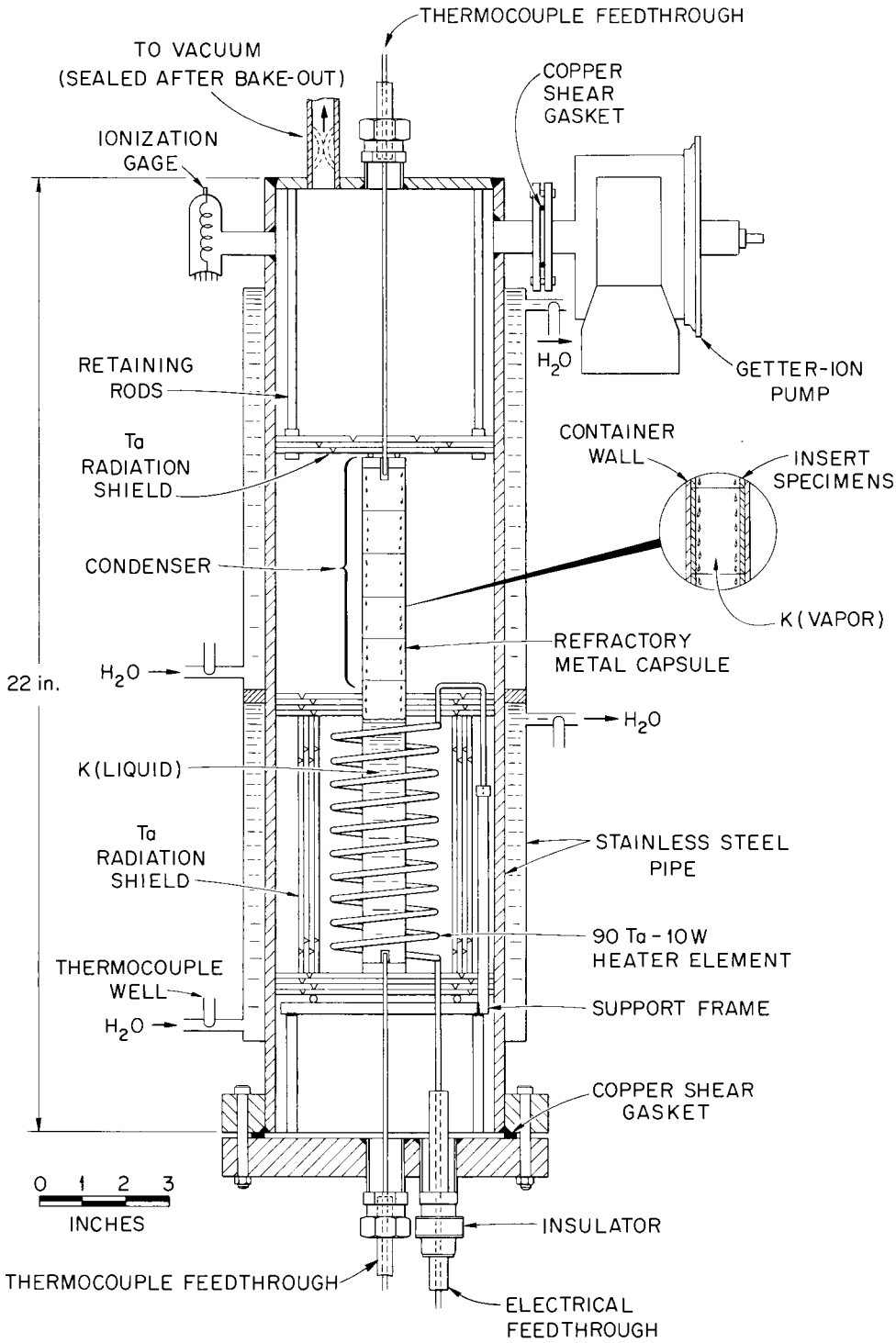

Fig. 5.1. Refractory Metal–Refluxing Potassium Capsule Test.

Table 5.1. Summary of Refluxing Potassium–Refractory Alloy Compatibility Tests

Test Number	Material		Temperature (°C)		Test Duration (hr)	Condensing Rate ($g\ min^{-1}\ cm^{-2}$)	Weight Change (mg/cm^2)	Results
	Insert	Container	Boiler	Condenser				
RC-28	W (CVD)	W	1315	1240	5000	0.33	−93 to +188	Mass transfer between CVD inserts and powder metallurgically produced capsule
RC-33	Nb[a]	Nb		1200	5000	0.32	b	Very heavy attack
RC-34	Nb	Nb		1210	5000	0.40	b	Heavy attack
RC-32	Nb–1% Zr[b]	Nb–1% Zr	1230	1210	5000	0.38	−3 to +1	No evidences of attack
RC-36	c	W–25% Re		1180	5000	0.30		Examination in progress
RC-37	c	W–25% Re	1250	1210	5000	0.33		Mass transfer deposit near top of vapor zone
	Nb–1% Zr	Nb–1% Zr	1215	1200	950	0.28		Test in progress
	Nb (CVD)	Nb		1200	1200	0.30		Test in progress

[a]Potassium contained approximately 300 ppm O before test.

[b]Insert specimens bonded to capsule.

[c]No insert specimens available.

We recently completed several experiments with unalloyed niobium that afford an interesting comparison to our earlier capsule studies with niobium alloys. Alloys of niobium that contain strong oxide formers such as zirconium or yttrium have shown negligible corrosion in boiling potassium at temperatures up to 1300 °C for times as long as 5000 hr (refs. 1,2). Unalloyed niobium, on the other hand, was heavily attacked in potassium initially containing < 30 ppm O (Fig. 5.2) and was virtually destroyed in potassium to which 300 ppm O was added (Fig. 5.3). In general, the inside surfaces of sleeve specimens from the condenser regions of both tests were relatively unattacked, while the outer surfaces that contacted the capsule were more heavily attacked. In the boiler region the situation was found to be reversed (i.e., the heaviest attack occurred on the inside surfaces). Table 5.2 lists the changes in oxygen concentration that occurred in the insert specimens from these tests. Specimens in the liquid region generally increased in oxygen while those in the vapor region either showed no change or lost oxygen.

Refluxing capsule investigations at NASA, Lewis Research Center[3] earlier had shown that the corrosion resistance of niobium alloys is strongly dependent upon the presence of strong oxide formers such as zirconium or hafnium. The present results on unalloyed niobium further emphasize the importance of the zirconium or hafnium alloying addition. These results also show that oxygen effects tend to be much more pronounced in refluxing than in nonboiling potassium systems. In the partitioning experiments conducted by Litman[4] on unalloyed niobium, oxygen

---

[1]J. R. DiStefano, D. H. Jansen, and B. Fleischer, Metals and Ceramics Div. Ann. Progr. Rept. June 30, 1967, ORNL-4170, p. 93.

[2]J. R. DiStefano, Refluxing Capsule Experiments with Refractory Metals in Boiling Metals, ORNL-4323 (1968).

[3]L. Rosenblum, C. H. Scheuermann, and T. A. Moss, "Space-Power-System Material Compatibility Test of Selected Refractory Metal Alloys with Boiling Potassium," pp. 699–710 in Alkali Metal Coolants, International Atomic Energy Agency, Vienna (1968).

[4]A. P. Litman, The Effect of Oxygen on the Corrosion of Niobium by Liquid Potassium, ORNL-3751 (July 1965). M.S. Thesis from the University of Tennessee.

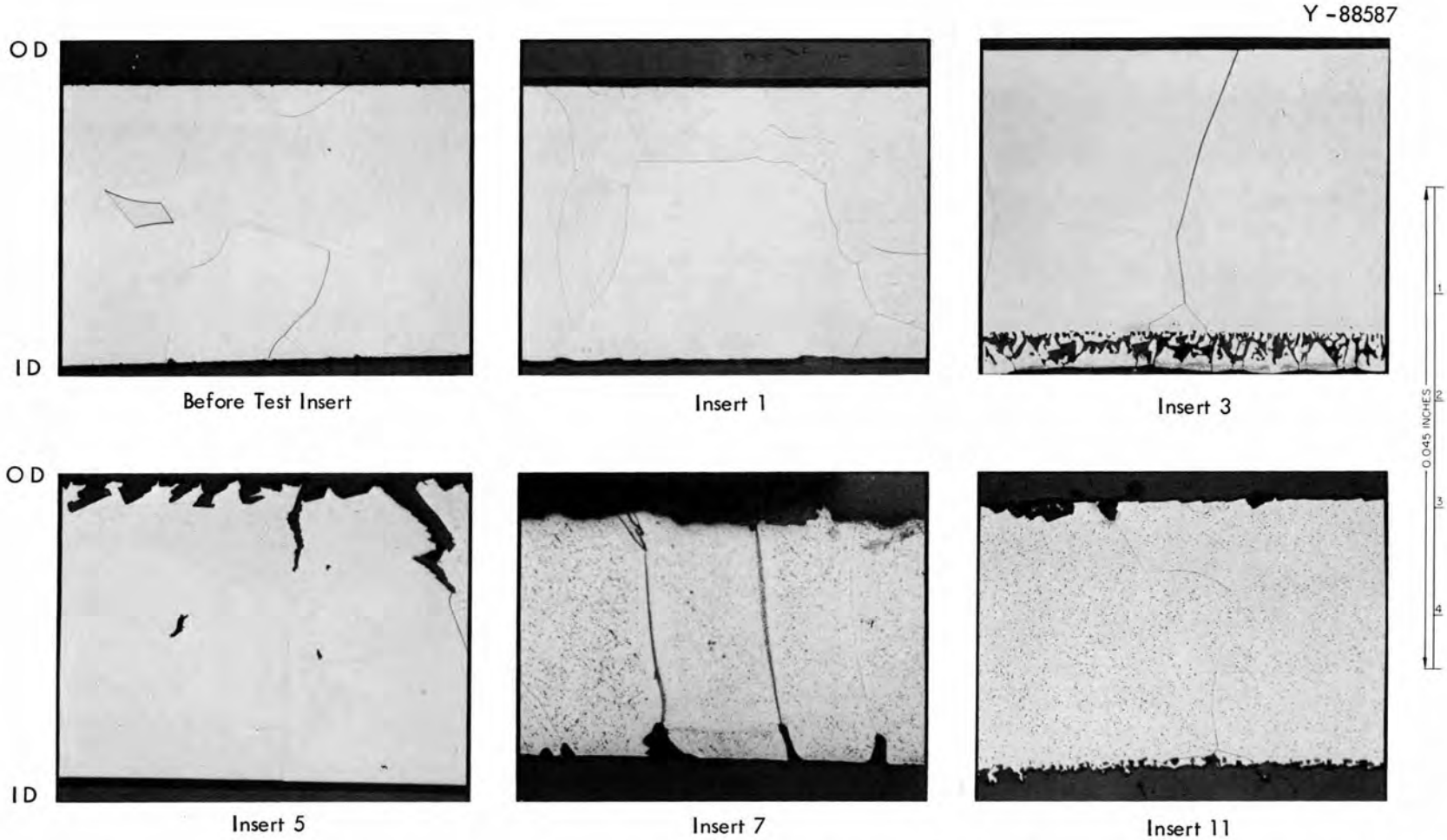

Fig. 5.2. Appearance of Niobium Insert Specimens Before and After Exposure to Refluxing Potassium for 5000 hr at 1200°C (RC-34).

Table 5.2. Changes in Oxygen Concentration of Niobium Insert Specimens from Refluxing Potassium Capsule Tests

Sample Number	Distance Above Liquid-Vapor Interface (in.)	Oxygen Concentration, ppm			
		RC-33		RC-34	
		Before	After	Before	After
1	(+4)–(+5)	150	170	160	60
2	(+3)–(+4)	150	140	160	120
3	(+2)–(+3)	150	130	160	150
4	(+1)–(+2)	150	250	160	100
5	(0)–(−1)	150	150	160	120
6	(0)–(+1)	150	180	160	120
7	(−1)–(−2)	150	320	160	140
8	(−2)–(−3)	150	230	160	450
9	(−3)–(−4)	150	240	160	1200
10	(−4)–(−5)	150	330	160	960
11	(−5)–(−6)			160	250

was depleted from commercially pure niobium in liquid potassium even when the oxygen level of the potassium exceeded several thousand parts per million. These same experiments showed only limited attack of the niobium with additions of up to 2400 ppm O to the potassium, although severe attack of the niobium resulted when the oxygen content of the niobium before test exceeded 1000 ppm. Although the condenser region of the niobium refluxing capsules generally showed oxygen migration in the direction predicted by partitioning experiments, that is, from the niobium to the potassium, the boiler region showed the opposite. Oxygen entering the boiler from the condenser would, of course, increase the average oxygen content of the boiler potassium, but even with this taken into account, the direction of oxygen migration in the boiler was not in accord with results from nonboiling capsules. This difference is most probably the result of the evaporative (distillation) effects accompanying the boiling process. Such effects may produce in the potassium local oxygen concentrations sufficient to drive oxygen into the niobium and cause gross attack of the niobium. Although Litman's results suggest that the first effect should precede the second, we observed attack in several areas where the oxygen content of the niobium had increased

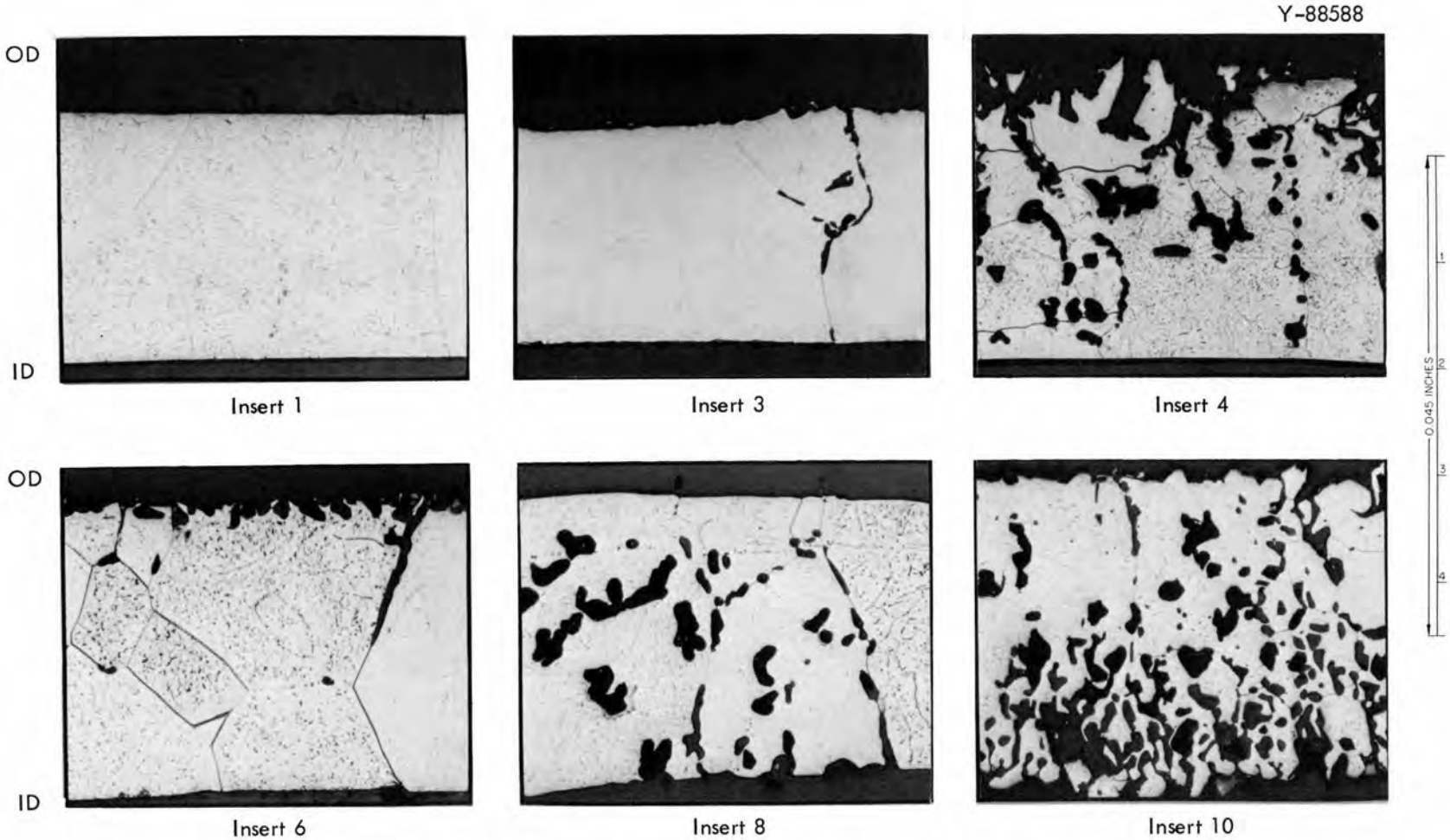

Fig. 5.3. Appearance of Niobium Insert Specimens After Exposure to Refluxing Potassium for 5000 hr at 1200°C (RC-33).

only slightly. A similar "enrichment phenomenon" was suggested by Busse et al.[5] to account for rapid attack in the evaporator regions of Nb–1% Zr heat pipes operated with lithium at 1500°C. Again, the effect was to cause transfer of oxygen from lithium to the Nb–1% Zr, the reverse of what occurs in the absence of boiling.

This phenomenon also could explain why attack of Nb–1% Zr was observed[3] in relatively small refluxing capsules operated by NASA Lewis but not in our refluxing experiments. The considerable difference in potassium volume and heater surface area between the NASA capsule design and our own may well have affected the extent of localized oxygen enrichment reached in the respective capsules.

Pure tungsten also showed extensive attack after 5000 hr at 1300°C (Fig. 5.4). The tube and end plugs of this capsule were constructed from a tungsten powder product, but the inserts were produced by chemical vapor deposition (CVD). Upon opening the stainless steel vacuum chamber that housed the capsule, we found that the potassium had leaked out of the tungsten tube through a 1.5-in.-long crack about 0.5 in. from the top of the capsule.

Since we could not definitely determine when the leak occurred, the weight and dimensional changes cannot be ascribed with any certainty to interaction with the potassium. We noted very large changes in weight (–13 to 23%) in the insert specimens. Wall thicknesses of inserts varied considerably from those before testing, and large variations in wall thickness were also evident in the tube wall opposite the inserts. The wall thickness of the boiler region of the capsule, however, was essentially unchanged from the before-test condition. Figure 5.3 illustrates the dissolution and deposition effects found on both the inside and outside surfaces of the inserts and the inside surface of the tube wall. The movement of tungsten within the capsule followed no uniform pattern. The upper three inserts showed a net loss of tungsten as a consequence of tungsten transfer from the outside surface.

---

[5]C. A. Busse et al., "High Temperature Lithium Heat Pipes," paper presented at Second International Conference on Thermionic Electrical Power Generation, Stresa, Italy, May 27–31, 1968.

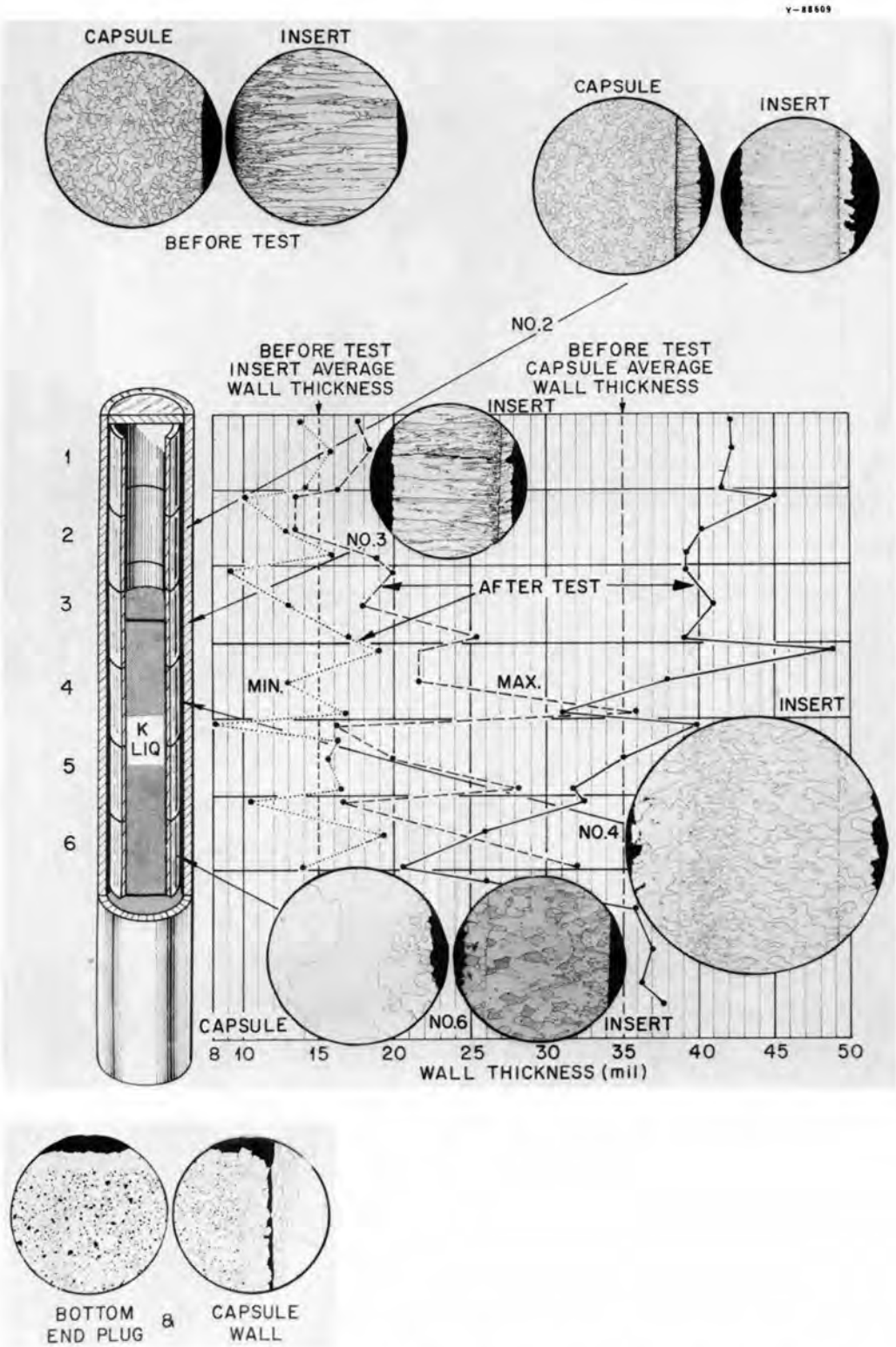

Fig. 5.4. Composite Showing Appearance of Tungsten and Variation in Wall Thickness After Exposure to Refluxing Potassium for 5000 hr at 1200°C.

The overall loss was offset somewhat by deposition of tungsten onto the inside surface. The wall adjoining these three upper inserts thickened as a consequence of a columnar deposit, pictured in Fig. 5.3. In the annular region between the wall and the lower three inserts, tungsten transfer between any one insert and the wall was in some areas toward the insert. Where the insert showed a deposit, the adjoining capsule wall decreased in thickness, and vice versa. Since the capsule material from the boiler region was unaffected, we believe that the corrosion effects in this test were a result of mass transfer between the CVD inserts and the powder-product capsule. Although each insert showed both dissolution and deposition effects that are difficult to explain, we suspect that impurities in the potassium, possibly halogens, may have given rise to gas transport effects that were responsible for what was observed.

To investigate this phenomenon further, we tested two W–26% Re capsules, one arc melted and the other a powder product, for 5000 hr at 1200°C in refluxing potassium. Preliminary examination showed a heavy deposit from mass transfer in the condenser region of the arc-melted capsule but not in the powder-product capsule. Detailed metallographic and chemical data have not yet been obtained.

Natural Circulation Loop Tests (D. H. Jansen)

We have completed a study of the effects of boiling and condensing potassium in small, natural circulation loop systems. The tests conducted under this program are listed in Table 5.3.

The eighth and final loop in this series was constructed of the molybdenum-base alloy TZM and was stopped after 4400 hr at a condenser temperature of 1200°C. Since tubing for this loop was supplied from bar stock and could not be deformed at room temperature, the loop was fabricated with welded miter joints instead of bends. We encountered no unusual problems in construction, and the loop operated successfully for 200 hr at which time it was interrupted by a creep-rupture failure of the dryer line. Inspection of the failure area showed extensive deformation of the pipe wall and suggested that this region, which was not monitored by a thermocouple, had run considerably hotter than the 1200°C intended in the design. We replaced all of the dryer section

Table 5.3. Test Conditions of Natural Circulation–Boiling Potassium Loop Tests

Loop Number	Material	Test Time (hr)	Temperature, °C		Condensing Rate ($g\ min^{-1}\ cm^{-2}$)
			Condenser	Subcooler	
NCL-1	Nb–1% Zr	2800	1130	650	0.2
NCL-2	Nb–1% Zr	350	1200	675	0.2
NCL-3	Nb–1% Zr	1200	1200	675	0.2
NCL-4	D-43	3000	1200	835	0.77
NCL-5	T-111	3000	1200	1040	0.47
NCL-6	D-43/TZM	3000	1200	1000	0.35
NCL-7	FS-85	1300[a]	1200	760	0.2
NCL-8	TZM	4400[a]	1200	650	0.13

[a]Test stopped by creep failure of dryer section.

that had been directly under the top horizontal heater with heavier-walled tubing and continued the loop test. When the originally scheduled 3000-hr test was completed, we elected to extend the test to 5000 hr. However, the loop was stopped just short of this revised goal by a creep failure of the top horizontal vapor line just downstream from the heavier-walled replacement section. Analysis of the loop is now under way.

The seventh loop test in this series, constructed of the alloy FS-85, also was interrupted by a creep failure of the dryer line after 1300 hr of operation at 1200°C. Examination of the loop was delayed pending procurement of a replacement section for the dryer line. The program, however, was phased out before procurement could be effected, and we are now examining the loop. Weight changes recorded on sleeve-type insert specimens contained in the condenser-subcooler region of the loop are shown in Fig. 5.5. The specimens from the condenser showed little weight change, while subcooler specimens gained an average of 10 mg/cm^2.

Forced Circulation Loop Tests (B. Fleischer, C. W. Cunningham)

D-43 Alloy Loop with D-43 Test Section (FCL-8). – Loop FCL-8, constructed of D-43, is the third in a series of forced convection loops

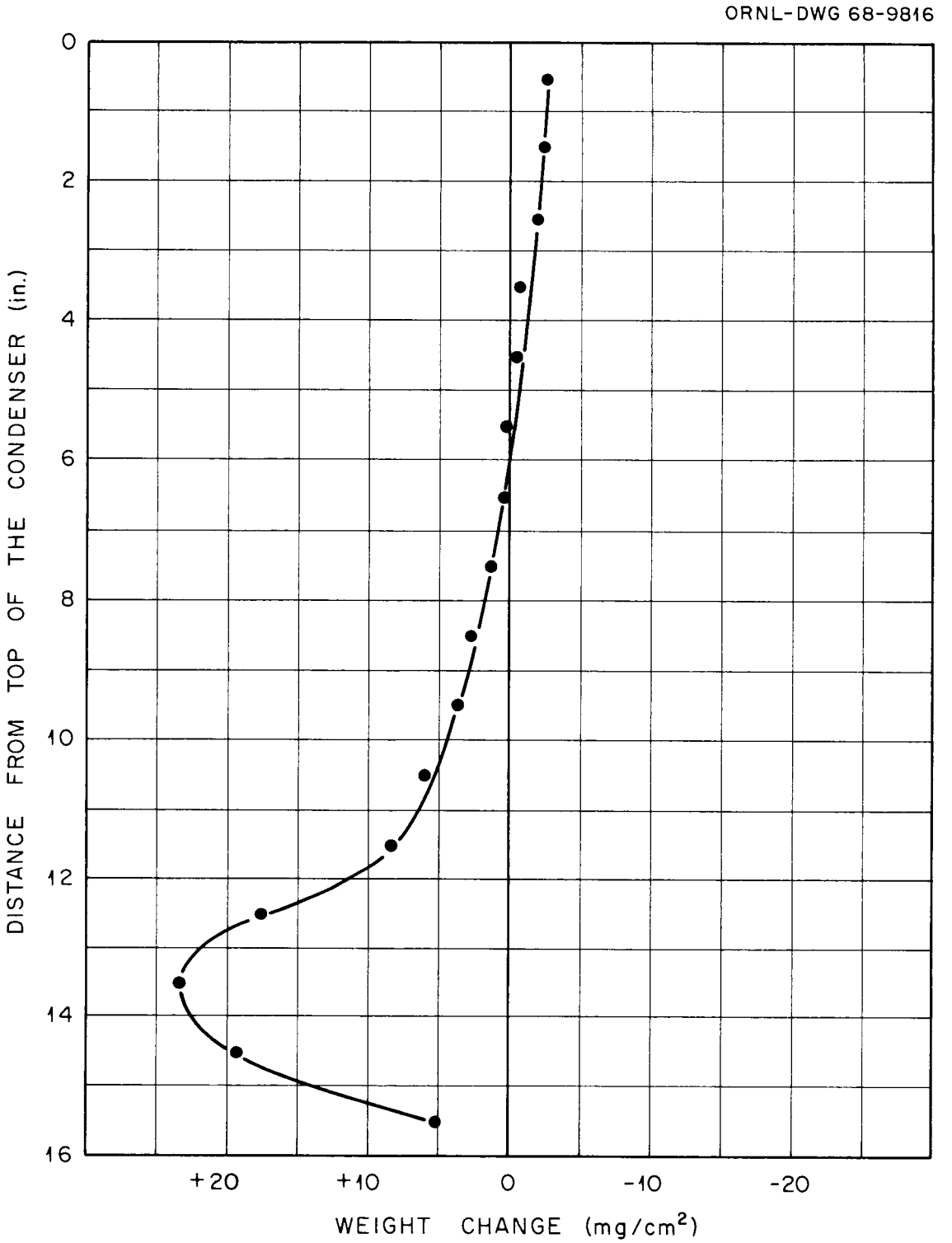

Fig. 5.5. Weight Change Data from Inserts from FS-85—Boiling Potassium Natural Circulation Loop 7 Stopped After 1300 hr. Weight change (milligram per centimeter squared) is plotted against distance (inches) from top of the condenser.

designed to evaluate the effects of boiling potassium and potassium vapor at high velocity on niobium-base alloys and on TZM.[6,7] A simplified schematic drawing and the operating conditions of this loop are shown in Fig. 5.6. Additional information regarding materials and test conditions is listed in Table 5.4.

Because of the embrittlement associated with D-43 welds and the fact that the loop contains more than 100 welds, we annealed the entire loop assembly for 2 hr at 1315 °C before filling it with potassium. Some of the annealing was done during subassembly, but the final assembly welds were annealed with the loop in place in the vacuum test chamber. A photograph of the loop taken before it was assembled in the vacuum chamber is shown in Fig. 5.7.

Operation of loop. The loop was terminated June 8, 1968, after having operated for the scheduled 10,000 hr at the design test section inlet temperature of 1215 °C. The loop operated at design conditions for 95.7% of the 10,451 hr since its startup on March 31, 1967. For three-fourths of this time, the boiler temperature was 1215 °C and for the remainder, 1215 °C $^{+10}_{-15}$. The chamber pressure as measured by a nude ion gage varied between 1.5 and 5.5×10^{-8} torr (Fig. 5.8).

During the last six months, loop operation was interrupted a total of 222 hr by equipment failures and for preventative maintenance. Repairs to a main transformer in the building required 6 hr of operation at reduced temperature. Separate failures of a constant voltage unit of the level controller and internal contacts interrupted the test for a total of 11 hr. This controller varied the helical induction pump voltage automatically to maintain a constant level of liquid potassium in the hot well of the condenser. Failure of a NaK pump in the secondary heat rejection circuit interrupted flow of NaK coolant to the potassium condenser and delayed the loop operation for 129 hr. Failures in the power supply to the helical induction pump interrupted operation for 76 hr.

---

[6] D. H. Jansen et al., Niobium–1% Zirconium Boiling-Potassium Forced-Circulation Loop Test, ORNL-4301 (in press).

[7] J. H. DeVan, Metals and Ceramics Div. Ann. Progr. Rept. June 30, 1960, ORNL-3970, pp. 185–186.

ORNL-DWG 67-11531R2

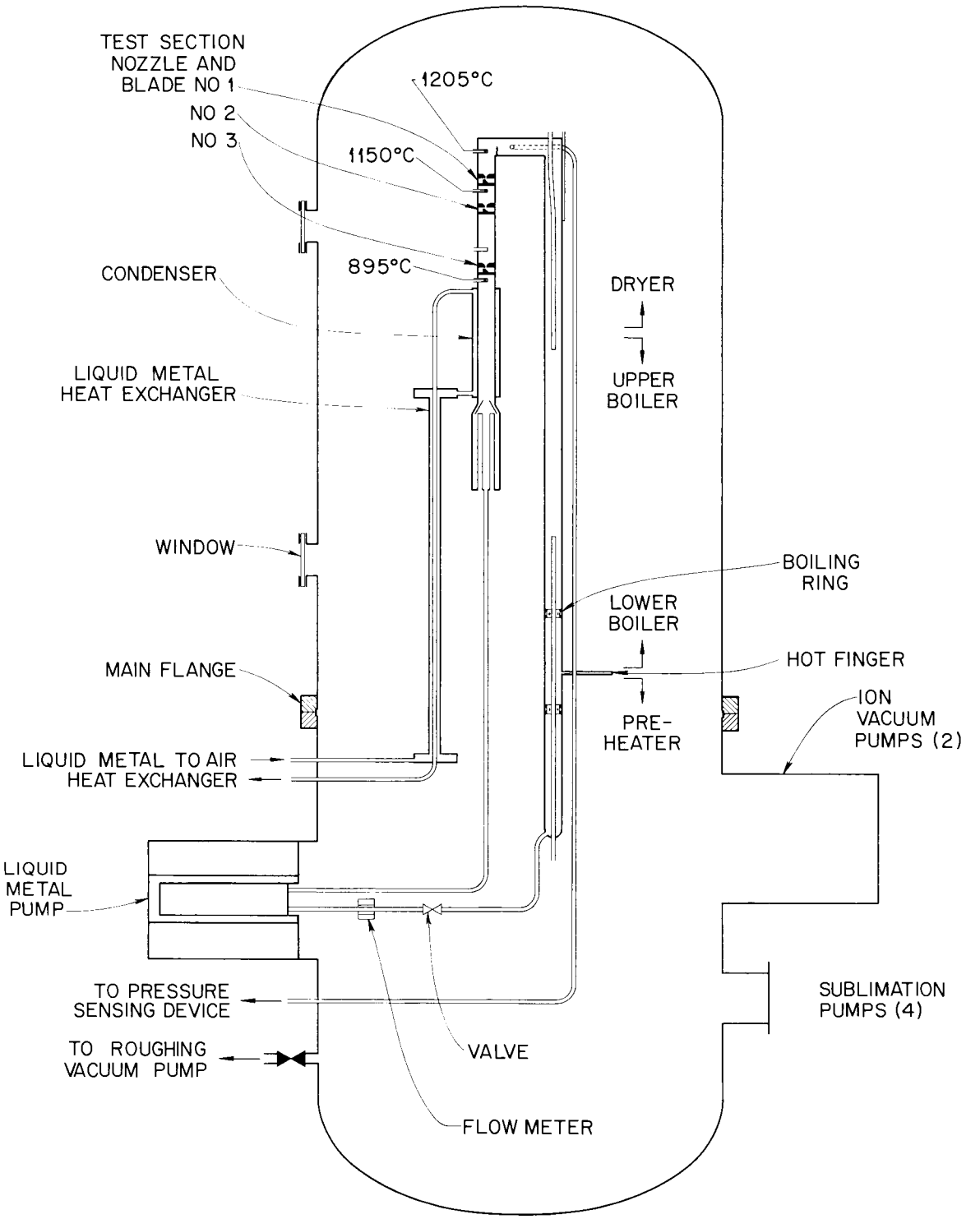

Fig. 5.6. Schematic Drawing of Forced Circulation Boiling Potassium–D-43 Alloy Loop (FCL-8).

Table 5.4. Selected Operating Parameters for D-43 Alloy Loop and Simulated D-43 Alloy Turbine Conditions

Nozzle 1 inlet conditions	
Temperature, °C	1215
Pressure, psia	259
Cold-leg conditions	
Temperature, °C	595
Pressure, psia	2.6
Maximum vapor velocity, fps (at exit of second nozzle)	2860
Approximate flow rate, lb/hr	37
Electrical heat input, kw	10
Test duration, hr	10,000
Vacuum environment, torr	1.5 to 5.5×10^{-8}
Calculated conditions of D-43 turbine	
Simulator 1	
Exit velocity, fps	1300
Exit quality, %	96
Simulator 2	
Exit velocity, fps	2860
Exit quality, %	83
Simulator 3	
Exit velocity, fps	1230
Exit quality, %	97

NaK pump failure. The NaK pump failure occurred in the parallel strips of silver that connect the Faraday pump cell to the secondary circuit of the transformer. Seven flat silver strips (0.030 in. thick by 1 in. wide by about 6 in. long) connect each side of the pump cell to the transformer secondary leads. The conductor had been in operation about 7000 hr. Before the failure and throughout the test, the NaK pump was operated slightly above its design voltage to obtain a NaK flow rate of 1.1 gpm at a pump temperature of 115°C. An air blower maintained temperatures of 150°C at the pump cell terminal and 145°C at the transformer terminal. A sheathed thermocouple within the leaves, near the middle of the new conductors, indicated about 260°C. Examination of the failure area of the silver conductors showed that the

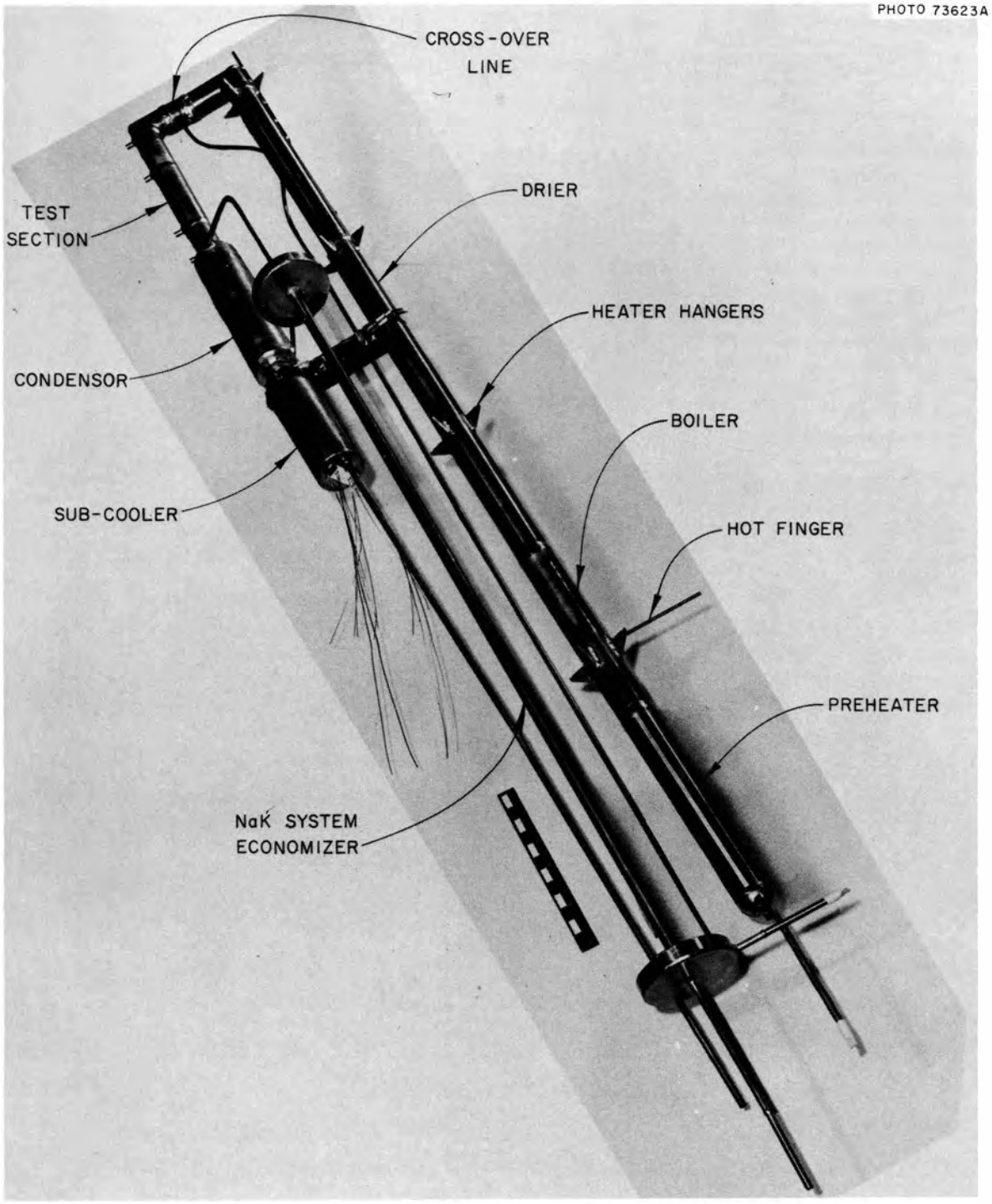

Fig. 5.7. D-43 Alloy Loop with D-43 Test Section (FCL-8) Shown Before Assembly in Vacuum Chamber.

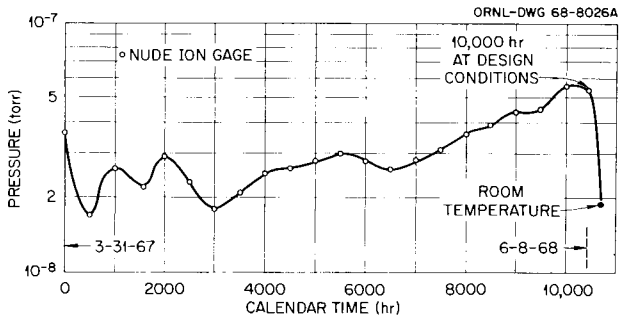

Fig. 5.8. Chamber Pressure During Forced Circulation Loop 8 Test.

the silver became embrittled and that some of the strips cracked, and that the remaining conductors then melted. The embrittlement of the silver was the result of grain boundary voids as revealed in the photomicrograph of the failed region shown in Fig. 5.9. Several cracks were also evident in this area. The unfailed conductor contained the same void pattern in the same general area. We believe the voids were caused by temperature drifts and temperature cycles encountered during normal operation. Since oxygen solubility in silver decreases with increasing temperature (up to about 400°C), voids would be expected to form at grain boundaries as oxygen is released internally during periods of temperature increase. An unexplained vibration at the pump cell may have helped to promote the cracking of the silver conductors. To complete the scheduled operation, we installed new silver conductors on the NaK pump.

Operation of helical induction pump. As mentioned above, loop operation was interrupted a total of 76 hr to make repairs and alterations to the power supply to the helical induction pump. Maintenance of electrical brushes, commutators, and a mechanical component in the variable transformer assembly of this power supply became necessary to ensure that the potassium pump continued to operate reliably. The potassium pump voltage is shown as a function of test duration in Fig. 5.10 along with other pertinent operational data. As noted previously, the pump voltage is automatically controlled to maintain a preset level of liquid in the hot well of the condenser. During the period from startup to 2000 hr, the voltage increased from 380 to 450 v due to closing of the flow control valve located between the pump

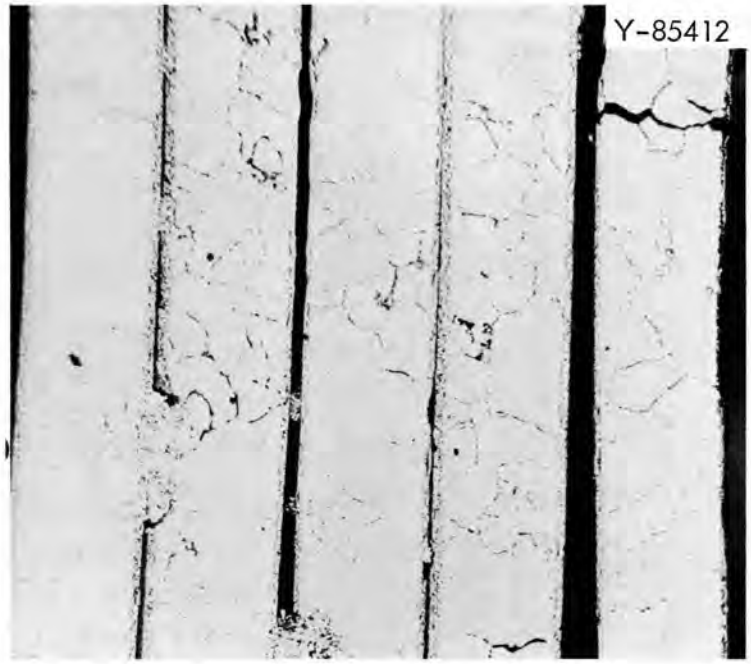

Fig. 5.9. Cross Section of Failed Silver Conductor Showing Grain Boundary Voids and Cracks. About 27×.

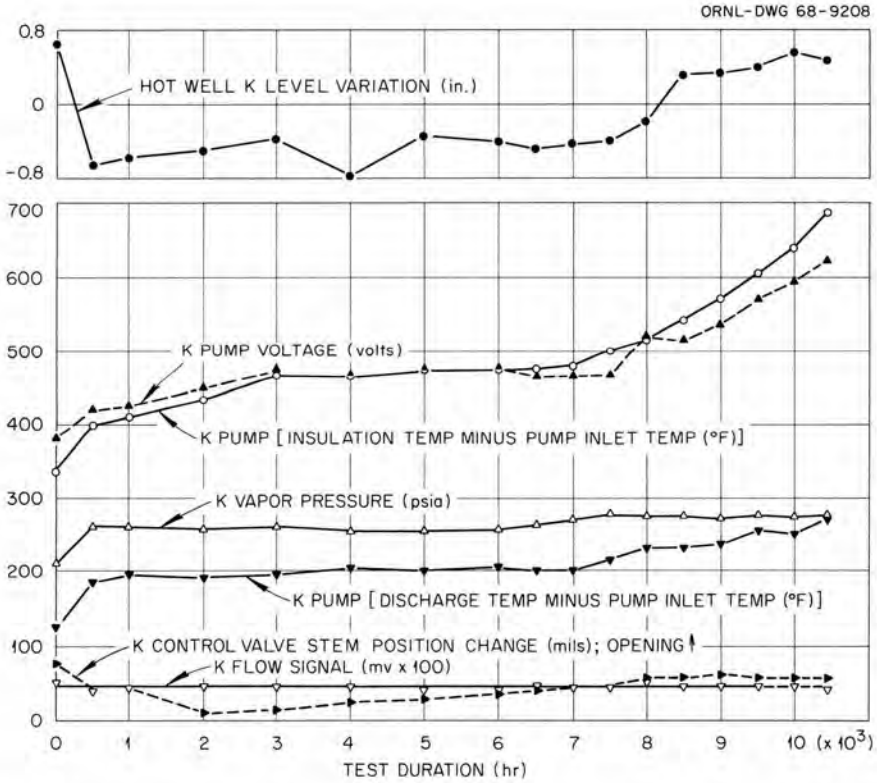

Fig. 5.10. Potassium Pump Characteristics as a Function of Test Duration for Forced Circulation Loop 8.

and the preheater inlet. This additional flow resistance improved operational stability by decreasing the oscillations in the liquid levels of the system. The voltage required to maintain constant flow at the proper liquid level in the hot well tended to increase with time. After 2000 hr, we arbitrarily limited the voltage to 475 v by gradually reopening the control valve to lower the resistance to flow in the system. After 7500 hr of operation, further opening of the valve was ineffectual in limiting the voltage. We added a saturable reactor to the circuit to supply the increasing voltage requirement, which reached 625 v by the end of the test. This increasing voltage requirement was accompanied by increasing temperatures in the pump that are also shown in Fig. 5.10. Pump temperatures are plotted as the difference between the 535°C pump inlet and the observed temperature. The temperature of the pump outlet at the end of the test was 745°C, and that of the pump insulation was 975°C. A definite explanation for the voltage increase is not known. Variations in the rate of potassium flow and saturation pressure are not sufficient to explain the change. A deterioration of the pump or an increasing flow restriction in the line or valve between the pump and the preheater inlet are possible explanations. We expect that posttest examination will explain the phenomenon.

Operation of ion pump. Unexpectedly, the General Electric "triode" ion pump currents increased exponentially with test duration as shown in Fig. 5.11. Without corrective action, it was predicted, the currents would have exceeded 100 ma. Since the maximum safe current for continuous operation was not known but was believed to be less than 100 ma, the pump vendor recommended corrective action called "Hi Potting." Hi Potting means increasing the pump supply voltage in steps above the normal operating level while limiting the pump current to a certain maximum value. This action vaporizes small whiskers of material that are known to grow with time on internal surfaces of pumps undergoing high vacuum and high voltage. Field emission currents that are associated with such whiskers can be eliminated by vaporizing the whiskers. A vendor attempted Hi Potting with his equipment but was unsuccessful because the current exceeded the capacity of his machine. We obtained an available radar power supply that was capable of operating up to

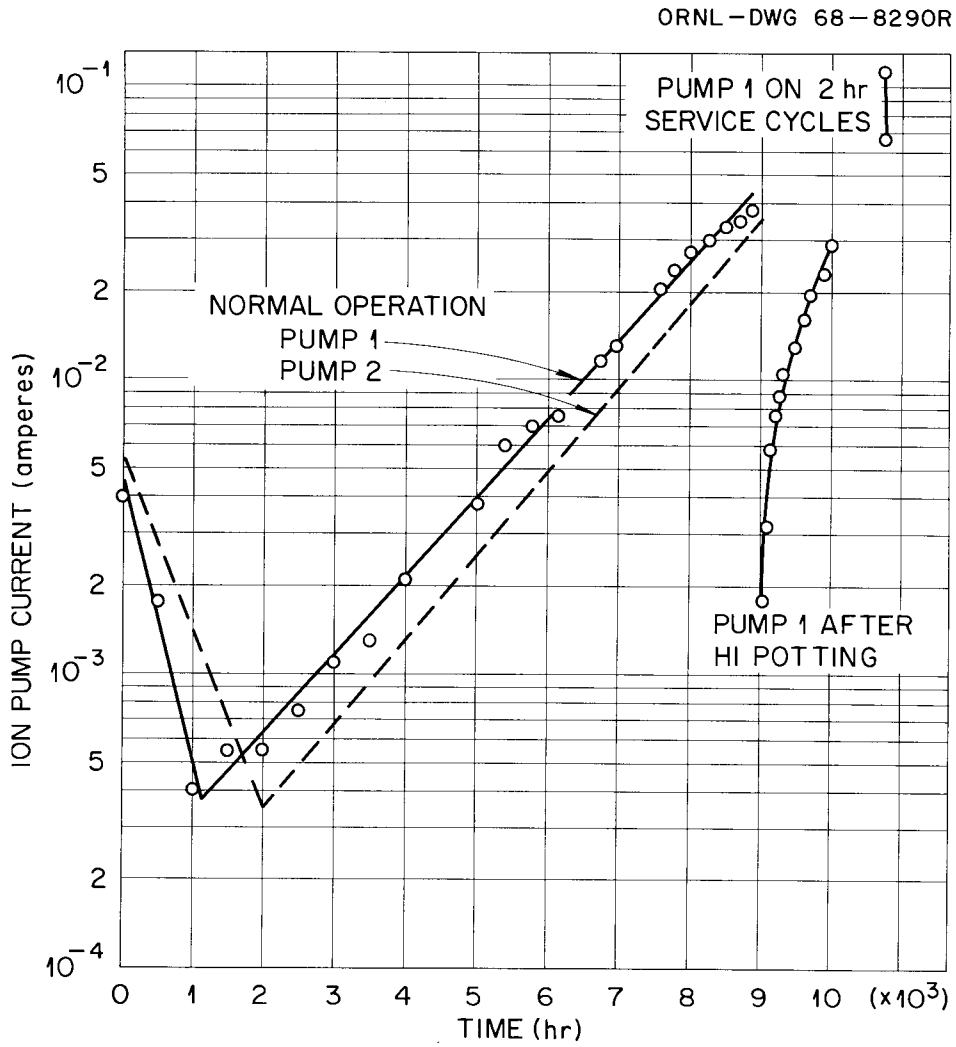

Fig. 5.11. Ion Pump Current During Forced Circulation Loop 8 Test.

15 kv and 600 ma. We were easily able to vary the maximum current setting by adjusting the power input to a power tube filament. With the larger power supply, we Hi Potted the ion pumps by step increases in voltage supply to 10 kv. Current peaks to 400 ma of about a minute duration were experienced. It took about 8 hr to treat one ion pump.

As shown in Fig. 5.11 the Hi Potting operation reduced the ion pump current by a least a factor of 10 in the normal operating range of 5.5 to 6.0 kv but, to our surprise, the rate of current rise was greater after Hi Potting. Figure 5.12 shows the normal current for the number

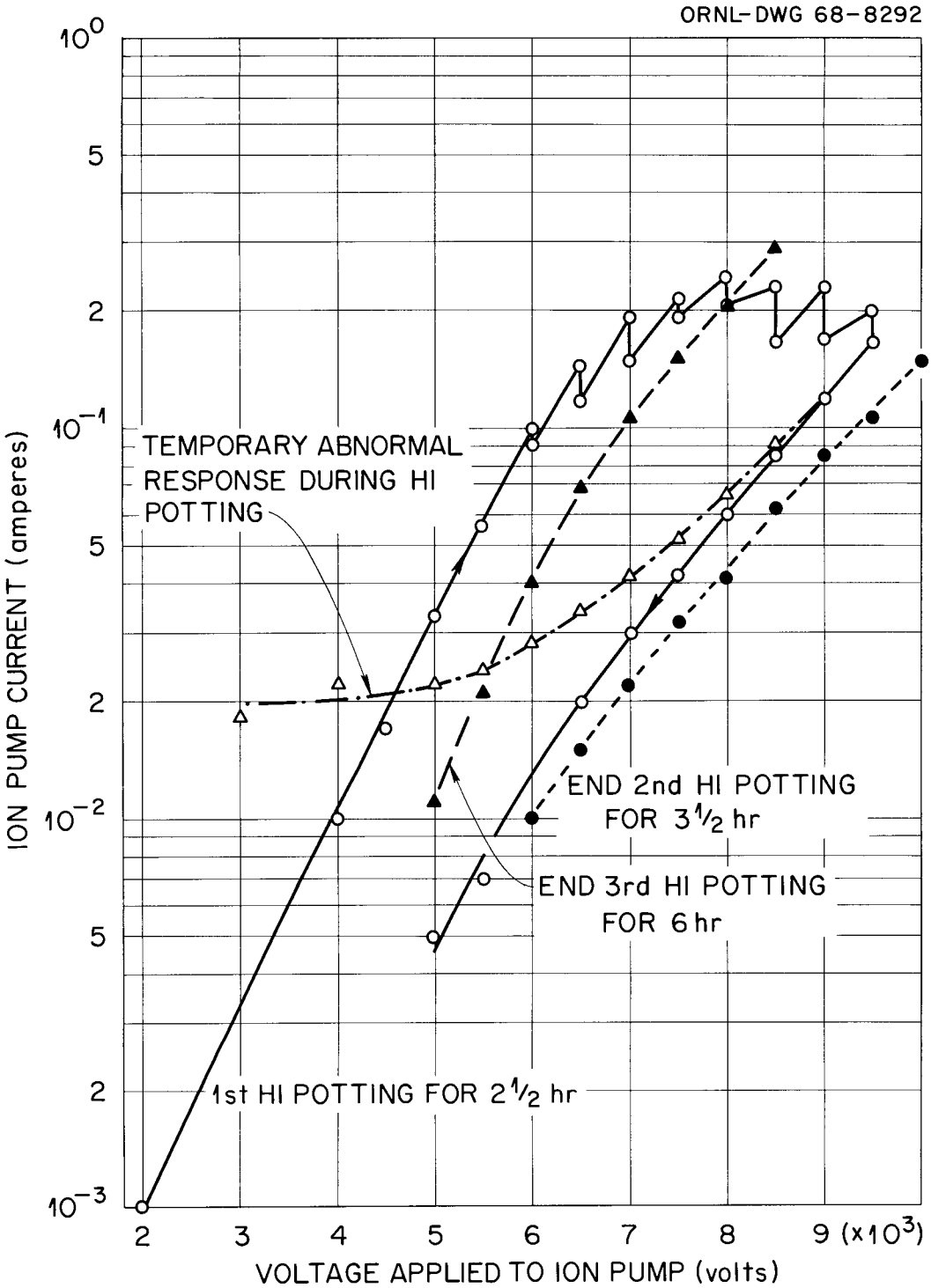

Fig. 5.12. Ion Pump Current as a Function of Applied Voltage for Forced Circulation Loop 8 Showing Effects of Hi Potting Operations.

one ion pump versus voltage and typical variations in pump currents during our first, second, and third attempts at Hi Potting. A further improvement might have been possible by applying the high voltages for still longer times.

During Hi Potting, there were instantaneous surges of current as the voltage was increased. These surges were accompanied by flashes of light that were visible through a viewing port. The number of surges, some sufficient to exceed the automatic current limit of the power supply, decreased to zero at each voltage level. Hot spots slowly disappeared as the current value decreased. We also observed an abnormal relationship of current versus voltage on a few occasions when the current increased in a matter of minutes to a value of 150 to 300 ma with a corresponding decrease in voltage before we manually shut down the Hi Potter. Following this experience, an unusual voltage-current relationship would temporarily exist as shown by the "abnormal" curve of Fig. 5.12.

The benefit of Hi Potting decreased with each attempt, and was eventually abandoned. Some temporary benefit was gained by operating one pump at 4.0 to 4.5 kv (normal voltage is 5.5 to 6.0 kv) with the Hi Potter while the other pump was off. Until the completion of the 10,000-hr test, the ion pumps were alternately operated for 2-hr intervals.

Gas analysis. A monopole residual gas analyzer was obtained and placed in operation before Hi Potting (after 7500 hr of operation). The significant peaks during normal loop operation were, in decreasing order, Ar, mass 28 (N_2 and/or CO_2), H_2, and CH_4. Other peaks were only a tenth as large or less. During Hi Potting, the same four major components and no others were present. The chamber pressure at one time during Hi Potting increased by two orders of magnitude from 4.5×10^{-8} to 7.2×10^{-7} torr. At the same time the principal peaks increased by a factor of about 80 for H_2, 10 for Ar, 20 for CH_4, and 2.5 for mass 28. An approximate residual gas composition was estimated for several modes of operation as shown in Table 5.5.

Table 5.5. Gas Composition (Weight Percent) in Vacuum Chamber Containing Forced Circulation Loop 8

Component	Normal Operation	During Hi Potting	Loop at Ambient Temperature
H_2	24	66	20
Ar	50	28	32
CH_4	2	3	0
Mass 28	24	3	48

Posttest inspection. The vacuum chamber bell was removed to disassemble the test loop on June 26, 1968. The loop was virtually unchanged in appearance (see Figs. 5.13 and 5.14). A NaK leak was observed below the lower NaK heat economizer expansion joint (Fig. 5.14). Because of the small amount of leakage, we think the failure occurred during cooling. There was only a thin layer of NaK on the inner surface of the lower bowl and none on the upper or bell-jar portion of the vacuum chamber. We are now disassembling and inspecting the loop.

Nb–1% Zr Alloy Loop with TZM Test Section (FCL-6). – We previously reported that minor amounts of deposits were found on the nozzles and blades and on the nucleation rings.[8,9] To further resolve the chemical nature of these deposits, we examined samples by electron microprobe analysis. Table 5.6 shows the composition of the surface layers. The layers were inhomogeneous, and the values shown in this table reflect the highest concentrations noted. Density variations also made quantitative analysis difficult; therefore, these values should be interpreted with caution.

---

[8]J. R. DiStefano, D. H. Jansen, and B. Fleischer, Metals and Ceramics Div. Ann. Progr. Rept. June 30, 1967, ORNL-4170, pp. 93–94.

[9]J. R. DiStefano, D. H. Jansen, and B. Fleischer, "Compatibility of Boiling Potassium with Refractory Alloys," Metals and Ceramics Div. Ann. Progr. Rept. June 30, 1968, ORNL-4370, Chap. 17.

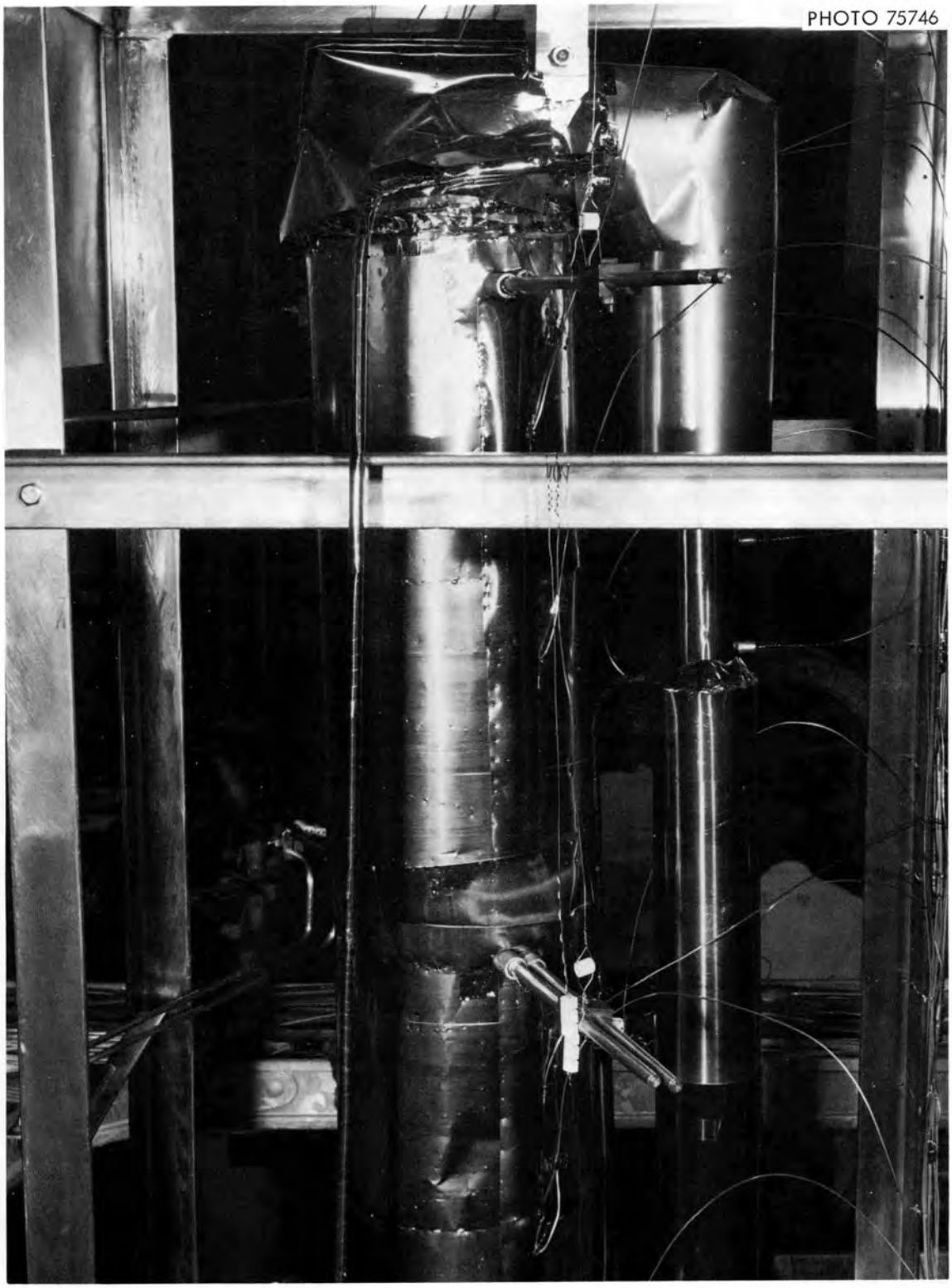

Fig. 5.13. After-Test Appearance of Upper Dryer, Crossover Line, and Nozzle Test Section from Forced Circulation Loop 8.

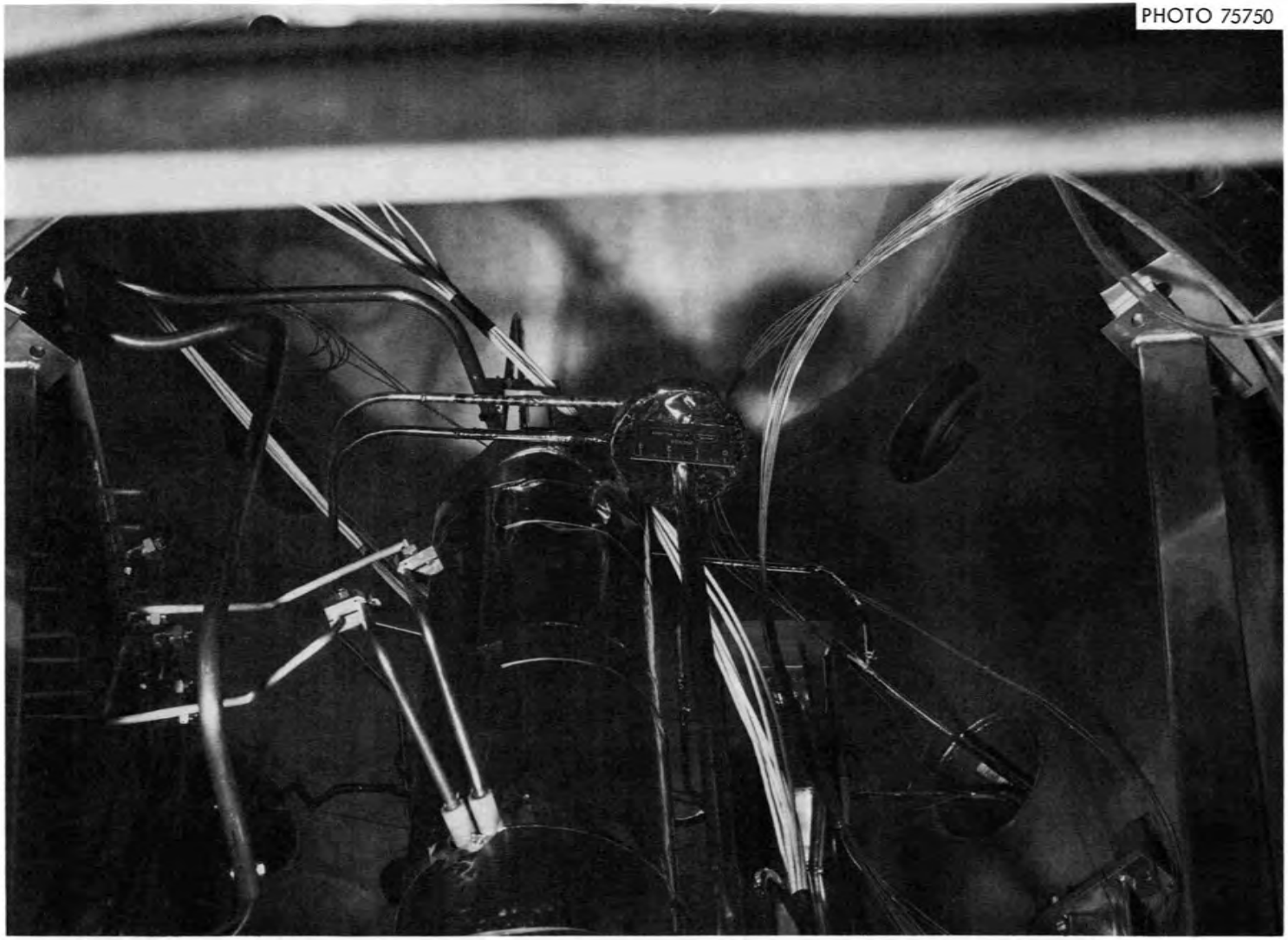

Fig. 5.14. After-Test Appearance of Lower Portion of Forced Circulation Loop 8 Showing Region of NaK Leak.

Table 5.6. Electron Microprobe Analysis of Inhomogeneous Deposits in Forced Circulation Loop 6

Sample	Composition,[a] wt %				
	Zr	Cr	Fe	Ni	Nb
TZM blade 2					
Metallic layer	4.1	74.5	4.9	trace	
Gray deposit	41.8	14.1	6.4		
TZM blade 3					
Metallic layer	20.5	41.7	40.7	3.3	
TZM nozzle 1					
Gray deposit	55.6				
TZM nozzle 2					
Gray deposit	59.6				
Nb–1% Zr nucleation ring					
Yellow layer	3.1	31.0	7.6	2.1	58.6
Gray deposit	52.6	2.3	17.9		

[a]All values based on maximum concentrations found.

From these data it is apparent that zirconium and stainless steel elements were transported to the test section. The only metallic element found in the gray deposits on the nozzles was zirconium, and the quantity present and previous x-ray diffraction data indicate that this and the grayish layer on blade 2 were oxide compounds.

Metallic-looking layers found on the blades contained significant fractions of Cr, Fe, Zr, and Ni. The chromium, iron, and nickel must have come from the stainless steel pump cell. It is interesting to note that these migrated even though the temperature of the stainless steel was below 480°C.

The very minute, grayish deposits found in the nucleation rings contained zirconium, iron, and nickel; whereas, the yellow layer contained these as well as niobium and nickel.

To further examine the nature of zirconium mass transfer in the system, we surveyed the zirconium content at the inside surface of the loop piping by direct electron microprobe analysis of the as-tested surfaces of samples selected from various locations around the loop.

Several 320-μ^2 areas were scanned on each sample with a 30-kv, 1-μ beam. We estimate that the effective beam penetration was less than 2 μ and that the effects of substrate interference were therefore minimal. Data thus collected are presented in Fig. 5.15, where a plot of temperature is also included for convenience. It is quite apparent from these data that zirconium migrated from the boiler to all other areas. The region of greatest loss, from 0.85 down to 0.35% Zr, occurred in the lower part of the boiler. The highest concentration noted, 7.4% Zr, was in the crossover line. We analyzed other locations to determine the effect of flow path on the deposition of zirconium. The data in Fig. 5.16 show that zirconium deposition was dependent on flow path at the top of the dryer and in the crossover line. This dependency was not evident, however, at the riser located at the entrance to the test section.

The foregoing data and operational information suggest the following sequence of events. Potassium entering the boiler dissolved zirconium from the boiler walls. At the boiling liquid interface, bubbles of potassium burst and expelled small droplets of the potassium-zirconium solution into the vapor stream. As the droplets were carried through the dryer, the potassium vaporized, leaving very minute particles or perhaps atoms of zirconium that were easily carried by the vapor stream. The zirconium content of the vapor stream was therefore higher than the equilibrium concentration at the temperature involved, and concentration gradient mass transfer necessarily followed. The zirconium-rich material found in the diffuser section of the nozzles would also be accounted for by this series of events.

Corrosion of Refractory Alloys by Lithium

J. H. DeVan A. P. Litman W. R. Huntley

The purpose of this program is to guide the selection of containment materials for the nuclear reactor portion of lithium-cooled power systems for space. The program is designed to investigate the chemical and metallurgical effects produced in refractory alloys during exposure

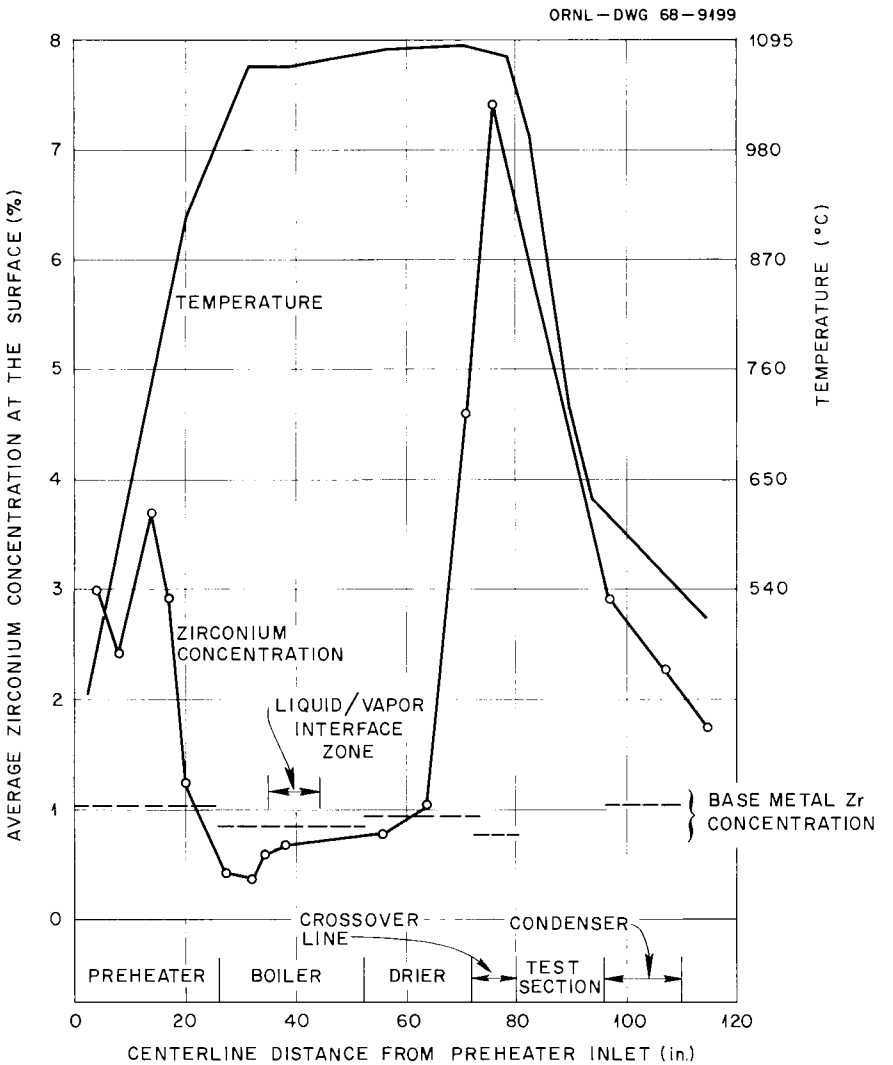

Fig. 5.15. Average Zirconium Surface Concentration Profile of Forced Circulation Loop 6.

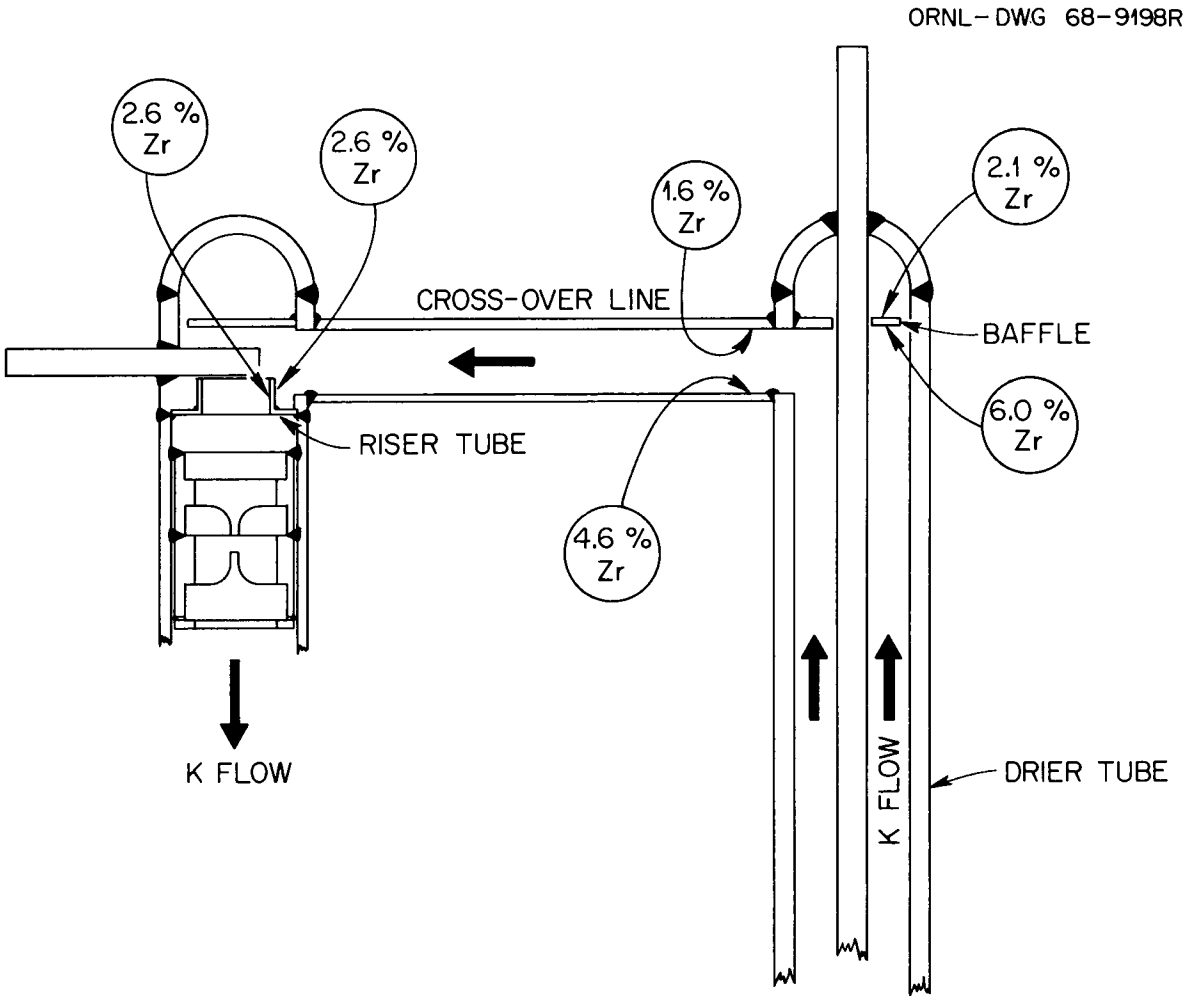

Fig. 5.16. Top Portion of FCL-6 Loop Showing Relation of Zirconium Deposition to Potassium Flow Path.

to lithium. The studies initially were centered around niobium-base materials but now have progressed to tantalum- and tungsten-base alloys. Our main objective is to evaluate the parameters that affect thermal-gradient mass transfer of these alloys in lithium between 1200 and 1650°C.

We use three experimental approaches: (1) capsule tests, (2) thermal convection loop studies, and (3) engineering-scale forced circulation loop experiments. Experiments run for 100 to 5000 hr. While the major purpose of our loop studies is to characterize mass transfer reactions, particularly those involving interstitial impurities, they also give important insight into the construction and operational problems of high-temperature refractory alloy systems.

Capsule Tests on Welds of Tantalum-Base Alloys (C. E. Sessions)

We conducted two series of 100-hr tests on T-111 and T-222 welds in lithium to evaluate the effects of oxygen contamination on weld corrosion. One test series was conducted at 1200°C and the other at 750°C. Welded coupons for these studies were prepared by joining two identical 1- × 0.5- × 0.060-in. sheet specimens to form a composite specimen 1 in. wide. All welds were made by the TIG process without filler metal and with two different welding atmospheres. The first atmosphere was our standard one, for which we evacuate the welding chamber to 2×10^{-5} torr and backfill with 99.996% Ar. For the second atmosphere, of lesser purity, we evacuated the chamber to only 5×10^{-2} torr before backfilling it with argon. One group of specimens was welded in the as-received condition, and a second group was oxidized to about 500 ppm O in a Sievert's apparatus at 1000°C before welding. The sequence of welding and annealing steps for specimens tested in lithium at 750°C is shown in Fig. 5.17; that for specimens tested at 1200°C shown in Fig. 5.18.

The changes in chemical composition for the coupons during welding are noted in Table 5.7. Interstitial concentrations were generally unaffected and showed no consistent differences between the two welding atmospheres. Analyses detected no change in the hafnium content of the weld bead during welding, despite the higher volatility of hafnium as compared with the other alloy constituents.

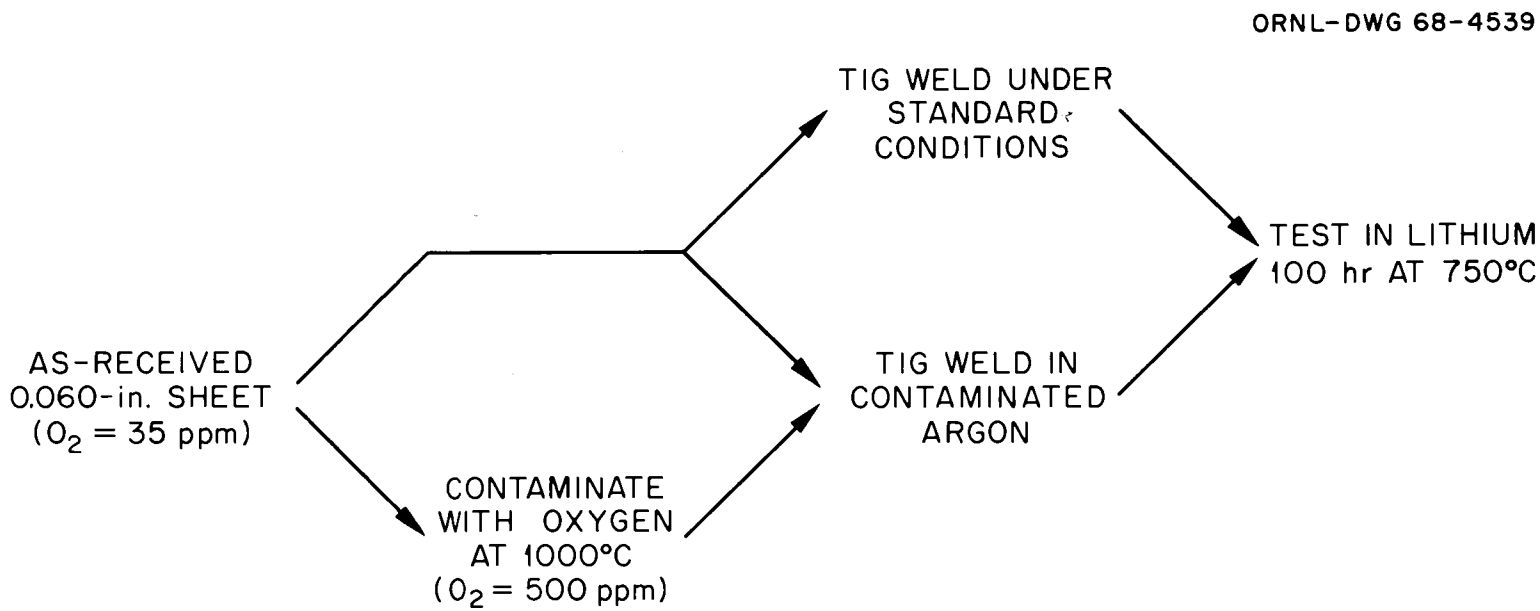

Fig. 5.17. Sequence Used in Preparing T-111 and T-222 Weld Coupons for Lithium Exposure at 750°C.

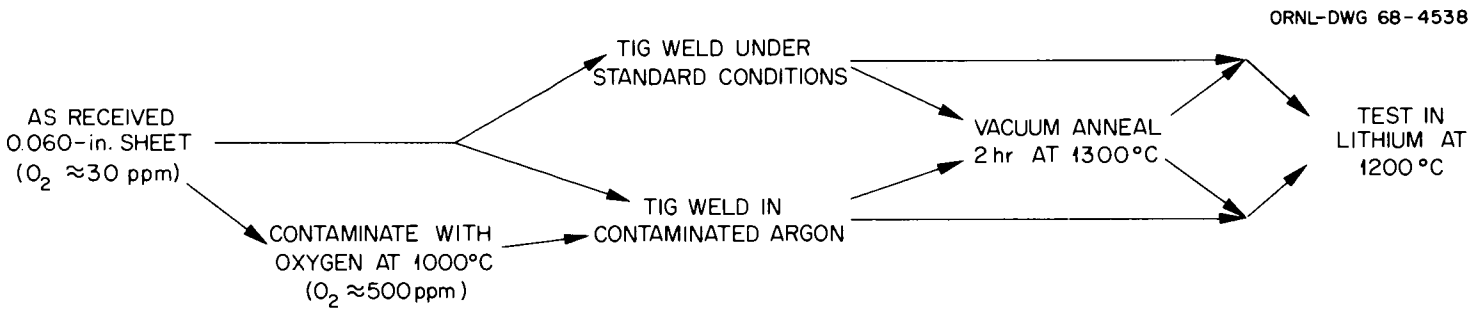

Fig. 5.18. Sequence Used in Preparing T-111 and T-222 Weld Coupons for Lithium Exposure at 1200°C.

Table 5.7. Composition of T-111 and T-222 Sheet Specimens Before and After Welding

Condition[a]	Chemical Composition									
	Base Metal					Weld Bead				
	O	N	C	Hf	W	O	N	C	Hf	W
	(ppm)			(%)		(ppm)			(%)	
				T-111						
AR	21	24	20	1.9	7.9					
	35	17	20	2.4	8.4					
AR-WP	13	23				33	38		2.2	8.1
AR-WU	68	29				33	17			
O-WU	530	17				730	37		2.5	8.3
				T-222						
AR	40	27	200	3.2	10.4					
	60	36	140	3.4	9.9					
AR-WP	48	18				35	29	160	3.1	9.8
AR-WU	42	13				43	19			
O-WU	400	22				480	34	150	3.1	10.2

[a]AR: as-received; O: oxidized at 1000°C; WP: welded in completely purged chamber; WU: welded in partially purged chamber.

Corrosion results from the exposure to lithium at 1200°C are given in Tables 5.8 and 5.9. As-received sheet specimens welded in our standard chamber atmosphere showed no corrosion at 1200°C with or without postweld annealing. This was also true of the coupons welded when the chamber had been evacuated to only 5×10^{-2} torr before backfilling with argon. In the coupons doped with 500 ppm O before welding, areas of base metal were heavily attacked when tested in the as-welded condition, but the weld bead and areas affected by the welding heat were unattacked. Postweld annealing at 1300°C effectively eliminated attack of the base metal. Chemistry changes produced by exposure to lithium were limited to a loss of oxygen from the weld-bead region (compare Tables 5.8 and 5.9 with Table 5.7).

Table 5.8. Results of 100-hr Capsule Tests on T-111 Weld Specimens in Lithium at 1200°C

Condition Before Corrosion Tests	Chemical Composition of Weld Bead After Test				Metallographic Appearance
	O	N	Hf	W	
	(ppm)		(%)		
	Welded in Standard Atmosphere[a]				
As-received	170(?)	22	2.4	8.3	No attack
As-received and annealed[b]	40	42			No attack
	Welded in Less-Pure Atmosphere[c]				
As-received	17	32			No attack
As-received and annealed[b]	26	40			No attack
As-oxidized	350	30			Weld zone unattacked; base metal attacked to 10 mils
Oxidized and annealed	650	56			No attack

[a]Welding chamber evacuated to 2×10^{-5} torr and back-filled with 99.996% Ar.

[b]Annealed for 2 hr at 1300°C in 10^{-7} torr vacuum.

[c]Welding chamber evacuated to 5×10^{-2} torr and back-filled with 99.996% Ar.

Table 5.9. Results of 100-hr Capsule Tests on T-222 Weld Specimens in Lithium at 1200°C

Condition Before Corrosion Tests	Chemical Composition of Weld Bead After Test					Metallographic Appearance
	O	N	C	Hf	W	
	(ppm)			(%)		
	Welded in Standard Atmosphere[a]					
As-received	27	33	150	3.1	10.8	No attack
As-received and annealed[b]	43	28				No attack
	Welded in Less-Pure Atmosphere[c]					
As-received	32	36				No attack
As-received and annealed[b]	59	45				No attack
As-oxidized	540	41	170			Weld zone unattacked; base metal attacked to 10 mils
Oxidized and and annealed[b]	460	36				No attack

[a]Welding chamber evacuated to 2×10^{-5} torr and back-filled with 99.996% Ar.

[b]Annealed for 2 hr at 1300°C in 10^{-7} torr vacuum.

[c]Welding chamber evacuated to 5×10^{-2} torr and back-filled with 99.996% Ar.

The results of the corrosion tests operated at 750°C are summarized in Table 5.10. These correspond closely to those obtained at 1200°C. Only those specimens contaminated to 500 ppm O before welding and not subsequently heat-treated showed attack. Again, attack was confined to the base metal rather than the weld bead or heat-affected zones. This effect is illustrated in Fig. 5.19 for a T-222 weld specimen tested in the as-oxidized condition at 750°C. The heat-affected zone shows a duplex grain structure, with the grains at the sheet surface much smaller than those in the interior. This indicates that the oxygen added to the specimen was preferentially concentrated near the surface before welding and inhibited grain growth there. The welding process would tend to homogenize the oxygen concentration in the vicinity of the weld bead and to cause precipitation of oxygen as HfO_2 in the adjacent heat-affected zone. This homogenization and precipitation may explain the fact that the weld and heat-affected zone were immune to lithium attack, while areas more distant from the weld, which contained a large amount of oxygen near the surface, underwent heavy attack.

Further capsule studies are in progress to evaluate the effects of welding and oxygen contamination on tantalum containing variable hafnium additions. Alloys being studied include pure tantalum, Ta–0.5% Hf, Ta–1% Hf, and Ta–2% Hf. The alloys are being given a solution heat treatment after oxidation to avoid the high concentrations of oxygen encountered at the surface of the specimens mentioned above. The welded coupons are being exposed for 100 hr between 800 and 1200°C.

Thermal Convection Loop Tests (C. E. Sessions)

We are conducting a program of thermal convection loop tests to compare the corrosion resistance of niobium, tantalum, and tungsten alloys in flowing, nonisothermal lithium, and to study reactions controlled by solid-state diffusion in niobium and tantalum systems. Figure 5.20 shows the loop design developed for these investigations. Note that the loop incorporates weighed insert specimens at all points along its length.

Table 5.10. Results of 100-hr Capsule Tests on T-111 and T-222 Weld Specimens in Lithium at 750°C

Condition Before Corrosion Tests	Welding Atmosphere[a]	Interstitial Concentrations in Fusion Zone, ppm						Metallographic Observation
		As Welded			After Test			
		O	N	H	O	N	H	
		T-111						
As-received	High purity	33	38	7	29	26	6	No attack
As-received	Lower purity	33	17	5	30	29	4	No attack
Oxidized at 1000°C	Lower purity	730	37	5	580	26	6	Five-mil attack on ends
		T-222						
As-received	High purity	35	29	3	37	22	6	No attack
As-received	Lower purity	43	19	13	75	57	9	Superficial attack at heat-affected zone
Oxidized at 1000°C	Lower purity	480	34	4	510	23	8	Ten-mil attack on ends

[a]High purity: chamber evacuated to 2×10^{-5} torr and backfilled with 99.996% Ar; lower purity: chamber evacuated to 5×10^{-2} torr and backfilled with 99.996% Ar.

PHOTO 91405

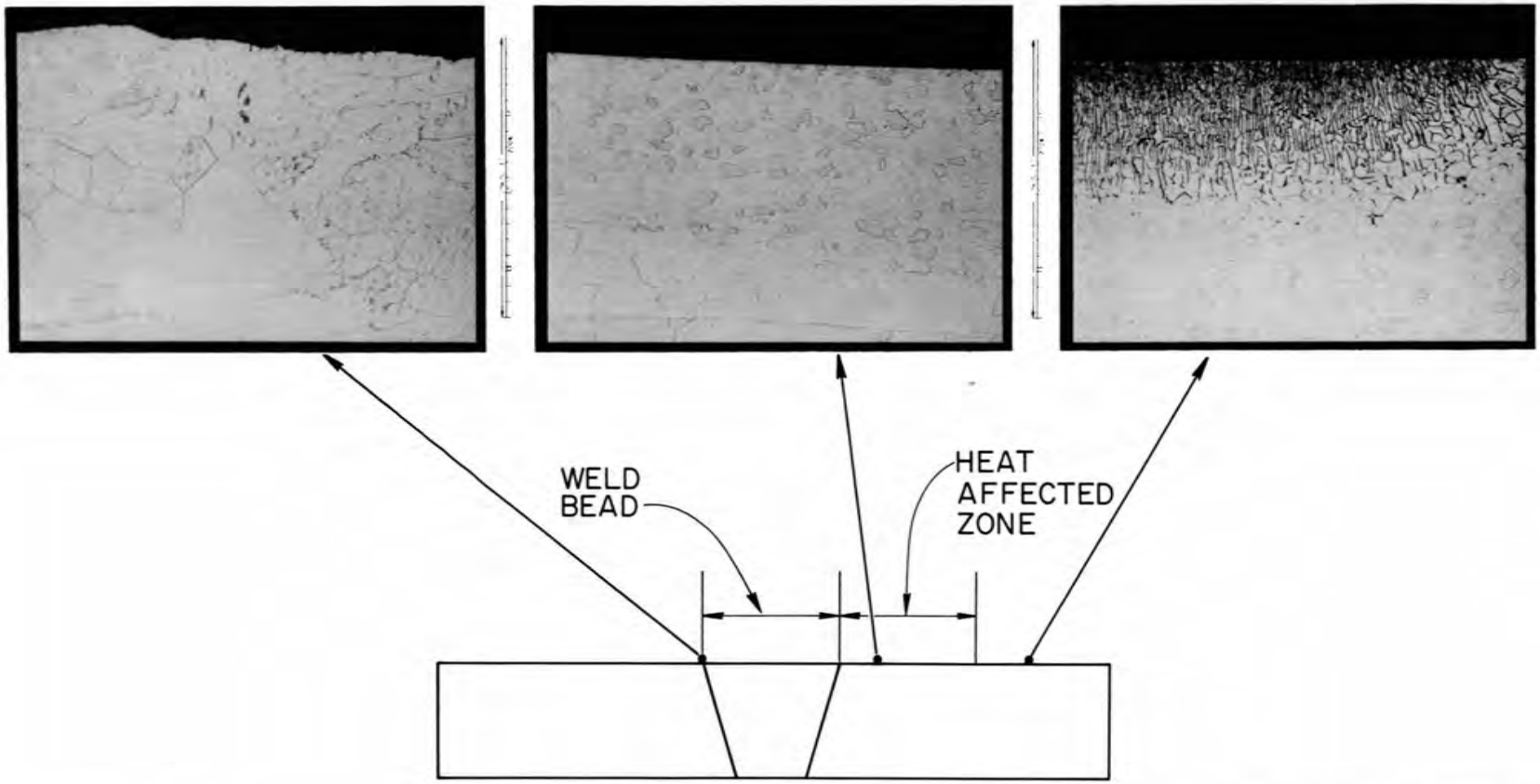

Fig. 5.19. Metallographic Appearance of Oxygen-Contaminated T-222 Weld After Exposure to Lithium for 100 hr at 750°C.

ORNL-DWG 64-75R

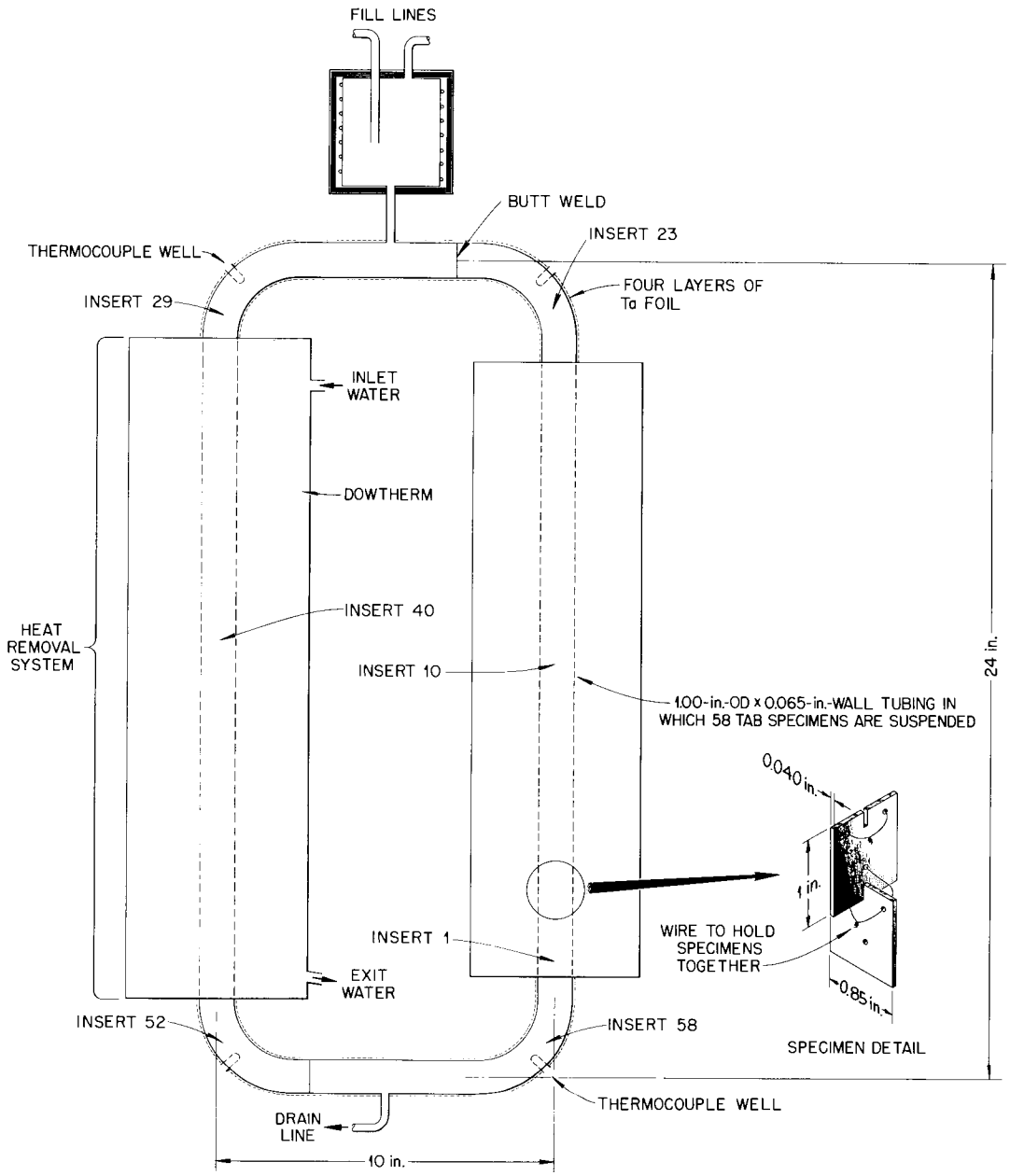

Fig. 5.20. Schematic of Lithium Thermal Convection Loop.

We have completed tests of niobium-base systems at 1200 and 1300°C and are evaluating the tantalum-base alloy T-222. Operating conditions of these loops are summarized in Table 5.11.

Niobium-base alloys tested for 3000 hr at a hot-leg temperature of 1200°C lost weight over about two-thirds of the loop length and gained weight over the remaining one-third.[10] The inverse was found for a Nb–1% Zr loop (TCL-5R) operated for the same period at a hot-leg temperature of 1300°C. The weight change profiles at the two temperatures are compared in Fig. 5.21.

The only visible or metallographic evidence of attack in the 1200°C loops was a thin, superficial layer of zirconium nitride deposited on a few cold-leg specimens. Chemical analyses of the inserts and tubing sections revealed a general loss of oxygen and a transfer of nitrogen and carbon from positions of high temperature to positions of lower temperature. Chemistry changes in the 1300°C test were more extensive and also more complicated. A loss of oxygen and an increase in nitrogen were found for the Nb–1% Zr inserts at all loop positions. Nitrogen increases were larger in the colder regions of the loop. The zirconium

[10] J. H. DeVan and C. E. Sessions, Nucl. Appl. 3, 102–109 (February 1967).

Table 5.11. Operating Conditions of Lithium Thermal Convection Loops[a]

Loops	Alloy		Temperature, °C	
	Loop Tubing	Inserts	Maximum Hot Leg	Minimum Cold Leg
TCL 1R	Nb–1% Zr	Nb–1% Zr	1190	1080
TCL 2R	Nb–1% Zr	TZM	1210	1060
TCL 3R	D-43	D-43	1200	1030
TCL 4R[b]	FS-85	FS-85	1220	1000
TCL 5R	Nb–1% Zr	Nb–1% Zr	1300	1120
TCL 6R	T-222	T-222	1350	1150

[a] Test duration: 3000 hr; flow rate: 5 to 10 fpm.

[b] Terminated after 502 hr.

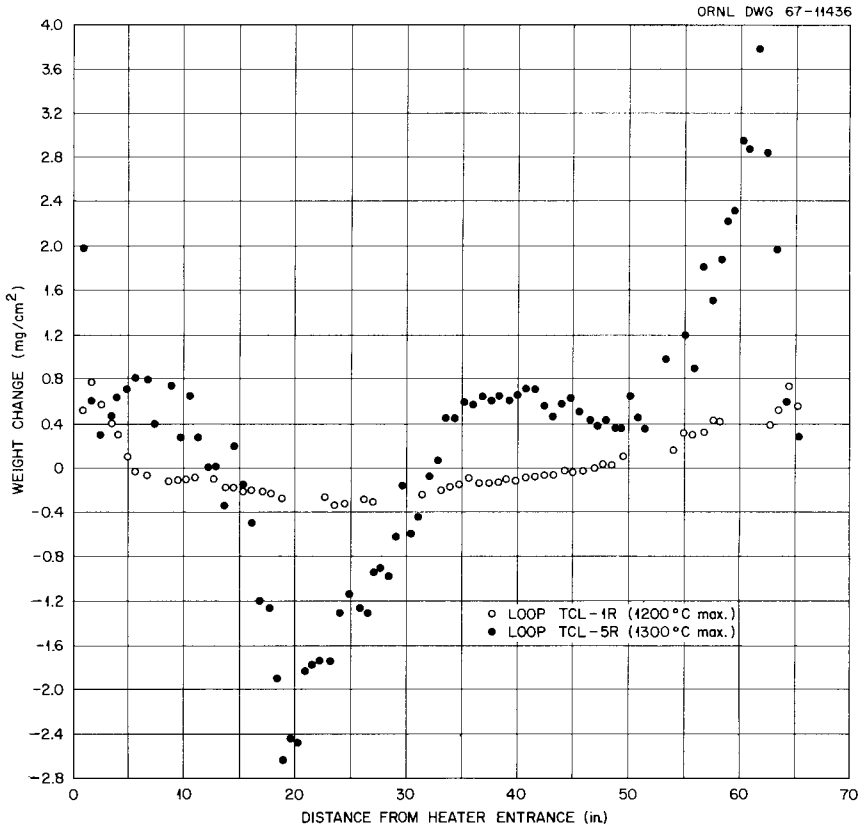

Fig. 5.21. Mass-Transfer Profile for Nb–1% Zr Inserts After Thermal Convection Loop Tests at 1200 and 1300°C Maximum Temperature.

concentration decreased in the hottest loop sections and increased in cold-leg regions.

The metallographic appearance of inserts from various positions within the 1300°C loop is shown in Fig. 5.22. Of particular interest is the presence of metallic mass-transfer deposits in the bottom part of the heater where the edges of insert specimens contacted the loop wall. In addition to this noncontinuous metallic deposit, specimens in this area exhibited a continuous nonmetallic layer. This layer increased in thickness up the heater section and was resolved into two distinct phases near the heater exit (Fig. 5.22). Stain-etching and x-ray diffraction showed the outer layer to be NbN and the inner layer to be Nb_2N. One other deposit is evident in Fig. 5.22 at the cooler exit and has been identified as a carbonitride of zirconium [i.e., Zr(C,N)]. This deposit was light gold and very similar to the superficial film of zirconium nitride found in the tests at lower temperatures.

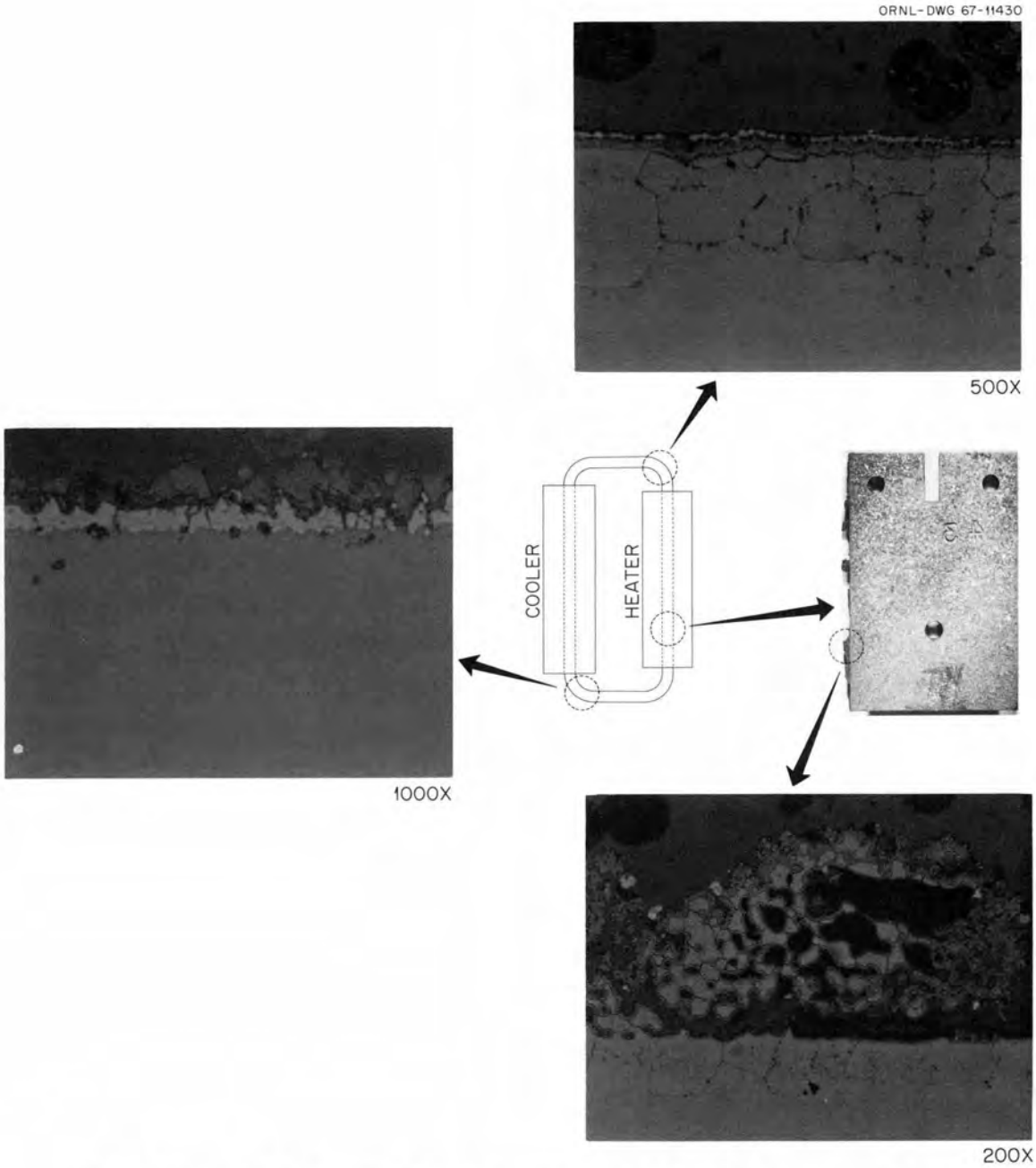

Fig. 5.22. Metallographic Appearance of Nb–1% Zr Thermal Convection Loop Test TCL 5R Operated with Lithium at 1300 °C Maximum Temperature.

The presence of deposits containing zirconium in the cold legs of these loops led us to examine the extent of zirconium depletion in the hotter loop regions and the relative contribution of zirconium to the total mass of material transferred between hot and cold sections. Insert specimens from the 1200°C loop, when analyzed by wet chemical techniques, showed no change in zirconium concentration from the 1% level of the before-test alloy. However, an electron probe microanalyzer with a 2- to 3-μ-diam beam size detected zirconium gradients in samples from areas where weight was lost. Changes in zirconium concentration were considerably greater in the 1300°C loop and were reflected in bulk sample analyses as well as in microprobe traverses. Figure 5.23 compares zirconium gradients that existed below the surface of insert specimens located in the same relative positions in the two tests. The concentrations of zirconium at the surfaces of both specimens varied from about 0.3% at the lithium-metal interface to 1% in the interior of the samples. Zirconium reached 90% of its initial concentration at a depth of 0.002 in. for the 1180°C insert and at 0.007 in. for the 1280°C insert from the test at higher temperature.

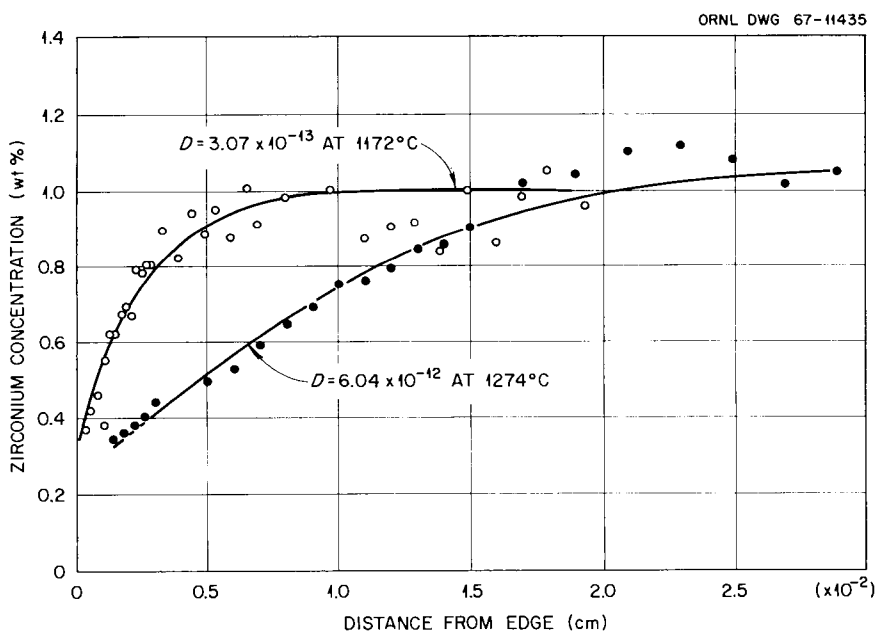

Fig. 5.23. Zirconium Concentration Gradient in Nb–1% Zr Fit with Error Function Solution of Fick's Second Law.

Based on arguments presented elsewhere,[11] the mass-transfer patterns in these loops suggest that the surface concentration of zirconium at each point in the system should have remained fixed throughout most of the test period. To check the validity of this boundary condition, we compared the observed zirconium concentration gradients of insert specimens with gradients computed by the error function solution to Fick's second law with the constant surface concentration assumption. We used a least-squares and iterating procedure to compute the gradient which best fit the experimental data. Two examples of computed gradients, shown by the solid lines of Fig. 5.23, are seen to agree very closely with the observed zirconium concentrations. These same computations yielded values for the diffusivity of zirconium in Nb–1% Zr at several temperatures. The results are plotted in Fig. 5.24 and agree well with extrapolations of published zirconium diffusivities determined

[11] J. H. DeVan and C. E. Sessions, Nucl. Appl. 3, 102–109 (February 1967).

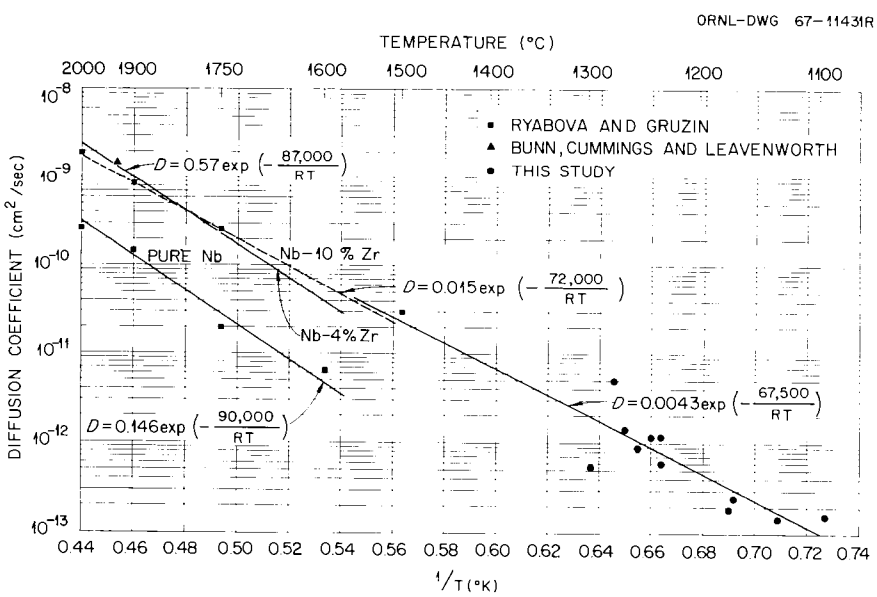

Fig. 5.24. Temperature Dependence of Zirconium Diffusivity in Nb–1% Zr Alloys.

in niobium alloys at higher temperatures.[12,13] This plot indicates the activation energy for zirconium diffusion in Nb–1% Zr to be 67,500 cal/mole.

If we assume that the zirconium surface concentration remains constant at any given point in the loop, the amount of zirconium entering or leaving each point in the system is given by the equation

$$M = \sqrt{\frac{4Dt}{\pi}}\,(C_o - C_s)\ , \qquad (5.1)$$

where

M = zirconium leaving Nb–1% Zr surface, g/cm^2,

D = zirconium diffusivity, cm^2/sec,

t = test time, sec,

C_s = zirconium surface concentration, g/cm^3,

C_o = initial zirconium concentration, g/cm^3.

To calculate the fraction of the weight changes in these tests due to zirconium diffusion out of the alloy, we determined the surface concentration of zirconium at each position in the loop by a standard x-ray fluorescence technique. These surface concentrations are plotted as a function of specimen position in Fig. 5.25. We then calculated the zirconium flux out of the specimens at each specific temperature for inserts in both the 1200 and 1300°C tests using Eq. (1); the values are presented in Figs. 5.24 and 5.25.

Figures 5.26 and 5.27 compare the calculated zirconium losses and the measured weight changes for the 1200 and 1300°C loops, respectively. In the 1200°C loop (Fig. 5.26), zirconium mass transfer accounts for

---

[12]G. G. Ryabova and P. L. Gruzin, "Investigating Diffusion Mobility of Zirconium in Zirconium-Niobium," pp. 120–126 in Metallurziya I Metallovedenize Christykh Metallov, Inz henerno-Fizicheskoy Institut, Trudy Nr. 3, Moskva, 1961. Translation FTD-TT-63-258, Wright-Patterson Air Force Base, May 1963.

[13]P. M. Bunn, D. G. Cummings, and H. W. Leavenworth, J. Appl. Phys. 33(10), 3009–3013 (October 1962).

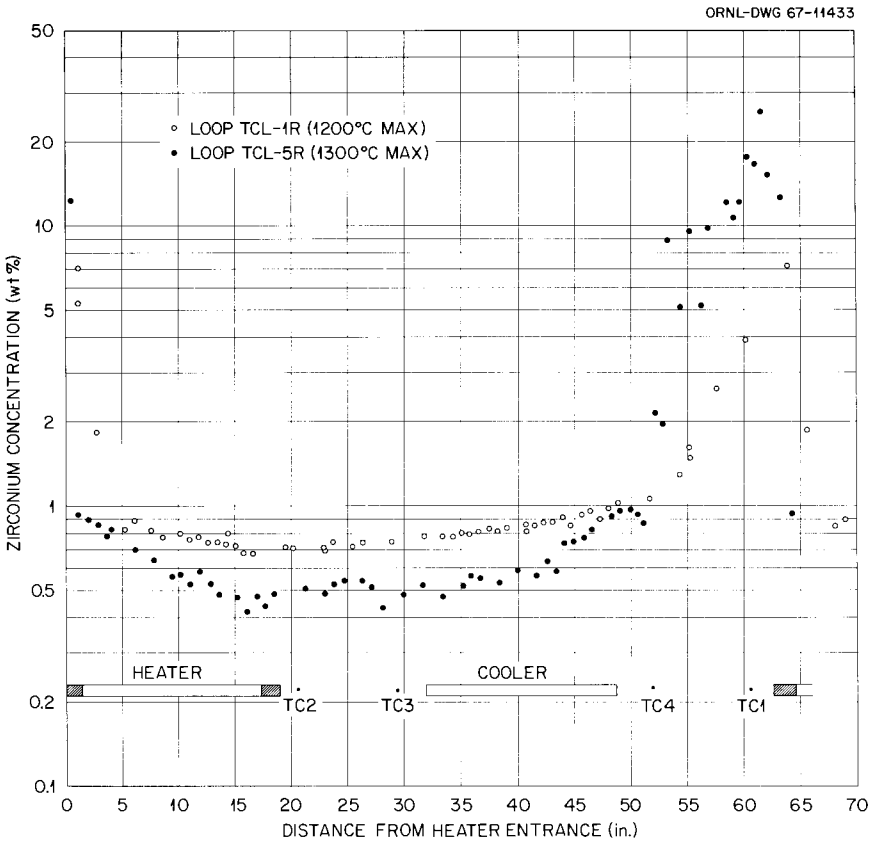

Fig. 5.25. Surface Zirconium Concentration of Nb–1% Zr Measured by X-Ray Fluorescence.

approximately one-half of the measured weight change. When changes in nitrogen concentrations are taken into account, as has been done on a limited number of specimens, the combined total of nitrogen and zirconium accounts for practically all of the observed weight changes in the 1200°C test. In contrast, Fig. 5.27 shows that the mass transfer of zirconium in the 1300°C loop tests, although greater in magnitude than at 1200°C, accounts for only a small fraction of the observed weight change. Interstitial concentration changes (oxygen, carbon, and nitrogen) in this test reflect a somewhat greater weight change than zirconium; however, niobium was the element primarily involved in the mass-transfer process at 1300°C. It is not clear whether the increased niobium transfer in this test resulted from the higher maximum operating temperature, a higher nitrogen concentration of the lithium, or a combination of these two factors.

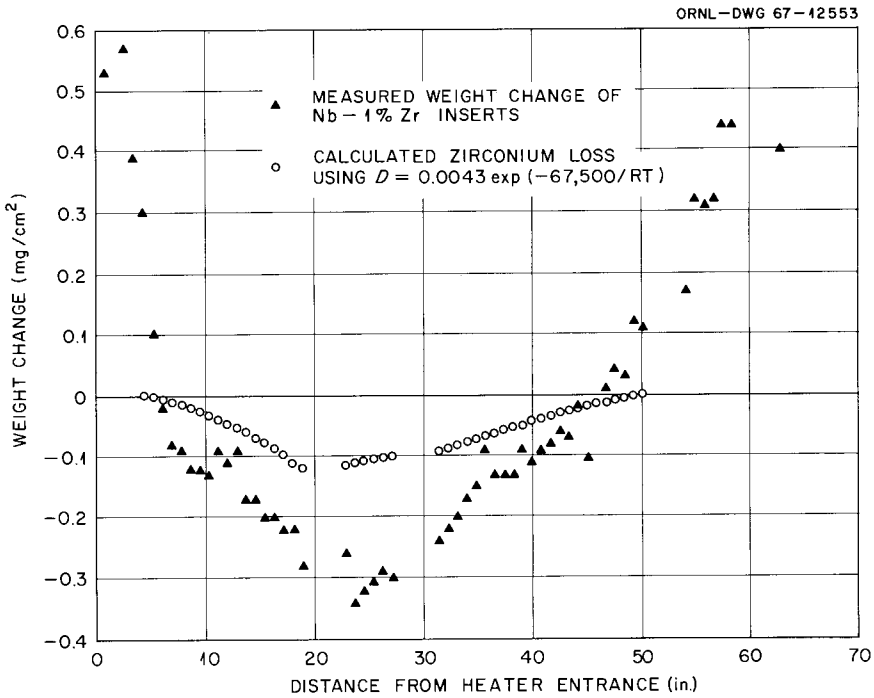

Fig. 5.26. Comparison of Weight Change with Calculated Zirconium Loss for Test in Which Maximum Hot-Leg Temperature was 1200 °C.

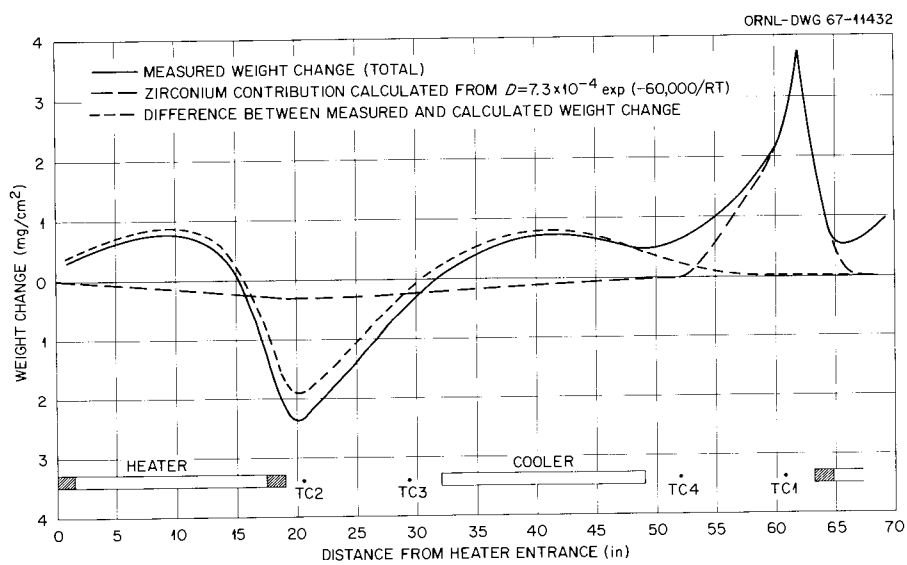

Fig. 5.27. Comparison of 1300 °C Weight Change with Calculated Zirconium Loss.

Forced Circulation Loop Tests (B. Fleischer, D. L. Clark)

The program for forced circulation-liquid lithium loops is designed to gain information on materials for fuel-element cladding and containment for lithium-cooled power systems for space. Tests scheduled under this program are listed in Table 5.12.

Table 5.12. Description of Forced Circulation Lithium Loops

Loop Number	Temperature, °C		Materials		
	Maximum	Minimum	Cold Leg	Hot Leg	Specimens
FCLLL-1	1370	1205	T-111	T-111	T-111
FCLLL-2	1370	1205	T-111	T-111	Tungsten alloys
FCLLL-3	1540	1205	T-111	Tungsten alloy	Tungsten alloys

T-111 Loop with T-111 Test Section (FCLLL-1). – Loop design. Our intent is to design a simple and economical T-111 alloy loop that will provide a test bed for studying new refractory materials, especially tungsten alloys at very high temperatures and high velocity. The design incorporates replaceable hot-leg and economizer sections with specimens appropriate for determining metallurgical and chemical changes as well as mechanical properties data. The hot leg is heated by direct resistance, and heat is removed by a radiator that transmits directly to the water-cooled walls of the vacuum chamber, thus eliminating a NaK heat-dump circuit. A concentric tube economizer reduces the large heat loads necessary to provide the required 165 °C ΔT in the system. The surge tank, dump tank, and hot trap will be combined as a single vessel. Provisions have been made for a bypass flow-through sampler for analysis of the lithium. A helical induction pump of T-111 alloy will provide forced circulation for the system. The loop will be installed in an available 4-ft-diam (120 ft^3) vacuum system which has been used for previous tests of material compatibility. The loop is shown schematically in Fig. 5.28, and a tabulation of loop design parameters is shown in Table 5.13.

ORNL-DWG 67-9135R

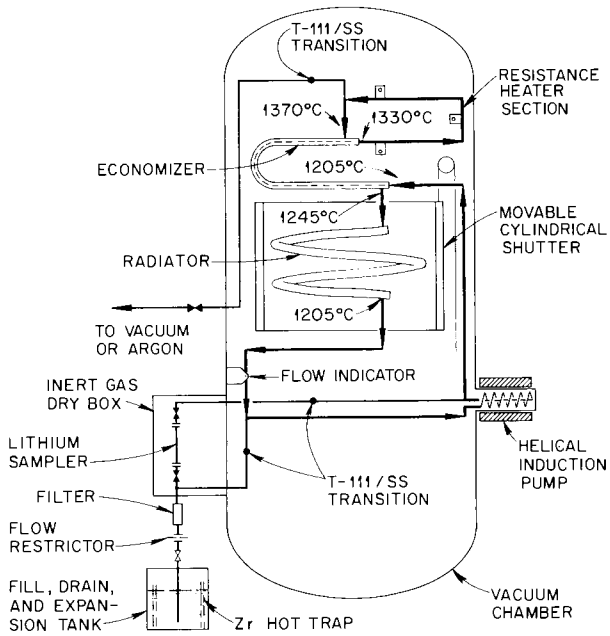

Fig. 5.28. Schematic of Forced Circulation—Liquid Lithium Loop.

With minor exception, all design has been completed, and drawings have been issued for construction. An instrument flow diagram that will show the loop instrumentation and control systems has been prepared and issued for comments. This drawing is not required for construction purposes but is of use during startup and operation. Two associated drawings showing level element details and the residual gas analyzer diagram have also been prepared and issued.

Recently we issued the installation detail drawings for an optical pyrometer. This includes the blackbody on the loop piping, the sight port, and the shutter arrangement to minimize sublimate deposit on the sight port. The shutter will be of quartz in order to allow for sighting and alignment of the optical pyrometer with the shutter closed. The shutter will be opened only during the actual measurement of the temperature by an automatic pyrometer.

Design details have been completed for the two 2-in.-ID by 6-in.-long tungsten mesh furnace assemblies that will heat metallurgical control specimens within the loop vacuum chamber. Eight T-111 specimens, each 1 1/2 by 2 3/4 in., will be located in an isothermal region of each

Table 5.13. Engineering Design Information for Forced Circulation—Liquid Lithium Loop FCLLL-1

General Information	
Material of construction	T-111 (Ta–8% W–2% Hf)
Heat transfer fluid	Lithium
Flow rate	5.8 gpm
Maximum velocity	20 fps at heater outlet
Maximum Reynolds number	99,000 at heater outlet
Total system pressure drop	41 psi
Pressure drop in 0.370-in. ID tubing	0.9 psi/ft
Maximum temperature	1370°C
Minimum temperature	1200°C
Number of test specimens in loop	100
Resistance-Heated Section and Electrical Equipment	
Heated section length	8 ft (1/2-in. OD × 0.65-in. wall tubing)
Heat input for 20°C, ΔT	26 kw (88,550 Btu/hr)
Current	2800 amps
Electromotive force across heater	9.31 v
Transformer rating	60 kva
Cross-section dimensions of copper bus bars	1/2 × 4 in.
Power loss in 15-ft bus bar system	1.0 kw
Emissivity coating on bus bars	3 to 5 mils of iron titanate
Maximum temperature of bus bars	425°C
Economizer	
Heat transfer for 165°C ΔT	82 kw
Length of economizer	10 ft
Outer tube size	7/8-in. OD × 0.065-in. wall
Inner tube size	1/2-in. OD × 0.065-in. wall
Lithium velocity in annulus	8.5 fps
Radiator	
Type of construction	28-in.-diam coiled tube
Tubing size	22 ft of 1-in. OD × 0.065-in. wall
Surface area of coil	5.76 ft^2
Heat loss at design conditions	23.3 kw
Heat loss with reflective shield	20.6 kw
Heat loss with no shield	31.6 kw
Lithium velocity	3.2 fps

Table 5.13 (continued)

Refective Shielding for Radiator	
Diameter of outer shell	34 in.
Diameter of inner shell	19 in.
Height of shield	26 in.
Number of reflective layers on each shell	2
Maximum temperature of second layer	620°C
Method of operation	Cables and pulleys

furnace with multiple layers of tantalum foil used as reflective insulation. Existing high current feedthroughs will be used for the power leads (vacuum vessel penetrations), and three tungsten-rhenium thermocouples will be provided for each furnace.

After a study of various epoxy materials now being used at ORNL and of manufacturer's data, both written and oral, we have selected a silicone rubber (Silastic RTV No. 732) to seal the bare-wire tungsten-rhenium thermocouples at the vacuum vessel penetrations. The installation of the silicone rubber will call for curing at room temperature for 3 to 4 days and then baking at 260°C for 1 hr. Gas and weight losses are expected to be less than 1% during this curing and baking. Subsequent operation at temperatures up to 260°C is considered permissible by the vendor, although the maximum expected for loop operation will be below 205°C at the feedthrough. All thermal elements will be continuous from the hot junction to the external cold junction reference box. All high-temperature thermocouples are W–3% Re vs W–25% Re.

Procurement and fabrication of materials other than T-111. All materials necessary for fabrication of FCLLL-1 have been received. Included are the special 1/8-in.-OD electric trace heaters and associated hermetic seals, the twin I-tube level indicating element, the sheath-type tungsten-rhenium thermocouples, a control magnetic amplifier, and the roll adapter sleeves. Fabrication of the stainless steel fill and drain tank and of the glove box was completed. The two units have been welded together, and the installation of heaters and thermocouples has been started.

The Welding and Brazing Laboratory has applied the high-emissivity coating of iron titanate on the copper bus bars and on the specified areas of the tantalum heater lugs. The Welding and Brazing Facility of the Plant and Equipment Division has fabricated the movable shade assembly.

Fabrication is under way in Building 9201-3 on the two furnaces for the metallurgical control specimens and elsewhere on the various components for the optical pyrometer installation.

Figure 5.29 shows various patterns of reflective insulation and the 3-in.-diam (ID) by 2-in.-wide rolls used for impressing these patterns. An existing 3-in.-diam by 4-ft-wide sheet metal roll is used in processing the insulation foil, and a 1/8-in.-thick Teflon backup strip is used on all passes. The reflective insulation material for FCLLL-1 will be 0.002-in.-thick tantalum foil.

A single pass using both rolls gives a simple herringbone pattern as shown by the right-hand strip below the rolls in Fig. 5.29. This pattern is well suited to half-lap installation on tubing 1 in. in diameter and larger. The next strip to the left has been passed through the rolls a second time in the reverse direction (crosshatch pattern) and with the indentation made on the reverse side. The left-hand strip below the rolls has been passed through the rolls a second time in the same direction with the indentation made on the reverse side. This pattern was used to provide eight layers of the reflective insulation to the 1/2-in. tube shown in the center of Fig 5.29. A prerequisite for good reflective insulation is a minimum of metal conducting area between the foil layers that still maintains reasonable separation of the individual layers. The spacing of the indentation on both sides of the foil should provide this condition. Consequently, we have selected this design for use on the 1/2-in. tubes for FCLLL-1.

On the left half of Fig. 5.29 are shown samples of foil that will be used for multiple-layered sandwiches of reflective insulation of various shapes. These sandwiches can be load bearing if required without sacrificing any appreciable insulation values. Rotation of adjacent layers from the position shown can reduce conduction losses. Wider sheets or strips of reflective insulation such as that shown on the

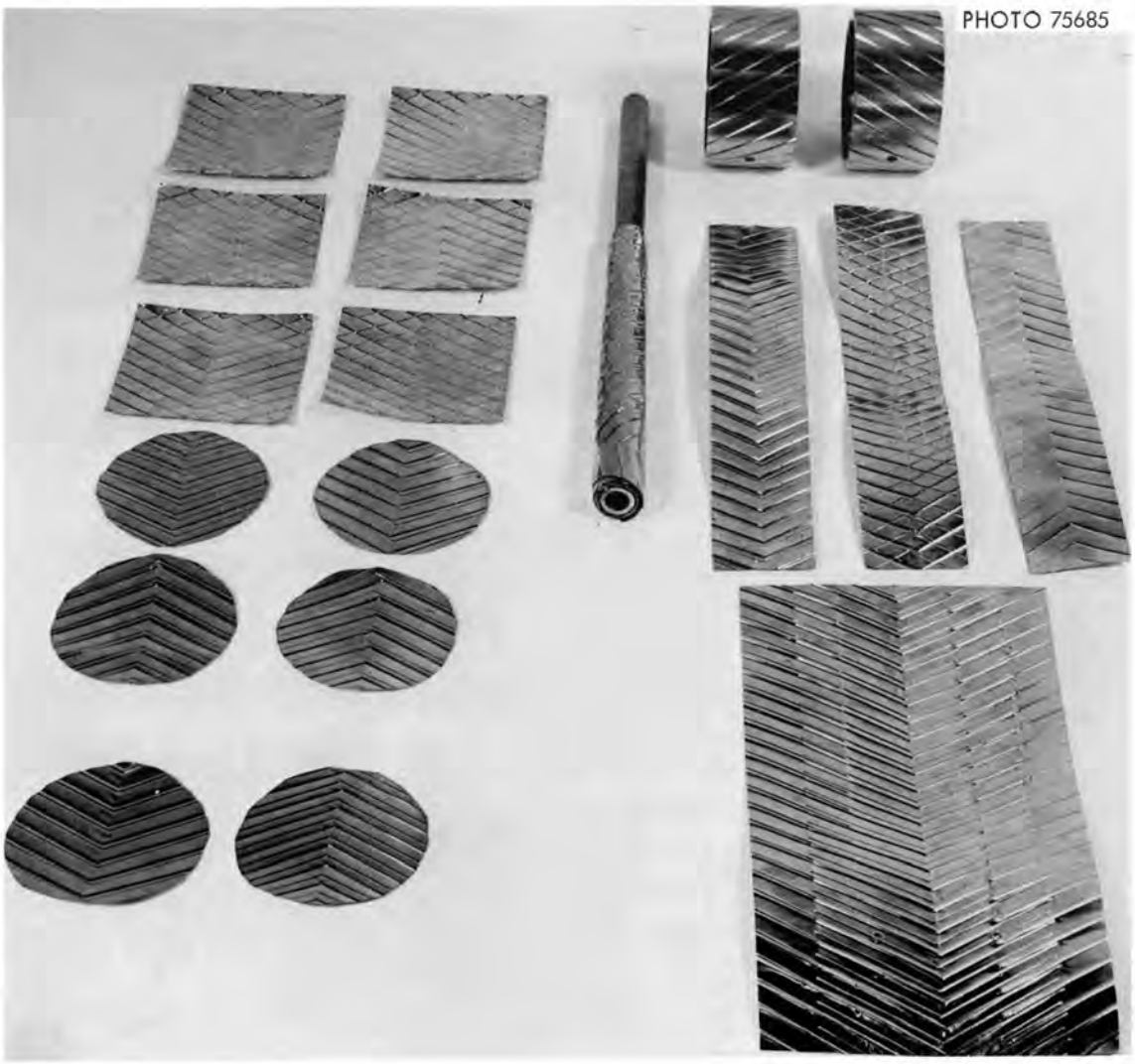

Fig. 5.29. Reflective Insulation and Associated Tooling for FCLLL-1.

lower right-hand section of Fig. 5.29 can be processed by multiple passes through the 4-in. (overall) width of the rolls.

Figure 5.30 shows the assembled 12 3/4-in.-OD by 18 3/4-in.-long stainless steel fill and drain tank with valves, filters, and flow restrictor installed. This assembly is mounted adjacent to the glove box, and a common floor pan is used for the two. Figure 5.31 shows the partially completed glove box including the 3/8-in.-OD tubing runs, 3/8-in. valves, sample section, and sample capsule. Marman "Conoseal" flanges and gaskets are provided for removing the sample section.

Fig. 5.30. Fill and Drain Tank Assembly for FCLL-1.

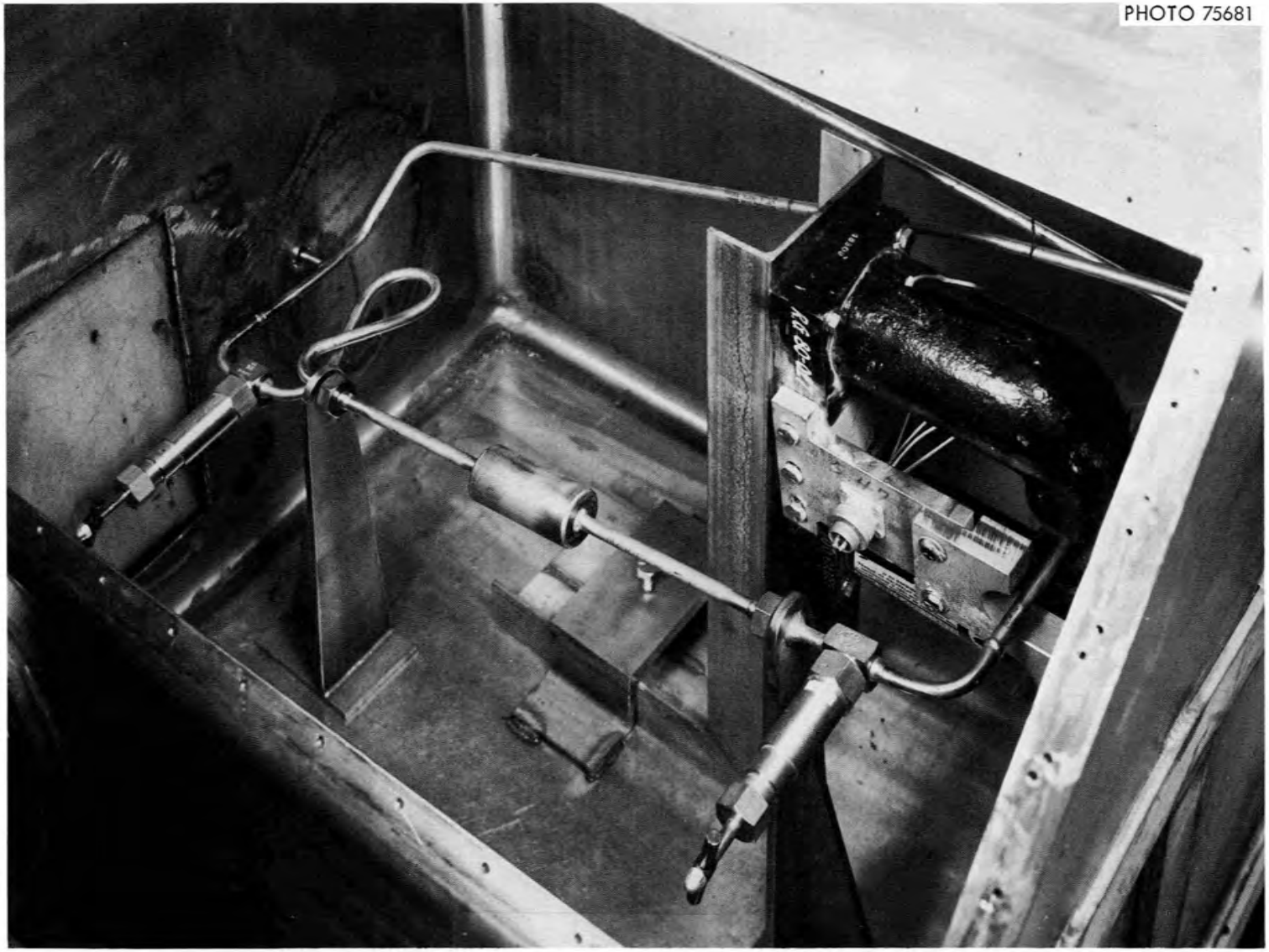

Fig. 5.31. Internal View of FCLLL-1 Glove Box for Lithium Sampling.

Lithium flow through the sample section will be monitored by the flowmeter magnet shown.

Figure 5.32 shows the reflective shields (34 in. in outside diameter by 19 in. in inside diameter) for the radiator coil in place on the frame of the test stand. Two layers of reflective insulation are used, the inner layer being tantalum foil and the outer layer being stainless steel. The structural members are also stainless steel. Hard-fired alumina pulleys with stainless steel axles are used with the lifting mechanism to prevent galling. A counterweight lessens the torque requirements on the magnetic feedthrough for the lifting mechanism.

Procurement of T-111 alloy. Efforts in the Materials Processing Laboratory to produce material from powder electrode meltdown have continued, but without success. On December 27, 1967, however, we received sheet material produced there from T-111 scrap material all heat-treated in the same batch (Heat CVO-252) for 4 hr at 1455°C in 5×10^{-5} torr vacuum. This material was supplied in two thicknesses and several dimensions. We received a total of 3.5 lb of 0.031-in.-thick sheet in the following sizes: two sheets 3 × 16 1/8 in.; one sheet 3 × 13 in.; one sheet 3 × 11 1/2 in.; one sheet 3 × 7 1/4 in. We also received a total of 21 lb of 0.100-in.-thick sheet in four pieces, each 2 15/16 × 30 1/2 in.

Ultrasonic inspection was not applicable for the 0.031-in.-thick material but showed the 0.100-in.-thick sheet acceptable. The dye-penetrant technique indicated only insignificant indications in both materials. Chemical analysis of both sheet forms is compared to the specification limits in Table 5.14.

To minimize the chance of further delay, contracts were written with vendors for the remaining materials. On January 25, 1968, Wah Chang Corporation received the contract for producing sheet materials 0.030 and 0.094 in. thick and bar stock 1 in. in diameter. On March 18, 1968, only ten days later than the delivery date requested, we received the following: one sheet, 8 × 36 × 0.030 in., that weighed 5.4 lb; three sheets, each 5.25 × 30 × 0.094 in., that totaled 27 lb; two 1-in.-diam rods, one 3 ft long and the other 2 ft long, that totaled 29 lb. Ultrasonic and dye-penetrant inspections showed all materials

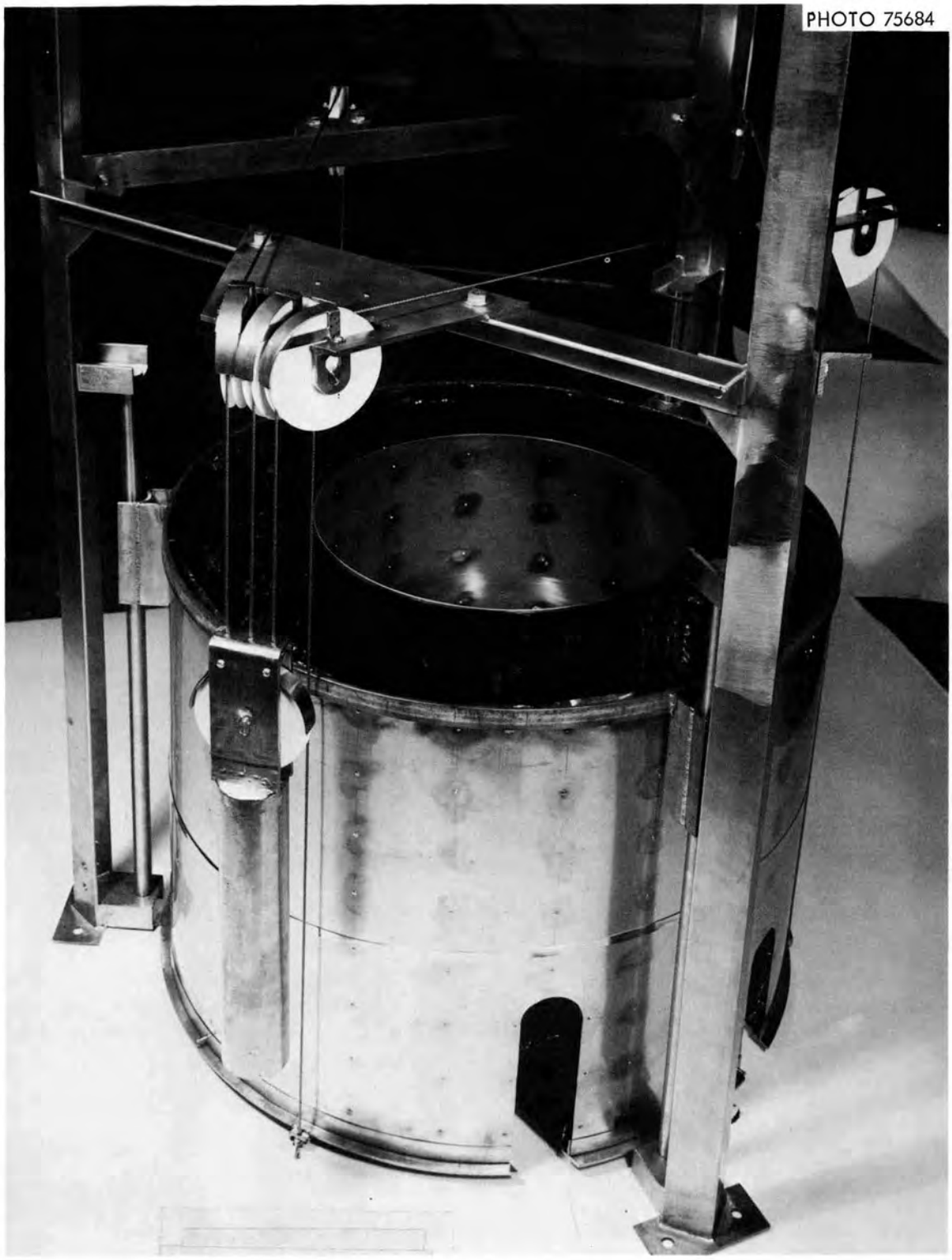

Fig. 5.32. Reflective Shield for FCLLL-1 Radiator.

Table 5.14. Chemical Analysis of T-111 Sheet Received from Material Processing Laboratory Compared to Specification Limits

Element	Specification Limits[a]	Concentration[b] Sheet Thickness, in.	
		0.031	0.100
C	100	53	26
O	300	50	50
N	200	16	6
H	20	2	2
W	7.2–8.8 wt %		8.8 wt %
Hf	1.8–2.3 wt %		2.0 wt %
Zr	200		1000[c]

[a]Values in parts per million maximum unless otherwise indicated.

[b]Values in parts per million unless otherwise indicated.

[c]This deviation from specification was accepted since zirconium is considered a beneficial element.

were 100% recrystallized and that the bar stock was 95 to 100% recrystallized. The history and composition of these products are shown in Table 5.15.

The contract for tubing was awarded to Superior Tube Company on January 26, 1968. On April 29, 1968, about 4 weeks after the estimated delivery date, we received the tubing described in Table 5.16.

Although the vendor certified that the tubing conformed to our penetrant and ultrasonic specifications, our own inspections showed numerous indications. The penetrant indications, some as deep as 0.009 in., were generally removed by filing. One tube containing a large number of indications was centerless ground to remove 0.011 in. from the outer surface of the tubing wall; this removed all defects. To investigate the ultrasonic indications, we gave all the material a light etch to remove approximately 0.002 in. from the surface. Post-etch penetrant inspection revealed indications at each previous site of

Table 5.15. History and Composition of T-111 Alloy Sheet and Bar Received from Wah Chang Corporation Compared to Specification Limits

Element	Specification Limits[a]	Wah Chang Ingot Analyses of Heat 650038[a]			Product Analyses[a,b]					
					Sheet Thickness (in.)				Bar (1-in. diam)	
					0.030		0.094			
		Top	Center	Bottom	Wah Chang	ORNL	Wah Chang	ORNL	Wah Chang	ORNL
W	7.0–9.0%	8.5%	8.8%	8.5%		8.2%				8.4%
Hf	1.8–2.4%	1.9%	2.0%	2.0%		1.9%				2.1%
C	< 50 ± 10	< 40	< 40	< 40	75	60	20		< 20	30
O	< 150 ± 20	< 50	< 50	< 50	80	150	80		90	90
N	< 75 ± 10	25	20	30	20	19	20		17	14
H	< 10 ± 2	2.3		2.7	1.4	< 1	1.6		3.2	< 1
Nb	< 2000	270	330	760		1000				1000
Zr	< 200	< 200	< 200	< 200		700[c]				1000[c]
Mo	< 1000	150	125	120		500				500
B	< 1	< 1	< 1	< 1		< 1				< 1
Cd	< 5	< 5	< 5	< 5		< 1				< 1
Co	< 30	< 5	< 5	< 5		< 10				< 10
Fe	< 500	20	20	20		50				10
Pb	< 50	< 50	< 50	< 50		< 1				< 1
Mn	< 100	< 10	< 10	< 10		< 1				< 1
Ni	< 200	< 10	< 10	< 10		< 1				< 1
Si	< 300	< 20	< 20	< 20		< 10				< 10
Ti	< 500	< 20	< 20	< 20		< 10				< 10
V	< 200	< 10	< 10	< 10		50				50
Total rare earths	< 100					< 10				< 10
Ta	Bal	Bal	Bal	Bal		Bal				Bal

[a]Values in parts per million unless otherwise indicated.

[b]All material annealed 1 hr at 1650°C in vacuum.

[c]Deviation accepted.

Table 5.16. T-111 Alloy Tubing Received from Superior Tube Company

Element	Specification Limits[b]	Superior Ingot Analyses[b]		Tubing Analyses, Outside Diameter, inches[a,b,c]							
				0.5				0.875		1.0	
		Heat		Heat							
				8227[c]		8171[d,e]		8227[e,f]		8171[f,g]	
		8171	8227	Superior	ORNL	Superior	ORNL	Superior	ORNL	Superior	ORNL
W	7.0–9.0%	7.55%	7.44%		7.9%		8.0%		7.9%		7.2%
Hf	1.8–2.4%	2.18%	2.30		2.1%		2.0%		2.0%		2.0%
C	< 50 ± 10	25	28	< 10	70	< 10	40	< 10	40	40	40
O	< 150 ± 20	21	9	42	27	39	40	31	35	45	26
N	< 100 ± 10	30	22	18	4	23	8	20	12	21	8
H	< 10 ± 2	0.7	5	1	< 1	3	< 1	4	< 1	3	< 1
Nb	< 2000				200		100		200		100
Zr	< 200				900[h]		900[h]		900[h]		900[h]
Mo	< 1000				60		6		60		6
B	< 1				0.6		0.6		0.6		0.6
Cd	< 5				< 0.2		< 0.2		< 0.2		< 0.2
Co	< 30										
Fe	< 500				3		10		10		10
Pb	< 50				< 0.2		< 0.2		< 0.2		< 0.2
Mn	< 100				< 0.1		< 0.1		< 0.1		< 0.1
Ni	< 200				1		1		1		1
Si	< 300				10		10		10		10
Ti	< 500				< 100		< 100		< 100		< 100
V	< 200				< 1		< 1		< 1		< 1
Total rare earths	< 100				< 20		< 20		< 20		< 20
Ta	Bal				Bal		Bal		Bal		Bal

[a]All material annealed 15 min at 1595°C in vacuum.

[b]All values in parts per million unless otherwise indicated.

[c]All tubing had 0.065-in. wall thickness.

[d]Total length received: 38 1/2 ft.

[e]Total length received: 28 3/4 ft.

[f]Total length received: 25 1/3 ft.

[g]Total length received: 39 ft.

[h]Deviation accepted.

ultrasonic defects. A typical defect uncovered by etching is shown in Fig. 5.33. These defects were also removed by filing. After removal of these indications, the tubing was again inspected ultrasonically and found to be free of all defects, thus confirming that all the previous ultrasonic defects were near-surface defects uncovered by the etching operation.

The T-111 material for the metallurgical specimens and the associated stringers for FCLLL-1 was received. An outside machine shop completed machining of both the prototypes and the production units for both the 8- and 10-unit stringers. Dimensional tolerances on all units were within requirements. The units are now being assembled.

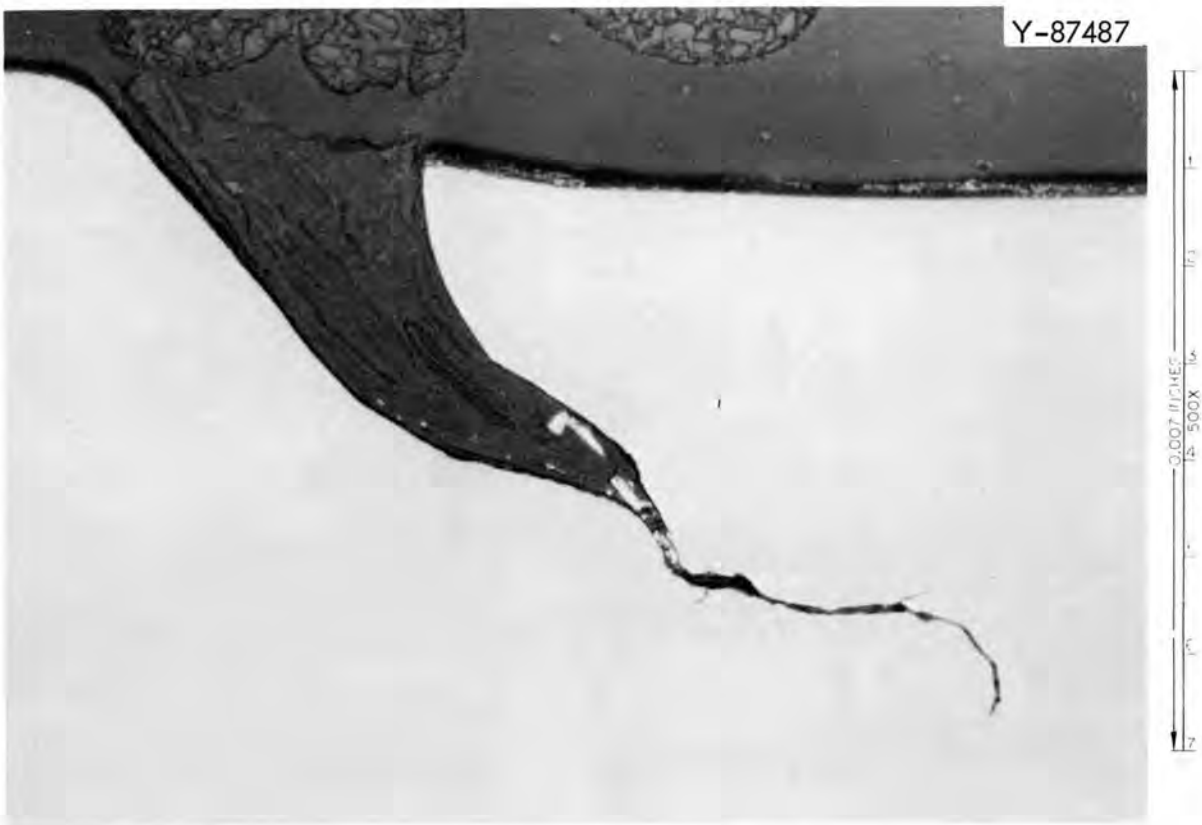

Fig. 5.33. Defect on Outside Diameter Surface of T-111 Tubing.

Fabrication of T-111 specimens and holders. After being machined, all specimens were identified, bright etched, measured, and weighed. The flat specimens were inserted into the holders and secured with shims welded in place. Some of the completed specimen units are shown in Fig. 5.34. Each unit is held in the tubing part by tack welds made about 1/4 in. from butt weld joints, that join the ends of the holder to the wall of the tubing.

Fabrication of T-111 fittings and tubing parts. All bending and machining has been completed for fitting and tubing parts. All bends and machined surfaces were penetrant inspected and found to be free of cracks. To prevent collapse during bending, "sugar filling" was used for two parts. After mechanical removal of the bulk of the sugar, the parts were flushed with 65°C water and rinse-dried with alcohol. To check for cleanliness, each part was soaked in 65°C water for 2 hr, and then a sample of the water was analyzed for sugar content. The analytical results indicated no residual sugar in the parts.

During processing, we maintained the identification of the starting material. The parts have all been washed in a laboratory-ware detergent, immersed in clean warm water and cold, distilled water, rinse-dried with alcohol, and stored in sealed plastic envelopes.

Fabrication of T-111 assemblies. Welding of parts for fabrication of the various piping assemblies has begun. All parts are handled with white gloves during fixturing. Only refractory materials are in contact with the loop parts during fixturing. Before and after welding, we weld a sample of titanium to check for pickup of oxygen and nitrogen. On-line meters monitor the oxygen and water levels in the dry box during welding.

Development of T-111 field welds. A technique has been developed for field welding of T-111 assemblies with the automatic equipment for field welding the refractory materials used in the boiling potassium studies. The weld has 80 to 90% penetration, which is ample to accommodate the stresses encountered during operation. One of the sample field welds has been tested in the as-welded condition in a lithium static capsule at 800°C for 100 hr to assess corrosion resistance.

Fig. 5.34

Fig. 5.34. Specimens Assembled in Specimen Holder Units.

Posttest metallographic examinations showed no corrosion attack. Several more tests are planned to confirm this.

Fabrication and testing of T-111 helical induction pump. (R. E. McDonald, H. C. Young, A. G. Grindell) The T-111 pump cell was fabricated, assembled into a stainless steel container, and tested. All components (Fig. 5.35) were TIG welded in a vacuum chamber except the container, which required electron-beam seal welds to minimize shrinkage and warpage. The Nb–1% Zr end of the Nb–1% Zr–stainless steel transition joint was braze-welded to T-111 with Nb–1% Zr filler wire. An interference fit of 0.001 to 0.002 in. between the container and helix was made by cooling the helix in liquid nitrogen and heating the container to about 425°C before assembling the two components. All parts were etched before welding, and all welds were inspected by dye penetration and radiography. The assembly was vacuum-annealed at 1315°C for 2 hr.

To check on the cell integrity and to permit a reasonable prediction of its performance in lithium at operating conditions, we tested the pump cell in a modified stainless steel flowmeter facility with potassium, to preclude damaging the test loop. The potassium contained 27 ppm O during filling and 43 ppm O after test.

We tested performance and cavitation at nominal pump inlet temperatures from 425 to 815°C. Figure 5.36 shows typical performance data at 815°C in potassium. The accuracy of our method of predicting pump performance from the head developed at zero flow at a given temperature is shown by the proximity of the predicted and measured values in Fig. 5.36. The predicted curve was calculated from a measurement of the shut-off pressure at 350 v and 425°C. Curves showing calculated pump performance in lithium at 1205°C are shown in Fig. 5.37.

We gathered data for cavitation in potassium at several temperatures under argon cover gas in the potassium expansion tank. Typical NPSH (net positive suction heads) at the point where a sudden drop in head was eminent are shown below for three flows at 450 v and 655°C

Flow, gpm	3.0	4.5	5.8
NPSH, psi	0.4	2.0	6.8 .

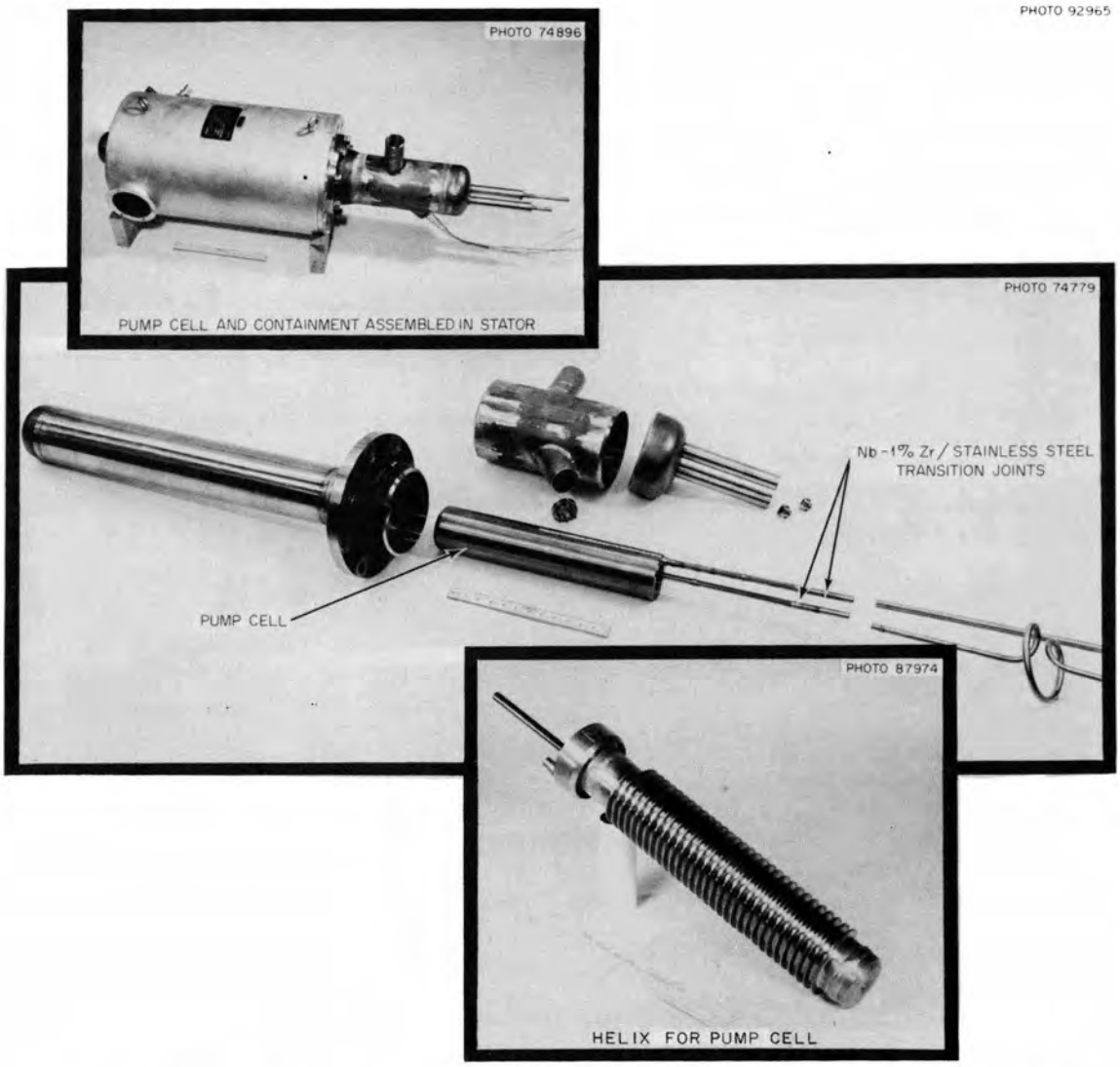

Fig. 5.35. T-111 Helical Induction Pump and Associated Stainless Steel Containment.

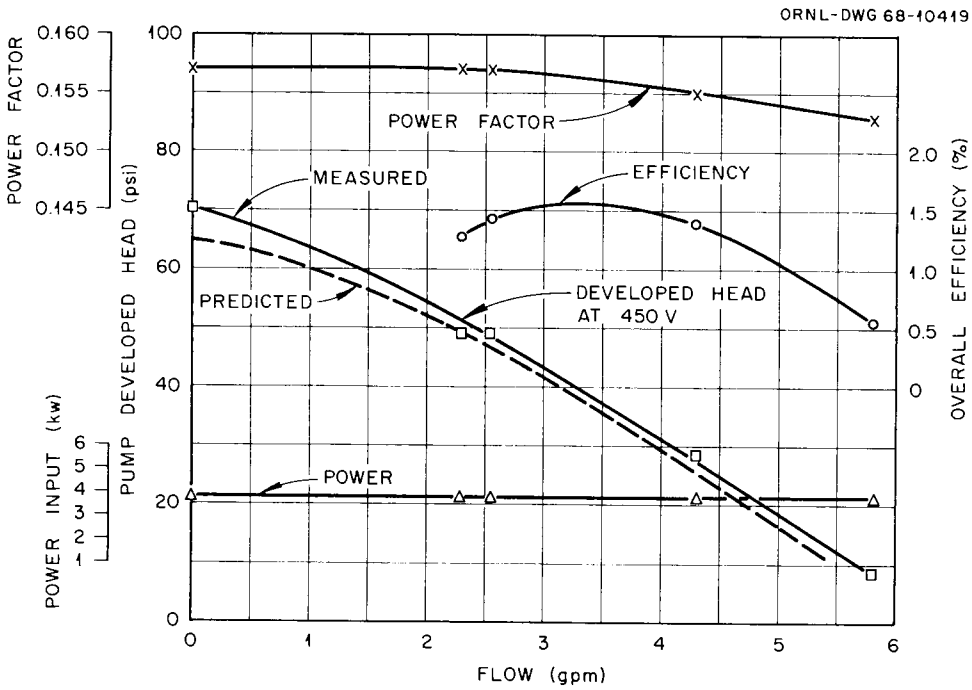

Fig. 5.36. Performance Curves for Helical Induction Pump (GE Model 5KY414PM1) with T-111 Pump Cell in Potassium Liquid at 815°C.

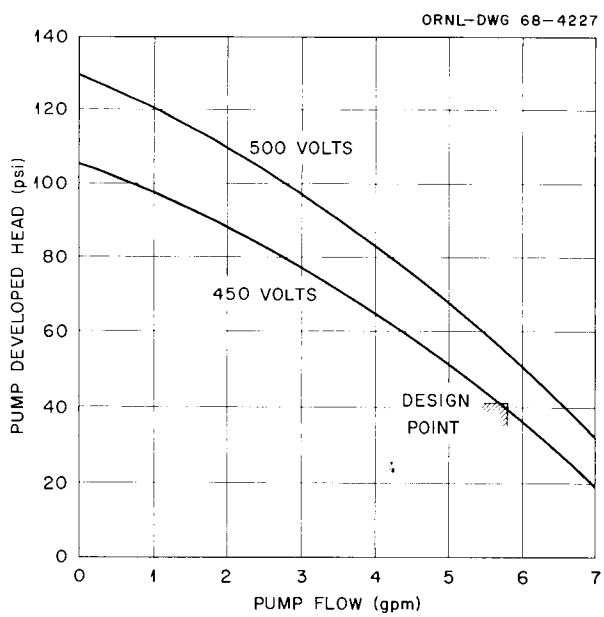

Fig. 5.37. Performance of T-111 Helical Induction Pump with Lithium at 1205°C (Calculated from Potassium Test Data at 815°C).

The vapor pressures of potassium at 655°C and lithium at 1205°C are equal (about 6 psia). Therefore, with lithium at 1205°C at the designed flow rate of 5.8 gpm, the gage pressure at the pump inlet must be a minimum of 7 psi above the local vapor pressure of 6 psi (or a total of 13 psia) to avoid cavitation.

The tests have shown that the pump will provide the designed head and flow rates for FCLLL-1 and that the complex cell is structurally sound.

Interactions in Refractory Metal–Alkali Metal Systems Containing Oxygen

R. L. Klueh

Diffusion of Oxygen in Niobium

A study of the oxygen-niobium-liquid potassim system has shown that oxygen is rapidly depleted from oxygen-doped commercially pure niobium in potassium at 600 and 815°C (ref. 14). The oxygen depletion rate was governed by the diffusivity of oxygen in niobium. The assumption that the final oxygen concentration had been maintained at the surface of the niobium throughout the experiments gave diffusion coefficients[15] for oxygen close to those in the literature.[16,17]

We have now completed similar tests of niobium in potassium at 1000 and 1250°C. The direction of oxygen migration in these systems was the same as at lower temperatures, although, as would be expected, depletion rates were considerably faster. The depletion rates at the higher temperature were again correlated with the solid-state diffusion

---

[14] A. P. Litman, The Effect of Oxygen on the Corrosion of Niobium by Liquid Potassium, ORNL-3751 (July 1965). M.S. Thesis, the University of Tennessee.

[15] A. P. Litman, Phys. Status Solidi 11, K47 (1965).

[16] C. Y. Ang, Acta Met. 1, 123 (1953).

[17] R. I. Jaffee, W. D. Klopp, and C. T. Sims, Trans. Am. Soc. Metals 51, 282 (1959).

model that appeared to fit the lower temperature results. Oxygen diffusivities were calculated from the relation[18]

$$\frac{\bar{c} - c_f}{c_i - c_f} = \frac{8}{\pi^2} \sum_{n=0}^{\infty} \frac{1}{(2n + 1)^2} \exp\left[-\frac{(2n + 1)^2 \pi^2 Dt}{4\ell^2}\right], \qquad (5.2)$$

where

c_i = initial oxygen concentration in niobium,

c_f = oxygen concentration at equilibrium,

$\bar{c}$ = average oxygen concentration at time t,

ℓ = half the specimen thickness (0.05 cm),

D = diffusion coefficient of oxygen in niobium.

The results of the calculations are shown in Table 5.17, and the averages of the calculated D's are compared in Table 5.18 with the results of Ang,[16] who used internal-friction measurements, and those of Jaffee, Klopp, and Sims,[17] who used hardness traverses. (The diffusion coefficients for 600 and 815°C were recalculated to correct a minor error in the original calculations.)

The Effect of Oxygen on the Compatibility of Tantalum and Potassium

We are studying the role played by oxygen in the corrosion of tantalum by potassium. A series of capsule tests is being conducted at 600, 800, and 1000°C to investigate (1) the partitioning of oxygen between the tantalum and potassium, (2) the dissolution of tantalum in the potassium, (3) the formation of corrosion products, and (4) the kinetics of the preceding processes. Oxygen effects are being investigated from the standpoint of the concentration of this impurity in the tantalum as well as in the potassium.

The test capsule being used for these studies is shown in Fig. 5.38. To protect the tantalum capsules from oxidation, they are sealed under vacuum in stainless steel outer capsules. Potassium was

---

[18] W. Jost, Diffusion in Solids, Liquids, and Gases, Academic Press, New York, 1960.

Table 5.17. Results of Calculation of Oxygen Diffusivity Coefficient

Temperature (°C)	Time (sec)	c_i [a] (ppm)	$\bar{c}$ [b] (ppm)	c_f [c] (ppm)	D [d] (cm^2/sec)
600	9×10^4	1000	630	85	3.5×10^{-9}
600	3.6×10^5	1000	300	85	3.5×10^{-9}
815	3.6×10^3	2400	1800	96	2.72×10^{-8}
815	9×10^4	2400	250	96	2.84×10^{-8}
815	3.6×10^5	2400	130	96	1.14×10^{-8}
1000	3.6×10^3	2600	550	160	4.59×10^{-7}
1000	7.2×10^3	2400	250	150	4.08×10^{-7}
1250	1.8×10^3	3200	230	145	1.94×10^{-6}
1250	3.6×10^3	3400	190	155	1.34×10^{-6}

[a] Initial oxygen concentration in niobium.

[b] Average oxygen concentration at time.

[c] Oxygen concentration at equilibrium.

[d] Diffusion coefficient of oxygen in niobium.

Table 5.18. Comparison of Diffusion Coefficients for Oxygen in Niobium (cm^2/sec)

Temperature (°C)	This Investigation	Internal Friction[a]	Hardness Traverses[b]
600	3.50×10^{-9}	1.81×10^{-9}	2.24×10^{-9}
815	2.23×10^{-8}	4.23×10^{-8}	4.07×10^{-8}
1000	4.35×10^{-7}	2.68×10^{-7}	2.19×10^{-7}
1250	1.64×10^{-6}	1.62×10^{-6}	1.10×10^{-6}

[a] C. Y. Ang, Acta Met. 1, 123 (1953).

[b] R. I. Jaffee, W. D. Klopp, and C. T. Sims, Trans. Am. Soc. Met. 51, 282 (1959).

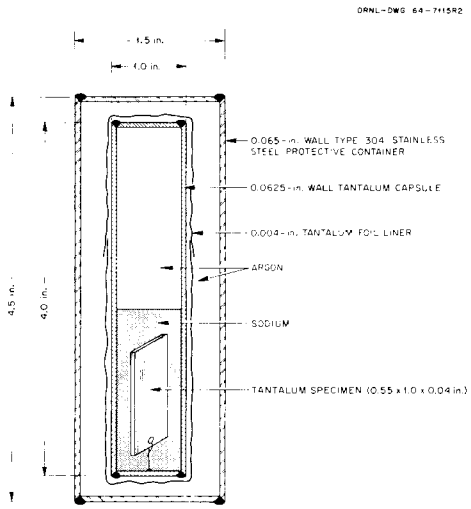

Fig. 5.38. Tantalum—Potassium Test System.

initially purified by zirconium gettering, and the oxygen level was then adjusted by direct additions of K_2O. Tantalum specimens with varying oxygen concentrations were prepared by oxidizing pure tantalum in a Sievert's apparatus[19] at 1000°C and annealing in vacuum at 1400°C. Homogeneity of the oxygen in the specimens was checked by hardness profiles. The relation between oxygen concentration (as determined by vacuum-fusion analysis) and hardness of the tantalum was also investigated to expedite determinations of the concentration of oxygen in the tantalum. The dependence of hardness on oxygen content agreed closely with the results of Gebhardt and Preisendanz,[20] and Perkins et al.[21]

The results of tests for 500 hr at 600°C are shown in Table 5.19. We systematically varied the oxygen concentration of the potassium from 100 to 3300 ppm and that of the tantalum from 40 to 1300 ppm. All of the tantalum specimens lost weight after exposure to potassium. Although vacuum-fusion analysis of the specimens revealed an oxygen loss, most of the weight loss was due to the loss of tantalum to the liquid. Weight losses increased with increasing amounts of oxygen in the potassium.

---

[19]J. R. DiStefano, Corrosion of Refractory Metals by Lithium, ORNL-3551, pp. 19–23 (April 1966).

[20]E. Gebhardt and H. Preisendanz, Z. Metallk. 46, 560 (1955).

[21]R. H. Perkins et al., Tantalum Annealing and Degassing and Hardness Effects of Dissolved Gases, LA-2136, pp. 9–13 (September 1957).

Table 5.19. Mass Transfer in the Tantalum-Oxygen-Potassium System at 600°C for 500 hr

Oxygen in Potassium[a]	Oxygen in Tantalum		Weight Change (mg/cm^2)	Tantalum in Potassium (ppm)
(ppm)				
Before Test	Before Test	After Test		After[b] Test
100	40	21	− 0.031	2200
600	40	23	− 0.039	6300
1000	40	18	− 0.088	4200
1400	40	24	− 0.30	5700
3400	40	25	− 0.92	12,000
100	600	190	− 0.57	3000
100	1300	1300	+ 0.50	2300

[a]Oxygen added as K_2O to potassium containing 100 ppm.

[b]Before test the potassium contained < 10 ppm Ta.

The results indicate that the role of oxygen in the tantalum-oxygen-potassium system is similar to that in the niobium-oxygen-potassium system.[14] In all tests but one, oxygen migrated from the tantalum to the potassium, contrary to thermodynamic predictions based on the free energy of binary potassium and niobium oxides. Of particular interest in Table 5.19 is the marked increase in the tantalum content of the after-test potassium brought about by increasing oxygen additions to the potassium. Since all of the potassium was consumed in the analysis of tantalum, the concentration of oxygen in the after-test potassium was not determined. Mass balances, however, indicate that the final oxygen concentration in the potassium in all but one test was about 200 to 300 ppm greater than before test. This oxygen was donated by the tantalum container, which before test contained 200 ppm O.

In the three tests in which the oxygen content of the potassium was 1000 ppm or greater, the tantalum specimens were covered by a dark gray scale. Although this scale appeared visually to be quite thick, diffractometer measurements showed only tantalum with no extraneous peaks.

Fig. 5.39. Tantalum, Which Initially Contained 600 ppm O, After Exposure to Potassium for 500 hr at 600°C. (Unetched.)

The addition of oxygen to the potassium produced no microstructural changes in the tantalum specimens. However, specimens that had been predoped with oxygen exhibited heavy attack. Figure 5.39 shows the microstructure of a specimen that contained 600 ppm O before test. Most of the attack seems to be along grain boundaries and is similar to the attack of niobium by potassium. The microstructure of a specimen containing 1300 ppm O is shown in Fig. 5.40 Again, most of the attack is along grain boundaries. When the specimen is etched, however, transgranular attack is also revealed (Fig. 5.41).

Partitioning of Oxygen Between Potassium and Zirconium and Sodium and Zirconium

Because zirconium is chemically active and interacts with impurities such as O, H, N, and C in alkali metals, it has been widely used

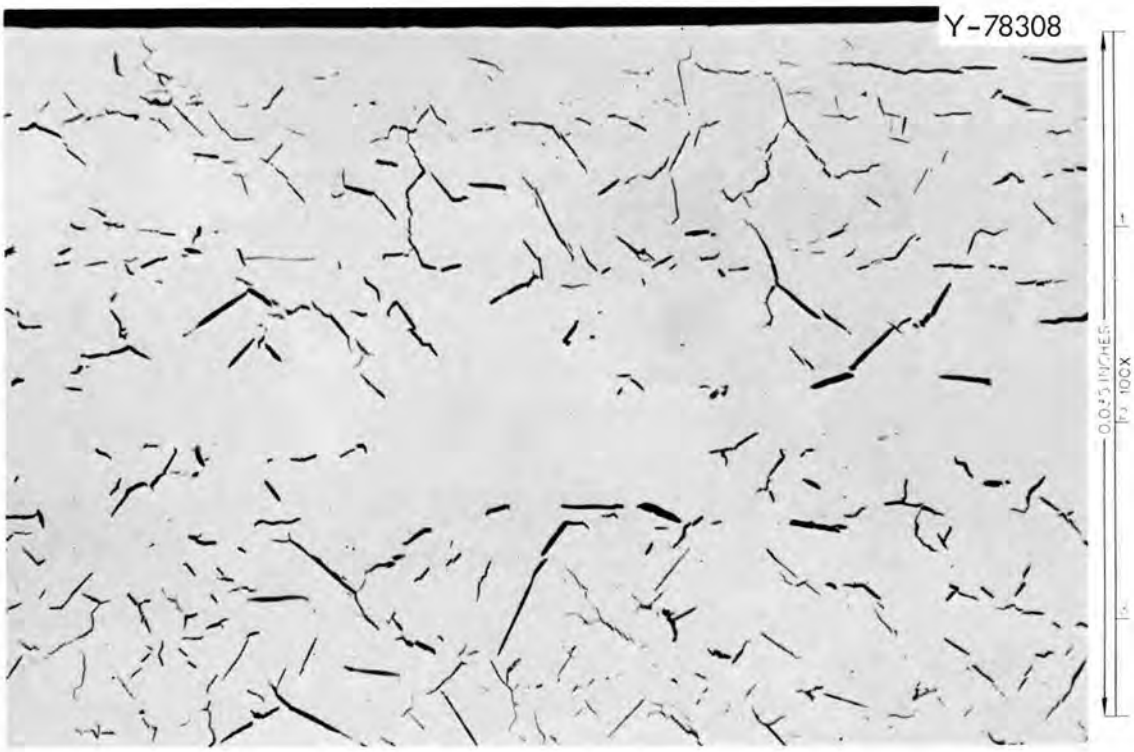

Fig. 5.40. Tantalum, Which Initially Contained 1300 ppm O, After Exposure to Potassium for 500 hr at 600°C. (Unetched.)

Fig. 5.41. Tantalum, Which Initially Contained 1300 ppm O, After Exposure to Potassium for 500 hr at 600°C. Etched in a solution of H_2O, HNO_3, and NH_4HF.

to purify alkali metals. The chemical affinity of zirconium for oxygen in alkali metals is also the basis for the gettering-vacuum-fusion (GVF) technique developed at ORNL[22] to determine the concentration of oxygen in potassium. Recovery experiments showed that in cases where large quantities of oxygen ($\geq$ 100 ppm) were added to potassium or where the potassium had been exposed to niobium at high temperatures, the GVF method was more accurate than either the mercury amalgamation or vacuum distillation methods for oxygen analysis.

The development of the GVF technique required an investigation of the partitioning of oxygen between zirconium and potassium. A series of capsule tests was conducted at 815°C in which zirconium tabs, ranging in thickness from 0.010 to 0.060 in., were exposed to potassium of known oxygen concentration. The movement of oxygen into the zirconium was compared against a diffusion-controlled model that treated the potassium as a stirred solution of limited volume and assumed that a linear relationship was maintained between the concentration of oxygen at the zirconium surface and the oxygen concentration in the potassium. Although this model appeared valid in terms of the effects of time and zirconium thickness on the uptake of oxygen by the zirconium,[22] the equilibrium partition coefficient (κ°) relating the oxygen concentration (in parts per million) at the zirconium surface to that in the potassium was many orders of magnitude smaller than predicted by thermodynamic considerations.

To check the validity of the experimentally determined κ° (on the order of 30), we conducted a subsequent series of capsule tests which, if the experimental value was correct, would have caused oxygen to migrate from the zirconium to the potassium. This did not occur, and the results suggested that under these experimental conditions $\kappa^\circ \gg 30$.

In light of these latter results, we are conducting further studies to determine if $\kappa^\circ_{815°C}$ may actually approach the large value predicted theoretically and what ramifications this may have on the GVF calculations. Simultaneously, we are studying the partitioning of oxygen between zirconium and sodium and evaluating the applicability of the GVF method to analyzing oxygen in sodium.

---

[22] A. P. Litman and J. W. Prados, Electrochem. Technol. 3, 228 (1965).

PART III.

RADIATION DAMAGE TO STRUCTURAL MATERIALS

6. BEHAVIOR OF REFRACTORY MATERIALS UNDER IRRADIATION

G. W. Keilholtz R. E. Moore D. A. Dyslin

Irradiation Damage to Nonfissionable Refractory Materials

The main objective of this task is to determine the changes in properties of high-temperature materials that result from their exposure to very large doses of fast neutrons. Carbides, nitrides, and silicides of refractory metals (Ti, Zr, Nb, Ta, W) in the form of solid cylindrical compacts 1/2 by 1/2 in. are being investigated. The specimens are irradiated in the ETR at 300 to 1100°C to fast neutron doses to about 5.4×10^{21} neutrons/cm^2 (> 1 Mev). Changes in the structural integrity, density, microstructures, and lattice parameters of these materials are determined as functions of neutron dose, flux, and irradiation temperature. From this work should emerge an understanding of fast neutron damage mechanisms that should be useful in reactor design and may make it possible to produce materials with greater neutron resistance.

Refractory Metal Carbides

Since the monocarbides of the refractory metals (e.g., Ti, Zr, Nb, Ta, and W) have melting points that are among the highest known, they have potential uses as components of high-temperature nuclear reactors and thermionic converters. The stability of carbides during neutron irradiation is being investigated with specimens that are solid cylinders 1/2 by 1/2 in. of each of the five carbides made by three processes: (1) hot-pressing, (2) slip-casting and sintering, and (3) explosion-pressing and sintering.

Low-Temperature Experiment. — One of the most interesting results[1] of the low-temperature (300–700°C) irradiations concerned the volume changes. There was an initial expansion to a maximum value and then a shrinkage at higher neutron doses. The data are plotted in Fig. 6.1.

---

[1]G. W. Keilholtz, R. E. Moore, and M. F. Osborne, Nucl. Appl. 4, 330 (1968).

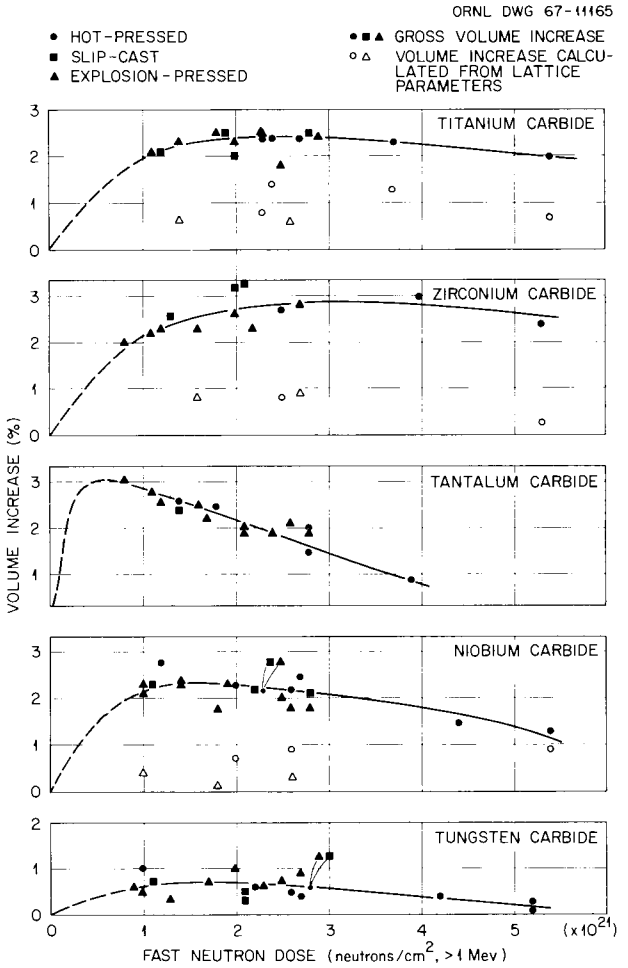

Fig. 6.1. Gross Volume Increase and Volume Increase Calculated from Lattice Parameters of Monocarbides of Ti, Zr, Ta, Nb, and W, Irradiated at Low Temperatures (300 to 700°C) as a Function of the Fast Neutron Dose.

Our attempts to explain the swelling-shrinkage phenomenon have led us to postulate the following mechanism:

1. Each fast neutron that strikes an atomic nucleus in the original crystal lattice of a carbide produces an average of N_d displaced atoms through a cascading process.

2. The regions of N_d displaced atoms, called primary disordered regions, are of much lower density than the original crystal lattice and are partially disordered.

3. Fast neutrons striking atomic nuclei in the primary disordered regions anneal these regions to produce regions of higher density with a greater degree of ordering called secondary disordered regions. We assume, however, that neutron annealing alone will not produce nearly complete ordering such as may occur during thermal annealing.

Assuming that thermal annealing is insignificant at 300 to 700°C in the low-temperature carbide irradiations, we derived a volume expansion equation based on the postulated mechanism:

$$\Delta V/V = (K_2 - 1) - (K_2 - 1)\, e^{-\bar{\sigma}_s N_d(\phi t)} + (K_1 - K_2)\, \bar{\sigma}_s N_d(\phi t)\, e^{-\bar{\sigma}_s N_d(\phi t)} \quad . \quad (6.1)$$

where

$\Delta V/V$ = fractional volume increase,

ϕt = fast neutron dose,

K_1 = density of original crystalline material/density of primary disordered regions,

K_2 = density of original crystalline material/density of secondary disordered region,

$\bar{\sigma}_s$ = average scattering cross section for atoms of the carbides for fast neutrons of the neutron energy spectrum,

N_d = average number of displaced atoms per collision of a fast neutron with an atomic nucleus.

Constants in the equation were evaluated from the data for niobium carbide as follows:

$K_1 = 1.055,$

$K_2 = 1.01,$

$\bar{\sigma}_s N_d = 8.15 \times 10^{-22}.$

The theoretical curve obtained from the equation is shown with the data plotted in Fig. 6.2. The fact that the derived equation fits the data with evaluated constants that are not physically unrealistic provides some confidence in the validity of the mechanism. We made several simplifying assumptions in deriving the equation, but the model will be refined and extended in future work with the aim of deriving a general equation that can predict high-dose neutron damage to refractory materials.

High-Temperature Experiment. — Hot-pressed and slip-cast specimens of the five carbides were irradiated in the ETR at 1000 to 1100°C (ref. 2) to fast (> 1 Mev) neutron doses from 1.5 to 4.8×10^{21} neutrons/cm^2.

---

[2]G. W. Keilholtz and R. E. Moore, Reactor Chem. Div. Ann. Progr. Rept. Dec. 31, 1967, ORNL-4229, p. 142.

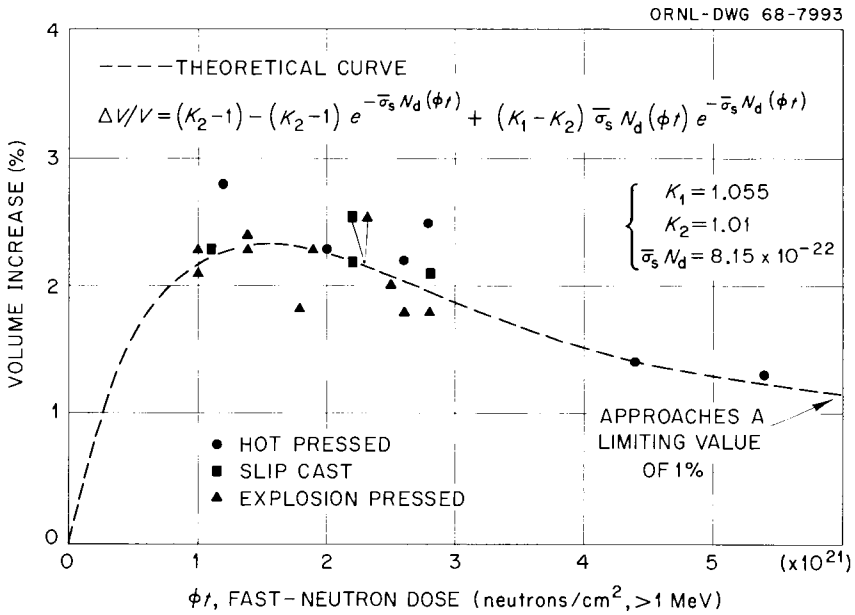

Fig. 6.2. Gross Volume Increase of Niobium Carbide Irradiated at Low Temperatures (300 to 700°C) as a Function of the Fast-Neutron Dose with a Theoretical Curve Based on a Postulated Damage Mechanism.

An in-reactor annealing effect on gross damage and dimensional changes at high temperatures is apparent when results are compared with those from the low-temperature irradiations. Virtually no gross damage occurred to the carbide specimens irradiated at 1000 to 1100°C. Also, volume expansion was much less at high temperature than at low temperature, as can be seen in Fig. 6.3. In fact, the carbides of Ta, Nb, and W shrank to less than their preirradiated volumes. X-ray diffraction examinations of the carbides irradiated at high temperature revealed no lattice parameter expansion, but there is line broadening that indicates that neutron damage is not completely annealed out.

Shrinkage to less than preirradiated volume is probably a consequence of the grains within the specimens being originally of less than theoretical density. Out-of-reactor tests duplicating the thermal history of the irradiation showed no volume changes, so the in-reactor annealing process must involve both neutron irradiation and thermal effects. The shrinkage can be understood if thermal annealing converts regions of partial disorder (assumed to be present in the postulated mechanism for low-temperature irradiation) into well-crystallized material closer to theoretical density than the original crystals. We plan to test this theory with out-of-reactor annealing experiments in which specimens irradiated at low temperature will be heated at high temperature to find whether dimensions and lattice parameters shrink to values observed in high-temperature irradiations.

Results of postirradiation examinations of explosion-pressed carbides irradiated at 1000 to 1100°C are still being analyzed; replication electron microscopy of carbides is still in progress.

Refractory Metal Nitrides

The stability of commercially procured specimens of the nitrides of Zr, Ti, Ta, and Nb toward fast neutrons is being investigated. The specimens are solid cylinders, nominally 1/2 by 1/2 in. The impetus in the nitride study stems from the potential uses of nitrides as high-temperature structural materials and from the interest in uranium nitride fuel in the LMFBR program.

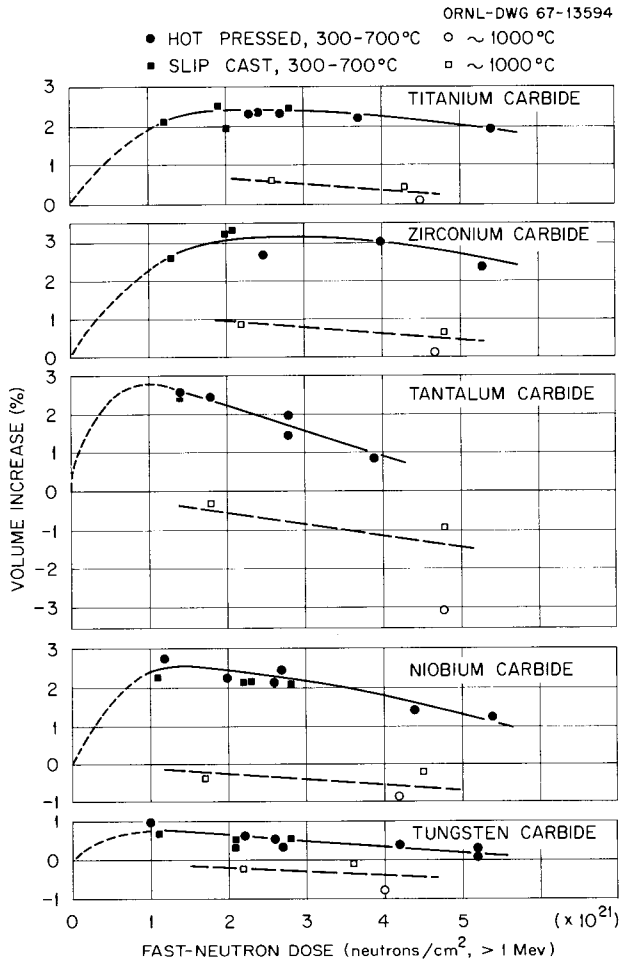

Fig. 6.3. Gross Volume Increase of Monocarbides of Ti, Zr, Ta, Nb, and W as a Function of the Fast Neutron Dose.

Low-Temperature Experiment (about 150°C). – The results[3] of low-temperature irradiation showed that the nitrides of titanium and niobium have some promise as radiation-resistant high-temperature materials. These nitrides generally withstood fast neutron doses to about 3.8×10^{21} neutrons/cm^2 (> 1 Mev), though severe fracturing occurred at higher doses.

High-Temperature Experiment (1000 to 1100°C). – Specimens from the same batches of nitrides that were irradiated at about 150°C were irradiated at high temperatures (1000 to 1100°C) to determine whether stability could be improved by in-reactor annealing. Postirradiation examinations are now in progress.

Refractory Metal Silicides

Commercially procured disilicides of Zr, Ti, Ta, and W in the form of solid cylinders 1/2 by 1/2 in. are being investigated to determine stability toward fast neutrons.

Low-Temperature Experiment (about 150°C). – Results of this experiment have been reported.[3] The disilicides of zirconium and titanium were generally undamaged to a dose of about 2×10^{21} neutrons/cm^2 (> 1 Mev), but severe fracturing occurred at higher doses. Tantalum disilicide fractured at doses of 1.5×10^{21} neutrons/cm^2 and above. Tungsten disilicide fractured at all doses above 0.4×10^{21} neutrons/cm^2. The silicides expanded very little (0.3 to 1.0%) in volume during irradiation.

High-Temperature Experiment (1000 to 1100°C). – The same silicides have been irradiated at 1000 to 1100°C to determine whether in-reactor annealing will improve their radiation resistance. Postirradiation examinations are in progress.

---

[3]G. W. Keilholtz and R. E. Moore, Reactor Chem. Div. Ann. Progr. Rept. Dec. 31, 1967, ORNL-4229, p. 143.

Effects of Irradiation on LMFBR Fuels

The objective of this task is to obtain information needed in the development of fuels for the LMFBR in coordination with other ORNL fuels and materials programs.

The Metals and Ceramics Division is preparing depleted fuel specimens for experiments designed to determine the effect of the (n,α) reaction on nitride fuels.

7. FAST-NEUTRON IRRADIATION EFFECTS ON ELECTRICAL INSULATORS

G. W. Keilholtz R. E. Moore D. A. Dyslin

The purpose of this program is to determine the effects of fast neutrons on the mechanical, physical, and electrical properties of materials suitable for use as electrical insulators in nuclear-powered thermionic converters. The main effort is on Al_2O_3 ceramics because their fabrication is well developed and because irradiation results obtained to date are encouraging. Property changes are determined as a function of neutron dose, flux, temperature, and neutron energy over the range of conditions applicable to realistic operation of thermionic converters. A summary of the irradiation schedule is shown in Table 7.1.

Table 7.1. Irradiation Schedule Summary

Experiment Number	Specimens	Irradiation Temperature (°C)	Neutron Dose (neutrons/cm^2) (> 1 Mev)	Irradiation Dates	
				In	Out
			$\times 10^{21}$		
37	Si_2ON_2, Al_2O_3 (25 μm), MgO	150	0.7–4	10-67	11-68
38	Three commercial types of Al_2O_3 (solids and shells)	600, 800, 1100	0.3–1.8	1-68	9-68
39	Three commercial types of Al_2O_3 (solids and shells)	600, 800, 1100	1–5	1-68	5-69
40	Trilayer units	600, 800, 1000, 1100	0.4–2	8-68	3-69
41	UC-UN depleted fuel specimens	1000	0.5–2.7	10-68	4-69
42	Trilayer units	600, 800, 1100	0.4–2	1-69	7-69
43	Si_2ON_2, Al_2O_3	600, 800 1100	0.7–4	3-69	4-70
EBR-II-1	Three commercial types of Al_2O_3 (solids and shells)	800	0.4–2	11-68	7-69

General Survey of Fast-Neutron Effects on Electrical Insulators

This task has the objectives of determining the effects of fast neutrons on a number of materials that have the properties required for use as thermionic insulators and establishing neutron damage mechanisms. The specimens are irradiated in the form of solid cylinders nominally 1/2 by 1/2 in. Although Al_2O_3 has dominated the task, other oxides such as BeO, MgO, and Y_2O_3 have been investigated. The list of materials has been expanded to include a new ceramic, silicon oxynitride (Si_2ON_2), which is reported to have an electrical resistivity comparable to that of Al_2O_3. Mixed oxides may be added to the program in the future.

High-density (99.8% of theoretical), large-grain (25 μm), translucent α-Al_2O_3 has been irradiated over the fast (> 1 Mev) neutron dose range 0.6 to 5.2×10^{21} neutrons/cm^2 between 300 and 600°C. The results[1] showed almost no fracturing of specimens that had received doses less than 2×10^{21} neutrons/cm^2, but doses above 3×10^{21} neutrons/cm^2 produced extensive fracture. The immediate cause of the fracturing appears to be grain-boundary separation, which begins at a dose of approximately 2.3×10^{21} neutrons/cm^2 and becomes progressively worse with increasing dose.

Specimens were irradiated at higher temperatures (700 to 1000°C) to determine whether in-reactor annealing would extend the useful life of Al_2O_3 as a thermionic insulator beyond a fast-neutron dose of 2 to 3×10^{21} neutrons/cm^2 (ref. 2). The results were encouraging, but more irradiations are needed to define completely the effect of temperature on property changes. A summary of gross damage effects at both low and high temperatures is presented in Table 7.2. The volume expansion at 1000°C was less than that at lower temperatures (300 to 600°C), but the specimens irradiated at 700 and 800°C expanded more than the low-temperature specimens did (Fig. 7.1). The question of whether the

---

[1]G. W. Keilholtz and R. E. Moore, Nucl. Appl. 3, 686 (1967).

[2]G. W. Keilholtz and R. E. Moore, Reactor Chemistry Div. Ann. Progr. Rept. Dec. 31, 1967, ORNL-4229, p. 144.

Table 7.2. Gross Damage to Irradiated Translucent α-Alumina of 99.8% of Theoretical Density

Fast-Neutron Dose (neutrons/cm^2) (> 1 Mev)	Temperature (°C)	Number of Specimens	Number of Specimens Damaged to Degree Indicated		
			No Damage	Minor Damage[a]	Severe Fracturing[b]
$\times 10^{21}$					
0.6–1.8	300–600	11	10	1	0
1.8–2.8	300–600	10	3	6	1
2.8–5.2	300–600	12	0	3	9
1.1	700	2	2	0	0
3.4	800	2	1	0	1
2.7	1000	2	0	2	0
3.8	1000	2	1	0	1

[a]Short fracture not traversing entire specimen.

[b]Fractures traversing entire specimen.

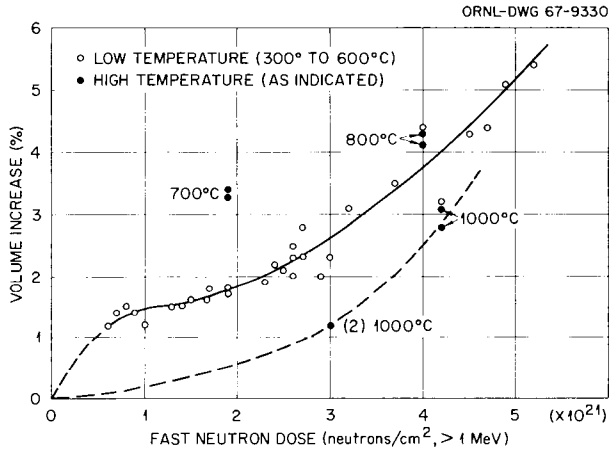

Fig. 7.1. Volume Increase of Irradiated Specimens of Translucent α-Al_2O_3 (99.8% of Theoretical Density) as a Function of the Fast-Neutron Dose.

volume expansion goes through a maximum at temperatures between 600 and 900°C must be answered, for it is pertinent to the design of thermionic converters.

Oxides (Al_2O_3, MgO, Si_2ON_2)

Low-Temperature Experiment (150°C). – A low-temperature (150°C), uninstrumented assembly containing large-grain (25 μm) translucent Al_2O_3, MgO, and Si_2ON_2 is being irradiated in the ETR. The irradiation is being extended beyond the end of FY 1968 to allow a larger neutron dose to be accumulated. The data obtained from the Al_2O_3 specimens can be compared with data for the same large-grain Al_2O_3 at higher temperatures. This should help establish the temperature range in which annealing of neutron damage becomes significant. The results for Si_2ON_2 will aid in evaluating its potential use as a thermionic insulator.

High-Temperature Experiment (600, 800, 1100°C). – A high-temperature experiment that will contain the same types of specimens as the low-temperature (150°C) assembly is being planned. Irradiation will begin in the last half of FY 1969.

Specific High-Density Al_2O_3 Commercial Products Considered for Thermionic Insulators

The objective of this task is to determine the effect of fast neutrons on the commercially available Al_2O_3 products that are being considered for use as thermionic insulators. The experiments are designed to encompass the conditions of neutron dose, flux, and temperature that an electrical insulator would be required to withstand in a practical, nuclear-powered thermionic converter. Three commercial types of Al_2O_3 ceramics in the form of both solid cylinders and thin-walled (0.020 in.) cylindrical shells are being tested in the ETR at three temperatures: 600, 800, and 1100°C. These specimens have small grain size, which should minimize grain boundary separation which has been found to be the precursor of fracture in large-grain Al_2O_3. The irradiation assemblies contain a few large-grain (25 μm) specimens for comparison purposes. The effect of dose rate on property changes is

being determined by running duplicate assemblies in the same flux profile for different time periods. The effects of neutron energy will be evaluated by comparing results from ETR irradiations with results from EBR-II irradiations.

Irradiations of Three Types of Al_2O_3 at 600, 800, and 1100°C in the ETR

Two identical, instrumented assemblies have been undergoing irradiation in the ETR since January 1968. Each contains the following types and numbers of specimens:

Commercial Type	Solid Cylinders (0.493-in. diam)	Cylindrical Shells (0.493-in. diam, 0.020-in. wall)
Coors AD-995	9	7
Wesgo AL-995	11	7
GE Opaque Lucalox	11	7

In addition, six solid cylinders of large-grain, translucent Lucalox were included in each assembly. The specimen arrangement, which is the same for both assemblies, was designed to achieve comparisons of property changes of each type of specimen at each temperature (600, 800, and 1100°C) over comparable flux ranges. Comparisons can be made between solids and shells of each specimen type under comparable conditions.

Short-Term Irradiation. — This assembly is scheduled for removal from the ETR in September 1968. The fast (> 1 Mev) neutron dose range is estimated to be about 0.3 to 1.8×10^{21} neutrons/cm^2.

Long-Term Irradiation. — This assembly will not be removed from the ETR until late in FY 1969.

Irradiation of Three Types of Al_2O_3 at 800°C in the EBR-II

This irradiation has been delayed, but we hope it can be started no later than November 1, 1968. Difficulties in design studies were encountered because of uncertainties about the gamma-heating rate in Row 8 that resulted from a change in the blanket material of the EBR-II. We have decided to circumvent this problem by irradiating simultaneously

several complete sets of specimens whose temperatures will bracket 800°C when capsule parameters are based on the heating rate uncertainty.

Metal-Clad Al_2O_3 Specimens (ETR)

The objective of this task is to test metal-clad Al_2O_3 cylinders under the conditions of neutron flux and temperature expected in operating thermionic converters.

An assembly containing units prepared at other installations has been designed and fabricated. These units consist of cylindrical shells of Al_2O_3 clad with metal on both the outside and the inside or on the outside only. Irradiation of this assembly will start about August 1, 1968, and will continue for more than six months. Most of the postirradiation examinations of the units will be carried out at ORNL.

Irradiation of Improved Al_2O_3

The results of irradiations of commercially available Al_2O_3 ceramics should provide information on the properties, such as grain size, density, porosity, and purity, that would provide maximum radiation resistance. The objective of this task is to prepare and irradiate improved Al_2O_3 specimens. No progress on this task will be made until specimens now being irradiated have been examined and the results have been evaluated.

8. MECHANICAL PROPERTIES RESEARCH AND LMFBR CLADDING AND STRUCTURAL MATERIALS DEVELOPMENT

C. J. McHargue J. R. Weir, Jr.

Work in this program includes studies of the high-temperature irradiation embrittlement and other technologically important aspects of radiation damage to fuel cladding materials at high neutron fluence. The work centers around types 316 and 304 stainless steel, Incoloy 800, and Hastelloy N and the effects of titanium concentration in these alloys on radiation damage. Associated with the program are studies of the effects of tubing fabrication variables on the properties of types 304 and 316 stainless steel and related compositions.

Irradiation Damage to Types 316 and Titanium-Modified Type 316 Stainless Steel

E. E. Bloom J. R. Weir, Jr.

Since types 316 and 316L stainless steel are potential cladding materials for liquid-metal-cooled fast-breeder reactors, we need to understand the effects of irradiation on their tensile and creep-rupture properties. The alloys are similar in composition to the more commonly used type 304 stainless steel alloy (which contains 18 wt % Cr and 10 wt % Ni), with the exception that they contain approximately 2.0 to 3.0 wt % Mo. Adding molybdenum improves the creep-rupture properties at elevated temperatures. Barnby[1] has attributed the improved strength to the precipitation of small $(Fe,Cr)_{23}C_6$ particles on dislocations during creep and has shown that creep strength was decreased by aging treatments that removed carbon from solution before testing. Our investigation of the effects of neutron irradiation on the mechanical properties

[1]J. T. Barnby, J. Iron Steel Inst. 204, 23 (1966).

involves tensile and creep-rupture tests on specimens in three conditions: annealed, annealed and irradiated, and annealed and aged at the irradiation temperature for the irradiation time. Variables under investigation include preirradiation heat treatment, irradiation temperature, and post-irradiation test conditions, such as test temperature and strain rate.

A second area of this program is an attempt to improve the mechanical properties of an alloy that has the basic composition of type 316 stainless steel by adding small amounts of titanium. Initially this involves an investigation of the effects of up to 0.5 wt % Ti on the tensile and creep-rupture properties in both the unirradiated and irradiated conditions.

Results on Standard Types 316 and 316L Stainless Steel

The chemical compositions of the two heats of material being investigated are listed in Table 8.1. There was a significant decrease in ductility for specimens irradiated to approximately 9×10^{20} neutrons/cm^2 (thermal) and 7×10^{20} neutrons/cm^2 (> 1 Mev) between 550 and 750°C and tested at 550, 650, and 750°C. The decrease in tensile ductility was independent of irradiation temperature over the range investigated.

Table 8.1. Chemical Compositions of Types 316 and 316L Stainless Steel

Element	Composition, wt %	
	316	316L
Carbon	0.068	0.02
Chromium	17.2	16.9
Nickel	12.5	12.7
Molybdenum	2.06	2.7
Magnesium	1.9	2.3
Silicon	0.5	0.58
Phosphorus	0.039	0.013
Sulfur	0.004	0.015
Boron	0.0005	

A summary of the creep-rupture data from tests at 650°C for standard types 316 and 316L stainless steel is listed in Table 8.2. It indicates that for type 316 stainless steel there is a reduction in rupture life and ductility due to irradiation and that the changes in properties are sensitive to the irradiation temperature. For the specimens irradiated at 550°C and tested at 650°C, there appears to be no effect on the creep rate, but there is a large reduction in ductility and, thus, in rupture life. An exception is the specimen that was post-irradiation tested at 30,000 psi. Its rupture life was 15 hr as compared to 180 hr for the specimen tested in the annealed condition and 437 hr for the thermal control specimen. It is possible that this specimen failed before second-stage creep was established and that the measured creep rate is thus not a true, second-stage creep rate. Note that the creep rate of the specimen aged 2000 hr at 550°C is essentially the same as that of the specimen that was tested in the annealed condition; this indicates that thermal aging effects are negligible. As the irradiation temperature is increased to 650 or 750°C, there is an increase in the postirradiation creep rate and ductility. In this case, however, there is also an increase in the creep rate of thermal control specimens that indicates that a thermal aging phenomenon is occurring.

Stress-rupture results for type 316L stainless steel irradiated and tested at 650°C are also listed in Table 8.2. It appears that the 0.02 wt % C alloy is significantly weaker, both in terms of rupture life and creep rate, than the 0.068 wt % C alloy. Since a boron analysis has not been performed on the low-carbon alloy, a direct comparison of ductility values is difficult.

Results on Titanium-Modified Types 316 and 316L Stainless Steel

Specimens of several vacuum-induction-melted heats of types 316 and 316L stainless steel containing various amounts of titanium (up to 0.5 wt %) have been irradiated at 650°C to approximately 9×10^{20} neutrons/cm^2 (thermal) and 7×10^{20} neutrons/cm^2 (> 1 Mev). Boron content ranged between 4 and 10 ppm, and the carbon content was approximately 0.02 for the low-carbon series and 0.05 for the high-carbon series. The effect of titanium on the stress-rupture ductility

Table 8.2. Creep-Rupture Properties of Types 316 and 316L Stainless Steel at 650°C

Heat Treatment and/or Irradiation Conditions	Stress (psi)	Rupture Life (hr)	Creep Rate (%/hr)	Total Elongation (%)	Reduction in Area (%)
		Type 316 Stainless Steel			
Annealed 1 hr at 1050°C	40,000	28	0.35	36.2	39.2
	35,000	91	0.14	29.6	50.4
	32,500	117	0.029	25.1	44.9
	30,000	180	0.024	54.5	32.9
	27,500	1732	0.0046	31.4	52.6
	25,000	1311	0.0069	30.9	57.8
Annealed 1 hr at 1050°C, irradiated approximately 2000 hr at 550°C	30,000	15	0.085	3.2	9.0
	25,000	252	~ 0.005	2.7	14.3
	20,000	5127	~ 0.00012	8.7	13.4
Annealed 1 hr at 1050°C plus 2000 hr at 550°C	30,000	437	0.030	33.0	62.0
	25,000	2305	0.0017	29.2	55.2
Annealed 1 hr at 1050°C, irradiated 2000 hr at 650°C	35,000	25	0.58	26.7	32.9
	30,000	199	0.032	13.8	26.4
Annealed 1 hr at 1050°C plus 2000 hr at 650°C	35,000	20	1.13	52.2	71.0
	30,000	146	0.14	37.5	75.2
Annealed 1 hr at 1050°C, irradiated approximately 2000 hr at 750°C	25,000	92	0.12	14.8	17.4
	20,000	137	0.064	9.3	6.7
	20,000	524	0.024	16.7	22.1
		Type 316L Stainless Steel			
Annealed 1 hr at 1050°C, irradiated approximately 2000 hr at 650°C	30,000	14	0.13	2.4	11.6
	25,000	216	0.037	9.5	12.9
	22,500	48	0.027	2.5	5.8
	20,000	370	0.009	5.4	8.4

at 650°C and 30,000 psi stress is shown in Fig. 8.1. For each carbon content there is a significant improvement in the ductility of both thermal control and irradiated specimens for all titanium contents. In the case of the 0.05 wt % C series the highest ductility occurred at 0.23 wt % Ti. However, since no alloy containing between 0.05 and 0.15 wt % Ti was available, it is not certain that maximum ductility does not occur at a somewhat lower titanium level. Results on the 0.02 wt % C series are not complete: specimens containing 0.45 wt % Ti

ORNL-DWG 68-10870

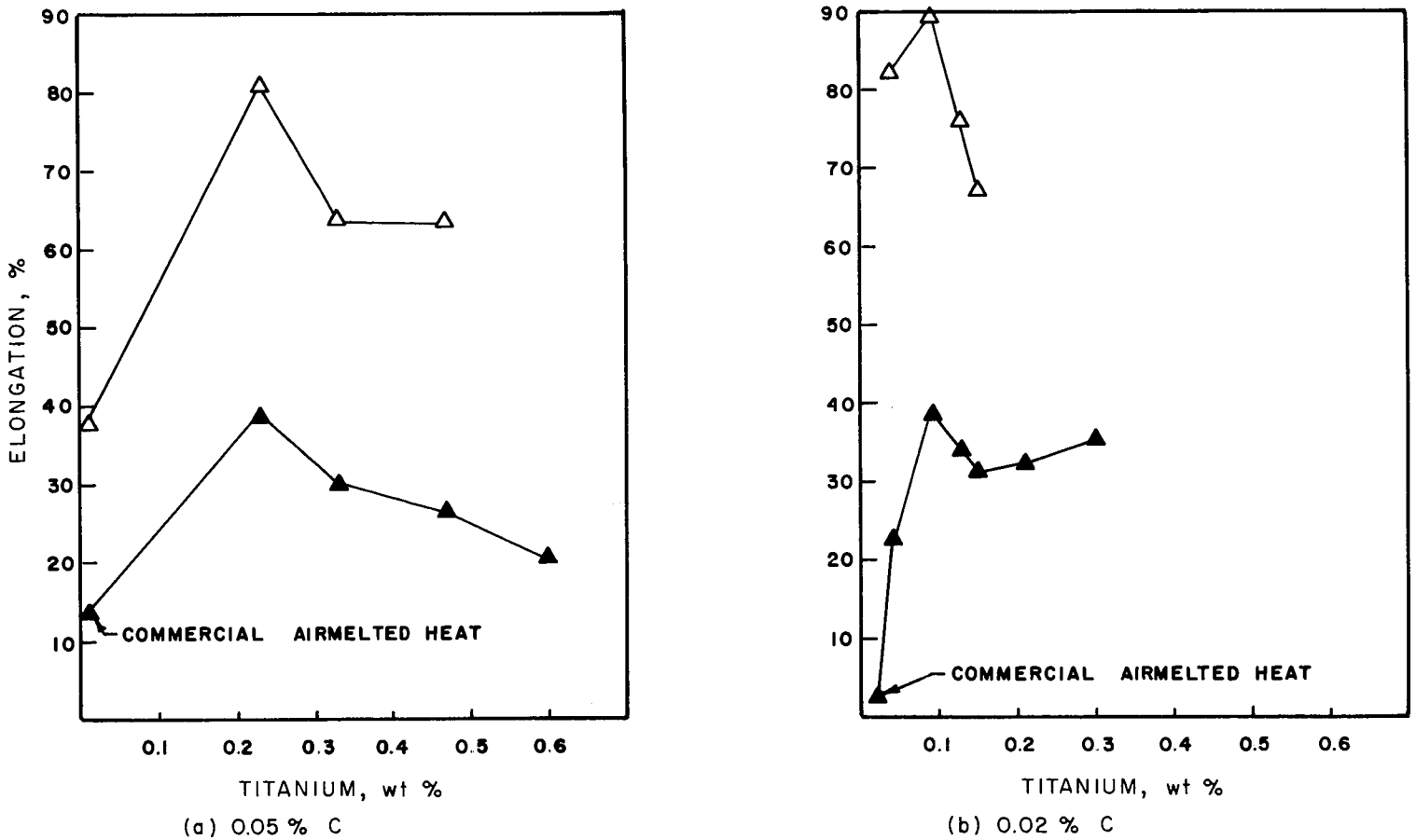

△ ANNEALED 1 hr AT 1050° C, AGED 2000 hr AT 650°C

▲ ANNEALED 1 hr AT 1050° C, AND IRRADIATED APPROXIMATELY 2000 hr AT 650° C, 9×10^{20} NEUTRONS/cm^2 (THERMAL) AND 7×10^{20} NEUTRONS/cm^2 (> 1 Mev)

Fig. 8.1. Effect of Titanium on the Creep-Rupture Ductility of Type 316 Stainless Steel Tested at 650°C and 30,000 psi Stress.

remain to be tested. All of the low-carbon alloys containing between 0.1 and 0.3 wt % Ti have had postirradiation ductilities in excess of 30% elongation.

Metallographic examination of tested specimens is under way. Figure 8.2 shows the fracture that occurred in type 316 stainless steel that was annealed 1 hr at 1050°C and tested at 650°C and 30,000 psi. The fracture is predominantly intergranular, and large voids or cracks have formed on grain boundaries normal to the applied load. In comparison, Fig. 8.3 shows the fracture that occurred in type 316 plus 0.23 wt % Ti stainless steel after annealing at 1050°C and testing at 650°C and 35,000 psi. In this case, the fracture is a transgranular shear fracture, and there was essentially no void formation during the

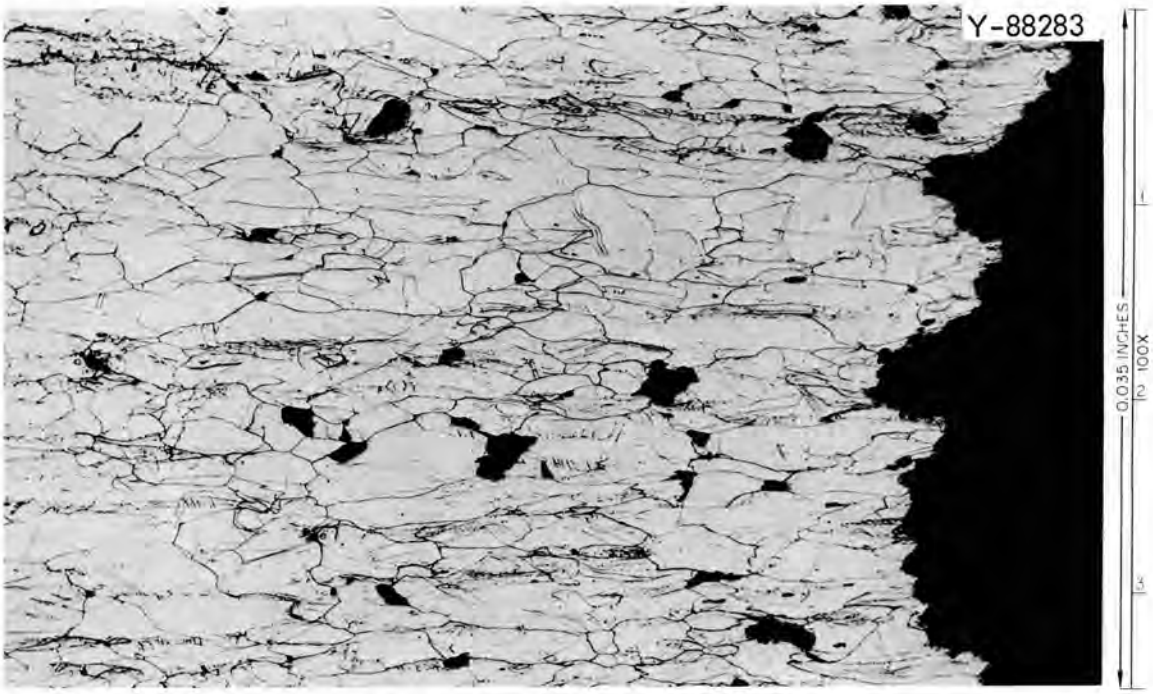

Fig. 8.2. Fracture of Type 316 Stainless Steel Annealed 1 hr at 1050°C and Tested at 650°C and 30,000 psi. Rupture life 91 hr, elongation 29.6%.

Fig. 8.3. Fracture of Type 316 Stainless Steel Plus 0.23 wt % Ti Stainless Steel Annealed 1 hr at 1050°C and Tested at 650°C and 35,000 psi. Rupture life 582 hr, elongation 47.0%.

test. Similar observations have been made in titanium-modified type 304 stainless steel and, possible mechanisms for the change in fracture mode have been discussed.[2]

Mechanical Properties of Titanium-Modified Type 304 Stainless Steel

E. E. Bloom J. R. Weir, Jr.

Evaluation of the mechanical properties of two 1500-lb vacuum-induction-melted heats of titanium-modified types 304 and 304L stainless steel is continuing. The compositions of these two alloys are listed in Table 8.3.

---

[2]E. E. Bloom and J. R. Weir, Jr., "Development of Austenitic Stainless Steels with Improved Resistance to Elevated-Temperature Irradiation Embrittlement," paper presented at ASTM Annual Meeting, June 26–28, 1968, San Francisco, California. To be published in the proceedings.

Table 8.3. Compositions of Titanium-Modified Types 304 and 304L Stainless Steel

Element	Composition, wt %	
	Heat 3756 Type 304L	Heat 60508 Type 304
Carbon	0.012	0.05
Chromium	19.5	19.0
Nickel	11.2	10.0
Titanium	0.19	0.21
Manganese	1.0	0.65
Silicon	0.05	0.8
Phosphorus	0.006	0.013
Sulfur	0.013	0.002
Boron	0.0003	0.0027
Nitrogen		
Total	0.006	0.009
Soluble		0.003

Specimens of heat 60508, which is type 304 stainless steel containing 0.2 wt % Ti, have been irradiated for about 1000 hr at 650°C. Neutron fluences for this experiment were approximately 2.6×10^{20} neutrons/cm^2 (thermal) and 2×10^{19} neutrons/cm^2 (> 1 Mev). On the basis of the initial boron content, 0.0027%, we calculated that approximately 19×10^{-6} atom fraction helium was produced during the irradiation. Figure 8.4 shows the effect of this irradiation on the stress-rupture properties at 704°C. Available results indicate that the rupture life of unirradiated specimens annealed 1 hr at 925°C is only one-eighth that of specimens annealed 1 hr at 1040°C. For both annealing treatments there is a reduction in rupture life due to irradiation: the rupture life of the 1040°C anneal appears to be reduced by about a factor of 4 to 5; the rupture life of the 925°C anneal is reduced by less than a factor of 2. Elongation as a function of rupture life is shown in Fig. 8.5. For specimens both annealed and irradiated, the ductilities are independent of annealing temperature. Irradiation causes a large reduction in ductility; however, the ductility is approximately constant at 9 to 12% for rupture lives between 10 and 1500 hr.

ORNL-DWG 68-10868

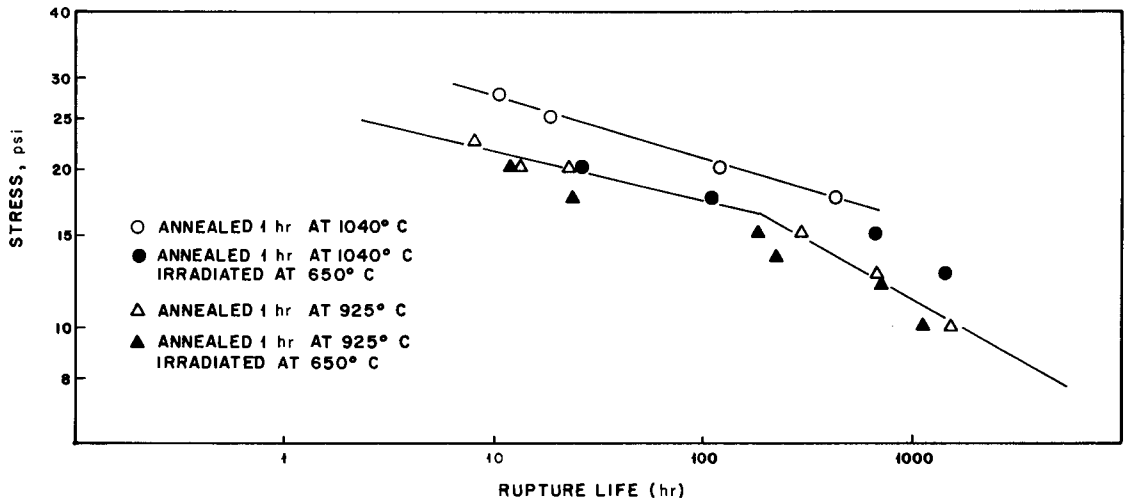

Fig. 8.4. Effect of Irradiation on the Stress-Rupture Properties of a 1500-lb Vacuum-Induction-Melted Heat of Type 304 Stainless Steel Plus 0.2 wt % Ti at 704 °C.

ORNL-DWG 68-10869

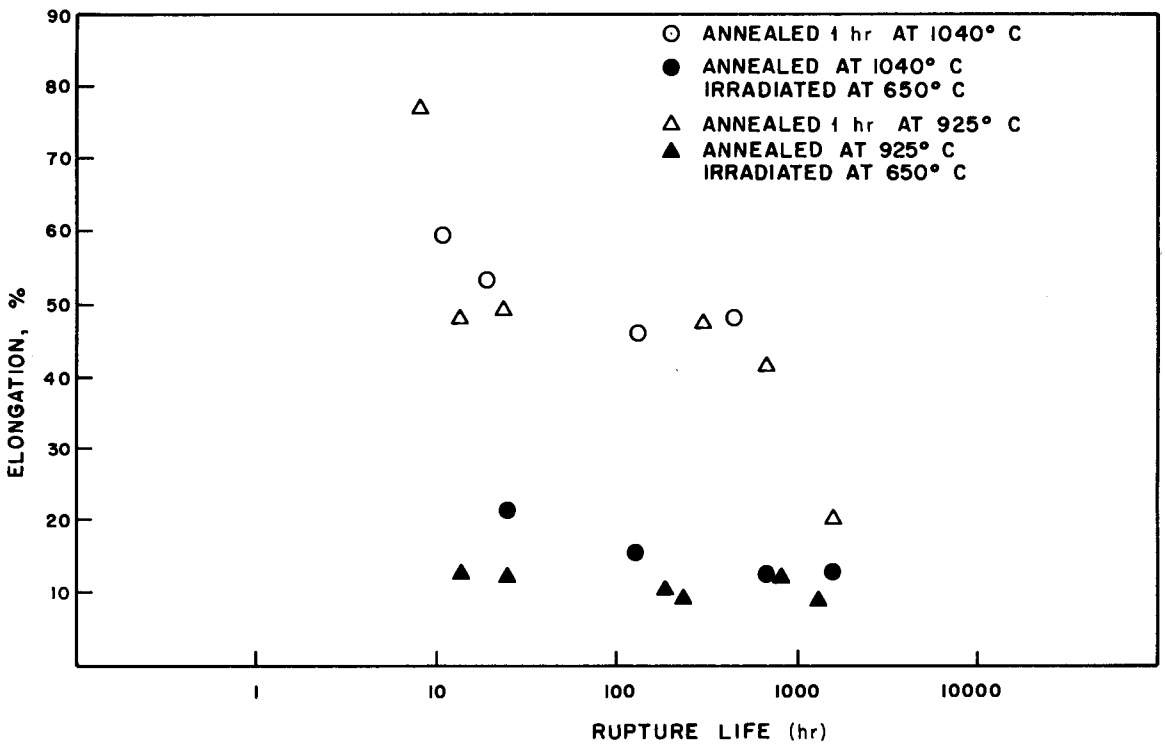

Fig. 8.5. Effect of Irradiation on the Ductility of Type 304 Stainless Steel Plus 0.2 wt % Ti.

Electron Microscope Evaluation of Titanium-Modified Type 304L Stainless Steel

G. T. Newman

A type 304L stainless steel with improved resistance to irradiation embrittlement has been developed by making small additions of titanium to the standard alloy. Optimum improvement in ductility has been recorded with alloys containing 0.2 wt % Ti, solution treated at 925°C for 1 hr. The role of titanium in improving postirradiation ductility is being studied by electron microscopy. The solution treatment resulted in a fine matrix precipitation in contrast to the grain boundary precipitation obtained at higher temperatures (> 1000°C). Larger angular precipitates (1/2 to 1 μ) were also present and were assumed to be the Ti(C,N) complexes observed as a yellow phase by optical metallography. Aging studies showed that the density of the fine precipitate increased with increase in aging time, but the size of the individual precipitates (about 500 A after aging 100 hr at 700°C) appeared relatively stable. Electron microprobe analysis of the larger precipitates obtained by carbon-extraction techniques revealed evidence of sulfur as well as titanium (carbon and nitrogen cannot be detected by this microprobe) in alloys aged at 850°C and higher, suggesting that resolution of the precipitate and segregation of trace impurities may be occurring.

Carbon-extraction techniques are also being applied to a series of alloys nominally containing 0.1, 0.2, 0.3, 0.4, and 0.5 wt % Ti. To date, work on the alloy containing 0.2 wt % Ti has revealed precipitates rich in titanium, titanium plus aluminum, and chromium plus iron. Electron diffraction data on the latter particles (0.2 to 0.4 μ in size) do not agree with those for the most frequently observed carbide in austenitic stainless steels, $(Fe,Cr)_{23}C_6$.

Drawing of Stainless Steel Tubing

G. A. Reimann

Work has continued on the investigation of the production of tubing from titanium-modified grades of types 304 and 304L stainless steel. Tubing has been fabricated from two heats (3756 and 60508) of the modified stainless steel.

Variations applied to the mandrel drawing approach have been limited to the amount of reduction per pass, the amount of reduction between anneals, and the substitution of plug drawing for the final pass.[3]

Approximately 150 ft of tubing 0.250 in. in outside diameter by 0.016 in. in wall thickness from heat 3756 has been submitted for nondestructive testing and property evaluation. About half of this tubing was drawn with two passes (25 to 29% reduction) between anneals, and the rest was drawn with anneals between each pass (14 to 16% reduction). Annealing conditions were 20 min at 1200°C. We have seen no significant differences that can be attributed to the drawing schedule.

The drawing schedule has been modified so that the finished tubing contained 5% cold work after a 1-hr anneal at 925°C before the last pass. The tubing is rather soft at this level of cold work and must be handled carefully to avoid bending and denting. If the tube emerges from the final pass with a slight bend, it is difficult to straighten on existing equipment without losing control of the diameter dimensions. Even though plug drawing is used on the last pass to minimize this problem, a small amount of spiral from reeling the previous pass from the mandrel is still evident.

Several tube shells from Latrobe Heat 60508 are in process for conversion into tubing 0.250 in. in outside diameter by 0.015 in. in wall thickness. This heat differs from heat 3756 in several respects. The chemistry is compared in Table 8.3, and the microstructure is shown in Fig. 8.6. We attempted to dissolve the second phase by heating in

---

[3]G. A. Reimann, "Fabrication of Small-Diameter Stainless Steel Tubing," Metals and Ceramics Div. Ann. Progr. Rept. June 30, 1968, ORNL-4370, Chap. 22.

hydrogen for 16 hr at 1200°C, but at least 25% of the second phase remained after this treatment (Fig. 8.6). Drawing the tubing from the as-extruded condition without attempting to remove the second phase produced no adverse effects, and the second phase disappeared after the equivalent of 6 hr at 1200°C during the drawing schedule.

We have drawn this heat down to tubes 0.387 in. in outside diameter by 0.010 in. in wall thickness.

Several more passes must be made before the final size is reached, but this heat of tubing has shown itself to be more susceptible to longitudinal cracking than heat 3756. The grain size of heat 60508 is somewhat smaller than that of heat 3756, and more nitride particles are present in the Latrobe heat (60508). The longitudinal cracking has been confined to the fromt of the tubes, which are repeatedly swaged for pointing.

The Effect of Cyclotron-Injected Helium on the Creep-Rupture Properties of Type 304 and 0.2% Ti-Modified Type 304L Stainless Steels

R. T. King J. R. Weir, Jr.

The effect of cyclotron-injected helium on the tensile properties of AISI type 304 stainless steel was shown to be qualitatively similar to that of helium produced by $^{10}B(n,\alpha)^{7}Li$ reactions.[4] It was also shown that a 0.2% Ti-modified type 304L stainless steel, which is resistant to radiation-induced high-temperature loss of ductility,[5] is not as severely affected by cyclotron-injected helium as the type 304 stainless steel alloy. However, since the mechanical properties of these materials at elevated temperatures are sensitive to the rate of deformation, it is necessary to know the effects of helium on their creep-rupture properties. We have therefore injected 2.0×10^{-5} atom fraction of helium into sets of specimens of both materials for creep-rupture testing.

---

[4]R. T. King and J. R. Weir, Jr., Quarterly Progress Report: Irradiation Effects on Reactor Structural Materials, February, March, April, 1967, BNWL-455, pp. 11.2–11.5.

[5]W. R. Martin and J. R. Weir, Jr., Solutions to the Problems of High-Irradiation Embrittlement, ORNL-TM-1544 (June 1966).

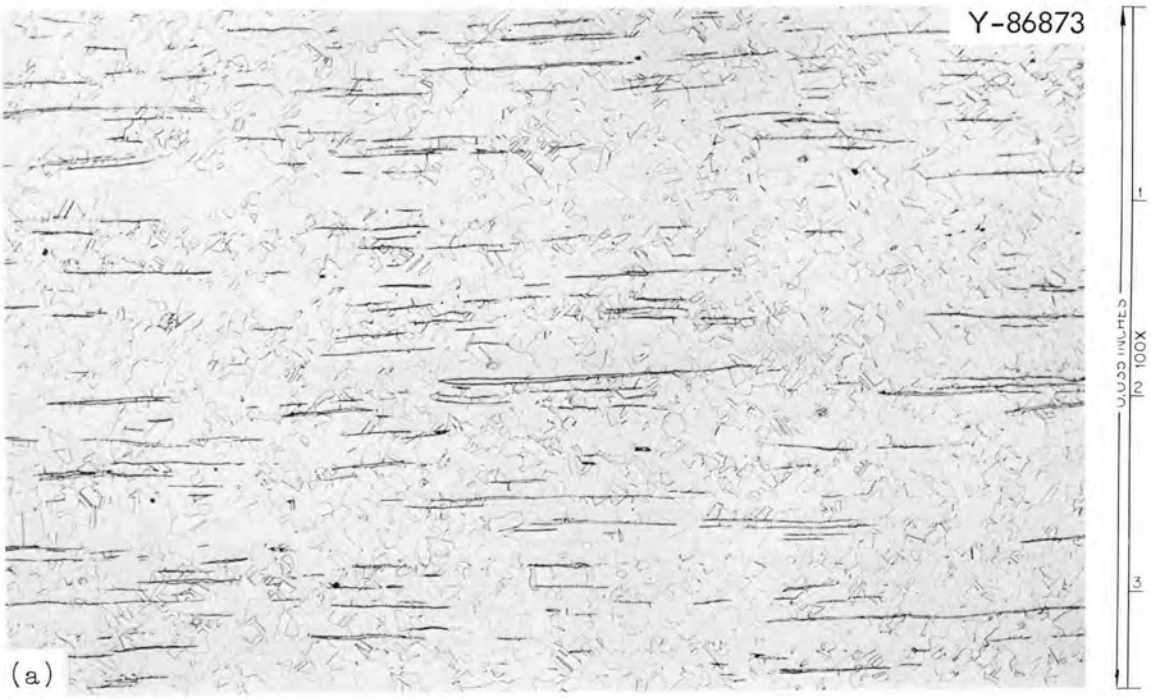

Fig. 8.6. Microstructures of Heat 60508, As Extruded, Comparing Structure (a) Before and (b) After 16 hr at 1200°C Heat Treatment.

Both materials were finish cold-rolled 50% to 0.010 in. thick; specimens were machined to a 0.25-in. gage width and a 0.75-in. gage length, and then annealed for 1 hr at either 1040 or 925°C. The grain sizes produced in the type 304 stainless steel were ASTM 5 and 6, and in the type 304L stainless steel plus 0.2% Ti the grain sizes were ASTM 7 and 8–8 1/2, respectively. Specimens of both materials, in both annealed conditions, were then bombarded with α particles at less than 200°C to a uniform concentration of 2.0×10^{-5} atom fraction of helium.

We then performed stress-rupture tests under 10 psig of static argon at 600 and 700°C. The stresses were selected to yield rupture times ranging from approximately 1 to 1000 hr. The results of these tests are shown as graphs of strain versus rupture life, and the stresses at which individual tests were run are indicated on the plots (Figs. 8.7 through 8.10).

At 600°C the type 304 stainless steel control specimens annealed at 925°C have consistently higher ductility than those annealed at 1040°C, although the different annealing temperatures do not cause much difference in rupture life (Fig. 8.7). At 700°C the type 304 stainless steel control specimens annealed at 925°C have consistently lower rupture life but higher ductility than those annealed at 1040°C (Fig. 8.8).[6]

The cyclotron-injected 2.0×10^{-5} atom fraction of helium substantially reduces both the rupture life and ductility of type 304 stainless steel (Figs. 8.7 and 8.8). The loss of ductility is generally greatest at 700°C, since the tendency for intergranular fracture increases with increasing temperature.

The behavior of the control specimens of the titanium-modified type 304L stainless steel is qualitatively similar to that of specimens of the type 304 stainless steel, although at high strain rates there is little effect of annealing on rupture life at 700°C (Figs. 8.9 and 8.10). The rupture life of the titanium-modified type 304L stainless steel alloy is consistently lower than that of the type 304 stainless steel. This may be explained on the basis of reduced solid-solution strengthening and

---

[6]With the exception of specimens tested at 600°C after annealing at 925°C, the strain to rupture tends to decrease with decreasing strain rate, or applied stress.

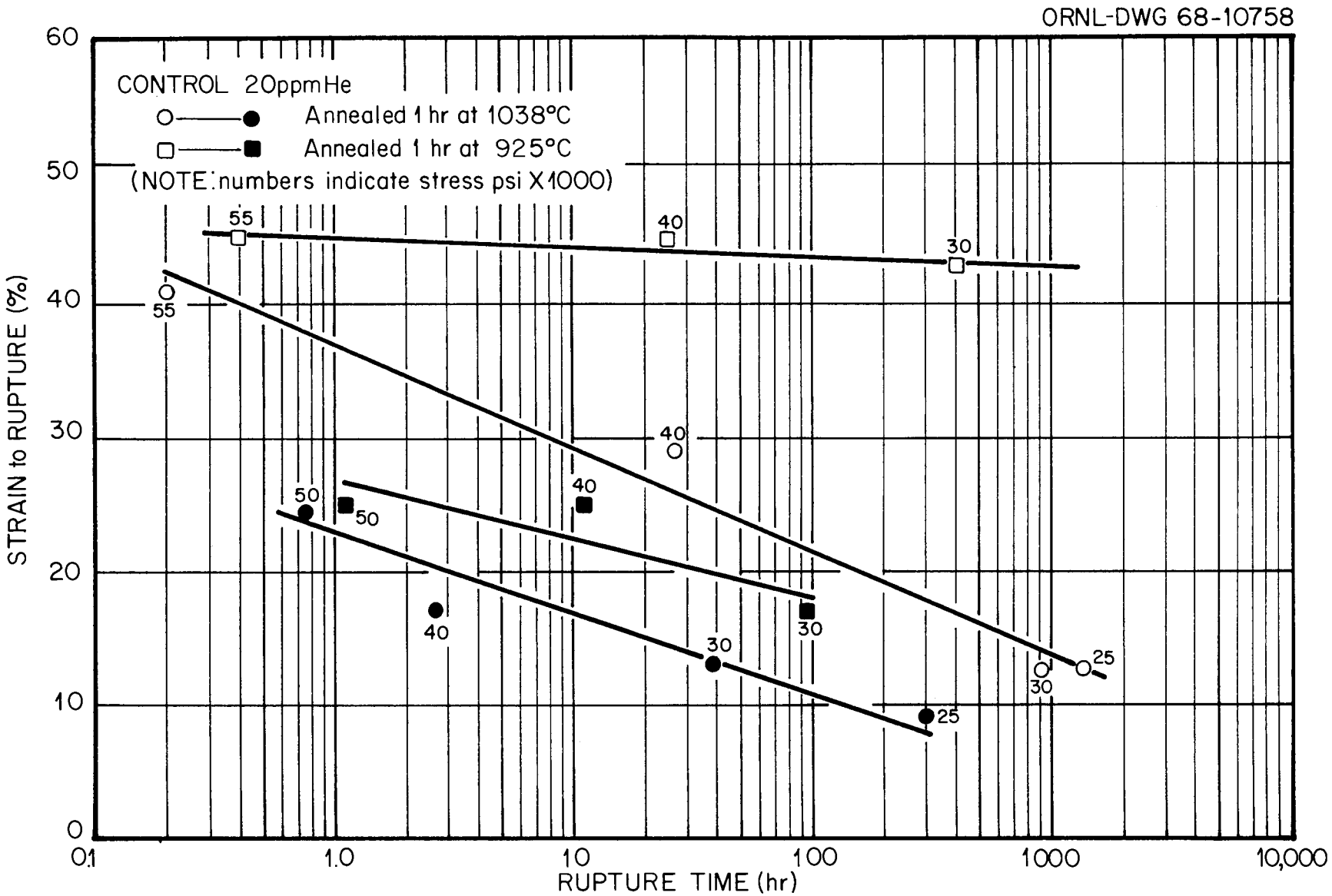

Fig. 8.7. Strain Versus Rupture Time of Type 304 Stainless Steel at 600°C.

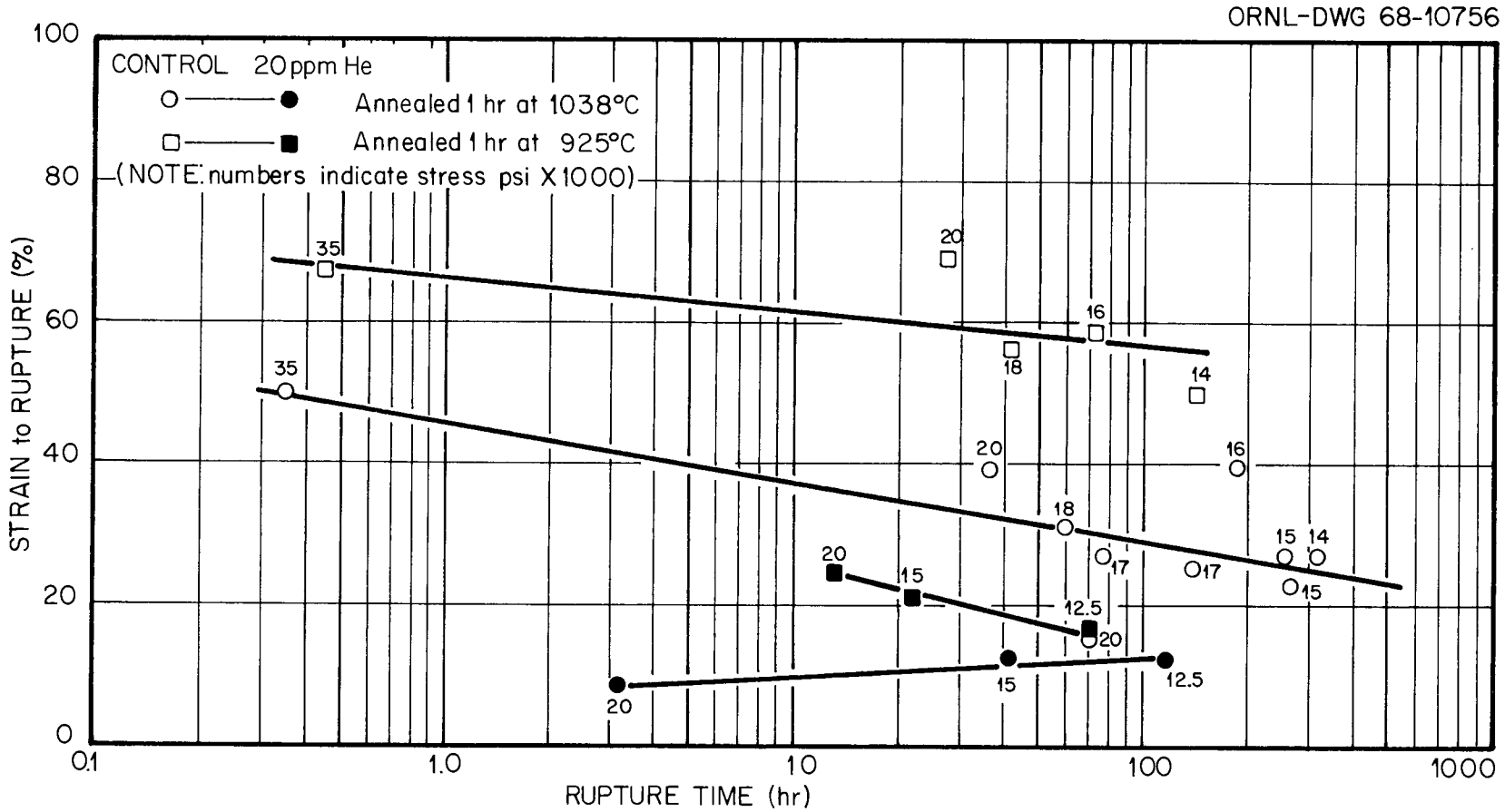

Fig. 8.8. Strain Versus Rupture Time of Type 304 Stainless Steel at 700°C.

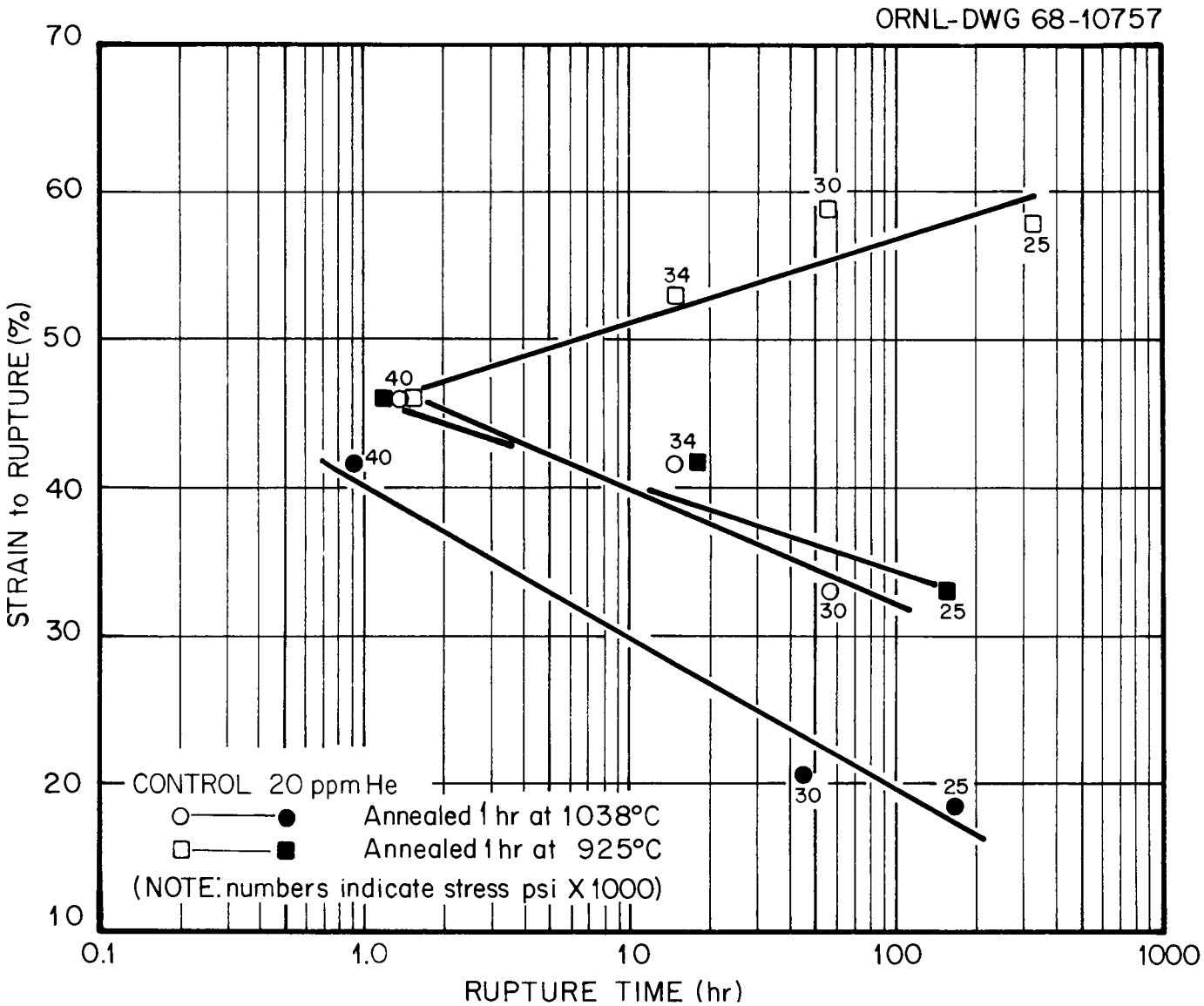

Fig. 8.9. Strain Versus Rupture Time of Titanium-Modified Type 304L Stainless Steel at 600°C.

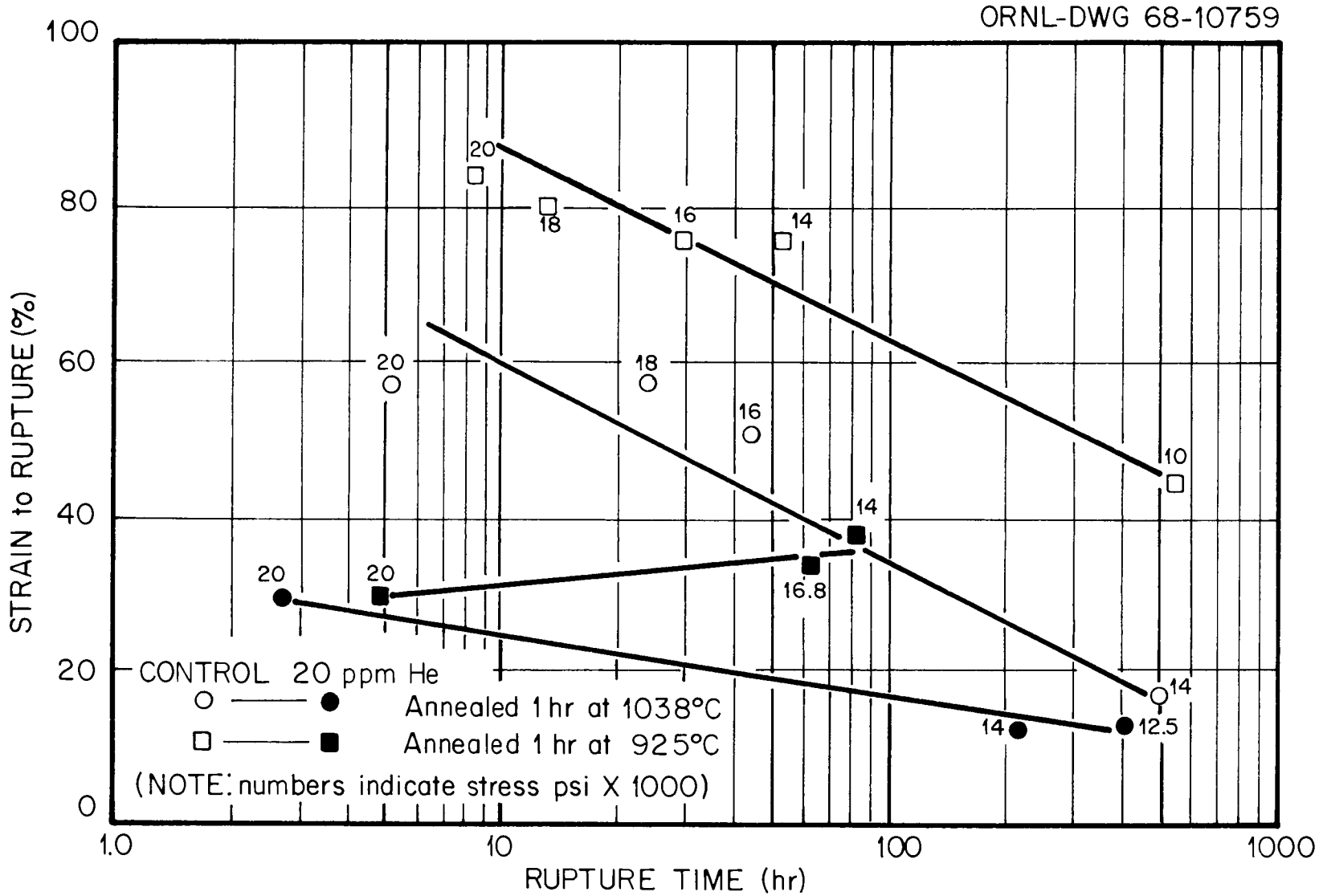

Fig. 8.10. Strain Versus Rupture Time of Titanium-Modified Type 304L Stainless Steel at 700°C.

carbide precipitate formation in the titanium-modified type 304L stainless steel, which causes more rapid second-stage creep rates and hence shorter rupture life.

In contrast to the behavior of the type 304 stainless steel, the rupture life of the titanium-modified alloy is not significantly reduced by 2.0×10^{-5} atom fraction of helium at either test temperature. Furthermore, the ductility of the titanium-modified alloy tested at high strain rates at 600°C is not altered by this amount of helium. At the slower strain rates, however, the ductility is reduced, though not as greatly as that of type 304 stainless steel. At 700°C the ductility loss due to helium is greater than at 600°C, but the ductility of the modified alloy annealed for 1 hr at 925°C (about 30%) remains significantly higher than that of type 304 stainless steel and does not vary greatly with strain rate in tests lasting up to 100 hr.

Electron microscopy and optical metallographic studies are in progress to aid in interpreting these results. We are also continuing to test cyclotron-bombarded specimens at lower stresses in order to obtain more information on the behavior of these materials at rupture times approaching 1000 hr.

Electron Microscopy of Irradiated EBR-II Fuel Cladding

J. O. Stiegler E. E. Bloom J. R. Weir, Jr.

This quarter, we concluded our study of the effects of irradiation temperature and fluence on the void population in a fuel pin irradiated in EBR-II and also examined the annealing behavior of the various void distributions present.

Irradiation temperatures varied continuously along the pin from the coolant inlet temperature of 370°C to a maximum temperature of 470°C, and the fast neutron fluence ranged from a maximum of 1.4×10^{22} neutrons/cm^2 at the center of the pin to a minimum of 0.8×10^{22} neutrons/cm^2 at its extremes. We took sections at intervals of 3 in. along the length of the cladding for examining the influence of irradiation temperature and fluence on the microstructure.

The preliminary examination showed that void density decreased and average void size increased with increasing irradiation temperature. Irradiation conditions, measured void densities, and calculated volume changes based on experimentally determined void distributions are listed in Table 8.4. We see that the increased growth at higher temperatures compensates for the reduced void density to render the overall swelling relatively weakly dependent on irradiation temperature for the conditions examined here.

Table 8.4. Irradiation Conditions and Void Density Measurements for Type 304L Stainless Steel

Specimen Number	Irradiation Temperature (°C)	Fast Neutron Fluence (neutrons/cm^2)	Voids per Cubic Centimeter	Volume Change (%)
		$\times 10^{22}$	$\times 10^{15}$	
1	370	0.8	1.4	0.07
2	398	1.2	1.3	0.15
3	430	1.4	1.3	0.17
4	460	1.3	0.9	0.16
5	472	0.9	0.4	0.08

Although the voids formed at the higher irradiation temperatures had crystallographic shapes, a variety of forms occurred within a single grain. We believe that complex shapes result from collisions of migrating voids and that surface diffusion reduces these to crystallographic shapes, but not all to the lowest energy octahedral form.

Precipitate particles, presumably carbides, on the order of 0.1 μ in diameter were dispersed along grain boundaries of the specimen irradiated at 470°C. Dislocation loops persisted up to the boundary, but a region about 500 A wide adjacent to the boundary was denuded of voids. This denuded zone decreased with decreasing temperature and at 440°C was only about 200 A thick. No grain-boundary precipitate particles were visible. The denuded zone increased with a further decrease in irradiation temperature, reaching a value of about 1500 A at 370°C, as is shown in Fig. 8.11. Again, there were no precipitate particles in the boundary,

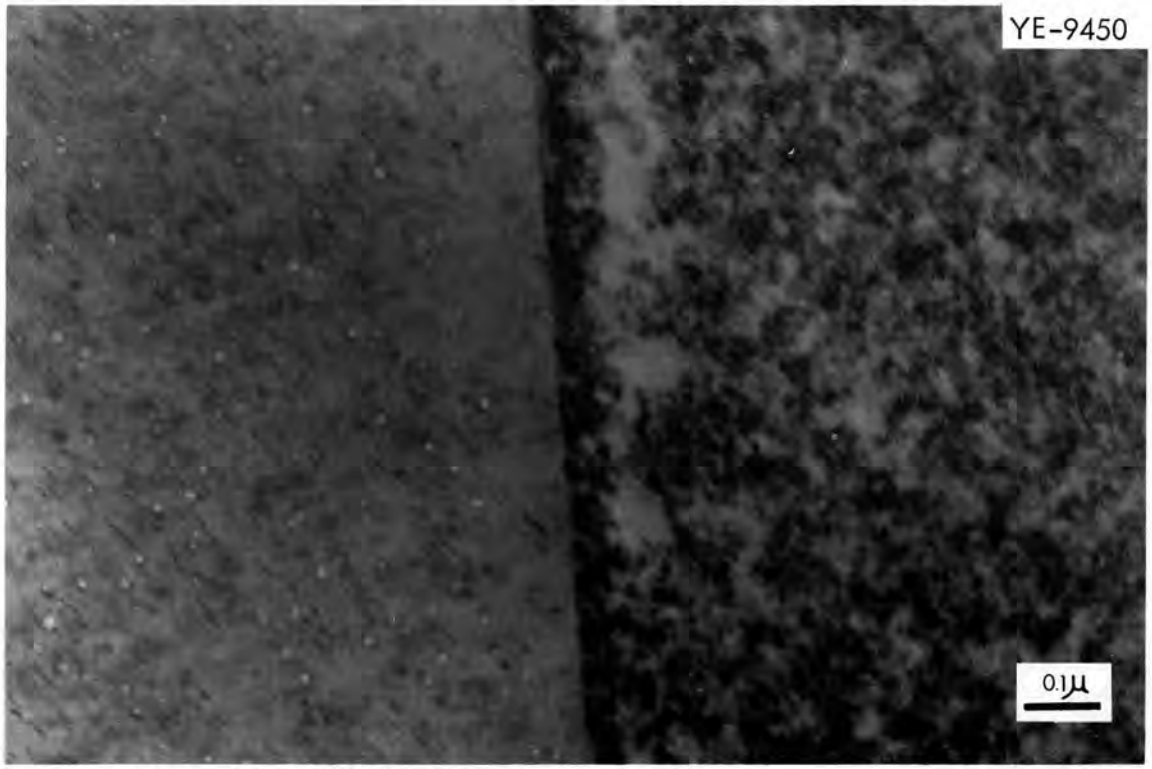

Fig. 8.11. Grain Boundary in Type 304L Stainless Steel Irradiated at 370°C to 0.8×10^{22} neutrons/cm^2. The grain at left is oriented such that the region denuded of voids is visible. The grain on the right is oriented for diffraction and shows a region denuded of dislocation loops.

but the dislocation loop distribution showed peculiar behavior in the vicinity of the boundary, as can also be seen in Fig. 8.11. The area between about 750 and 1500 A from the grain boundary was denuded of loops, but within 750 A of the grain boundary there was a very high density of loops. We suspect that impurities play an important part in nucleating the loops.

It is not readily apparent from Fig. 8.11 that the defects do exist as loops because of the overlapping of their images. If we tilt the foil to reduce contrast, however, loops ranging up to 500 A in diameter become clearly evident.

Annealing of Defects

The annealing of the irradiation damage in specimen 3 (irradiated at 430°C to 1.4×10^{22} neutrons/cm^2) was studied by isochronal anneals of

1 hr at temperatures between 475 and 900°C and by isothermal anneals at 700°C for times between 1 and 100 hr.

Annealing 1 hr at 475°C did not change the character of the dislocation loops or the size distribution of the observable voids. After 1 hr at 600°C, the dislocation loops had converted to a dislocation network, and the total void density had decreased from 12.7×10^{14} voids/cm^3 (as irradiated) to 9.6×10^{14} voids/cm^3. With increasing annealing temperature, there was a continuous decrease in both dislocation and void density, as can be seen from the values listed in Table 8.5. Histograms of void density as a function of void size after various anneals are shown in Fig. 8.12. Void density decreases because of the annealing of the smaller voids, those with initial diameters less than approximately 150 A, while the density of larger voids remains essentially unchanged. Thus, after 1 hr at 800°C, the only remaining voids had diameters between 150 and 300 A. After 1 hr at 900°C, the voids had completely disappeared. Similar results (i.e., rapid annealing of the smaller voids with little change in the density of larger voids) were obtained from the isothermal anneals.

Specimen 1, as irradiated, contained voids with diameters between 67 and 187 A. In this case, all voids were eliminated after annealing 1 hr at 700°C. In comparison, specimen 5 contained voids with diameters as large as 300 A, and annealing at 800°C was required for complete elimination of the voids.

The results of the annealing treatments are consistent with the annealing behavior of quenched voids in aluminum reported by Volin and Balluffi.[7] In their work, void dissolution was controlled by the diffusion of vacancies away from the void. They felt that exchange of vacancies between the void and the lattice occurred rapidly enough that the equilibrium vacancy concentration was maintained at the surface of the void at all times. Since this concentration varies exponentially with the reciprocal of the void radius, the dissolution rate increases rapidly as the void size decreases. Consequently, small voids are

[7]T. E. Volin and R. W. Balluffi, Phys. Status Solidi 25, 163 (1968).

Table 8.5. Dislocation and Void Densities for Various Postirradiation[a] Annealing Treatments

Annealing Treatment	Dislocation Density (cm/cm^3)	Void Density per Cubic Centimeter
	$\times 10^9$	$\times 10^{14}$
1 hr at 600°C	31	9.6
1 hr at 700°C	7.6	5.0
1 hr at 800°C	1.7	0.8
1 hr at 900°C	< 0.1	0
10 hr at 700°C	2.1	2.3
100 hr at 700°C	0.8	0.3

[a]Irradiated at 430°C to 1.4×10^{22} neutrons/cm^2.

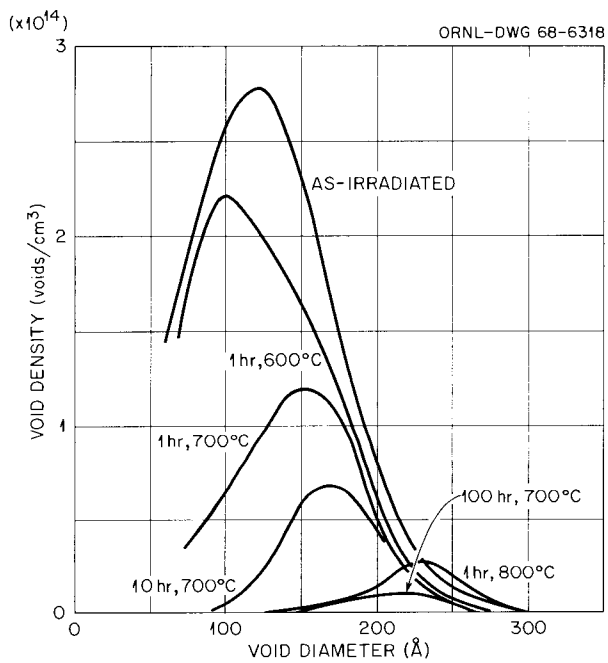

Fig. 8.12. The Effects of Annealing on the Void Size Distribution in Type 304L Stainless Steel.

eliminated quickly while large ones barely change size at all. As the small voids dissolve, the vacancy concentration in the lattice increases over the equilibrium value and may be sufficient to cause some large voids to grow. The curves presented in Fig. 8.12 show that the tendency for this is slight except possibly for the anneal of 1 hr at 800°C. The increased lattice concentration of vacancies does slow the dissolution rate of all voids from that predicted by the treatment given by Volin and Balluffi.

The shapes of the void distribution curves for the annealed specimens reflect this process. The density of small voids does not go to zero, however, for larger ones as they shrink must pass through the range of small sizes. The tails of the distribution curve at the end that shows the large void sizes are hardly influenced until either high-temperature or long-time annealing treatments are encountered.

That the small voids developed in section 1 annealed at a significantly lower temperature than the larger ones in sections 3 and 5 agrees with this view of the annealing process. It suggests that periodic annealing may provide a means for controlling swelling of reactor components if it is done frequently enough that a population consisting only of small voids is present; otherwise, excessively high temperatures will be required to eliminate the voids in reasonable times.

Some Effects of Grain Size on the Radiation Damage of Incoloy 800

D. G. Harman

Initial testing of irradiated Incoloy 800 showed grain size to be an important variable influencing creep ductility: greater creep strains were noted for the finer grain sizes.

We selected four heats of materials with carbon levels of 0.03 and 0.12 wt % and titanium levels of 0.1 and 0.3 wt % and heat-treated cold-worked material to obtain a range of grain sizes, as is shown in Fig. 8.13. We then irradiated buttonhead tensile specimens in the ORR at 700°C and 2 to 3 $\times 10^{20}$ neutrons/cm^2 (thermal) while we held identical control specimens at 700°C in a laboratory furnace for the duration of the reactor cycle (about 1100 hr).

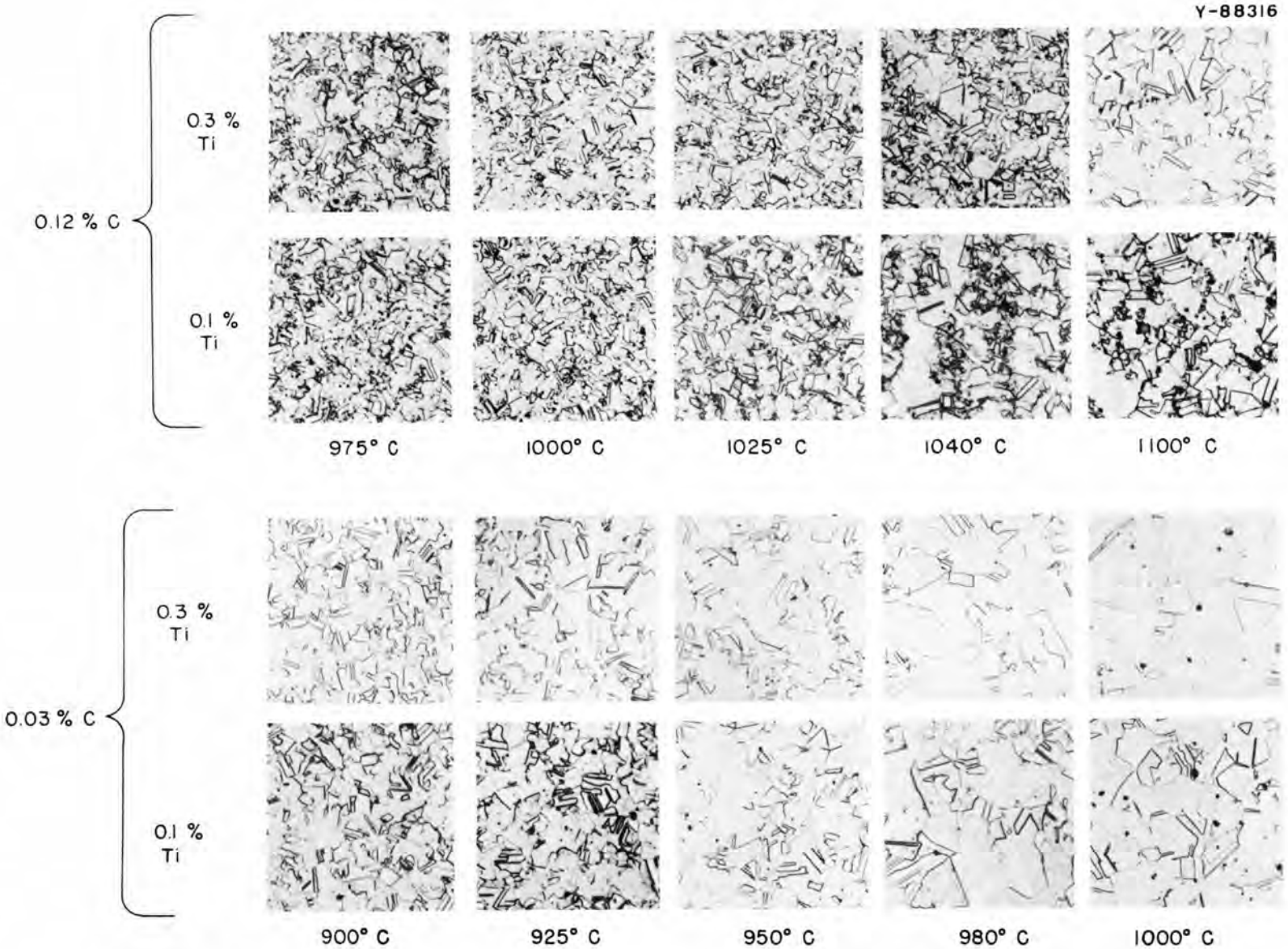

Fig. 8.13. Microstructure of Experimental Incoloy 800. The four alloys were held for 30 min at indicated temperatures to obtain desired grain size. 500x.

We have evaluated the specimens irradiated at 700°C: tensility tested at 0.002 and 0.05 min^{-1} and creep-rupture tested at 10,000 and 12,000 psi. The testing of the tensility of the control specimens has been completed; however, the corresponding creep-rupture tests are just getting under way and will be reported later.

The tensility results are listed in Table 8.6. We have not completed our evaluation of these data, but certain trends are evident. All four heats of material show an increasing ultimate tensile strength with increasing grain size (i.e., increasing annealing temperature) for both the irradiated and control specimens, and this is more pronounced at the slower strain rate. In most cases, the 0.2% yield strength decreases with increasing grain size.

The uniform elongations for both the irradiated and the control specimens seem to be quite independent of grain size, but are lower for the slower strain rate. Radiation reduced the uniform elongation by about 30% of the control value at the faster strain rate and by about 50% at the slower strain rate. The 0.3% Ti heats showed slightly higher losses than the 0.1% Ti heats.

Total elongation values of 50 to 70% are noted for the control specimens. Radiation reduced these to 11 to 23% for the two 0.1% Ti alloys and to 7 to 14% for the two with 0.3% Ti. The material with finer grain size showed better postirradiation ductility, and this was more pronounced for the 0.1% Ti alloys. The high-carbon heats showed less radiation damage to the total tensile elongation, but this was probably due to the finer grain sizes, as was shown in Fig. 8.13.

Figures 8.14 and 8.15 show the postirradiation creep elongations and rupture times, respectively. As expected from previous test results, the 0.1% Ti heats showed much higher creep elongations than did the 0.3% Ti heats. Also apparent from Fig. 8.14 are the significant effects of grain size and stress level. Creep elongations as high as 100% were measured for both carbon levels when tested at the lower stress. As can be noted from the figure, this is possible only for the material with finer grain size. It is also significant that the values for creep elongation are independent of carbon level when the grain size is considered.

Table 8.6. Short-Time Tensile Strength Test Results for Incoloy 800 Irradiated and Tested at 700°C [a]

Annealing Temperature (°C)	Strain Rate (min^{-1})	Strength, psi		Elongation, %	
		0.2% Yield	Ultimate Tensile	Uniform	Total
		$\times 10^3$	$\times 10^3$		
		0.1% Ti, 0.03% C			
900	0.05	23.6(22.9)	34.5(36.4)	12.4(19.0)	22.9(58.0)
925	0.05	24.2(22.3)	35.9(37.7)	11.8(15.0)	13.8(51.0)
950	0.05	21.8(21.5)	35.4(37.4)	12.5(17.0)	17.8(59.0)
980	0 05	19.1(17.5)	38.5(41.1)	11.9(17.0)	14.8(53.0)
900	0.002	21.1(17.3)	23.4(24.3)	2.7(8.6)	18.4(61.0)
925	0.002	19.4(17.5)	23.0(24.4)	6.1(10.8)	22.0(64.6)
950	0.002	20.6(18.0)	24.6(25.3)	7.2(9.3)	19.8(59.3)
980	0.002	18.5(16.0)	26.9(27.9)	7.3(10.5)	13.7(56.7)
1000	0.002	15.5(13.9)	27.5(28.9)	7.7(13.0)	10.9(53.5)
		0.3% Ti, 0.03% C			
900	0.05	(23.0)	(40.0)	(17.0)	(53.0)
925	0.05	(22.8)	(40.7)	(17.0)	(59.0)
950	0.05	36.7(21.8)	40.6(42.0)	9.5(18.0)	11.3(62.0)
980	0.05	(17.2)	(43.4)	(18.0)	(47.0)
900	0.002	20.8(19.3)	24.2(25.2)	4.7(12.5)	11.9(68.9)
925	0.002	21.4(20.8)	26.3(30.6)	5.4(12.2)	10.0(53.6)
950	0.002	20.3(18.3)	25.6(27.8)	5.1(7.6)	10.1(48.1)
980	0.002	19.5(15.7)	28.4(30.0)	6.0(11.7)	7.7(50.8)
1000	0.002	18.2(15.0)	29.3(31.8)	5.8(9.5)	8.1(52.4)
		0.1% Ti, 0.12% C			
975	0.05	26.7(29.6)	35.0(42.1)	11.6(14.8)	27.5(58.6)
1000	0.05	26.1(30.0)	35.5(41.8)	10.5(14.7)	20.0(55.9)
1025	0.05	24.6(28.1)	35.4(42.6)	11.4(14.0)	20.3(44.3)
1040	0.05	24.0(27.2)	37.1(43.7)	12.1(16.0)	21.3(58.0)
975	0.002	19.5(17.7)	21.3(22.8)	5.4(8.5)	38.4(67.9)
1000	0.002	18.4(20.4)	21.6(25.6)	5.6(7.5)	31.5(76.6)
1025	0.002	19.5(17.9)	22.6(26.5)	5.9(7.7)	24.7(70.5)
1040	0.002	19.2(20.0)	24.0(27.5)	6.9(8.0)	26.0(54.7)
1100	0.002	18.9(18.0)	26.6(32.3)	8.4(10.5)	20.8(49.6)

Table 8.6 (continued)

Annealing Temperature (°C)	Strain Rate (min^{-1})	Strength, psi		Elongation, %	
		0.2% Yield	Ultimate Tensile	Uniform	Total
		$\times 10^3$	$\times 10^3$		
		0.3% Ti, 0.12% C			
975	0.05	29.2(28.0)	36.6(38.1)	7.4(12.1)	13.6(52.0)
1000	0.05	28.4(27.2)	37.4(38.7)	8.1(13.5)	13.6(53.7)
1025	0.05	27.9(25.9)	38.5(40.0)	7.9(15.0)	11.6(49.5)
1040	0.05	27.1(25.5)	42.6(39.9)	10.9(15.0)	13.6(49.2)
975	0.002	20.8(22.8)	22.3(27.5)	4.7(7.3)	13.1(69.7)
1000	0.002	22.3(22.5)	24.1(28.0)	4.4(8.0)	12.8(68.4)
1025	0.002	22.4(21.1)	25.1(29.5)	5.1(7.1)	11.3(57.9)
1040	0.002	22.3(21.4)	25.1(29.8)	5.9(10.0)	12.1(60.2)
1100	0.002	21.3(19.9)	28.7(35.9)	6.1(11.2)	12.1(53.8)

[a]Specimens irradiated to 2 to 3 $\times 10^{20}$ neutrons/cm^2 (thermal) in the ORR and control specimens (control data in parentheses) held at 700°C for the duration of irradiation.

ORNL-DWG 68-10897

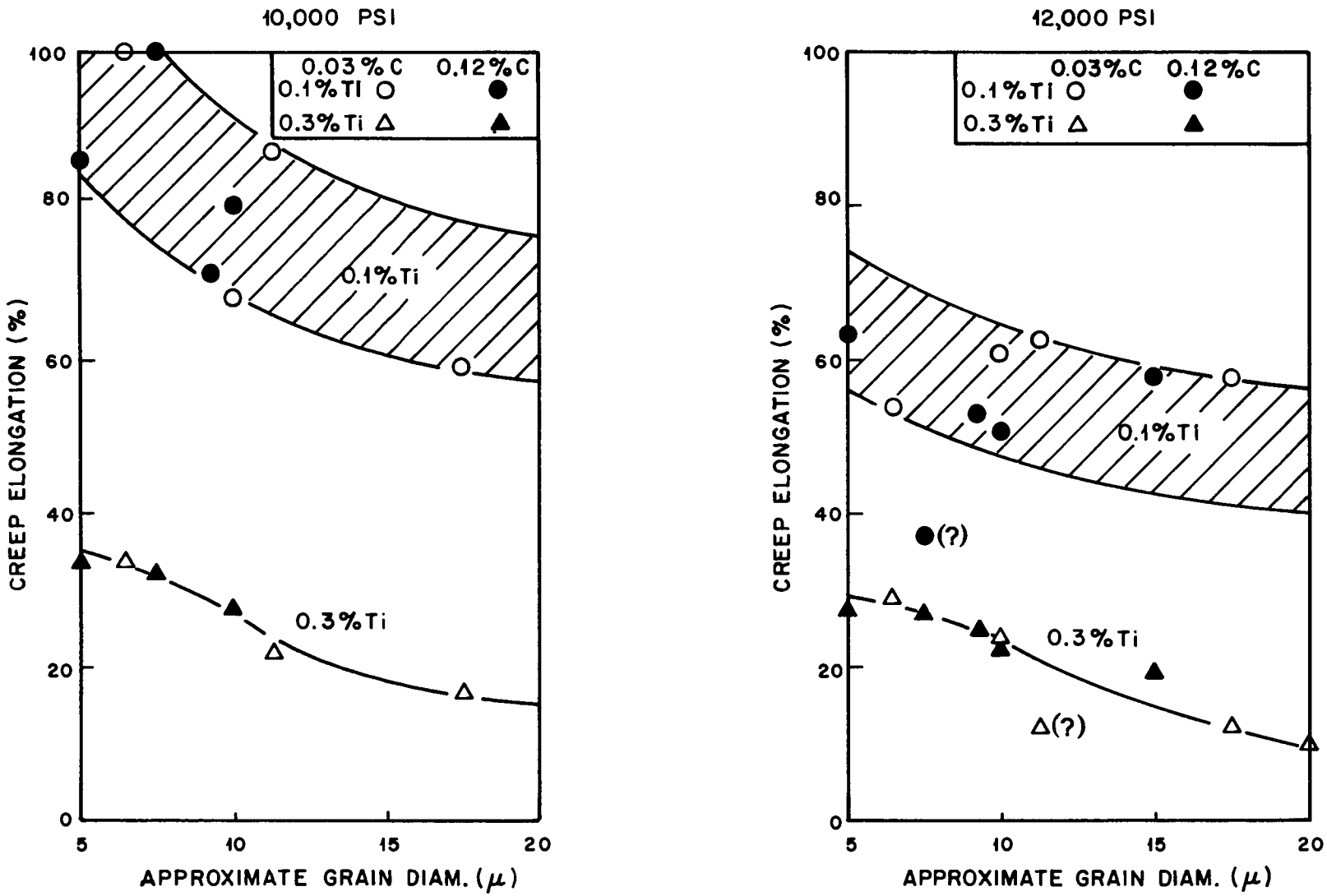

Fig. 8.14. Postirradiation Creep Elongation of Incoloy 800. Specimens were irradiated in the ORR at 700°C to a thermal fluence of 2 to 3 × 10^{20} neutrons/cm^2 and tested in air at 700°C.

ORNL-DWG 68-10896

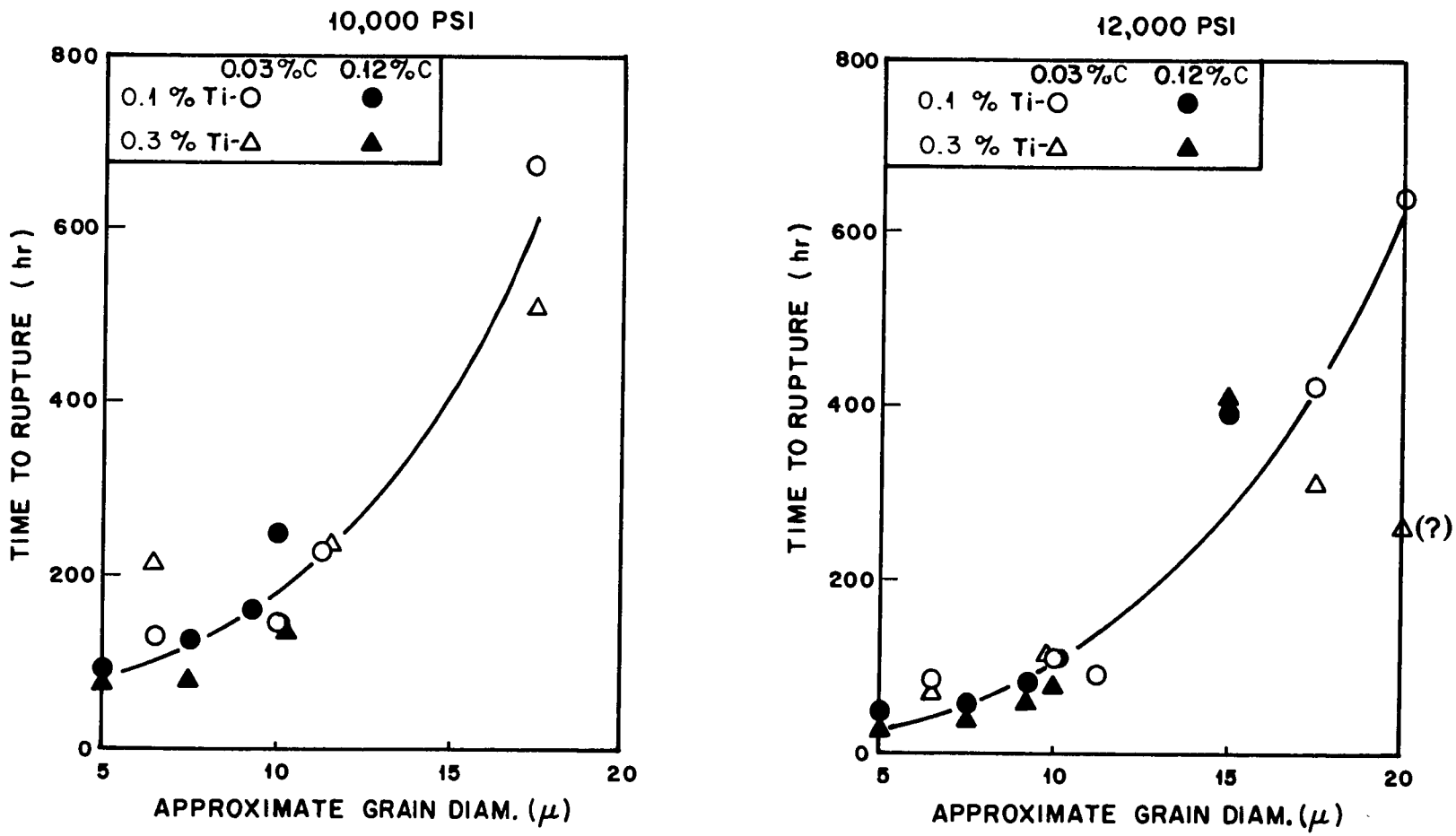

Fig. 8.15. Postirradiation Creep Rupture of Incoloy 800. Specimens were irradiated in the ORR to a thermal fluence of 2 to 3 × 10^{20} neutrons/cm^2 and creep tested in air at 700°C.

As expected, the larger grain size provided longer rupture times, as can be seen in Fig. 8.15. Also, the 0.1% Ti heats showed slightly longer rupture lives than the 0.3% Ti heats with the same carbon content, probably because of the higher ductilities of these alloys. A tendency for longer rupture times is evident for the high-carbon as compared with the low-carbon alloys when tested in the large-grained condition. Whether or not this is an aging effect will be determined upon completion of the control tests.

We believe that this experiment shows that careful control of the grain size of Incoloy 800 of a particular composition may be able to produce the desired combination of strength and ductility. It should be remembered that these are small vacuum-melted heats of material, but many of our observations should indicate important variables for commercial application.

Voids in Vanadium Irradiated in EBR-II

F. W. Wiffen J. O. Stiegler

We recently obtained from United Nuclear Corporation (UNC) unalloyed vanadium used as cladding in the fueled part of a (U,Pu)C fuel pin irradiated in row 4 of EBR-II for 2850 hr at power. The cladding was stripped from the fuel at BMI and was received at ORNL as segments of tubing. The original tube had an inner diameter of 0.257 in. and a wall thickness of 0.022 in. Irradiation conditions reported[8] by UNC are a calculated cladding surface temperature of 630°C and peak fluence of 1.7×10^{22} neutrons/cm^2 ($E > 0$). Postirradiation examination at BMI indicated an increase of 0.4% in the outer diameter of the cladding and a change in the Knoop microhardness from 136 for the unirradiated material to 151 after irradiation. No effect due to the irradiation was seen in metallographic examination. The irradiated vanadium was rated as "moderately ductile" as a result of fuel decladding operations and room-temperature bend tests.

---

[8] D. Stahl and A. Strasser, Post-Irradiation Examination of High-Density (U,Pu)C Pellet-Fueled EBR-II Rods Irradiated to 30,000 Mwd/T, UNC-5198 (Jan. 24, 1968).

Transmission electron microscopy of segments of the cladding revealed a high density of defects produced by irradiation. The most obvious features, as shown in Fig. 8.16, is the uniform distribution of voids. In a typical section of foil, there were 508 countable

Fig. 8.16. Transmission Electron Photomicrograph of Vanadium Irradiated in EBR-II to an Approximate Fluence of 1.7×10^{22} neutrons/cm^2 ($E > 0$) at a Temperature near 630°C. The void population has an average diameter of 117 A and a density of 3.4×10^{15}/cm^3.

voids per 10^{-8} square centimeter of foil area. The size distribution of these voids, classified by diameters measured with a Zeiss Particle Size Analyzer on prints at 200,000×, is shown in Fig. 8.17. The average diameter of the 1700 voids represented in Fig. 8.17 is 117 A. Assuming a value for the foil thickness of 1500 A gives a total density of 3.4×10^{15} voids/cm^3 and a total void volume of 3.7×10^{-3} cubic centimeter of voids per cubic centimeter of foil. Some of the larger voids were regularly faceted, but the crystallography of the bounding planes has not yet been determined. A high density of platelets was also observed in the irradiated material. A few of these can be seen in Fig. 8.16, but most are not visible under the contrast conditions of this photograph. This system of precipitate platelets is on planes of the form {110} and has not yet been studied in detail.

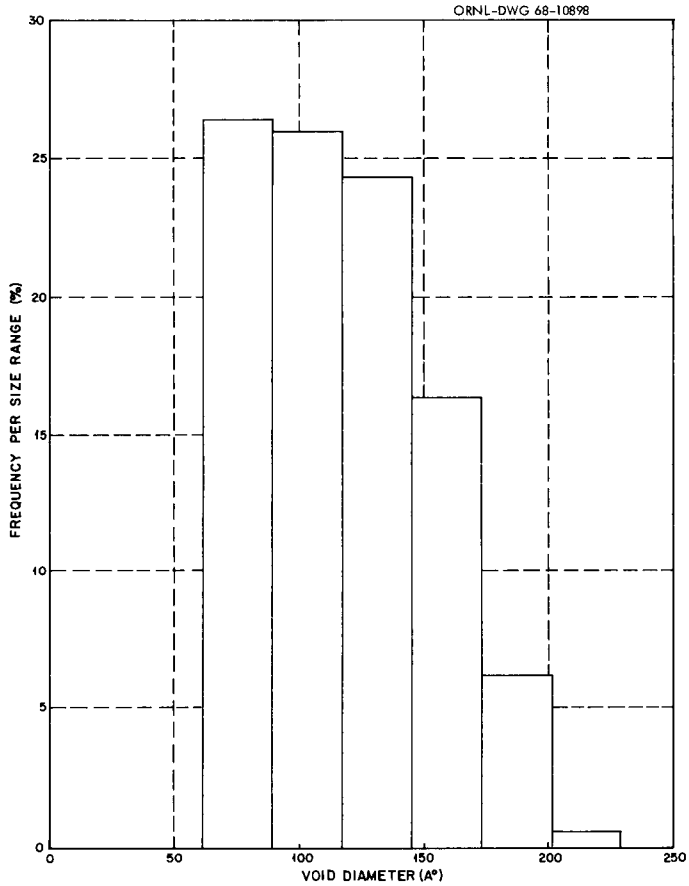

Fig. 8.17. Void Size Distribution for Vanadium Specimen Shown in Fig. 8.16.

Comparison of Laboratory and Commercial Heats of Titanium-Modified Hastelloy N

C. E. Sessions H. E. McCoy

We have found that small additions of titanium significantly improve the mechanical behavior of Hastelloy N under irradiation, and we are evaluating several small heats.

In our development work, we irradiated both laboratory (2-lb) and commercial (100-lb) heats of Hastelloy N with varying concentrations of titanium and carbon. The alloy base composition is Ni–12% Mo–7% Cr–0.2% Mn. These alloys have been irradiated in several different experiments to thermal neutron fluences of 2 to 5×10^{20} neutrons/cm^2 in the ORR and the ETR. Although several irradiation temperatures have been investigated, we shall consider only the results for specimens irradiated at 500 to 650°C in order to assess the effects of our titanium modification on high-temperature irradiation damage. We shall compare the behavior of the small laboratory melts with that of larger commercial melts of this material.

Commercial Melts

A partial list of 100-lb commercial heats on which we have accumulated preliminary data is given in Table 8.7. The titanium concentration varies from 0 to 1.2%, with only a small variation in carbon content (0.06 to 0.09%). The ranges of stress-rupture properties listed in Table 8.7 were obtained from an approximate fit of a plot of the stress-rupture life of the few data points that are available for each heat. All data considered were for a comparable pretest heat treatment of a 1-hr anneal at 1175°C in argon, but undoubtedly reflect differences in (1) grain size and (2) thermal aging during the irradiation cycle due to variations in titanium content.

The properties of these same alloys in the unirradiated condition are also given in Table 8.7. The ranges result from uncertainties due to the small number of tests available. The 40,000-psi rupture life at 650°C for unirradiated material containing zero titanium is about 200 hr, and creep fracture occurs at total strains of between 15 and 25%.

Table 8.7. Effect of Titanium Additions on Creep Properties of Commercial Heats of Hastelloy N Tested at 650°C and 40,000 psi

Heat Number	Contents, wt %		Creep-Rupture Properties			
			Unirradiated		Irradiated	
	Titanium	Carbon	Rupture Life (hr)	Strain[a] (%)	Rupture Life (hr)	Strain[a] (%)
21546	0	0.07	200	15–25	10	2.5–5
65535	0.15	0.07	250	10–22	70	2.5–4
66541	0.27	0.08	320	13–23	200	2–3
21545	0.52	0.06	700	20–30	400	3–19
66548	0.45	0.06	300	14–27	400	4–8
67550	0.71	0.08	Test incomplete		2000	4–12
67549	0.99	0.08	1500	35–40	2000	2–8
67548	1.20	0.09	Test incomplete		2500	6–17

[a]Range for three different stress levels.

A small but apparently insignificant increase in both rupture life and fracture strain is found for titanium levels up to 0.5% Ti. A large increase in both strength and ductility is found, however, at the 0.99% Ti level where fracture would be predicted in 1500 hr after 35 to 40% strain.

The postirradiation stress-rupture properties are also given in Table 8.7, and the variation of the rupture life with titanium content is shown in Fig. 8.18. These samples were irradiated at temperatures from 500 to 650°C in a thermal neutron fluence of from 2 to 5×10^{20} neutrons/cm^2. Again, all data are for the same preirradiation heat treatment of 1 hr at 1175°C. The postirradiation creep-rupture life at 650°C and 40,000 psi increased markedly with increasing titanium levels from approximately 5 hr at zero titanium to 3000 hr at 1.2% Ti. At 760°C, where the creep strength is much lower, we also find a beneficial strengthening effect of titanium; the rupture life at 20,000 psi increased from approximately 0.2 hr at zero titanium to 200 hr at 1.2% Ti. At 760°C, a smaller improvement in rupture life is

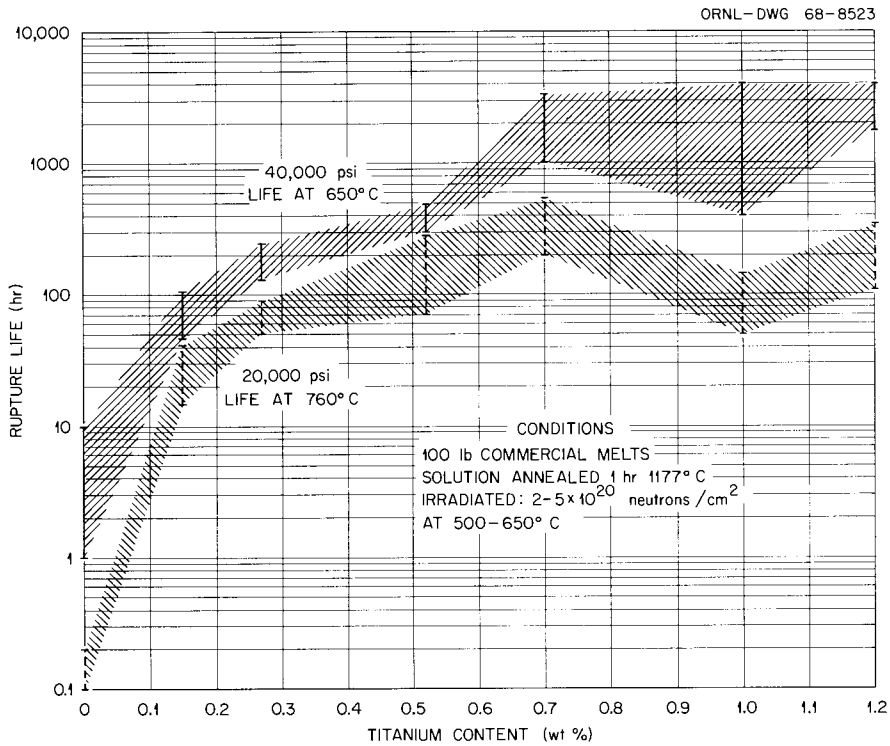

Fig. 8.18. Variation in Stress-Rupture Life with Titanium Content for Irradiated Hastelloy N.

found for increases in titanium content above about 0.2% than that observed at 650°C. The postirradiation fracture strain for the commercial heats varied from 2 to 5% for the heats containing less than 0.27% Ti to 3 to 19% for alloys containing 0.5 to 1.2% Ti.

Laboratory Melts

For comparative purposes, although the data are not tabulated, we observed that 2-lb laboratory heats of unirradiated Hastelloy N containing increasing titanium concentrations at 4000 psi and 650°C had rupture lives from 45 to 1050 hr. This increase in rupture life was progressive with increasing titanium from 0 to 1.0%. The fracture strain for the laboratory melts showed an increase with titanium level from 10 to 15% up to 22 to 27% over the range of titanium investigated.

In small laboratory heats following irradiation, we found an increase in the rupture life at 40,000 psi and 650°C from 70 to 1000 hr for titanium levels from 0 to 1.0%, which is somewhat less than that

observed for the commercial alloys. We also found a progressive increase in the fracture strain from 2 to 13% for additions of up to 1.0% Ti.

In summary, the observed properties indicate that the commercial heats of titanium-modified Hastelloy N parallel the out-of-reactor results for laboratory melts almost exactly. A small difference between laboratory and commercial heats resulted, however, for the irradiation condition in that greater strengthening is found with titanium for commercial heats than would have been predicted from the laboratory heat results. Also, the fracture strain following irradiation is slightly less for commercial heats than for the laboratory heats, which had higher purity.

9. RADIATION EFFECTS IN ALLOYS AND STRUCTURAL MATERIALS

D. S. Billington M. S. Wechsler

We have been studying radiation damage and radiation hardening and embrittlement in the body-centered cubic metals. The emphasis on this class of metals is motivated largely by the practical problem of the radiation embrittlement of pressure-vessel steels. This type of embrittlement, experienced by the pressure vessels of many operating reactors, increases their susceptibility to catastrophic brittle fracture. Such brittle fracture incidents could have serious consequences that bear on the public safety.

Our research into the cause of the radiation embrittlement of pressure-vessel steels indicates that the embrittlement is closely connected with radiation hardening. The increase in the yield stress of the steels upon irradiation permits stresses that exceed the inherent cleavage fracture stress, thus permitting the initiation and propagation of a running cleavage crack at higher temperatures than would be possible in the absence of irradiation. The precise origin of the radiation hardening is not known yet, but it is almost certainly due largely to the defect clusters produced by radiation, which serve as barriers to dislocation motion on which plastic deformation depends.

To better understand how and why radiation produces an increase in the yield and flow stresses, it is helpful to experiment with metals less complicated than steels. Pressure-vessel steels contain a variety of impurities and eutectoid decomposition products whose individual effects tend to be masked. For this reason it is helpful to work with other materials capable of better characterization. Therefore, the effort on steel was supplemented in the past by experiments on iron and niobium, both of which have the same basic crystal structure and exhibit a tendency toward the same type of low-temperature brittleness as steel. Niobium is a particularly useful material for study because it can be prepared in rather high purities and in single-crystal form.

The study of niobium has developed around two major themes: the influence of impurities, especially interstitial ones, and radiation

hardening and its relation to the defect clusters seen by electron microscopy. This report starts with a description of the use of autoradiography for determining impurity distributions in zone-refined niobium. Then, some measurements of resistivity and internal friction are described in which the trapping and releasing of oxygen and carbon impurities at traps produced by radiation are detected. The trapping of these impurities at defects produced by radiation has an effect on mechanical properties, as is seen in the radiation anneal hardening that takes place when irradiated niobium is annealed between 150 and 400°C. Some observations of this type are also specified below.

The defect clusters produced by radiation with which the radiation hardening is associated can be observed as black spots or loops by transmission electron microscopy in niobium and many other metals. On the other hand, the defect clusters are not detected in iron and steel by this technique except after very high exposures or upon post-irradiation annealing. Since the defect clusters are visible in niobium, the density and size distribution of the clusters were correlated with the magnitude of the radiation hardening. Furthermore, dislocation channeling was studied, a phenomenon in which the dislocations set in motion by plastic deformation cause the defect clusters to disappear. This report gives the results of a fairly detailed study of the crystal geometry of these dislocation channels and the extent to which strain is concentrated within the channels. The fact that strain is so concentrated is consistent with the coarse slip bands observed on the surface of irradiated-and-deformed metals. This is what causes the rate of work hardening and the ductility of nominally ductile metals to decrease upon irradiation.

Unfortunately, budgetary limitations in FY 1969 require that the work on niobium be discontinued. This report indicates the present status of the research. A separate report will be issued later to review the entire program on niobium and to indicate the directions that this line of investigation should take when conditions permit.

The work on radiation damage to iron and particularly to steel is continuing and will be included in future reports in this series.

Inhomogeneous Distribution of Tantalum and Tungsten in Zone-Refined Niobium

R. E. Reed

The electron-beam floating-zone melting (EBFZM) technique is widely used for purification and single-crystal growth of the refractory metals. In the case of niobium, previous work at ORNL[1,2] has shown that the major purification mechanism is generally volatilization. The tantalum and tungsten impurities in niobium were not appreciably affected by the EBFZM method because of their low vapor pressures and the high zoning speeds that were above those needed for effective zone refining.[3]

Barthel[4] has shown that for tungsten impurities in molybdenum, the EBFZM technique results in a "banded" structure. In this, the tungsten was distributed in alternate "impurity rich" and "impurity poor" layers that were parallel to the liquid-solid moving interface. This was attributed to turbulent convection currents in the liquid due to thermal gradients that resulted in periodic remelting of the moving liquid-solid interface. In a later paper, Barthel[5] showed that this fluctuation in the growth rate will change the effective distribution coefficient towards one. In addition, the dependence of the distribution coefficient

---

[1]R. E. Reed, Radiation Metallurgy Section Solid State Division Progress Report for Period Ending February 1966, ORNL-3949, p. 35.

[2]R. E. Reed, C. L. Brooks, and R. P. Tucker, Radiation Metallurgy Section Solid State Division Progress Report for Period Ending January 1968, ORNL-4246, p.89.

[3]F. H. Cocks, R. M. Rose, and J. Wulff, J. Less-Common Metals 10, 157–168 (1966).

[4]J. Barthel and R. Scharfenberg, pp. 133–139 in Crystal Growth, ed. by H. S. Peiser, Pergamon Press, New York, 1968.

[5]J. Barthel and K. Eichler, Kristall und Technik 2(2), 205–215 (1967).

on the zoning speed as given by Burton et al.[6] was eliminated by these fluctuations. Therefore, at any zoning speed the effectiveness of zone refining of impurities with distribution coefficients greater than one will be reduced by fluctuations in the zone speed.

This report describes some preliminary work using microradiography to detect this inhomogeneous distribution of tungsten and tantalum impurities in niobium single crystals.

Experimental Procedure

Our starting material was 1/2-in.-diam niobium rod swaged from a 3-in.-diam ingot, melted by the electron-beam process, that was supplied by Wah Chang Corporation, Albany, Oregon. The following list shows the chemical analysis for this material:

Element	Weight (ppm)
C	20
O	130
N	46
H	3
Ta	586
W	338

A 1/2-in.-diam niobium rod was given one EBFZM pass at 10 cm/hr zoning speed and 1×10^{-6} torr. Power to the electron beam was shut off quickly at the end of the pass. A 3-cm length that included the finish end was cut from the as-zoned rod. This specimen was then sectioned longitudinally along the rod axis by spark-erosion machining. One half was ground flat on 600-grit abrasive paper while the other half was planed flat by spark machining. Both were chemically polished in a nitric-hydrofluoric acid mixture.

These two specimens plus four sets of "standards" consisting of niobium metal with various tantalum and tungsten impurity levels were irradiated in the center hole of the D_2O tank of the Bulk Shielding Reactor for 24 hr. The thermal neutron flux in this position is

[6] J. A. Burton, R. C. Prim, and W. A. Slichter, J. Chem. Phys. 21, 1987 (1953).

1.2×10^{12} neutrons cm^{-2} sec^{-1}. The samples were allowed to decay radioactively for 24 hr.

Autoradiographs were taken by placing the samples and one set of the standards on 2- by 2-in. Ilford nuclear emulsion plates with 100-μ-thick L-4 type emulsion. Figure 9.1 is a print from an autoradiograph plate (the light and dark areas are reversed from those on the autoradiograph) showing a typical arrangement of specimens and standards. A Jarrell-Ash Recording Micro-Photometer Model 23-100 measured the percentage of light transmitted through the exposed plate for the standard and zoned specimens. We made a calibration curve from the measurements on the standard specimens to find the variation of tantalum and tungsten content in the zoned specimen.

Results and Discussion

The autoradiographs were taken using β^- emission from neutron-activated tantalum and tungsten impurities in the niobium. Table 9.1 lists the nuclear properties necessary to calculate the relative activities of the β^- emissions. The activity due to a neutron-activated impurity element can be calculated as follows:

$$A = Nf\sigma SD \ , \qquad (9.1)$$

where

A = activity from the impurity in disintegrations per second,

N = number of atoms present of the impurity element,

f = flux of thermal neutrons in neutrons cm^{-2} sec^{-1},

σ = thermal neutron cross section,

S = saturation factor = $(1 - e^{-\lambda t_i})$, where $\lambda = \frac{0.693}{T_{1/2}}$,

t_i = irradiation time, and $T_{1/2}$ = half-life of radionuclide, and

D = decay factor = $e^{-\lambda t_d}$, where $\lambda = \frac{0.693}{T_{1/2}}$, t_d = decay time measured from the finish of the neutron irradiation, and

$T_{1/2}$ = half-life.

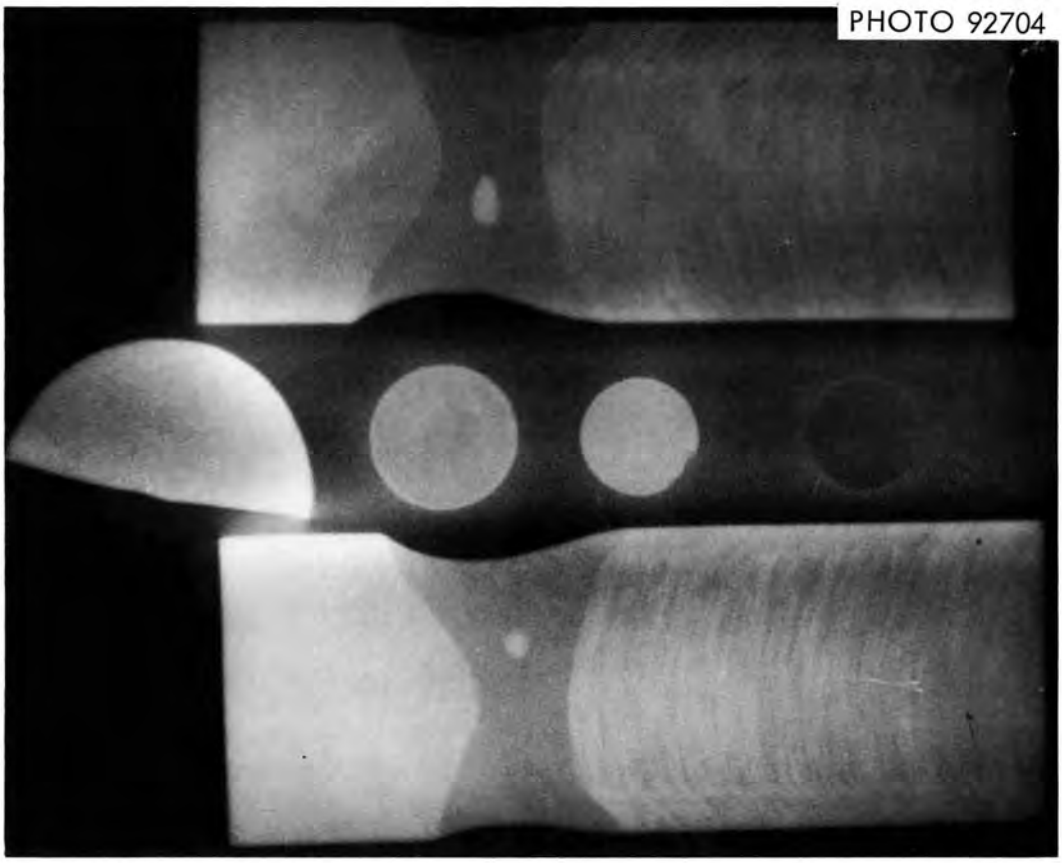

Fig. 9.1. Print from Autoradiographic Plate of Electron-Beam Zone-Refined Niobium Containing Tantalum and Tungsten Impurities. 3×.

Table 9.1 Nuclear Data for Tantalum and Tungsten

Property	Tantalum	Tungsten
Nuclear reaction	$^{181}Ta(n,\gamma)\ ^{182}Ta$	$^{186}W(n,\gamma)\ ^{187}W$
Abundancy	^{181}Ta 99.98%	^{186}W 28.4%
Thermal neutron cross section, barns	19	34
Radionuclide	^{182}Ta	^{187}W
Type decay	β^-	β^-
β^- energy, Mev	99% 0.52	15% 1.3; 85% 0.63
Radionuclide half-life	115 days	24.1 hr

The relative activity of the tungsten and tantalum impurities will then be

$$\frac{A(^{187}W)}{A(^{182}Ta)} = \frac{N(^{186}W)\ \sigma(^{186}W)\ S(^{187}W)\ D(^{187}W)}{N(^{181}Ta)\ \sigma(^{181}Ta)\ S(^{182}Ta)\ D(^{182}Ta)} \tag{9.2}$$

For a 24-hr irradiation, the relative activity of tungsten to tantalum can be calculated for the material with the chemical analysis shown above and the nuclear data in Table 9.1. Immediately after the irradiation, the relative activity will be

$$A(^{187}W)/A(^{182}Ta) = 23.97\ . \tag{9.3}$$

Thus almost all of the activity (about 96%) will be due to the tungsten impurity in niobium. However, it is more practical to make the first autoradiograph at some later time. In this case, the first plate was a 15-min exposure made 25.6 hr after the irradiation. Thus the relative activity was reduced to $A(^{187}W)/A(^{182}Ta) = 11.43$. For this exposure the activity was still largely due to the tungsten impurity (about 91%). The last autoradiograph in the series was a 2-hr exposure made 9 days after the end of the irradiation. For this case the relative activity was $A(^{187}W)/A(^{182}Ta) = 0.049$, which means that the tantalum impurity now created most of the activity (about 95%). Hence, by taking autoradiographs within one day and then about 10 days after the neutron irradiation, it is possible to record the distribution of tungsten and tantalum impurities in niobium metal.

Another factor to consider is the range of penetration of the β^- particles into the photographic emulsion. The energies of the beta emission from ^{187}W and ^{182}Ta are 0.63 and 0.52 Mev, respectively. These energies are similar enough that we may assume that the emulsion will respond in the same manner to each radionuclide. From data for penetration of electrons into aluminum as a function of energy we estimated that about 80% of the β^- particles were stopped in the 100-μ-thick nuclear emulsion on the autoradiographic plate.

Figure 9.2 is an enlarged print (about 6×) of an autoradiograph taken 26.1 hr after the irradiation. Thus, the activity registered on this plate is due largely to β^- emission from ^{187}W. Note first that the area that was the liquid zone before the electron-beam power was shut off is lighter on the plate (darker on print, Fig. 9.2), indicating that the liquid contains less tungsten than the solid. In fact, tentative calculations from the microphotometer readings give an effective distribution coefficient (concentration of tungsten in solid divided by concentration in the liquid) of $K = 1.06$. The niobium-tungsten phase diagram predicts a $K > 1$. The tantalum distribution coefficient calculated from later autoradiographs resulted in $K = 1.14$. Note that these are preliminary figures. Second, the zoned section of the rod shows evidence that the tungsten is inhomogeneously distributed. It occurs

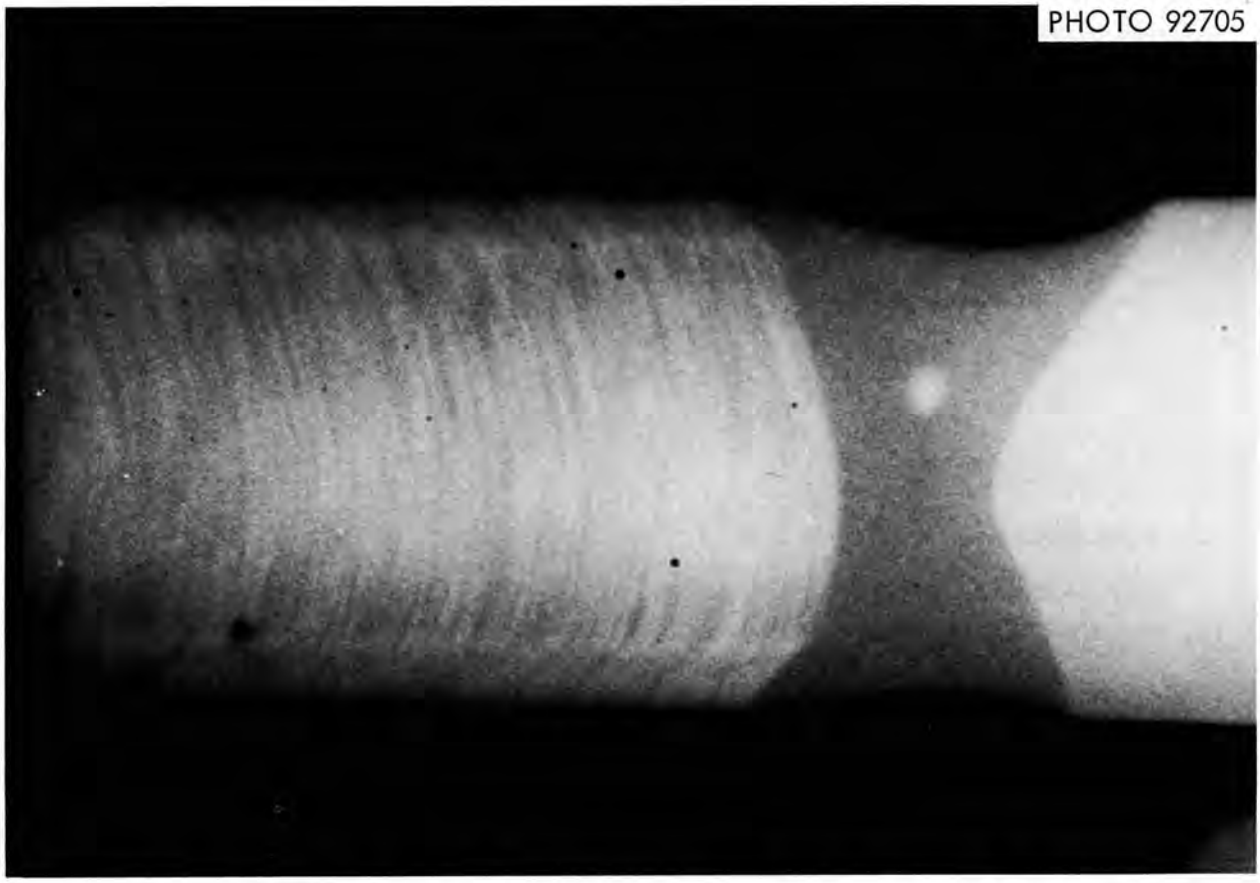

Fig. 9.2. Print from Autoradiographic Plate of Zoned Niobium Containing Tungsten and Tantalum Impurities. 6×.

in alternate bands of impurity "rich" and "poor" layers that are roughly parallel to the liquid-solid moving interface. This was also true for the tantalum impurity. Third, the liquid-solid interface is not planar but is appreciably curved.

Because of problems caused by an inhomogeneous background on the autoradiographic plate the distribution coefficients quoted here are tentative calculations. This inhomogeneous background was caused by gamma-radiation concentrations from the greater mass (compared to that of the thin standard disks) of the massive, zoned specimens. Future autoradiographs will use specimens and standards of the same thickness. The darkening due to the gamma radiation is slight, but the inhomogeneous nature of this background "fog" did affect the microphotometer readings.

Conclusions

Tantalum and tungsten impurities are inhomogeneously distributed in as-zoned niobium rod. They lie in alternate layers of impurity "rich" and "poor" regions that are parallel to the moving liquid-solid interface during zoning. An autoradiographic technique shows promise for obtaining quantitative measurements on the distributions of tantalum and tungsten.

The Effect of Interstitial Impurities on Postirradiation Annealing Phenomena in Niobium

J. M. Williams J. T. Stanley W. E. Brundage

In previously reported work[7–11] we have been concerned with characterizing the interstitial impurity levels of several niobium materials

---

[7]J. M. Williams, J. T. Stanley, and W. E. Brundage, Quarterly Progress Report: Irradiation Effects on Reactor Structural Materials, November, December 1966–January 1967, BNWL-CC-1053, p. 11.18.

[8]J. T. Stanley, J. M. Williams, and W. E. Brundage, Quarterly Progress Report: Irradiation Effects on Reactor Structural Materials May, June, July, 1967, BNWL-532, p. 11.17.

[9]J. T. Stanley, J. M. Williams, and W. E. Brundage, Radiation Metallurgy Section Solid State Division Progress Report for Period Ending January 1968, ORNL-4246, pp. 42–55.

prepared in the laboratory and determining the effects of these impurities on property changes during postirradiation annealing.

We estimated interstitial impurity levels by internal-friction and resistivity measurements; in two cases controlled additions of oxygen provided a further check on the analyses. Postirradiation annealing studies up to 200°C revealed that decreases in resistivity in the Stage III region (about 150°C) were attributable to segregation of oxygen in solid solution at dislocation loops produced by radiation.[10,11] In the present work, we have extended postirradiation annealing studies to about 550°C for most of the samples. Also, interstitial impurities have been chemically analyzed for comparison with the results of the physical methods. This report concerns itself with materials previously labeled C, D, E, F, G, and P (refs. 7 and 8). We first present a brief recapitulation of the experimental procedures, then a new summary and comparison of the interstitial impurity levels as determined by the various methods, and, finally, the results of annealing up to 550°C.

Experimental Procedures

Sample Preparation. — Sample materials were zone-refined niobium rods swaged and drawn to 0.030-in.-diam wire suitable for both internal friction and resistivity measurements. The wires were annealed and outgassed by resistive heating to a high temperature in a high-vacuum system. The annealing temperatures and final vacuums achieved during outgassing have been reported.[7,8]

After thorough outgassing, controlled quantities of oxygen were added to two of the materials, F and G. For material F, this was done by reheating the wire to about 1100°C in a dynamic atmosphere of 5×10^{-6} torr of oxygen. From the approximate pumping speed of the sample at this temperature, we estimated the weight of oxygen added as

---

[10] J. M. Williams, J. T. Stanley, and W. E. Brundage, Metal Sci. J. 2, 100 (1968).

[11] R. Bullough, J. T. Stanley, and J. M. Williams, Metal Sci. J. 2, 93 (1968).

about 250 ppm. Approximately 50 ppm O was added to material G by anodizing the surface and dissolving the oxide as described previously.[8]

Annealing and Measuring Procedures. — We measured internal friction in an inverted torsion pendulum placed inside an evacuated chamber. Grips and mounting fixtures were designed so that the samples could be mounted and dismounted without being bent. Thermocouples were mounted on both grips, and separate heaters maintained the grips at the same temperature. Except where otherwise noted, internal friction samples were annealed *in situ*.

We measured resistivity with the samples immersed in liquid helium inside a superconducting magnet that created a field of 17.5 kilogauss. It was necessary to use fine niobium wire for the primary potential contacts that establish the gage lengths of the samples, for platinum leads would have become too radioactive during the irradiations. To make measurements, we welded platinum wires to these niobium contacts and in turn soldered copper leads to the platinum.

Except for material G, all resistivity samples were isochronally annealed in a dynamically evacuated tube furnace over the entire temperature range studied. The samples were dismounted from the resistivity sample holder for each anneal and were thus subjected to considerable handling that resulted in the breaking of some of the niobium potential contacts after repeated mountings. Some of the scatter in the annealing data at higher temperatures may be caused by slight changes in the sample geometry attendant upon replacing these leads. Resistivity samples from material G were annealed in a silicone-oil bath up through 225 °C and were not dismounted between anneals. Sample holders used in these experiments left the length of these samples unconstrained to allow for thermal expansion and contraction during annealing and cooling to liquid helium.

Irradiation Procedures. — Table 9.2 gives the ORNL irradiation facilities employed, the neutron fluences, and the irradiation temperatures for the irradiations of the various samples. The irradiation temperature was measured in each case by a thermocouple spot-welded to a dummy sample placed inside the irradiation capsule with the rest of the samples.

Table 9.2. Information on Niobium Sample Irradiations at 45°C

Sample	Facility	Neutron Fluence (neutrons/cm^2) (> 1 Mev)
		$\times 10^{18}$
C, D	LITR, C-41	1
E, F	LITR, C-41	2
G	BSR, liquid nitrogen cryostat	2

Chemical Analyses. — Oxygen and nitrogen were analyzed by the vacuum-fusion technique, and carbon was analyzed by the combustion technique.

Results

Material Characterization. — Table 9.3 compares the impurity levels determined by the various techniques. In some cases more than one analysis was obtained for a given material. The values determined by internal-friction measurements and the total impurity concentrations determined from resistivity measurements were reported previously.[7,10] Unfortunately (as is indicated by Fig. 11.20 in ref. 7), preirradiation internal friction was not measured above 200°C on material F. Thus, we have no determination for C and N based on internal-friction data in this material.

It is apparent from Table 9.3 that there is general agreement among the various methods to the extent that they all rate the samples in the same order as concerns the total and individual impurity concentrations. However, there is considerable disagreement in detail. To the limited extent that nitrogen is present, there is good agreement between the internal-friction and vacuum-fusion analyses. However, for carbon and oxygen the apparent discrepancies amoung the various methods warrant further discussion.

For carbon, we consider the agreement between internal-friction and chemical analyses to be satisfactory in view of the present

Table 9.3. Comparison of Interstitial Impurity Analyses for Niobium Impurity Concentrations in Parts Per Million by Weight

Material	Chemical Analysis			Internal Friction[a]			Resistivity[b]
	C	O	N	C	O	N	Total
C	20	17	9	~ 3	< 3	10	17
		60	16				
		10	< 1				
		40	10				
D	62	16	10	~ 30	< 3	10	69
E	11	13	2	< 4	< 4	< 4	5
		22	< 1				
F	150	330	< 1		260		250
G	15	96	< 1	< 4	85	< 4	50
P[c]		2	2				3
		3	1				

[a]Determined from internal-friction data of Powers and Doyle. [R. W. Powers and M. V. Doyle, J. Appl. Phys. 30, 514 (1959).]

[b]Determined by dividing residual resistivity by 0.0039 microhm-cm $(ppm)^{-1}$. [C. S. Tedmon, Jr., R. M. Rose and J. Wulff, Trans. Met. Soc. AIME 230, 1732 (1964).]

[c]Parma-1 material used in deformation experiment. (J. T. Stanley, J. M. Williams, and W. E. Brundage, Quarterly Progress Report: Irradiation Effects on Reactor Structural Materials, May, June, July, 1967, BNWL-532, p. 11.17.)

uncertainties associated with applying these methods to carbon. These uncertainties arise partly from the fact that carbon is scarcely soluble in niobium. The Snoek effect measures only the amount of carbon retained in solution during cooling from the fairly high temperatures used in preparing the materials and is insensitive to precipitated carbon. Furthermore, as previously mentioned,[7] the carbon retained in solution precipitates during the observation of the Snoek peak. Also the resistivity is sensitive primarily to the carbon in solution. Combustion analysis, on the other hand, measures all the carbon in the sample, although this method is considered inaccurate below 25 ppm for

the sample weights employed. To summarize, we have physical evidence for carbon in materials C, D, and F. In materials C and D this evidence is derived from measurements of internal friction. As will be seen later, material F like material D exhibits a large annealing stage in the temperature region where carbon is mobile, and we attribute this to precipitation of carbon. This lends credibility to the relatively high carbon analysis for this material.

In comparing the resistivity results with the internal-friction results for materials F and G, we find that the internal-friction results indicate somewhat larger oxygen concentrations than the total impurity concentration computed from the resistivity. It might be mentioned that the value of Tedmon, Rose, and Wulff[12] of 0.0039 microhm-cm $(\text{ppm})^{-1}$ is the lowest value of the resistivity contribution we have found in the literature for any interstitial impurity in niobium. Thus, the total concentration determined from resistivity measurements should represent an approximate upper limit. In computing the oxygen concentration from the Snoek peak one assumes

$$C(\text{ppm O}) = KQ_p^{-1} , \tag{9.4}$$

where Q_p^{-1} is the internal friction at the peak. The Powers and Doyle[13] value for K is 3.64, but other values in the literature range from 2.65 to 4.09 (refs. 14–18) for low concentrations of oxygen. Thus, there is considerable latitude in estimating the concentration from

---

[12]C. S. Tedmon, Jr., R. M. Rose, and J. Wulff, Trans. Met. Soc. AIME 230, 1732 (1964).

[13]R. W. Powers and M. V. Doyle, J. Appl. Phys. 30, 514 (1959).

[14]C. Y. Ang and C. Wert, Trans. AIME 197, 1032 (1953).

[15]Z. C. Szkopiak, Strain Aging Phenomena in Niobium (Ph.D. Thesis, University of London), Battersea College of Technology, Res. Rep. No. BCT/MET/25 (1964).

[16]Z. C. Szkopiak, Internal Friction in Niobium Oxygen Solid Solution, UKAEA TRG Report 1151(C/X) 1966.

[17]R. Gibala and C. A. Wert, Acta Met. 14, 1095 (1966).

[18]R. L. Stephenson and H. E. McCoy, private communication.

measurements of internal friction. In any case, the relative discrepancy between the internal-friction and resistivity results appears worse for material G than for material F. Even after the carbon in material F has precipitated, the remaining resistivity corresponds to at least 200 ppm O. Possible sources of variations in damping values for interstitial impurities include the presence of substitutional impurities[16] and preferred orientation of the recrystallized texture. The wires used in these experiments had a bamboo structure with grains ranging from 1 to 3 mm in length. Since wires F and G were drawn from different starting crystals, they could have had different recrystallization textures and did in fact have different substitutional impurity contents. Material F had tantalum and tungsten totaling about 369 ppm, and material G had a total of 594 ppm of these impurities.[19]

The vacuum-fusion results for oxygen are generally greater than those from the other methods, although they are quite reasonable for materials F, G, and P. For materials C, D, and E, we believe the lower values indicated by internal friction are more correct. The internal-friction values are consistent with the total impurity concentrations indicated by the resistivity values and also agree with those of other workers using similar techniques for preparing samples.[20–22]

Postirradiation Annealing Studies. — The isochronal annealing results are shown in Fig. 9.3. Changes in resistivity are taken with respect to the preirradiation values. Annealing results up to 200°C

---

[19] J. M. Williams, J. T. Stanley, and W. E. Brundage, Quarterly Progress Report: Irradiation Effects on Reactor Structural Materials, November, December 1966–January 1967, BNWL-CC-1053, p. 11.18.

[20] Warren De Sorbo, Phys. Rev. 132, 107 (1963).

[21] Reiner-Joachim Dinter, Z. Metallk. 58, 70 (1967).

[22] A. Köthe and F. Schlät, Phys. Status Solidi 21, K73. (1967).

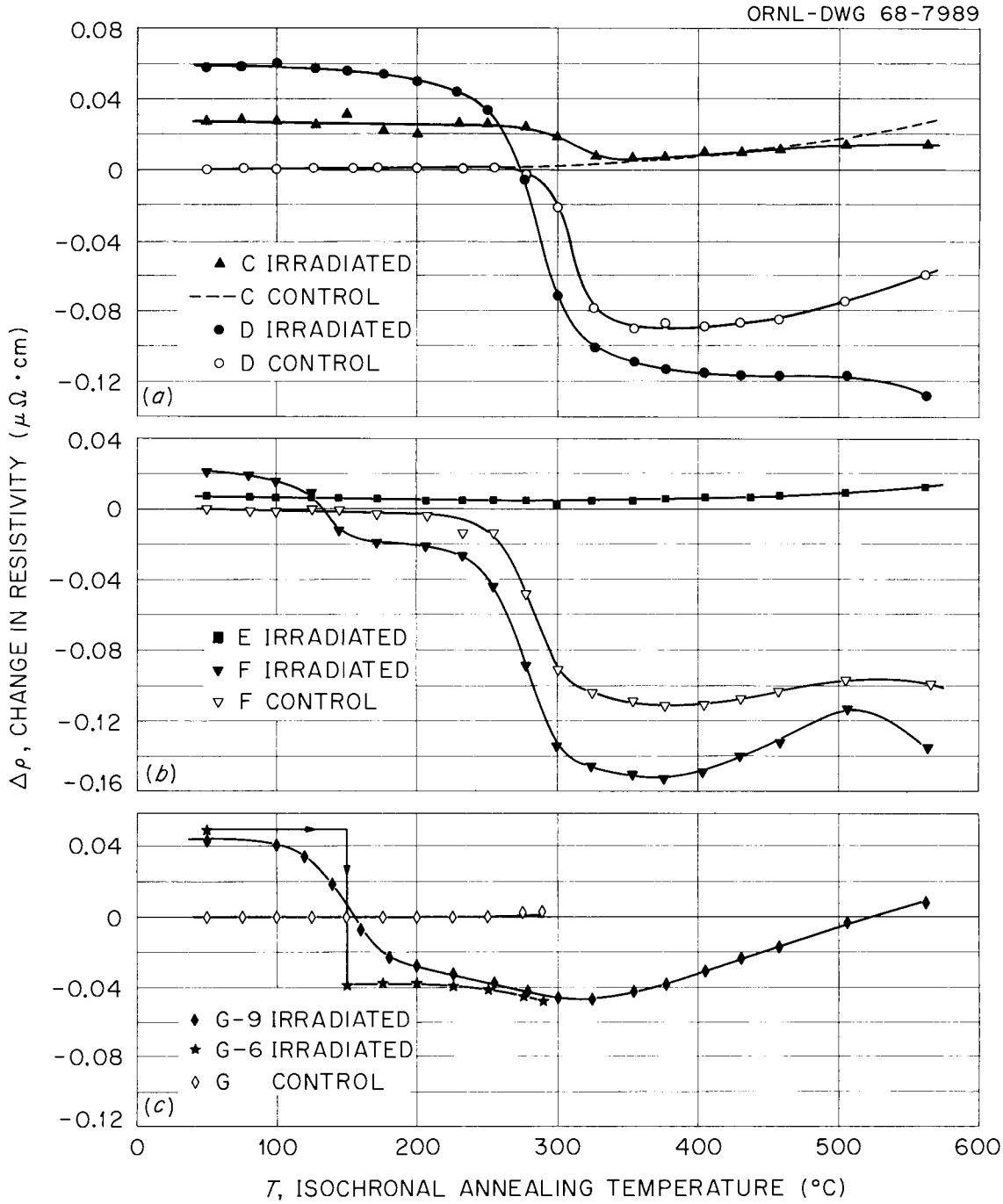

Fig. 9.3. Isochronal Annealing Curves for Niobium Samples. One-hour annealing periods (except specimen G-6, 2-hr anneal).

have been presented previously.[19,23–25] Figure 9.3 shows that only samples F and G, which exhibited oxygen Snoek peaks, show substantial resistivity decreases below 200°C. Removal of oxygen from solid solution by association with defects produced by radiation causes the resistivity to drop below the preirradiation value in this temperature region. Sample G-6 [Fig. 9.3(c)] was first isothermally annealed at 150°C and then isochronally annealed at higher temperatures. The entire resistivity decrease at 150°C was previously correlated in time with the oxygen Snoek peak decrease for this material.[24]

Figure 9.4 shows a replotting of the annealing results for material G [Fig. 9.3(c)] together with isochronal annealing results for an internal-friction sample that had previously been isothermally annealed at 150°C. We obtained the internal-friction data by annealing the samples at the temperatures shown and returning them to 150°C to measure the Snoek peak height. We used scales on the ordinates that show the resistivity decrease for sample G-6 at 150°C graphically equal to the internal-friction decrease at 150°C for G-3. Thus the isothermal line at 150°C represents both the internal-friction decrease and the resistivity decrease at this temperature. The internal friction starts to increase by 300°C, and by 550°C it goes above the preirradiation value by about 20%. Upon isochronal annealing above 150°C, sample G-6 showed a slight increase in resistivity and then decreased gradually between 200 and 325°C, the temperature range where the internal friction started to increase. Thus, although these two properties decreased in phase at 150°C, they do not increase in phase with increasing temperature, for the internal friction increases at a lower temperature than the resistivity and to a greater extent relative to the decrease at 150°C.

---

[23]J. T. Stanley, J. M. Williams, and W. E. Brundage, Quarterly Progress Report: Irradiation Effects on Reactor Structural Materials, May, June, July, 1967, BNWL-532, p. 11.17.

[24]J. T. Stanley, J. M. Williams, and W. E. Brundage, Radiation Metallurgy Section Solid State Division Progress Report for Period Ending January 1968, ORNL-4246, pp. 42–55.

[25]J. M. Williams, J. T. Stanley, and W. E. Brundage, Metal Sci. J. 2, 100 (1968).

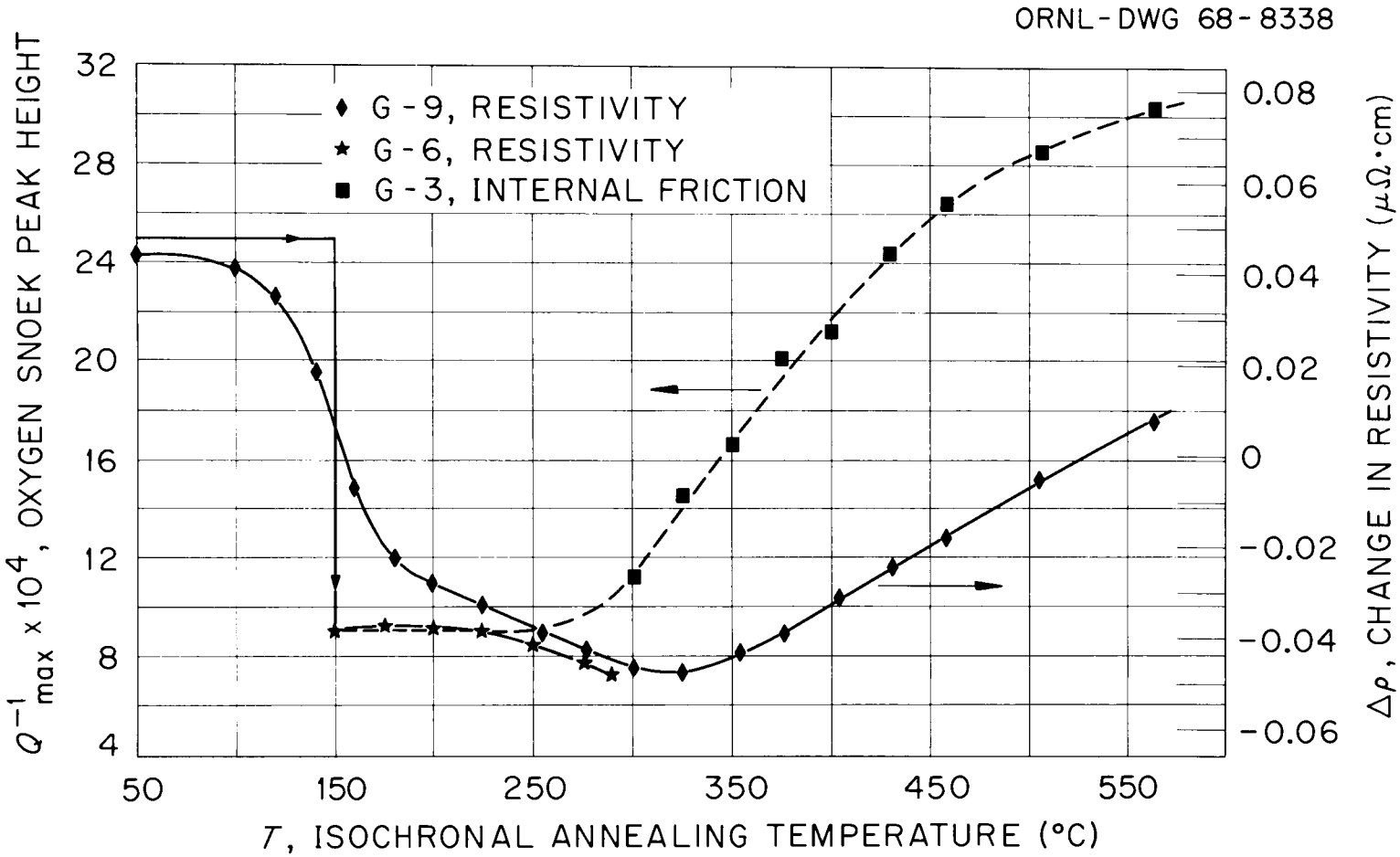

Fig. 9.4. Comparison of Postirradiation Annealing Behavior of Oxygen Snoek Peak and Resistivity for Niobium Material G. For anneals above 400°C the sample used for measurement of internal friction was dismounted from torsion pendulum and annealed in a manner similar to resistivity specimen. See text.

Discussion

We attribute the large decrease in resistivity between 200 and 350°C in materials D and F [Fig. 9.3(a) and (b)] to carbon precipitation. It occurs in both irradiated and unirradiated materials and therefore is primarily due to carbon in solution before irradiation. The effects of irradiation on carbon precipitation are not yet well understood because the precise state of the carbon in these materials before irradiation was not well defined. We presume that some of the carbon was precipitated before irradiation. Thus, in irradiated materials, carbon might precipitate on defects produced by radiation or join existing nuclei. In material D, irradiation appears to have increased the amount of precipitation and lowered slightly the temperature at which it occurs, whereas in material F irradiation has had little effect. Possibly the oxygen, being more mobile than carbon, gets first claim on the dislocation loops in material F, but in the oxygen-free material D the loops are accessible to carbon. There is a suggestion of carbon precipitation in the irradiated C material [Fig. 9.3(a)] but not in the control C material.

Irradiated material E [Fig. 9.3(b)] exhibits only a small, gradual decrease in resistivity up to 350°C, after which there is a slight increase, possibly due to contamination. The curve for sample E control is not shown, but its resistivity curve increases slightly over the whole temperature range until it merges at about 450°C with the one for the irradiated material E. Thus, for a niobium material containing only small amounts of oxygen and carbon, no significant changes in resistivity are observed.

We now turn our attention to the results for the high-oxygen, low carbon material G, shown in Fig. 9.4. It has now been established[25] that the annealing stage at about 150°C in irradiated niobium is due to the trapping of oxygen at loops or clusters of defects produced by radiation, a process that removes the oxygen from solid solution and decreases the resistivity and the height of the internal-friction Snoek peak for oxygen. Furthermore, the kinetics of the oxygen removal is consistent

with this interpretation.[26] It is to be expected that upon annealing at higher temperatures the oxygen will dissociate from the loops produced by radiation and return to solid solution with an attendant increase in resistivity and internal friction. A previous report showed increase in internal friction upon annealing up to about 500°C.[24] This increase in internal friction was irreversible, in that subsequent anneals at lower temperatures did not cause a return to the lower internal friction. This suggests that the loops produced by radiation are removed by annealing when the oxygen dissociates from them. The irreversible dissociation of oxygen from the loops occurs upon annealing above about 300°C. However, a reversible evaporation of oxygen may occur at lower temperatures, as shown by Köthe,[27] and some evidence for this is seen in Fig. 9.4 in the slight increase in resistivity at 175 to 200°C for sample G-6.

A major problem exists in explaining the larger increase above 300°C in Fig. 9.4 for internal friction as compared to resistivity when the two properties are normalized as described above. One possibility is that the increase in resistivity due to the return of oxygen to solid solution is partly compensated by a decrease in resistivity due to the annealing of the loops produced by radiation. Another possibility is that upon annealing at the higher temperatures, a contribution to the internal friction (measured at 150°C) is made from an additional source; other evidence for a "pseudo Snoek peak" is presented elsewhere in this report.[28]

---

[26]R. Bullough, J. T. Stanley, and J. M. Williams, Metal Sci. J. 2, 93 (1968).

[27]A. Köthe, Acta Met. 16, 357 (1968).

[28]J. T. Stanley, "Pseudo Snoek Peak in Niobium," pp. 222–230, this report.

Pseudo Snoek Peak in Niobium

J. T. Stanley

During some recent investigations into the effect of oxygen on the annealing of neutron-irradiated niobium, a number of specimens were prepared that exhibited an anomalous behavior of the oxygen Snoek peak. The purpose of this report is to describe the characteristics of the internal-friction peak that appears in these specimens — what we will here call the pseudo Snoek peak — and present the evidence that this pseudo Snoek peak is not a true Snoek peak.

Specimen Preparation

The specimens discussed in this report, all prepared from niobium stock obtained from Wah Chang Corporation, contained about 367 ppm Ta and 227 ppm W as major metallic impurities. The bar stock was remelted in an electron-beam floating-zone apparatus to produce single crystals 3/16 in. in diameter that were subsequently swaged and drawn to 0.030-in.-diam wire. Pieces of wire were pickled in a mixture of hydrofluoric and nitric acid, formed into a hairpin shape, and then placed into a vacuum apparatus for annealing. The wires were heated by passing an electric current through them. A number of samples for measurements of internal friction and resistivity were cut from each hairpin. These specimens were given a three part designation (e.g., S5-A-1, where the first part, S5, is the number of the starting single crystal; the second part, A, designates the hairpin; and the third part, 1, designates the individual specimen). Table 9.4 lists the annealing conditions for the various specimens discussed in this report.

The wires after annealing at high temperature had a bamboo grain structure with grains 1 to 3 mm long. The grain boundaries had an etched appearance, apparently due to preferential evaporation. Microscopic examination of the specimens revealed other structures, more faintly etched, that might be subgrain boundaries. Figure 9.5 is a photomicrograph that shows these markings on the surface of one of the specimens.

Table 9.4. Annealing Conditions for Niobium Hairpins

Hairpin Number	Temperature[a] (°C)	Time (min)	Vacuum Pressure (torr)
S5-A	1880	~ 5	9×10^{-7}
	2100	~ 5	7×10^{-7}
	2100	12	1×10^{-9}
S5-B	2100	4	2×10^{-6}
	2100	8	1.5×10^{-7}
	2100	11	3×10^{-8}
	1700	30	5×10^{-8} oxygen bled in to raise pressure from 2 to 5×10^{-8} torr
27-A	2200	100	2×10^{-9}
57-A	1900	5	4×10^{-7}
	2100	15	1×10^{-8}

[a]Specimens were heated gradually to the temperature shown; where more than one temperature is given, the specimen was heated more than once, the current being shut off between each heating.

Fig. 9.5. Photomicrograph of Surface of Niobium Wire (S5-A) Annealed at High Temperature. Wire axis is vertical in photo and the approximately horizontal dark band is a grain boundary. 200×. Reduced 50%.

Experimental Procedures and Results

We measured resistivity with the samples immersed in liquid helium inside a superconducting magnet. A field of about 17.5 kilogauss suppressed the superconductivity of niobium. We spot welded small niobium wires to the specimens to serve as potential leads and define a gage length about 1 in. long. The resistivity was measured by the potentiometer technique with a Rubicon Six Dial Microvolt Potentiometer. With these techniques, we could measure resistivity changes as the result of annealing or irradiation with a precision of ±0.01 microhm, but the absolute resistivity values are only accurate to ±4% because of the limited precision of the measurements of the lengths and diameters of the samples.

We measured internal friction in an inverted torsion pendulum placed inside an evacuated chamber. Grips and mounting fixtures were designed so that the samples could be mounted and dismounted without being bent. Thermocouples were mounted on both grips, and separate heaters maintained the grips at the same temperature.

The characteristic behavior of a specimen with a pseudo Snoek peak is shown in Fig. 9.6. The internal friction measured as temperature was increased shows no sign of an oxygen Snoek peak, but measurements made as temperature was decreased show that a large internal-friction peak appears at about the same temperature as the oxygen Snoek peak. After this initial treatment, the pseudo Snoek peak does not change with time, at least for temperatures below 250°C (the effect of further annealing at higher temperature has not yet been investigated). The pseudo Snoek peak shown in Fig. 9.6 happens to be the largest yet observed. The heights of the pseudo Snoek peaks of various specimens are listed in Table 9.5. The small peak at 295°C in Fig. 9.6 is apparently a carbon Snoek peak, since it is at the temperature of the carbon peak found by Powers and Doyle.[29] A carbon peak has been found in all but one of the specimens that exhibit the pseudo Snoek peak. The heights of the carbon peaks for the various specimens are given in Table 9.5.

---

[29] R. W. Powers and M. V. Doyle, J. Metals 9, 1285 (1957).

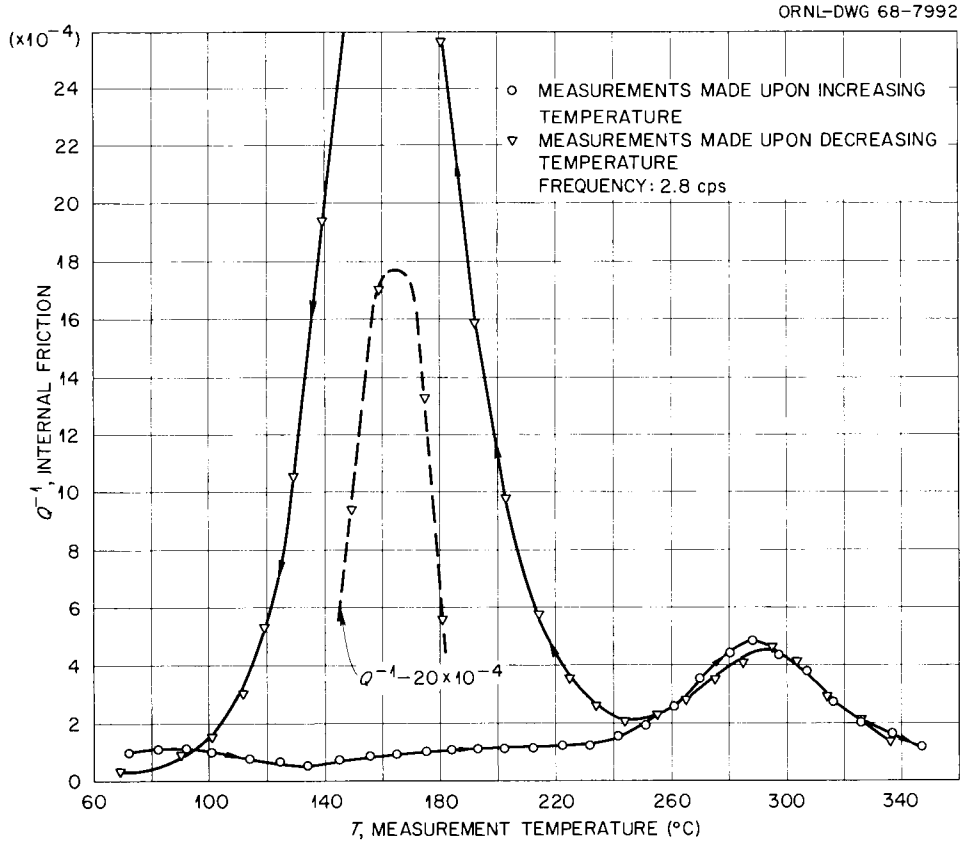

Fig. 9.6. Internal Friction vs Temperature of Specimen Nb-S5-A-3 Showing Characteristic Behavior of Pseudo Snoek Peak.

The behavior outlined above is in sharp contrast to that of specimens exhibiting a normal Snoek peak. These specimens were prepared by giving first annealing treatments similar to those listed in Table 9.4 and then adding oxygen[30] during annealing at about 1100°C. Specimens treated in this way showed oxygen peaks during the first run measurements, and the heights of the peaks remained constant for all runs on unirradiated specimens.

We investigated the effect of irradiation on the pseudo Snoek peak by irradiating specimen Nb-S5-A-4 to a fluence of 1×10^{18} neutrons/cm^2 (> 1 Mev) at 50°C. After irradiation and annealing at 145°C for 24 hr, we noted no change in the height of the

[30]J. T. Stanley, J. M. Williams, and W. E. Brundage, Quarterly Progress Report: Irradiation Effects on Reactor Structural Materials, May, June, July, 1967 BNWL-532, p. 11.17.

Table 9.5. Characteristics of Specimens Exhibiting Pseudo Snoek Peaks

Specimen	Internal Friction		Residual Resistivity		Chemical Analysis		
	Pseudo Peak	Carbon Peak	ρ_o	Concentration $= \rho_o$ 0.00068	(at. ppm)		
	$Q_\rho^{-1} \times 10^4$		($\mu\Omega$-cm)	(at. ppm)	C	O	N
S5-A-1			0.071	104	155		
S5-A-2			0.058	86		98	59
						230	66
S5-A-3	37.5	3.5	0.073	109		57	6
S5-A-4	20	3.5					
27-A-1	3.5	N.D.[a]			84	75	13
27-A-2			0.0017	25			
27-A-3			0.016	24			
27-A-4						126	6
57-A-1	2.5	2.0					
57-A-2	7.2[b]						
S5-B-1	4.5	12.5[c]				92	66
S5-B-2			0.2684	346	480[d]		
S5-B-3			0.1840	272			

[a]Not detectable.

[b]Measured after irradiation.

[c]Carbon precipitates during measurement.

[d]S5-B-2 and S5-B-3 were combined for carbon analysis.

pseudo Snoek peak. Internal friction was measured at three different frequencies for this specimen with the results shown in Fig. 9.7. The peak temperatures are plotted against logarithm of frequency in Fig. 9.8 for specimens showing pseudo Snoek peak behavior and normal Snoek peak. There appears to be a small temperature difference between the temperature of the Snoek peak and the temperature of the pseudo Snoek peak for a given vibration frequency. This temperature difference is only 1.5°C at 0.8 cps, but we believe it is a real effect. The two straight lines in Fig. 9.8 have the same slope, corresponding to an activation energy of 26,800 cal/mole.

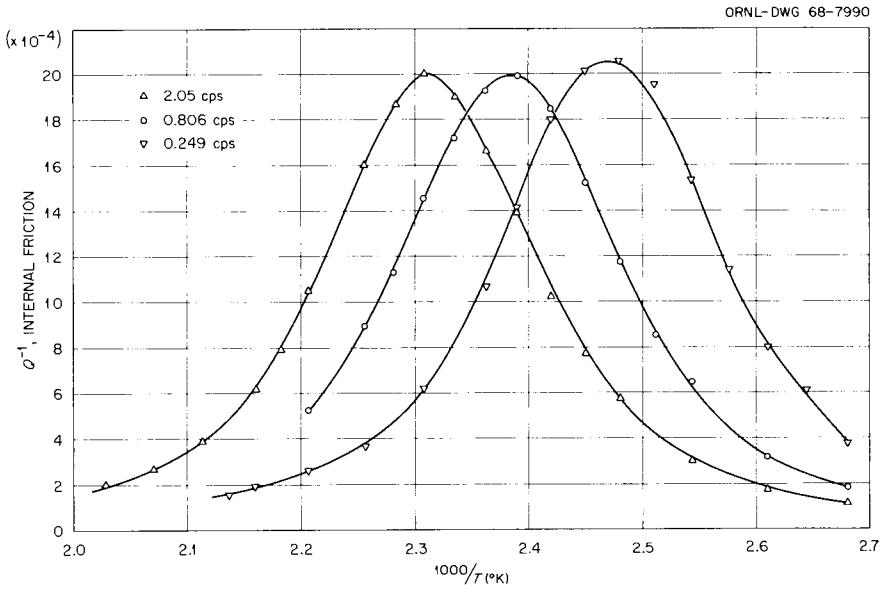

Fig. 9.7. Internal Friction vs Reciprocal Temperature of Specimen Nb-S5-A-4 for Different Vibration Frequencies.

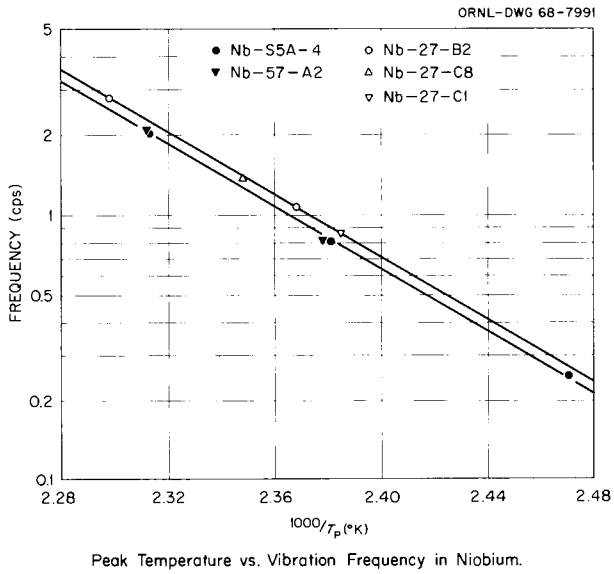

Fig. 9.8. Arrhenius Plots for Snoek Peak (Open Points) and Pseudo Snoek Peaks (Filled Points) in Niobium.

Discussion

The results presented in the previous section show that what we are calling the pseudo Snoek peak has many characteristics the same as those of the normal Snoek peak. Thus, our first task is to present the arguments that the pseudo Snoek peak is different from the real Snoek peak.

Clearly the most distinguishing characteristic of the pseudo Snoek peak is that it does not appear upon first measurement of specimens that were outgassed at high temperatures. However, after the initial series of measurements, which are made up to about 340°C, the pseudo Snoek peak appears fully developed. The initial reaction of many who have seen these data is that the specimen became contaminated with oxygen during the measurements. Contamination, however, can be ruled out by a number of arguments. Specimen Nb-27-A-1, which showed only a small pseudo peak, was deliberately held at 350°C for 16 hr in a vacuum of 2×10^{-2} torr to see if the peak would incraase. A small increase from 3.5 to 5×10^{-4} was observed, but this was much smaller than the increase observed in specimens S5-A-4 and -3, which were held only a few hours at 350°C in a vacuum of 10^{-4} torr.

Another argument against contamination is the resistivity measurement that was made on Nb-S5-A-3 after the pseudo Snoek peak had been fully developed. The resistivity of this specimen was 0.073 microhm-cm at 4.2°K. If we assume that this residual resistivity is entirely due to interstitial impurities and use the value of Tedmon, Rose, and Wulff[31] for the resistivity contribution of an oxygen atom, then the total interstitial impurity content would be 110 ppm (atomic). However, the height of the internal-friction peak in this specimen corresponds to 570 ppm (atomic) oxygen if we use the value of Szkopiak[32] for the conversion of peak height to oxygen concentration. It should be noted that

---

[31] C. S. Tedmon, Jr., R. M. Rose, and J. Wulff, Trans. Met. Soc. AIME 230, 1732 (1964).

[32] Z. C. Szkopiak, Internal Friction in Niobium Oxygen Solid Solution, UKAEA TRG Report 1151(C/X) 1966.

Szkopiak's value is the lowest value yet reported in the literature while the resistivity conversion factor is also the largest reported in the literature; therefore, if other reported values were used, the discrepancy between the two values would increase. There is also some evidence from measurements of internal friction and from chemical analyses that sample Nb-S5-A-3 contains some carbon, and so a fraction of the residual resistivity must be due to carbon making the discrepancy between residual resistivity and oxygen peak height even greater.

The results of the vacuum-fusion analysis made on specimen Nb-S5-A-3 after the measurements of internal friction were somewhat inconclusive. The specimen was cut into two parts, and one piece was etched in hydrofluoric-nitric acid to remove about 0.001 in. from the diameter before the analysis was made. The other part was analyzed without etching. The etched half showed an oxygen content of 340 ppm (atomic) while the unetched half showed an oxygen content of 57 ppm (atomic). The same procedure was used on another specimen cut from the Nb-S5-A hairpin, which had not been used for any measurements of internal friction or resistivity. In this case, analysis showed 230 ppm (atomic) in the etched sample and 97 ppm (atomic) in the unetched sample. We believe that these results also indicate that contamination is not the cause of the large peak for internal friction in specimen Nb-S5-A-3.

A second major difference between the behavior of the normal Snoek peak and the pseudo Snoek peak was observed for the irradiated specimens. Specimens with a normal Snoek peak showed a decrease of the Snoek peak after irradiation and annealing at 150°C (ref. 33). This is caused by migration of oxygen atoms to defects produced by radiation (primarily, small, prismatic dislocation loops). The specimen with a pseudo Snoek peak, however, did not show the decrease after irradiation and annealing. This implies that these really are two different effects occurring in this temperature range.

---

[33] J. T. Stanley, J. M. Williams, and W. E. Brundage, Radiation Metallurgy Section Solid State Division Progress Report for Period Ending January 1968, ORNL-4246, pp. 42–55.

We are unable to offer a satisfactory explanation for the pseudo Snoek peak or even to state what conditions are necessary for its occurrence. From the limited experience available, however, it does appear that a large concentration of oxygen in solution suppresses the pseudo Snoek peak.

Radiation Anneal Hardening in Niobium

S. M. Ohr R. P. Tucker[34]

We have reported[35] changes in the tensile properties and distribution of defect sizes present in neutron-irradiated polycrystalline niobium after postirradiation anneals between 200 and 800°C. In addition to a 5.8-kg/mm^2 increase in the yield stress following irradiation to a fluence of 2×10^{18} neutrons/cm^2 (> 1 Mev), a further increase of up to 8.5 kg/mm^2 in yield stress was observed upon annealing in the temperature range 200 to 400°C. We suggested that carbon atoms migrate to defects produced by radiation during the anneal and then are trapped by the defects. The trapped carbon atoms strengthen the defects as barriers to dislocation motion, thus causing further increase in the yield stress. This proposed strengthening mechanism was based in part on the experimental evidence of Williams et al.,[36,37] who used internal-friction and electrical resistivity techniques, that indicates that carbon atoms migrate in the temperature range where the hardening peak was observed. Here we describe the result of a further investigation into radiation anneal hardening and an analysis of the hardening process.

---

[34]Oak Ridge Graduate Fellow from the University of Tennessee under appointment from Oak Ridge Associated Universities.

[35]S. M. Ohr, R. P. Tucker, and E. D. Bolling, Radiation Metallurgy Section Solid State Division Progress Report for Period Ending January 1968, ORNL-4246, pp. 55–66.

[36]J. M. Williams, J. T. Stanley, and W. E. Brundage, Quarterly Progress Report: Irradiation Effects on Reactor Structural Materials, November, December 1966–January 1967, BNWL-CC-1053, p. 11.18.

[37]J. M. Williams, J. T. Stanley, and W. E. Brundage, Metal Sci. J. 2, 100 (1968).

Figure 9.9 shows transmission electron micrographs of the deformation structures of as-irradiated and postirradiation-annealed niobium. In the as-irradiated sample, the structure is characterized by numerous dislocation channels from which defect clusters have been removed by moving dislocations. In samples that were given postirradiation anneal at 400°C for 2 hr and subsequently deformed to nearly identical strains, there is very little evidence of dislocation channeling. This observation is consistent with the conclusion reached previously that the defect clusters are strengthened as barriers by the trapped interstitial impurities.

Additional evidence in support of the impurity trapping mechanism of radiation anneal hardening is found in an experiment in which the carbon content in niobium samples was reduced from the previous level of 60 to 30 ppm by weight. In these low-carbon samples, the maximum hardening was observed after an anneal at 300°C for 2 hr, and the magnitude of the anneal hardening was reduced roughly by one-half. In addition, a small increase in the yield stress was also observed after

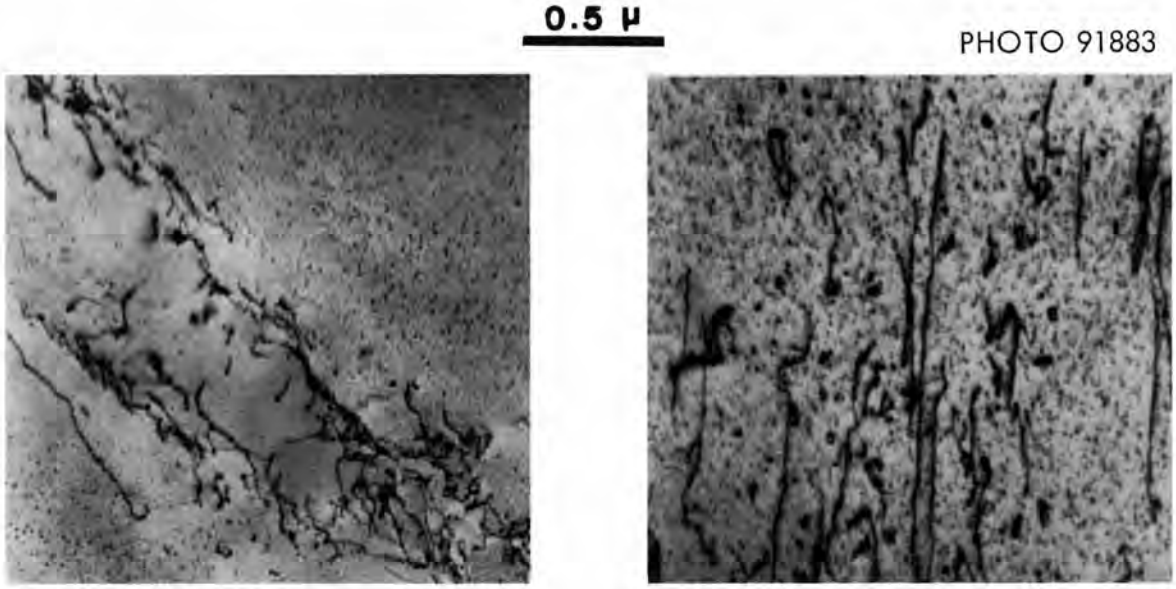

(a) 2×10^{18} neutrons/cm^2 (E > 1 Mev) $\epsilon = 2.0$ %

(b) 2×10^{18} neutrons/cm^2 + 400°C 2 hrs $\epsilon = 1.7$ %

Fig. 9.9. Deformation Structure of (a) As-Irradiated and (b) Postirradiation Annealed Niobium.

a 2-hr anneal at 150°C. According to Williams et al., this is the temperature range where interstitial oxygen migrates to defect clusters. Thus, all of the evidences accumulated so far indicate clearly that the radiation anneal hardening in niobium is impurity controlled.

Let us consider in detail the mechanism of radiation anneal hardening in niobium in terms of dispersed barrier interaction between trapped interstitial impurity atoms and moving dislocations. Following neutron irradiation to a fluence of 2×10^{18} neutrons/cm^2 (> 1 Mev), defect clusters identified as dislocation loops at a density of 6.1×10^{15}/cm^3 with an average diameter of 93 A have been observed by transmission electron microscopy in niobium.[38] With 60 ppm C by weight in niobium, the maximum number of carbon atoms available per loop defect is approximately 4000. During postirradiation anneals, some of these carbon atoms are believed to migrate to the loops. The kinetics of impurity migration to dislocation loops has been discussed recently by Bullough et al.[39] for the case of oxygen migration in niobium. They found that in the early stage of impurity migration, the number of impurities, N, that arrive at the loop in time, t, is given by

$$N(t) = 5.3\ C_o\ (ADt/T)^{3/5}\ , \qquad (9.5)$$

where C_o is the initial concentration of impurity in solution, A is the interaction parameter of Cottrell and Bilby, D is the diffusion constant, and T is the absolute temperature. The resistivity measurements of oxygen migration in niobium indicate that a $t^{3/5}$-law is obeyed until about 20% of the available impurities have reached the loops. The rate of arrival of impurities then decreases rapidly, and the impurity atmosphere around the loops is saturated. According to the available diffusion data for carbon in niobium[40] the saturation of impurities on

---

[38] R. P. Tucker and S. M. Ohr, Phil. Mag. 16, 643 (1967).

[39] R. Bullough, J. T. Stanley, and J. M. Williams, Metal Sci. J. 2, 93 (1968).

[40] R. W. Powers and M. V. Doyle, J. Appl. Phys. 30, 514 (1959).

dislocation loops is expected to occur after 2 hr at 300°C. By this time, approximately 840 carbon atoms arrive at the loop, or roughly 8 carbon atoms per atomic site around the loop. Cochardt et al.[41] have shown theoretically that an edge dislocation in iron can accommodate about 8 carbon atoms per atomic site. Thus, the hardening maximum observed after anneals around 300°C for 2 hr is consistent with the formation of saturated Cottrell atmospheres of carbon atoms around the loops as predicted by the kinetics of impurity migration.

It is not now known how the trapped carbon atoms around the dislocation loops would interact as a group with moving dislocations. It has been estimated[42] that the interaction energy of a carbon atom with a dislocation in iron is approximately 0.5 ev. This interaction energy leads to the maximum restoring force per single carbon atom of

$$F_m = \mu b^2/16 \ , \tag{9.6}$$

where μ is the shear modulus and b is the Burgers vector. For a group of carbon atoms, the maximum restoring force may be written as $n\mu b^2/16$, where n is the multiplication parameter. The increase in the yield stress is then given by

$$\Delta\sigma = 2\ F_m/b\ell = n\mu b^2/8\ b\ell \ , \tag{9.7}$$

where ℓ is the planar spacing of the defects. After neutron irradiation to a fluence of 2×10^{18} neutrons/cm^2 (> 1 Mev), the spacing ℓ is found to be 1.3×10^{-5} cm, and the magnitude of anneal hardening, $\Delta\sigma$, after 300°C for 2 hr is 7.3 kg/mm^2. With these available data, the multiplication parameter, n, is 7.2. This is very close to the estimated number of carbon atoms trapped per atomic site after the postirradiation anneal.

---

[41] A. W. Cochardt, G. Schoek, and H. Wiedersich, Acta Met. 3, 533 (1955).

[42] A. H. Cottrell, Dislocations and Plastic Flow in Crystals, p. 134, Oxford University Press, London, 1953.

Since the moving dislocation intersects the defect at a point, it is reasonable to expect that only the carbon atoms present in a single atomic plane interact by contact with moving dislocations.

Dislocation Channeling in Neutron-Irradiated Niobium

R. P. Tucker[43] · M. S. Wechsler

In recent years, there have been a considerable number of observations by transmission electron microscopy of defect clusters resulting from neutron irradiation (e.g., for body-centered cubic metals, iron,[44,45] molybdenum,[46–50] and niobium[38,51]). Plastic deformation following irradiation produces pathways cleared of defect clusters in a matrix that retains its as-irradiated appearance. The cleared pathways generally coincide with traces of planes upon which slip is expected. It is, then, reasonable to associate the formation of these pathways with a defect-sweeping action by dislocations moving on the slip plane. The term "dislocation channel" describes the cleared pathway observed by transmission electron microscopy (TEM), and the term "dislocation channeling," describes the process by which the pathway or channel forms. The dislocation channel observed in TEM foils is bounded by the surfaces of the foil and by the walls of the channel. The "channel plane" is one

---

[43]Oak Ridge Graduate Fellow from the University of Tennessee under appointment from Oak Ridge Associated Universities.

[44]B. L. Eyre, Phil. Mag. 7, 2107 (1962).

[45]B. L. Eyre and A. F. Bartlett, Phil. Mag. 12, 261 (1965).

[46]B. Mastel, H. E. Kissinger, J. J. Laidler, and T. K. Bierlein, J. Appl. Phys. 34, 3637 (1963).

[47]M. E. Downey and B. L. Eyre, Phil. Mag. 11, 53 (1965).

[48]B. Mastel and J. L. Brimhall, Acta Met. 13, 1109 (1965).

[49]J. D. Meakin and I. G. Greefield, Phil. Mag. 11, 277 (1965).

[50]P. Rao and G. Thomas, Acta Met. 15, 1153 (1967).

[51]S. M. Ohr, R. P. Tucker, and M. S. Wechsler, "Radiation Hardening in bcc Metals Niobium and Iron," in Proceedings of the International Conference on Strength of Metals and Alloys, Japan Institute of Metals, Fendai, Japan, 1968.

of a set of planes parallel to the wall of the channel, and the "channel trace direction" is along the line of intersection of the channel wall and the foil surface.

Several years ago, Cottrell[52] proposed that each dislocation slipping on a plane upon which defect clusters are scattered would sweep away some of the defects, making the passage of subsequent dislocations on the swept plane easier and resulting in localized "runaway" slip. One of the first direct observations of dislocation channels was made by Greenfield and Wilsdorf[53] in irradiated-and-deformed copper. Seeger and Essmann[54,55] indicated the correlation between dislocation channels and coarse, surface slip-markings in irradiated copper. Recently, Sharp[56] studied the effects of deformation temperature, dose, and strain on the width of defect-free channels in single crystals of neutron-irradiated copper and compared these results with those for surface slip bands. On the basis of the agreement between the channel width and channel spacing when compared with values for slip bands determined from surface replicas, Sharp's results strongly indicate a correspondence between surface slip markings and dislocation channels.

In body-centered cubic metals, dislocation channels have been observed in irradiated-and-deformed iron,[45] molybdenum,[46,57] and niobium.[38,51] The dislocation channels in molybdenum were found to be consistent with slip on {110} and {112} planes.[46,57] In the past, however, relatively little was reported on dislocation channeling in the

---

[52]A. H. Cottrell, "Point Defects and the Mechanical Properties of Metals and Alloys at Low Temperatures," p. 1 in Vacancies and Other Point Defects in Metals and Alloys, The Institute of Metals, London, 1958.

[53]I. G. Greenfield and H.G.F. Wilsdorf, J. Appl. Phys. 32, 827 (1961).

[54]U. Essmann and A. Seeger, Phys. Status Solidi 4, 177 (1964).

[55]A. Seeger, "Work Hardening of Metal Single Crystals, Slip Lines, and Transmission Electron Microscopy," p. 3 in The Relation Between the Structure and Mechanical Properties of Metals, H.M. Stationery Office, London, 1963.

[56]J. V. Sharp, Phil. Mag. 16, 77 (1967).

[57]J. L. Brimhall, Trans. Met. Soc. AIME 233, 1737 (1965).

body-centered cubic metals aside from the observation that it exists. Our study was conducted to investigate in greater detail the crystal geometry of channeling in neutron-irradiated niobium. Particular configurations of dislocation channeling were observed using several diffraction vectors that permitted the Burgers vectors of prominent dislocations snagged along the walls of the channel to be deduced. We also examined one case under stereo conditions, which permitted an unambiguous determination of the channel shape. As a result of the study, we found that most of the channel planes were {110}, although a few cases of {112} channel planes were also observed. Some conclusions are drawn concerning the number of dislocations sweeping along the channel from observations of the offset of such markers as low-angle boundaries and dislocation helices when they are intersected by dislocation channels. Finally, some discussion is given of the mechanism of dislocation channeling.

Experimental Details

The niobium used in this study was obtained as dendritic powder from CIBA Limited. The powder was drop-cast to yield a small ingot, which was subsequently swaged into 3/16-in.-diam rod. The rod was seeded and given two electron-beam molten-zone passes, yielding a single crystal oriented for maximum resolved shear stress on the $(\bar{1}01)$ [111] slip system (see refs. 58 and 59 for details on the desired orientation). The single crystal was cold-rolled to sheet about 0.13 mm thick from which tensile samples 4.2 mm wide and 12.7 mm in gage length were stamped. The samples were given a recrystallization anneal at 1050°C for 1 hr at about 3×10^{-8} torr. This resulted in an average grain

---

[58] R. P. Tucker, The Effect of Neutron Irradiation on Plastic Deformation in Niobium Single Crystals, ORNL-TM-1583 (November 1966).

[59] R. P. Tucker, R. E. Reed, and M. S. Wechsler, Radiation Metallurgy Section Solid State Division Progress Report for Period Ending February 1966, ORNL-3949, p. 63.

diameter of 44 μ (see Fig. 28 of ref. 60). The impurity content of the recrystallized material is shown below:

Impurity	Content by Weight (ppm)
C	60
O	38
H	2
N	5
Ta	20
W	10
Zr	10
Hf	5
Fe	1

Although no systematic study has yet been conducted to characterize this material, the grains exhibit a preferred orientation with [111] nearly perpendicular to the sample surface as determined by the electron diffraction patterns for electron microscope foils taken from the tensile samples.

The tensile samples from which we cut the TEM samples were two of those used in a fluence-dependence study described in a previous report.[60] The irradiations were carried out in tube 12 of the hydraulic facility of position F-8 in the ORR where the neutron flux as determined by nickel monitors was 2.0×10^{13} neutrons cm^{-2} sec^{-1} (> 1 Mev) and the irradiation temperature was below 50°C. The fluences received by the samples examined for dislocation channels were (sample A) 1.8 and (sample B) 4.4×10^{18} neutrons/cm^2. After a waiting period for radioactive decay, the sheet samples were deformed in tension in the laboratory at room temperature at a crosshead speed of 0.01 cm/min, which corresponds to a strain rate of 1.3×10^{-4}/sec. Samples A and B were examined in the electron microscope after being strained 2.7 and 6.6%, respectively. These strains correspond essentially to the strain at the lower yield stress, the lower yield stress being reached at a lower strain for sample A. The stress-strain curves for the two samples show

[60] M. S. Wechsler, R. P. Tucker, and S. M. Ohr, Radiation Metallurgy Section Solid State Division Progress Report for Period Ending January 1968, ORNL-4246, p. 66.

well-defined, sharp yield drops with a difference between the upper and lower yield stresses of 3.38 (sample A) and 3.81 kg/mm^2 (sample B). The curves are generally smooth in appearance with only the slightest evidence of "jerky flow." The lower fluence sample (sample A) is above the fluence level where saturation in the fluence dependence of the yield stress begins (see Fig. 30 in ref. 60). The particular sample examined as sample A exhibits yield stresses somewhat higher than expected for its fluence level and actually even higher than the corresponding stresses for sample B. For sample A, the upper and lower yield stresses were 14.44 and 11.06 kg/mm^2, respectively, and for sample B, 14.16 and 10.35 kg/mm^2, respectively.

Pieces about 6 mm square were cut from the deformed sheet samples and electrolytically thinned to about 2500 A in a solution that was 85 parts nitric acid and 15 parts hydrofluoric acid by volume. The foils were examined in a Hitachi 11A electron microscope operated at 100 kv and equipped with a stage that could be tilted and rotated. The two degrees of freedom in the stage were used to obtain stereo pairs of photographs and were convenient for varying the diffraction vector, $\vec{g}$ For the stereo pairs, the normal to the foil surface was tilted approximately 8.5° from the electron beam. In correlating the micrographs and diffraction patterns, we allowed for both the intermediate lens rotation and the extra inversion of the image by the objective lens for the micrograph. The micrographs were printed to give normal positive prints (i.e., with the emulsion of the plate facing the emulsion of the printing paper).

Results

In this section we present a series of transmission electron micrographs illustrating various features of dislocation channeling in irradiated-and-plastically-deformed niobium. On the right below are the principal features for each case listed on the left:

Case 1.	a.	Regular channel array composed of two sets of channels, one set perpendicular to foil surface and one set inclined.
	b.	Snagged dislocations primarily on only one side of channel 2
	c.	Tangles at channel intersections
Case 2.	a.	Regular channel array
	b.	Paired dislocation channels
	c.	Channel-channel offset
	d.	Channels in early stage
	e.	Tangles at channel intersections
Case 3.	a.	Triangular pattern of channels
	b.	$\vec{g} \cdot \vec{b}$ criterion applied
	c.	Channel-channel offset
	d.	Conclude {110} type channel planes
Case 4.	a.	Dislocation array in channel
	b.	Splitting off of channels due to cross slip
	c.	Channel not perpendicular to foil surface
	d.	Edge-screw character analyzed
	e.	$\vec{g} \cdot \vec{b}$ criterion applied
	f.	Some tangle dislocations identified
Case 5.	a.	Dislocation helix with depleted zone
	b.	Channel-boundary offset
	c.	Channel-helix offset
Case 6.	a.	Channel-boundary offset
	b.	Channel created at channel-boundary intersection
	c.	Channel extending across boundary
	d.	Depleted zone near boundary
Case 7.	a.	Sample A (all others were sample B)
	b.	Dislocation cell structure within channel
	c.	Dislocations not rigidly confined to channel

Case 1 (Fig. 9.10). — Figure 9.10 shows a nearly rectangular grid in sample B composed primarily of two sets of channel traces, denoted by 1 and 2. The plane of the micrograph is (111), and the operating reflection is $[\bar{1}10]$. As shown in the figure, the approximate trace directions for channels 1 and 2 are $[\bar{1}\bar{1}2]$ and $[\bar{1}10]$, respectively. For channel 1 the channel interface is sharp, the dislocation lines are largely out of contrast, and the faint images of the dislocation lines indicate that their projections in the (111) plane are parallel to the trace direction, $[\bar{1}\bar{1}2]$. This suggests, as discussed more fully below (e.g., see case 4), that the channel plane 1 is perpendicular to the foil surface and thus identified to be $(1\bar{1}0)$ and that the channeling

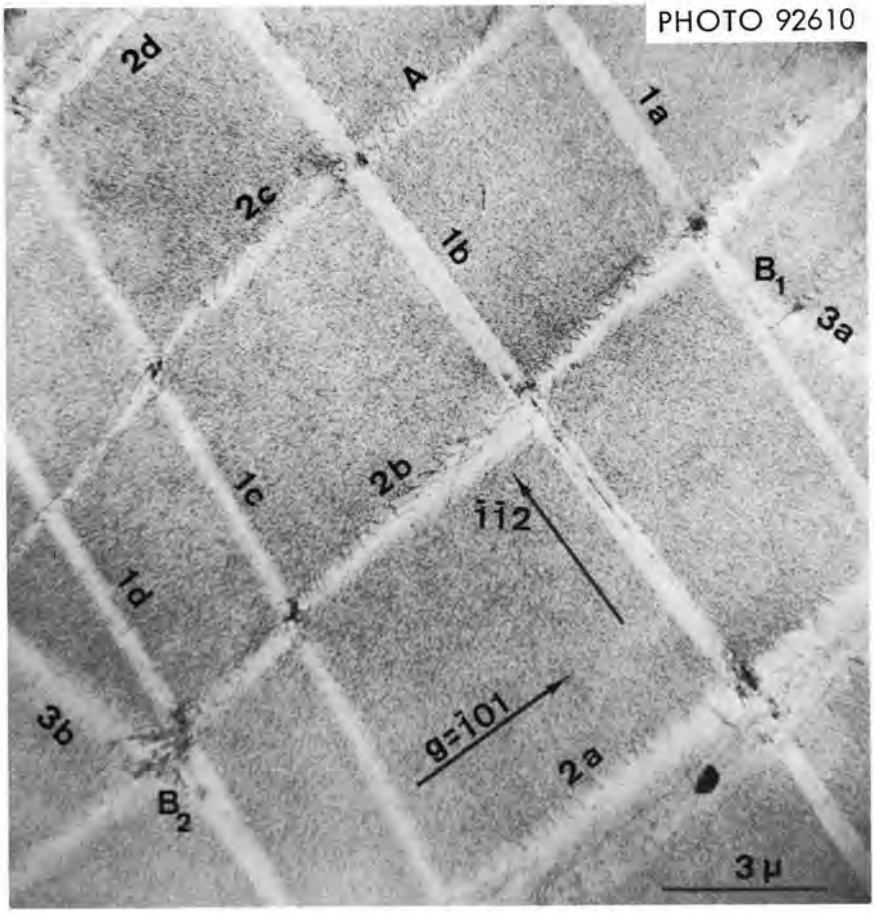

Fig. 9.10. Nearly Rectangular Pattern of Dislocation Channels in Sample B as Revealed by Transmission Electron Microscopy. (Case 1).

dislocations seen in the micrograph are probably screw dislocations with Burgers vector $(a/2)[11\bar{1}]$. On the other hand, the edges of channel 2 are less well defined, the dislocations at their edges are in strong contrast, and the projections of the dislocations in (111) generally appear to lie across the channel trace (e.g., at A in channel 2c). From this we conclude that those of channel 2 are inclined to the foil surface and are identified as (110) and that the channeling dislocations have $(a/2)[\bar{1}11]$ for their Burgers vector (see case 4).

It is interesting that the dislocations in channel 2 appear to be associated preferentially with one wall of the channel. We note also that channels labeled 1 are straight and of uniform width over rather long distances. The defect density near the channel walls is the same as it is well within the matrix. An increased defect density would be

expected if channeling dislocations caused defect loops unfavorably oriented for the sweeping process to move to the channel wall, say by prismatic slip. On the other hand, if many errant dislocations penetrated the channel walls, say by cross slipping into the matrix, a region of gradually increasing defect density adjacent to the channel would be expected. For channel 2, there is some suggestion of variation in defect density near the channel wall. This can, however, be accounted for on the basis of the wedge-shaped matrix region formed because of the inclined walls of channel 2.

A feature noted repeatedly is the dislocation tangling at the intersections of the channels. Another feature seen occasionally is the splitting and veering off of dislocation channels as seen in Fig. 9.10 at B_1 and B_2. This is discussed further for case 4 below.

Case 2 (Fig. 9.11). – Several interesting features are seen in the micrographs of Fig. 9.11 which are of overlapping areas in sample B. The plane of the foil is again near (111). Here the channels also form a rather orderly array, but the crystal geometry is less certain than for the channels in Fig. 9.10. From the observed trace direction, $[1\bar{2}1]$, we judge that the channels that lie diagonally in the micrographs (e.g., A and A′) are most likely $(\bar{1}01)$ planes channeled by $[1\bar{1}1]$ dislocations. The determination of the indices of the generally vertical channels (channels V) is less certain because of their lack of parallelism and their changes of direction. The {110} plane that has a trace nearest the direction of these channels is $(\bar{1}10)$. In Fig. 9.11, tangles are observed at the intersections of most channels, and in some cases the local tilting of the lattice due to the tangle is sufficient to cause essentially complete diffraction of the beam, which produces the dark regions at some intersections. Several dislocations can be seen in the matrix outside of the well-formed channels. These dislocations are, we presume, contributing to the formation of the numerous, ill-defined, narrow channels in Fig. 9.11(a) (e.g., at B), which are along the trace direction $[1\bar{2}1]$ for $(\bar{1}01)$ planes.

A noteworthy feature occurs where the nearly vertical channels, V_1–V_4, cross the diagonal ones, A_1–A_4, in Fig. 9.11. At many of these intersections, the diagonal channel experiences an offset, with the

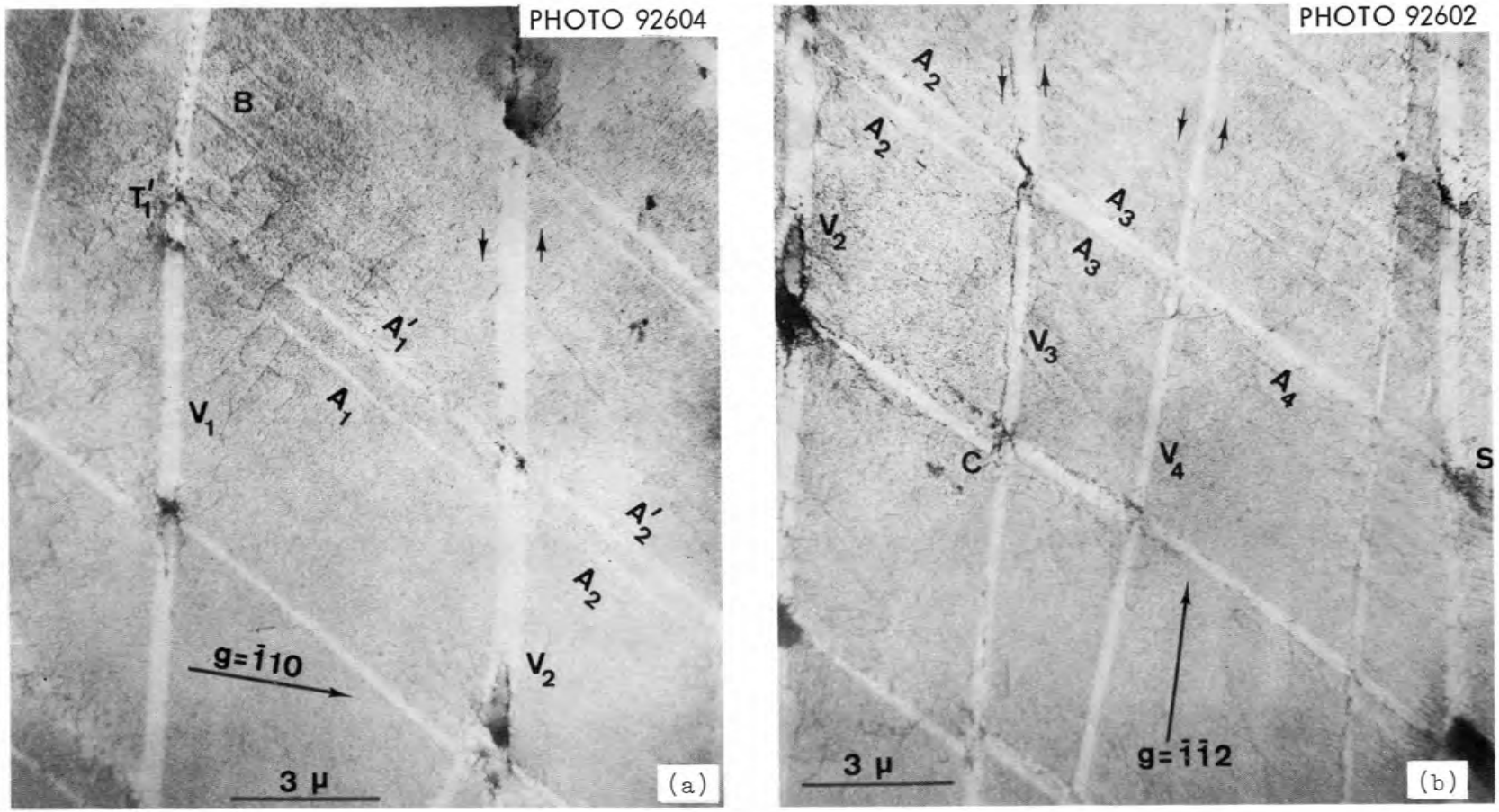

Fig. 9.11. Cross Grid of Dislocation Channels Showing Dislocation Tangles at Intersections and Channel-Channel Offset (Case 2).

segment to the right of the vertical channel sheared upward with respect to the segment to the left. For example, such an offset is seen at C in Fig. 9.11(b). Another interesting feature is the pair of channels A and A′, whose entire length can be seen in Fig. 9.11. Tangles are again seen at the ends of the channels and at most intersections along their lengths. The upper channel segments, A_1', A_2', and A_3', are essentially straight and in line, while the lower channel segments, A_1, A_2, A_3, and A_4, are offset from one another at intersections with V channels. It seems reasonable to postulate the following sequence of events. Initially, a diagonal channel extended from S to T_1', possibly due to the operation of a source at S. Then, the channels V_2, V_3, and V_4 operated, causing the shear displacements indicated by the arrows in Fig. 9.11. This caused the channel that previously extended from S to T_1' to consist of the offset segments A_4, A_3, A_2, and A_1. Finally the source at S operated again to produce the in-line channel segments A_3', A_2', and A_1'.

Case 3 (Fig. 9.12). – Figure 9.12 shows an equilateral-triangular pattern of channels on a (111) foil surface from sample B. The sketch in Fig. 9.12(a) gives the number designations of the channels, the channel trace directions as obtained from the electron diffraction patterns, and the slip systems operating in the channels. The operating slip systems (i.e., the planes of the channels and the Burgers vectors of the slip dislocations) were deduced as described below. This determination was facilitated by the diffraction contrast analysis of electron micrographs of the same field taken with $[01\bar{1}]$, $[10\bar{1}]$, and $[1\bar{1}0]$ operating reflections ($\vec{g}$ vectors), as shown in Fig. 9.12(b), (c), and (d), respectively. The vertex angles of the triangle in Fig. 9.12 were measured in the micrographs to be 60° ±2.5.

Now consider planes of the {110}, {112}, and {123} types as possible slip planes. There are two sets of three {110}-type planes that give traces 60° apart in a (111) plane. Of these two sets, only one – $(01\bar{1})$, $(10\bar{1})$, and $(1\bar{1}0)$ – will give rise to channel traces in the observed ⟨112⟩ directions. The traces for the other set – (011), (101), and (110) – form an equilateral triangle rotated 60° about [111] from the trace directions observed. The normals for the three {110} planes corresponding to the observed channel traces lie in the (111). Thus,

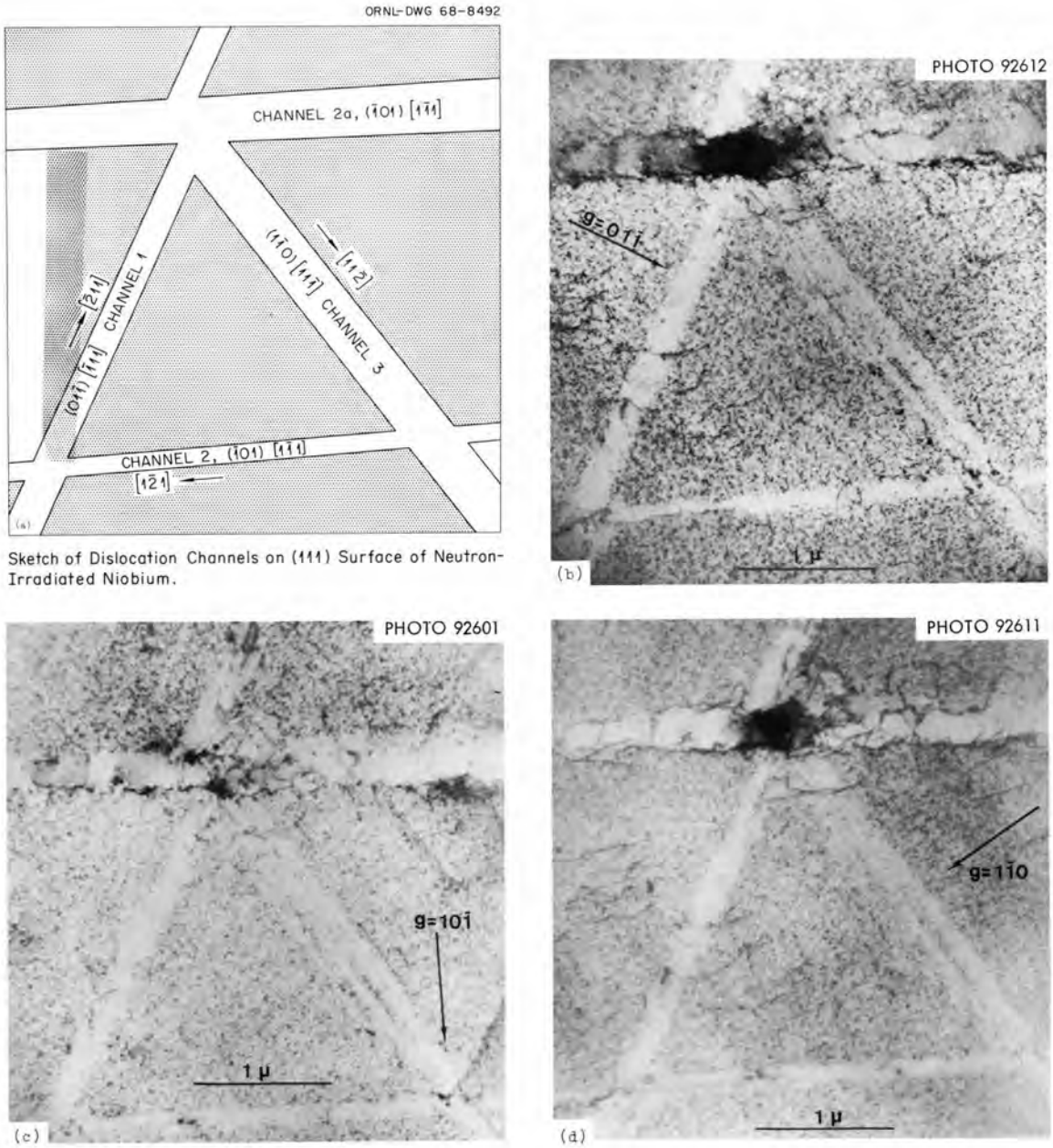

Sketch of Dislocation Channels on (111) Surface of Neutron-Irradiated Niobium.

Fig. 9.12. Triangular Pattern of Dislocation Channels from Sample B. (a) Sketch of Channel Geometry, (b) Transmission Electron Micrograph for $\vec{g} = [01\bar{1}]$, (c) Transmission Electron Micrograph for $\vec{g} = [10\bar{1}]$, (d) Transmission Electron Micrograph for $\vec{g} = [1\bar{1}0]$. (Case 3).

the channeled {110} planes would form a right equilateral-triangular prism whose axis is along [111]. Since there are no {112} planes that give ⟨112⟩ traces in a (111) plane, {112} channel planes may be discounted. As for {123} planes, there are two planes of this type that give traces in each of the required ⟨112⟩ directions. In all cases the angle between the normals to these {123} planes and [111] is 22° 12'.

Now consider the contrast of the dislocations for the various operating reflections shown in Fig. 9.12. Most of the dislocations lie parallel to, but not always in, the channel trace. In body-centered cubic metals, the ⟨111⟩ close-packed direction is the normal slip direction and hence the direction of the Burgers vector for slip dislocations. Diffraction contrast theory[61] predicts that when the Burgers vector, $\vec{b}$, lies in the reflecting plane the dislocation is invisible if it is pure screw and generally exhibits weak contrast or is invisible if it is pure edge. Thus $\vec{g} \cdot \vec{b} = 0$ means invisibility or weak contrast for dislocations, where $\vec{g}$ is the diffraction vector. In Tables 9.6 and 9.7 the contrast for dislocations under three operating reflections (see Fig. 9.12) is compared to $\vec{g} \cdot \vec{b}$ for ⟨111⟩ Burgers vectors. From these tables we conclude that the Burgers vector for dislocations lying parallel to the traces of channels 1, 2, and 3 are (a/2) $[\bar{1}11]$, (a/2) $[1\bar{1}1]$, and (a/2) $[11\bar{1}]$, respectively.

It should be noted, as shown in Table 9.7, that the [111] dislocations are always invisible for reflections from planes of the 111 zone. However, since the tensile axis lies in (111) to within a few degrees, [111] dislocations would be subjected to little or no shear stress under uniaxial tension for the sample geometry used. These dislocations could experience stress resulting from the nonuniaxial stress state that exists in polycrystalline material; nevertheless, [111] dislocations are expected to be of relatively little importance in the deformation under consideration. Therefore, the three reflections in Fig. 9.12 bring into contrast essentially all the channeling dislocations that remain snagged along the channel walls.

---

[61] P. B. Hirsch *et al.*, *Electron Microscopy of Thin Crystals*, p. 171ff, Butterworths, London, 1965.

Table 9.6. Observed Contrast for Dislocations in Case 3

Channel Number	Contrast for Dislocations Parallel to Channel[a,b]		
	$\vec{g} = [01\bar{1}]$ [Fig. 9.12(b)]	$\vec{g} = [10\bar{1}]$ [Fig. 9.12(c)]	$\vec{g} = [1\bar{1}0]$ [Fig. 9.12(d)]
1	W	S	S
2, 2a	S	W	S
3	S	S	W

[a]S equals strong contrast, that is, the dislocation is visible ($\vec{g} \cdot \vec{b} \neq 0$).

[b]W equals weak contrast, that is, the dislocation is invisible ($\vec{g} \cdot \vec{b} = 0$).

Table 9.7. Values of $\vec{g} \cdot \vec{b}$ for Burgers Vector Determination in Case 3

$\vec{b}$	$\vec{g} \cdot \vec{b}$		
	$\vec{g} = [01\bar{1}]$	$\vec{g} = [10\bar{1}]$	$\vec{g} = [1\bar{1}0]$
$(a/2)[111]$	0	0	0
$(a/2)[\bar{1}11]$	0	−1	−1
$(a/2)[1\bar{1}1]$	−1	0	1
$(a/2)[11\bar{1}]$	1	1	0

Table 9.8 lists the possible planes for each channel and indicates the direction of the projection on (111) of the ⟨111⟩-type Burgers vector lying in the channel planes. We see that only the {110} slip planes perpendicular to the (111) plane contain dislocations whose Burgers vectors would project on the (111) along the required ⟨112⟩ channel traces. Table 9.8 also shows that the projection of the Burgers vector for channeling dislocations on the {123}-type planes would not be parallel to their channel trace directions but rather could be parallel to either of the other two channel directions in Fig. 9.12. Since we do observe dislocations lying parallel to the direction of the

Table 9.8. Crystal Geometry of Channels in Case 3

Channel Number	Possible Channel Planes	$\vec{b}$ for Channeling Dislocations	Direction of Projection of $\vec{b}$ in (111)		Trace Direction	Angle Between [111] and Plane Normal
			Crystal Direction	Parallel to Channel		
1	$(01\bar{1})$[a]	$(a/2)[\bar{1}11]$	$[\bar{2}11]$	1	$[\bar{2}11]$	90°
1	(231)	$(a/2)[1\bar{1}1]$	$[12\bar{1}]$	2	$[\bar{2}11]$	22° 12'
1	(213)	$(a/2)[11\bar{1}]$	$[\bar{1}\bar{1}2]$	3	$[\bar{2}11]$	22° 12'
2	$(\bar{1}01)$[a]	$(a/2)[1\bar{1}1]$	$[1\bar{2}1]$	2	$[1\bar{2}1]$	90°
2	(123)	$(a/2)[11\bar{1}]$	$[\bar{1}\bar{1}2]$	3	$[1\bar{2}1]$	22° 12'
2	(321)	$(a/2)[\bar{1}11]$	$[\bar{2}11]$	1	$[1\bar{2}1]$	22° 12'
3	$(1\bar{1}0)$[a]	$(a/2)[11\bar{1}]$	$[\bar{1}\bar{1}2]$	3	$[\bar{1}\bar{1}2]$	90°
3	(132)	$(a/2)[1\bar{1}1]$	$[1\bar{2}1]$	2	$[\bar{1}\bar{1}2]$	22° 12'
3	(312)	$(a/2)[\bar{1}11]$	$[\bar{2}11]$	1	$[\bar{1}\bar{1}2]$	22° 12'

[a]Plane deduced to be the operating one in Fig. 9.12.

channel in which they move, we conclude that the channel planes are the {110} set indicated in Table 9.8. There are, however, dislocations in contrast in Fig. 9.12(b), for example, which do not lie parallel to channel 1. These dislocations extend beyond the width of the channel, however, and are not clearly associated with the channel. Similar observations apply to a few dislocations crossing channels 2 and 3.

It should be noted that channel 3 does not appear to be cleared of defects to the same extent as channels 1 and 2. This might suggest that channel 3 is inclined to the foil surface and thus is (312) or (132) (see Table 9.8). Since dislocations lie along the trace of channel 3 [Fig. 9.12(b) and (c)], which is not possible for the ⟨111⟩ dislocations on these two {123} planes, we believe that the appearance of channel 3 can be accounted for on the basis that it is in an early stage of formation. Perhaps the dislocations forming channel 3 originate from the dislocation tangle at the intersection of channels 1 and 2a and thus were generated at a later stage in the deformation than those sweeping channels 1, 2, and 2a.

We examined another equilateral-triangular channel pattern from sample B, for which micrographs are not shown, using the stereo technique. The channel trace directions in the (111) were the same as those for case 3. From an examination of the stereo pairs, it appeared that all of the channel planes in this particular field were perpendicular to the plane of the (111) foil surface. Thus, the crystal geometry of these channels was determined uniquely to be the same as the set of {110} planes indicated in Table 9.8.

It seems clear from the offset in channel 1 that channel 2a formed after channel 1 or, at the least, continued to serve as an active slip channel after channel 1 formed. The offset in the direction of channel 2a is about 1.5 cm in prints at a magnification of 50,500×. Thus, the actual magnitude of the offset in channel 1 is about 3000 A. Now, for niobium the Burgers vector for slip dislocations is 2.86 A (ref. 62), and the magnitude of its component in the direction of channel 2a is 2.70 A. Therefore, we conclude that approximately 1100 dislocations

---

[62] C. S. Barrett, Structure of Metals, p. 647, McGraw-Hill Book Company, New York, 1952.

have traveled along channel 2a to produce the offset observed in channel 1. It is interesting to note that the width of channel 2a is also about 3000 A. The spacing between {110} planes in niobium is 2.33 A, and thus approximately 1300 $(\bar{1}01)$ planes are needed to account for the width of channel 2a. The ratio of the number of dislocations sweeping the channel to the number of adjacent (101) planes within the channel is 0.9. As will be discussed, this ratio need not be taken as evidence that only approximately one dislocation has moved down each plane within the channel.

Case 4 (Fig. 9.13). — The field of view chosen for case 4 is of particular interest, for in it is displayed an array of channeling dislocations at an early stage of channel formation. The area discussed as case 4 is shown in Fig. 9.13, where — as before — the plane of the foil from sample B is (111). As mentioned previously, this region overlaps slightly the area shown in Fig. 9.10. The number designations of channels and the channel trace directions as obtained from the electron diffraction pattern are shown in Fig. 9.13(a). Figure 9.13(a) and (b) show the field under reflections $[0\bar{1}1]$ and $[1\bar{1}0]$, respectively. Here we observe channel traces along ⟨110⟩ directions as well as in ⟨112⟩ directions. In particular, the traces of channels 2 and 3 lie along $[01\bar{1}]$ and $[\bar{1}10]$, respectively. There are no {123} planes which give $[01\bar{1}]$ or $[\bar{1}10]$ traces in a (111) plane; thus, we need consider only {110} and {112} planes for channels 2 and 3. The $(\bar{2}11)$ and the $(11\bar{2})$ planes which are perpendicular to the (111) plane can be ruled out as planes for channels 2 and 3, respectively, on the basis that no dislocations seen in these channels lie along the channel trace direction, which would necessarily follow for channel planes perpendicular to the foil surface. Furthermore, the only ⟨111⟩ direction lying in these planes is [111], which, as argued for case 3, is not expected to be an important slip direction for the deformation geometry used. The (211) plane would give a trace in the $[01\bar{1}]$ direction as required for channel 2 and would contain dislocations with $(a/2)[\bar{1}11]$ Burgers vectors. However, $[\bar{1}11]$ dislocations would be in contrast for $\vec{g} = [1\bar{1}0]$ [see Fig. 9.13(b)]. Since the dislocations in channel 2 are out of contrast

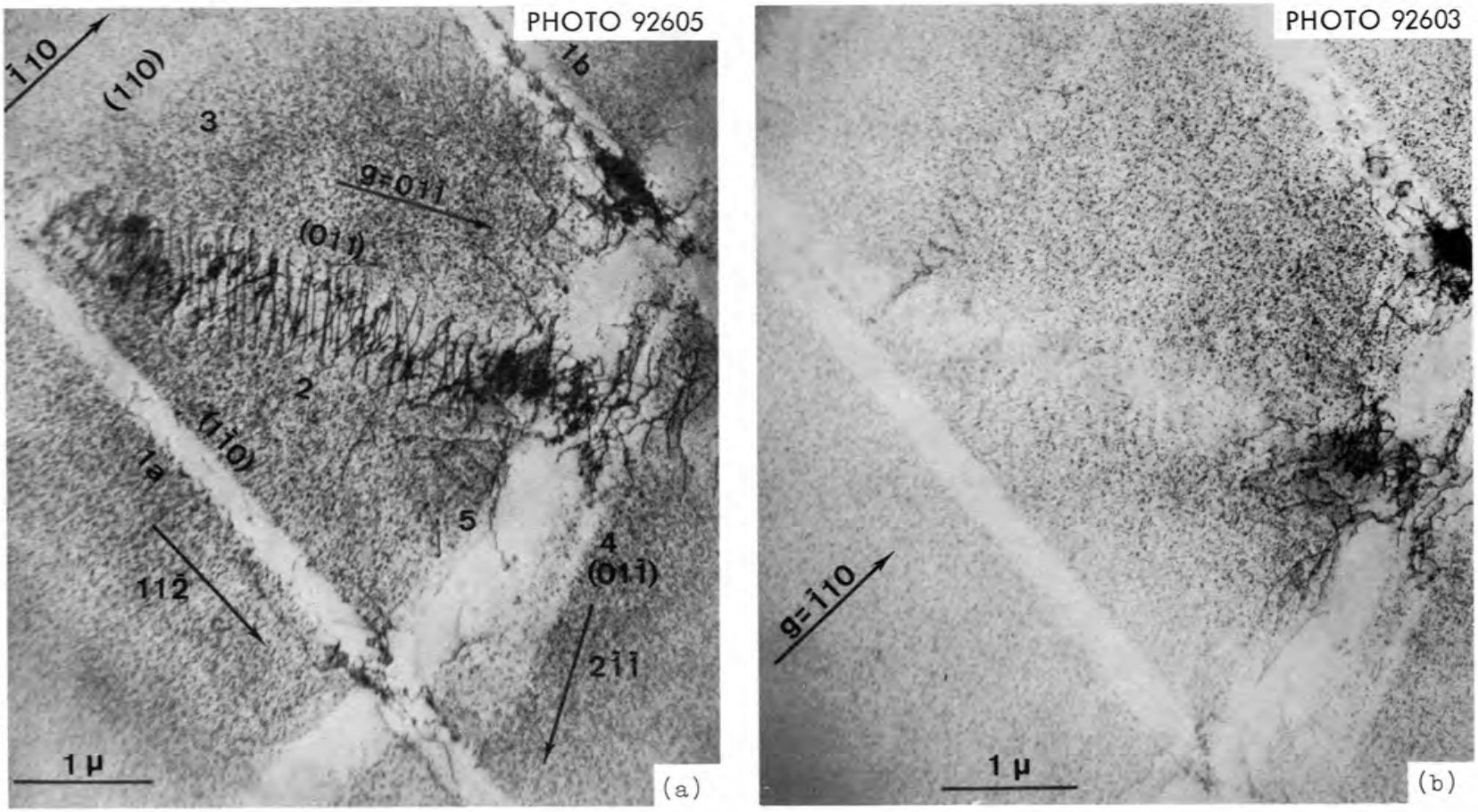

Fig. 9.13. Paired Dislocations along Channel in Sample B. (a) Visible with $\vec{g} = [01\bar{1}]$ and (b) (b) invisible with $\vec{g} = [\bar{1}10]$. (Case 4).

in Fig. 9.13(b), the (211) plane is ruled out as the channel plane. A similar argument, when applied to channel 3, which shows an absence of dislocation contrast in the channel for Fig. 9.13(a), rules out the (112) plane with $[11\bar{1}]$ dislocations. Therefore, we conclude that the channel planes for channels 2 and 3 are (011) and (110), respectively, which are inclined 35° 16' to the foil surface (see Table 9.9). Following the analysis outlined in case 3, we find the crystal geometry for the remaining channels in case 4 to be as given in Table 9.9. Channel 5 is the relatively wide curved channel lying in the direction from lower left to upper right in the micrographs. Because of its curvature, we have not attempted to analyze channel 5.

Table 9.9. Crystal Geometry of Channels in Case 4

Channel Number	Channeled Plane	$\vec{b}$ for Channeling Dislocations	Channel Trace Direction
1a, 1b	$(1\bar{1}0)$	$(a/2)[11\bar{1}]$	$[11\bar{2}]$
2	(011)	$(a/2)[11\bar{1}]$	$[01\bar{1}]$
3	(110)	$(a/2)[\bar{1}11]$	$[\bar{1}10]$
4	$(01\bar{1})$	$(a/2)[\bar{1}11]$	$[2\bar{1}\bar{1}]$

It is interesting to note from Table 9.9 that dislocations channeling along channels 1 and 2 have the same Burgers vector. Thus, dislocations moving in channel 1a can transfer to channel 2 by cross slipping from $(1\bar{1}0)$ to (011). If the dislocations observed in channel 2 were pure screw with a $(a/2)[11\bar{1}]$ Burgers vector, then their projection on the (111) plane would lie in the $[11\bar{2}]$ direction. If they were pure edge, then their projection would lie in the $[\bar{1}10]$ direction. The dislocations in channel 2 actually make an angle of about 45° with the $[11\bar{2}]$ direction. Thus, the dislocations appear to lie almost exactly half-way between the pure edge and pure screw orientations. However, the edge character may have been introduced during thinning. In this event, the dislocations observed in channel 2 could have cross slipped from the $(1\bar{1}0)$ plane; the fact that no tangle is observed at the

intersection of channels 1a and 2 would support this. Note, however, that there is tangling at the intersections of channel 2 with channels 3 and 5 for which the channeling dislocations have Burgers vectors different from those in channel 2. There is some suggestion that many of the dislocations seen in channel 2 are paired, with the two dislocations comprising the pair lying in opposite walls of the channel. These paired dislocations appear to have about the same length but are displaced with respect to one another. This is precisely the displacement expected for the projection of dislocation lines lying on opposite walls of a channel inclined to the foil surface, such as channel 2.

In general, the tangles at the intersections of channels are rather complex, three-dimensional dislocation arrays. However, focusing attention on the tangle at the intersection of channels 2 and 5, comparison of Fig. 9.13(a) and (b) indicates that $[11\bar{1}]$ dislocations that are the channeling dislocations for channel 2 make up part of the tangle. In Fig. 9.13(b), dislocations with $(a/2)[\bar{1}11]$ and $(a/2)[1\bar{1}1]$ Burgers vectors are expected to be in contrast. Since channel 5 appears curved, its plane is somewhat uncertain. If, however, we take the directions of channels 4 and 5 to be parallel, then $[\bar{1}11]$ dislocations would move in channel 5 and would have a projection in (111) along the channel direction. In Fig. 9.13(b), dislocations with this characteristic are observed in the tangle as well as dislocations making an angle of approximately 60° with the direction of channel 5. The dislocations lying at 60° to the channel direction are rather sharply kinked in at least two places. Although we are not able to determine the Burgers vector for these dislocations from the available reflections, dislocations with a Burgers vector of either $(a/2)[1\bar{1}1]$ or $(a)[010]$ would satisfy the geometry observed and should be in contrast in Fig. 9.13(b). The $(a)[010]$ dislocations could result from the following reaction:

$$(a/2)[11\bar{1}]_{(011)} + (a/2)[\bar{1}11]_{(01\bar{1})} \rightarrow (a)[010] \ .$$

Dislocation reactions of this kind in body-centered cubic metals have been discussed by Hartley[63] and are found to be energetically favorable.

Case 5 (Fig. 9.14). – A striking feature observed in a (111)-foil from sample B is the dislocation helix shown in Fig. 9.14(a) and at higher magnification in Fig. 9.14(b). Aside from the fact that helices are rather infrequently observed in high-purity metals,[64] its occurrence here is of particular interest since the offset produced where a channel crosses it provides a measure of the number of dislocations moving along the channel. Furthermore, there is an opportunity for comparing the number of dislocations moving in a given channel within a grain with the number in the same channel crossing the boundary seen at the upper right in Fig. 9.14(a).

The helical character of the feature in Fig. 9.14 is clearly seen in the segment to the left of the vertical channel trace [A′, Fig. 9.14(b)]. Discrete, closed prismatic loops exist at A, Fig. 9.14(b), with the same axis as the helix. The line feature lies along $[01\bar{1}]$, and lower magnification micrographs indicate that it extends over a distance of at least 9.5 μ. The axis of the linear dislocation array is in general straight, but it does exhibit some twisting as seen at B, Fig. 9.14(a). Notice also that the spot damage believed to be interstitial in nature[65,66] is depleted on either side of this array. The spacing between turns and loops is essentially uniform over the length of the feature and is about 280 A as determined from Fig. 9.14(b). The radii of the helix and loops in Fig. 9.14(b) are approximately 350 to 450 A.

Helical dislocations are generally considered (e.g., by Mitchell[67]) to form from screw dislocations by climb processes with the axis of the

---

[63] C. S. Hartley, Phil. Mag. 14, 7 (1966).

[64] J. P. Hirth and J. Lothe, Theory of Dislocations, p. 580, McGraw-Hill Book Company, New York, 1968.

[65] R. P. Tucker and S. M. Ohr, Phil. Mag. 16, 643 (1967).

[66] S. M. Ohr, R. P. Tucker, and M. S. Wechsler, "Radiation Hardening in B.C.C. Metals Niobium and Iron" in Proceedings of the International Conference on Strength of Metals and Alloys, Japan Institute of Metals, Jendai, Japan, 1968.

[67] J. W. Mitchell, J. Appl. Phys. 33, 406 (1962).

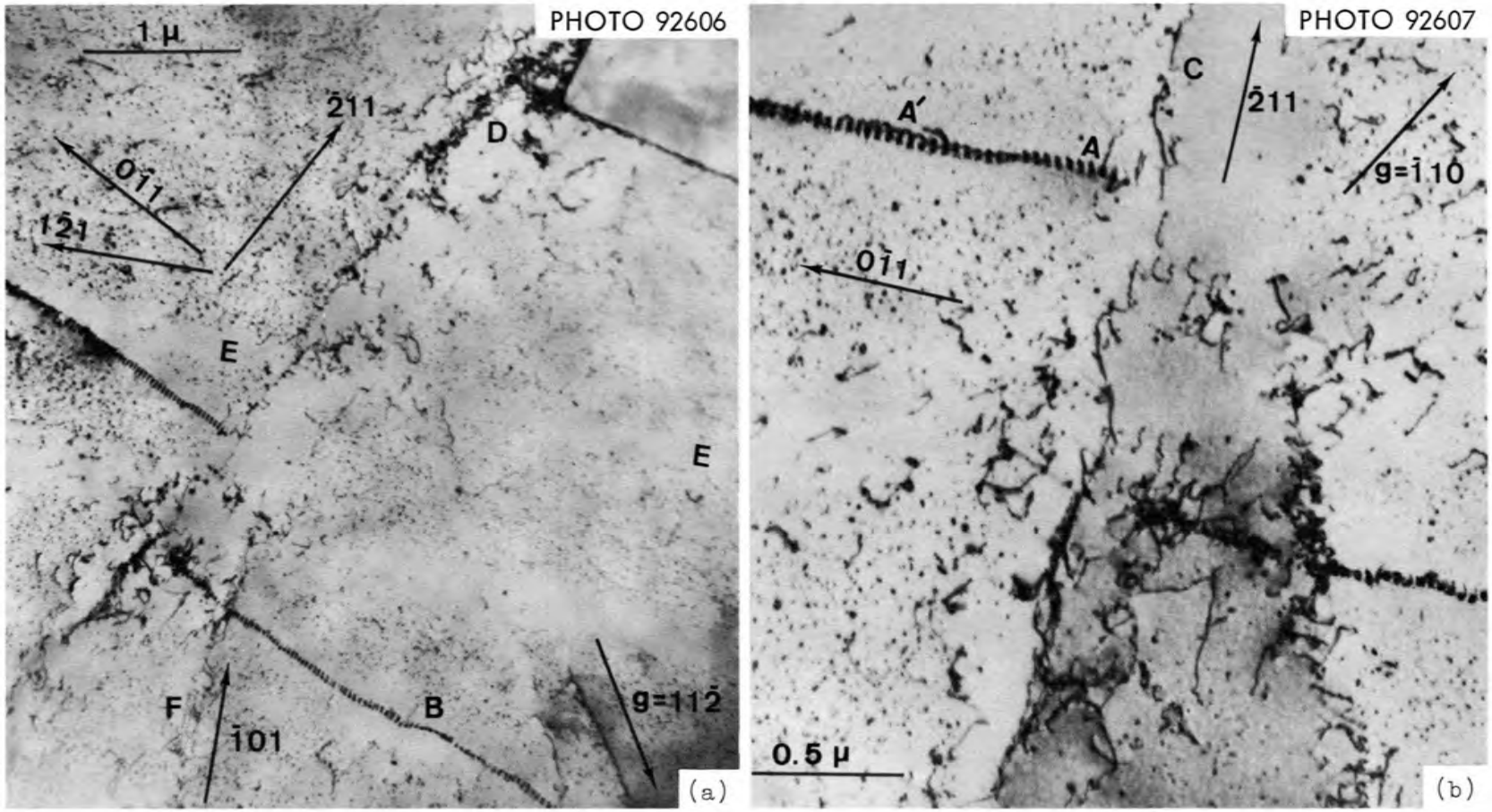

Fig. 9.14. Channel-Helix and Channel-Boundary Offsets in Sample B. (a) Low magnification and (b) high magnification. (Case 5). Reduced 6%.

helix in the direction of the Burgers vector of the screw. The great length of the helix in Fig. 9.14(a) along $[01\bar{1}]$ suggests that it originated from a grown-in $[01\bar{1}]$ screw dislocation.

The trace of the channel that caused the offset in the helix [nearly vertical in Fig. 9.14(b)] is along $[\bar{2}11]$, and the channel plane is probably $(01\bar{1})$. This is so because the $\langle 111 \rangle$ dislocations in the other possible channel planes, (231) and (213), lie across the channel trace instead of along it as observed for example at C, Fig. 9.14(b). The offset of the helix in the $[\bar{2}11]$ as determined from Fig. 9.14(b) is 9500 A. The dislocations with $(a/2)[\bar{1}11]$ Burgers vectors moving in $(01\bar{1})$ produce the observed offset. The component of a $(a/2)[\bar{1}11]$ Burgers vector in the $[\bar{2}11]$ direction is 2.70 A. Therefore, the number of dislocations required to give the observed offset of the helix is about 3500. From Fig. 9.14(a), the channel width is 4500 A. Since the spacing between {110} planes is 2.33 A, approximately 1900 $(01\bar{1})$ planes are needed to account for the channel width. The ratio of the number of dislocations to the number of channeled planes is 1.8, twice the ratio found in case 3.

From Fig. 9.14(a), the offset in the boundary is found to be about 6700 A, which corresponds to the passage of 2500 $[\bar{1}11]$ dislocations. Therefore, approximately 1000 more dislocations have passed the helix than have crossed the boundary. This is consistent with the observed dislocation pileup and tangling at the side of the boundary facing the helix [D, Fig. 9.14(a)].

In Fig. 9.14(a), two channels cross the linear array at angles not perpendicular to its axis. The channel marked E lies along $[1\bar{2}1]$ and is perpendicular to $[\bar{1}01]$. In this case, the channeled plane is most likely the $(\bar{1}01)$ with $(a/2)[1\bar{1}1]$ the Burgers vector for the channeling dislocations. The trace of channel F is in the $[\bar{1}01]$ direction with (101) as the most likely channel plane. The angle between the normal to the (101) plane and the [111] direction is 35° 16'. Considerable dislocation structure is observed in channel F. Very little, if any, offset is to be seen where these channels cross the linear feature.

Case 6 (Fig. 9.15). — In contrast to previous cases for sample B, the plane shown in Fig. 9.15 is (112). The diffraction patterns indicate that the offset feature is a low-angle grain boundary. The trace of channel G (approximately horizontal) lies within 4° of $[3\bar{1}\bar{1}]$. The numerous dislocations seen nearly parallel to the edge of the channel are consistent with $(a/2)[\bar{1}11]$ screw dislocations moving on the channel plane $(0\bar{1}1)$. The projection of $[\bar{1}11]$ in (112) lies along $[\bar{4}21]$, which is about 9° from $[3\bar{1}\bar{1}]$, the trace direction of the channel plane, $(0\bar{1}1)$, in (112). Although not clearly apparent in Fig. 9.15, other micrographs show that the trace of channel G continues along $[3\bar{1}\bar{1}]$ to the left of the boundary and that the channel labeled K is another channel that terminates at the offset in the region between K and G. It seems reasonable to suggest that channel K was initiated as a result of stress concentrations at the offset.

The magnitude of the offset in the boundary in Fig. 9.15 provides the basis for a calculation of the number of channeling dislocations operating in channel G. The offset displacement corresponds to 12,100 A, and the component of the Burgers vector $(a/2)[\bar{1}11]$ along $[\bar{4}21]$ is 2.52 A. Therefore, about 4800 dislocations are required to produce the offset. The width of the trace of channel G corresponds to 4000 A, which is provided by a stack of about 1600 $(0\bar{1}1)$ planes intersecting (112). Thus, on the average about 4800/1600 = 3 $[\bar{1}11]$ dislocations have been channeled down each (011) plane, about three times that calculated for case 3. The magnitude of the channeling shear due to channel G in Fig. 9.15 is also seen by the displacement of the channel trace at H to its position at H′. It is apparent that channel H-H′ must have formed before channel G.

The offset, almost horizontal segment of the boundary in Fig. 9.15, is remarkably straight, which suggests that the channeling dislocations were distributed uniformly across channel G. It is interesting, also, that the boundary is lengthened in the region of the offset. Another feature in Fig. 9.15 is the depleted region adjacent to the boundary, for example at J. The defect clusters in these samples are considered to be interstitial in nature.[65,66]

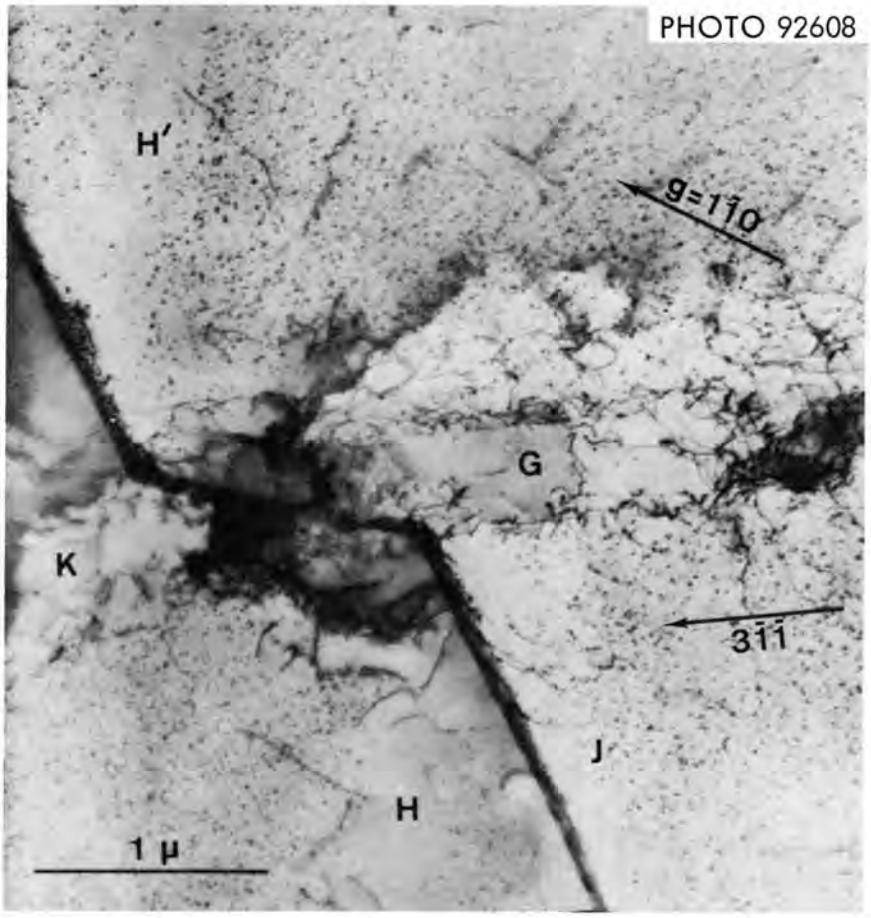

Fig. 9.15. Large Channel-Boundary Offset in a (112) Foil from Sample B. (Case 6).

Case 7 (Fig. 9.16). – In comparison to sample B, which has been the focus of attention in the preceding discussion, the area of the (111) foil from sample A seen in Fig. 9.16 exhibits some unexpected features. Both the fluence and the strain in sample A were less than in sample B, namely, 1.8×10^{18} neutrons/cm^2 and 2.7% as compared to 4.4×10^{18} neutrons/cm^2 and 6.6%. Although the yield stresses in sample A were slightly greater than those in sample B, the density of defect clusters produced by radiation in sample A is noticeably lower than in sample B.

A striking feature seen at M within the main channel in Fig. 9.16 is the rather well-developed cell structure. The cell walls generally lie along crystallographic directions that are important in the crystal slip geometry. The dark tangle lying across the main channel to the

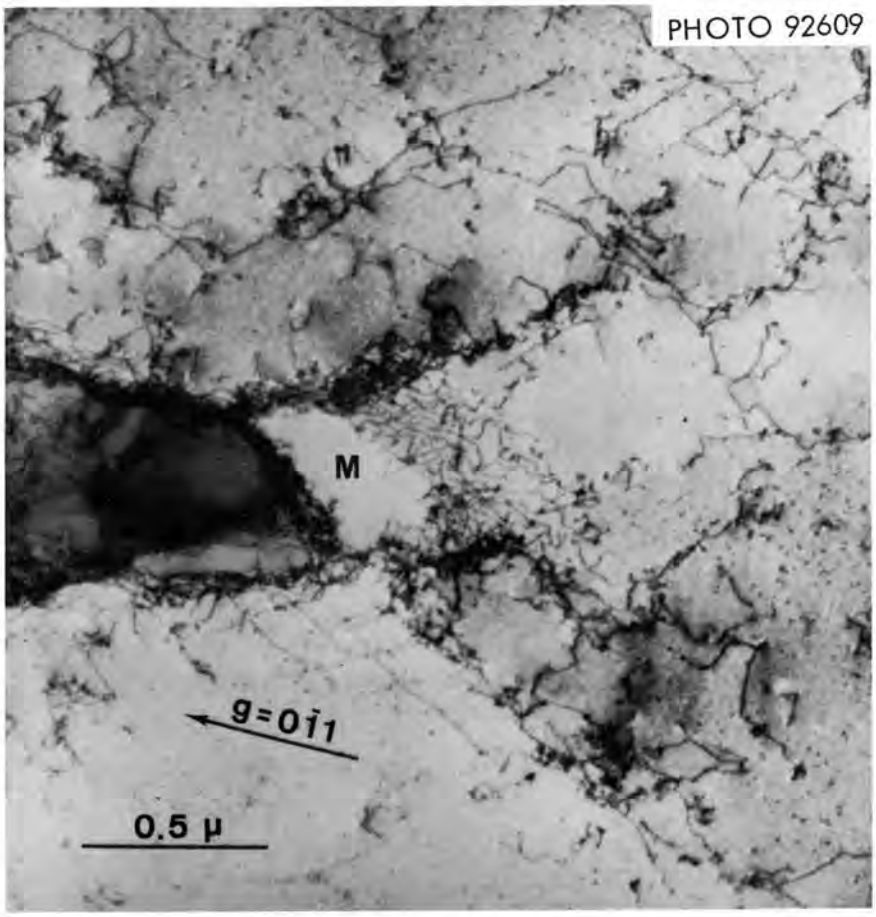

Fig. 9.16. Cell Structure Within Channel Observed in Sample A After 2.7% Nominal Tensile Strain. (Case 7).

left of M is in the $[11\bar{2}]$ direction, and to its right the cell walls are aligned with the channel trace direction, $[\bar{1}2\bar{1}]$. On the other hand, to the left of this dark tangle the uppermost cell wall is in the $[0\bar{1}1]$ direction. When viewed under the $[\bar{1}10]$ reflection, in a micrograph not shown here, an entirely different set of more or less parallel, joggy dislocations are brought into contrast to form an interlaced network with those seen to the right of M in Fig. 9.16. where $\vec{g} = [0\bar{1}1]$. The high concentration of dislocations in the cell walls is in marked contrast to the cell interior (e.g., at M), which is almost entirely free of dislocations. The fact that a cell structure is observed after only 2.7% nominal strain in the sample emphasizes that the strain is concentrated in the channel.

Discussion

The observation of an offset where microstructural features are crossed by dislocation channels is quite significant, because it provides a measure of the direction and the magnitude of the shear displacements produced by the channeling dislocations. Three types of offsets are illustrated above: channel–channel (cases 2 and 3), channel–helix (case 5), and channel–low-angle boundary offsets. Table 9.10 summarizes the results. We conclude from the column on the extreme right that, on the average, 1 to 3 dislocations move along the channel per atomic plane. This agrees with Sharp's estimates of 2 to 3 dislocations per plane for neutron-irradiated copper.[68] Sharp estimated this quantity by dividing the shear displacement as observed from slip markings by the channel width observed by transmission electron microscopy. Since our determination is based on the shear displacement and channel width for the same channel, the contention that surface slip lines correspond to dislocation channels is strengthened.

The formation of a cell structure within a dislocation channel for a sample given only 2.7% nominal strain (Fig. 9.16) emphasizes, as we have said, the fact that strain is heavily concentrated in the channel. Nevertheless, within the channel the strain appears to be distributed uniformly. This is seen quite clearly in Fig. 9.15 since the offset segment of the low-angle boundary is straight. This, again, is a conclusion, based on surface replicas, reached by Sharp.[68] The uniformity of shear within the channel is consistent with the observation that there generally appear to be no defect clusters within the cleared channel when the channel plane is perpendicular to the plane of view. If, on the average, two dislocations per plane are considered to sweep down the channel, it is not necessary to assume that each plane receives two dislocations. Macroscopic uniformity of slip within the channel would also be achieved if packets of, say, 20 dislocations swept down single planes spaced about ten planes apart. But for complete annihilation of the damage clusters within the channel, the spacing between the

[68] J. V. Sharp, Phil. Mag. 16, 77 (1967).

Table 9.10. Offsets Observed in Sample B

Case	Type of Offset	Channel		Number of Planes per Channel Width	Offset		$\vec{b}$ for Channeling Dislocations	Number of Dislocations per Offset	Ratio[b]
		Plane	Width (A)		Magnitude[a] (A)	Direction[a]			
2[c]	Channel-channel	$(\bar{1}10)$	2500–3330	1070–1430	3330	$[11\bar{2}]$	$(a/2)[11\bar{1}]$	1230	0.9–1.2
3[c]	Channel-channel	$(\bar{1}01)$	3300	1290	3000	$[1\bar{2}1]$	$(a/2)[1\bar{1}1]$	1110	0.9
5[c]	Channel-helix	$(01\bar{1})$	4500	1930	9500	$[\bar{2}11]$	$(a/2)[\bar{1}11]$	3520	1.8
5[c]	Channel-boundary	$(01\bar{1})$	4500	1930	6710	$[\bar{2}11]$	$(a/2)[\bar{1}11]$	2490	1.3
6[d]	Channel-boundary	$(01\bar{1})$	3960	1600	12,080	$[\bar{4}21]$	$(a/2)[\bar{1}11]$	4790	3.0
Not discussed[c]	Channel-boundary	$(\bar{1}10)$	5550	2380	5940	$[11\bar{2}]$	$(a/2)[11\bar{1}]$	2200	0.9

[a]As observed in plane of view.

[b]Ratio: number of dislocations per offset divided by number of planes per channel width.

[c]Plane of view: (111).

[d]Plane of view: (112).

dislocation packets should not exceed the diameter of the clusters, which corresponds to about 35 planes.

The precise mechanism of the removal of the defect clusters by the slip dislocations is still a matter of conjecture. One possibility is that the motion of the channeling dislocation produces an input of energy that is largely converted into heat. This heat of plastic deformation will cause an increase in temperature possibly capable of annealing the damage clusters produced by radiation. Each $(a/2)\langle 111\rangle$ dislocation produces a shear displacement of $b = \sqrt{3}\ a/2$, and the $\{110\}$ spacing is $\sqrt{2}\ a/2$, where a is the lattice parameter. Therefore, each dislocation gives rise to a shear strain of $\sqrt{3}\ /\sqrt{2}$. If, from Table 9.10, we consider about two dislocations per plane to operate in the channeling shear, the shear strain becomes $2\sqrt{3}\ /\sqrt{2} = 2.5$. This shear occurs at a shear stress level corresponding to the yield stress, or about $\tau = 7.1\ \mathrm{kg/mm^2}$. The energy of plastic deformation per unit volume is, therefore,

$$E_{PD} = 18\ \mathrm{kg/mm^2} = 42\ \mathrm{cal/cm^3}\ . \tag{9.9}$$

Niobium has a specific heat at room temperature of about $0.06\ \mathrm{cal\ gm^{-1}\ deg^{-1}} = 0.54\ \mathrm{cal\ cm^{-3}\ deg^{-1}}$. Therefore, under adiabatic conditions, if all the energy of plastic deformation were converted into heat, the temperature rise would be about 80°C. This would appear to be an upper estimate, since some heat diffuses away from the incipient channel and some energy is stored in dislocations and defects produced during the deformation. On the other hand, the simple calculation above assumes that the energy of plastic deformation is distributed equally among all the atoms in the channel. It is quite possible that, since the dislocations are impeded by the defect clusters, the energy is expended in localized bursts at the defect clusters. This would cause a large local increase in temperature of the defect cluster, possibly for a sufficiently long period to permit the clusters to anneal.

A second mechanism is the chopping up of damage clusters as slip dislocations pierce through them. An analysis of the size distribution

of damage clusters in as-irradiated niobium (Fig. 11.25, ref. 69) showed the distribution to be sharply peaked at a cluster size of 80 A. The number of clusters at 60 A was about 6% of the number at the peak size, and at 40 A the number was negligibly small. This suggests that a reduction in the effective dimension of the cluster may cause it to become unstable.

A third approach to an understanding of how the defect clusters are removed in the channeling process is the sweeping up of the clusters by the slip dislocations. It is clear that in a process of this type the clusters must somehow be incorporated into the slip dislocations and not simply swept aside. This is suggested by the fact that the concentration of clusters is not higher at the walls of the channels.

Finally, it is possible that the defect clusters are annihilated by virtue of the production of antidefects during the motion of the channeling dislocations. The damage clusters in as-irradiatiated niobium have been found to be mostly of interstitial type, and thus vacancies created by the nonconservative motion of jogs on the channeling dislocations may annihilate the clusters. Earlier work has shown (Fig. 11.27, ref. 69) that small defects are observed in irradiated niobium annealed to 600°C, which may be due to the aggregation of vacancies produced by radiation. In the as-irradiated niobium these vacancies dispersed as isolated defects or aggregates containing only a few defects. It may be that the slip dislocations tend to drag these vacancies to the interstitial clusters where mutual annihilation takes place. Evidence has been presented[70] for the absence of channeling in the radiation-anneal-hardened niobium (i.e., irradiated niobium annealed at about 400°C that exhibits a further increase in yield stress; see Fig. 11.23, ref. 69). The radiation-anneal-hardening may be due to the trapping of interstitial impurities at radiation-produced vacancies. The trapping of oxygen in irradiated and annealed niobium has been

---

[69]S. M. Ohr, R. P. Tucker, and E. D. Bolling, Radiation Metallurgy Section Solid State Division Progress Report for Period Ending January 1968, ORNL-4246, pp. 55–66.

[70]S. M. Ohr and R. P. Tucker, "Radiation Anneal Hardening in Niobium," p. , this report.

revealed by internal friction and resistivity measurements by Williams, Brundage, and Stanley.[71] Thus, the absence of channeling in radiation-anneal-hardened niobium may be an indication that the vacancies produced by radiation are associated with interstitial impurities and are therefore not available for the role of antidefects for the interstitial type of defect clusters.

The above discussion has focused attention on the mechanism of the removal of defect clusters from the cleared channels. A related question is how the dislocation channeling process is initiated. Figures 9.10 and 9.11 illustrate that the channels are often widely and regularly spaced, suggesting that the presence of one channel may trigger the formation of another one. As pointed out by Sharp,[72] this is evidence for a long-range internal stress in the irradiated-and-deformed material. Thus, it seems likely that a group of dislocation channels, corresponding to a coarse slip band on the surface, is initiated at a single point of stress concentration, activating the formation of one dislocation channel which rapidly produces others in its neighborhood. The dislocation tangles at the intersection of channels or where a channel crosses another microstructural feature may well serve as concentrations of stress from which additional channels emanate. An example of the first of these is seen in Fig. 9.12, where channel 3 appears to be generated by the tangle at the intersection of channels 1 and 2a; the second is illustrated in Fig. 9.15, where a channel appears to be generated at the intersection of another channel and a low-angle boundary. Also, a number of narrow channels apparently in an early state of development are seen at B in Fig. 9.11(a). These appear to have originated at small dislocation tangles in the channel segment above T_1' to the left of B.

The phenomenon of dislocation channeling probably plays a central role in the plastic deformation of irradiated metals. The yield stress

---

[71] J. M. Williams, J. T. Stanley, and W. E. Brundage, Metal Sci. J. 2, 100 (1968).

[72] J. V. Sharp, Phil. Mag. 16, 77 (1967).

is likely governed by the stress to initiate the formation of dislocation channels, and the work-hardening behavior depends upon the manner in which strain is concentrated in the channels and in which the channels propagate to encompass the entire gage section of the sample.

The Temperature Dependence of Radiation Hardening

S. M. Ohr

In formulating a theory of dispersed barrier hardening, Fleischer[73,74] considered the interaction between a straight dislocation and a center of tetragonal distortion. He derived a force-distance relationship by assuming that the stress from the dislocation is uniform over the volume of the defect. However, in order to predict the temperature dependence of the yield stress in analytical form, he adopted a modified force function that substantially deviates from the expression originating directly from the model for the interaction of dislocations and defects. The modified force function predicts that the square root of the yield stress, τ, is directly proportional to the square root of the absolute test temperature, T. Despite the lack of exactness in the Fleischer theory as discussed recently by Ono,[75] temperature dependence of this type has been observed for hardening due to impurities, quenching, and irradiation in crystals of various structures. The purpose of this report is to discuss on the basis of continuum theory the applicability of the linear relationship between $\tau^{1/2}$ and $T^{1/2}$ for contact interaction between dislocation loops and straight dislocations.

In the continuum theory of defect interaction, the interaction energy is obtained as the work required to form a defect in the presence of the stress field of another defect. On the basis of isotropic elasticity theory, Kroupa[76] has calculated the interaction energy between

---

[73]R. L. Fleischer, Acta Met. 10, 835 (1962).

[74]R. L. Fleischer, J. Appl. Phys. 33, 3504 (1968).

[75]Kanji Ono, J. Appl. Phys. 39, 1803 (1968).

[76]F. Kroupa, Phil. Mag. 7, 783 (1962).

a straight dislocation and a dislocation loop. The expression for the interaction energy is given by

$$E_{int} = b^{OG} \iint_A \sigma_{13}\, dA + b^{OP} \iint_A \sigma_{33}\, dA \ , \qquad (9.9)$$

where b^{OG} and b^{OP} are the glide and prismatic components, respectively, of the loop Burgers vector and σ_{ij} is the stress tensor component for the straight dislocation. The integrals are performed over the area of the circular loop with radius R. The retarding force is obtained through $\vec{F} = -\nabla E_{int}$.

A portion of the work of moving the dislocation over the loop is done by the applied stress, which exerts a force on the dislocation $F_a = \tau b \ell$, where ℓ is the length of dislocation segment involved in the process. The remaining work in forcing the dislocation toward the loop is supplied by thermal fluctuations. The activation free energy for surmounting the loop as a barrier is obtained from

$$\Delta G = \int_{r_m}^{r_a} (F_r - F_a)\, dr \ , \qquad (9.10)$$

where F_r is the radial component of the retarding force, r_a is the distance from the center of the loop to the dislocation where the applied force is equal to the retarding force, and r_m is the value of r where the retarding force is maximum.

The interaction energy has been calculated for various relative orientations between the dislocation and the loop exactly from Eq. (9.9), (ref. 76). The results indicate that the force-distance curves exhibit a sharp discontinuity at r = R. The force on the dislocation is found to be independent of r when the dislocation is inside the loop. Outside the loop, the force is in general a complex function of r; hence, a simple temperature dependence of hardening cannot be obtained. When the

dislocation is normal to the loop, however, the interaction obeys the inverse-square force law, that is,

$$F_r = F_m R^2/r^2 , \qquad \text{for } r \geq R$$
$$= -F_m, \qquad \text{for } r \leq R , \tag{9.11}$$

where F_m is the maximum retarding force and is given by $f_1(\theta)\mu b^{OG} b/2$ for a screw dislocation and by $f_2(\theta)\mu\nu b^{OP} b/(1-\nu)$ for an edge dislocation. The function $f(\theta)$ represents the angular dependence of the retarding force, while b is the Burgers vector of the straight dislocation, μ is the shear modulus, and ν is Poisson's ratio. Such a force-distance curve is shown schematically in Fig. 9.17, where the shaded area corresponds to the activation free energy of the process as defined by Eq. (9.10). The maximum retarding force, F_m, occurs where the dislocation comes into contact with the loop, that is, $r_m = R$. When the dislocation is parallel to the loop, F_m is infinite, so that the process of overcoming the loop cannot take place by thermal activation.

The interaction energy has also been calculated for the approximation of an infinitesimal loop.[73,76] In this approximation, the stress

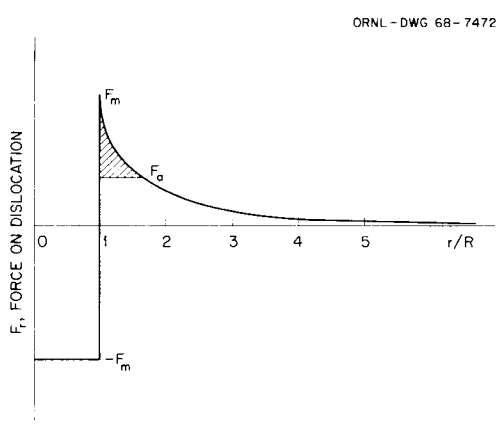

Fig. 9.17. Schematic Force-Distance Curve for a Circular Dislocation Loop and a Straight Dislocation That Lies Normal to the Loop. There is a sharp discontinuity at r = R, where the dislocation comes into contact with the loop. The shaded area corresponds to the activation energy of the process.

field of the dislocation is assumed not to vary appreciably over the area of the loop, and the integrals in Eq. (9.9) are replaced by the area of the loop times the values of σ_{ij} at the center of the loop. The approximation is generally considered to apply when the dislocation is at distances greater than 2 R from the center of the loop. In this case, the inverse-square force law is always found, since E_{int} is directly proportional to σ_{ij} and since σ_{ij} is always proportional to $1/r$. In view of the sharp discontinuity found for the exact calculation discussed above, the force-distance curves obtained using the infinitesimal loop approximation are cut off at $r = R$.

In cases where the inverse-square force law is obeyed, the activation free energy is found from Eqs. (9.10) and (9.11) as

$$\Delta G = F_m R[1 - (\tau/\tau_o)^{1/2}]^2 , \tag{9.12}$$

where $\tau_o = F_m/b\ell$ is the applied stress needed to overcome the barrier in the absence of thermal fluctuation. From the rate equation, $\dot{\epsilon} = \dot{\epsilon}_o \exp(-\Delta G/kT)$, where $\dot{\epsilon}$ is the strain rate and $\dot{\epsilon}_o$ is the frequency factor, the activation free energy may be set equal to a multiple of k T,

$$\Delta G = \alpha\ k\ T , \tag{9.13}$$

since $\alpha = \ln(\dot{\epsilon}_o/\dot{\epsilon})$ may be assumed to be constant in a given test. From Eqs. (9.12) and (9.13) we obtain

$$(\tau/\tau_o)^{1/2} = 1 - (T/T_o)^{1/2} , \tag{9.14}$$

where $T_o = F_m R/\alpha k$ is the critical temperature above which thermal activation alone is sufficient to move the dislocation past the loop. Thus, the linear relationship between $\tau^{1/2}$ and $T^{1/2}$ is obtained directly from the theory of defect interaction. The difference between the present result and that of Fleischer is in the expressions for the activation free energy and T_o, where the Burgers vector in Fleischer's theory is here replaced by the loop radius.

In conclusion, the continuum theory of defect interaction does not in general predict a simple temperature dependence of yield stress. However, in cases where the interaction is governed by the inverse-square force law, the linear relationship between $\tau^{1/2}$ and $T^{1/2}$ is expected.

PART IV.

TECHNIQUES OF FABRICATION AND TESTING

10. TUNGSTEN METALLURGY

W. O. Harms

The object of this program is to develop economical methods for producing high-quality tungsten and tungsten-alloy tubing with good creep-rupture properties at high temperatures, good microstructural stability, good ductility at low temperatures, and good weldability. We fabricate tubing both by modification of conventional techniques based on extrusion, tube reduction, and warm drawing and by direct chemical vapor deposition (CVD) through the hydrogen reduction of heavy-metal halides. Our program includes complete physical and metallurgical evaluation of both fabrication processes.

Primary and Secondary Working of Tungsten and Tungsten Alloys

W. R. Martin

Extrusion of Tungsten and Tungsten Alloys (R. E. McDonald)

We are improving techniques for extruding tungsten and tungsten-alloy billets. We are using a 1250T Watson-Stillman horizontal press that has been extensively modified into a high-speed refractory-metal extrusion press. The extrusion press has been instrumented to record stem load, die load, hydraulic pressure, tie-rod load, ram speed and ram travel during extrusion to permit better control of the extrusion conditions. From the improved control, we hope to enhance the quality of the extruded product.

The extrusion process consists of heating the billet by induction in an argon atmosphere, manually transferring the billet to the press container, inserting the backup tooling, advancing the press ram to contact the tooling, and applying high pressure for extrusion. The total time from furnace to completed extrusion is 8 to 12 sec.

With this process we have extruded unalloyed tungsten, W–5% Re, W–25 or 26% Re, and W–25, 26, or 30% Re–30% Mo billets consolidated by powder metallurgy, chemical vapor deposition, and arc-casting techniques.

The data for all of these extrusions produced during the last 2 1/2 years are given in Tables 10.1 through 10.4. Primary extrusions have been made for billet temperatures as high as 2200°C, reduction ratios up to 6.5, and speeds up to 24.5 ips. Extrusion ratios of 9 have been obtained for molybdenum-clad duplex extrusion billets. At temperatures above 1800°C, we found that a molybdenum foil boat in the container keeps the billet from alloying with the steel container, which would cause serious tears and surface defects on the extruded part. An important result from our work was our recognition of the tungsten-metal oxide, which forms naturally during extrusion, as a lubricant.[1] Before this, glass used as the billet lubricant resulted in poor surfaces and short tooling life. With the tungsten oxide, improved surfaces on the extruded product and longer die life have been obtained.

A major portion of our work is directed toward producing tubular products by the floating-mandrel process[2] developed at our laboratory for refractory metals. Tube shells 1 3/8 to 1 7/8 in. in outside diameter and 3/4 to 1 in. in inside diameter are obtained by the primary extrusion of the 3-in.-diam billets. Recently, larger tubes 2 1/4-in. in outside diameter by 1 1/4 in. in inside diameter have been produced from 4-in.-diam billets. Two 6-in.-diam billets of tungsten were extruded to a 3 3/8-in. outside diameter and 2 3/8 in. inside diameter by our tube-shell extrusion technique under our supervision[3] at the Fansteel Metal Center. The tube shells were approximately 6 ft long and are the largest tube-shell extrusions of tungsten made to date.

---

[1]R. E. McDonald and C. F. Leitten, Jr., Method for Extruding Molybdenum and Tungsten (to U.S. Atomic Energy Commission), U.S. Patent 3,350,907. November 7, 1967.

[2]R. E. McDonald and G. A. Reimann, Floating-Mandrel Extrusion of Tungsten Alloy Tubing, ORNL-4210 (February 1968).

[3]R. E. McDonald, "Tube-Shell and Duplex Extrusions," Metals and Ceramics Div. Ann. Progr. Rept. June 30, 1968, ORNL-4370, Chap. 16.

Table 10.1. Tungsten-Alloy Primary Tube-Shell Extrusions

Extrusion Number	Consolidation Method[a]	Extrusion Conditions: Preheat Billet Temperature (°C)	Reduction Ratio	Ram Force (tons): Maximum	Ram Force (tons): Minimum	Speed (ips)	Extrusion Constant (psi)	Tube-Shell Dimensions, in.: Diameter: Outside	Diameter: Inside	Length
							$\times 10^3$			
				Unalloyed Tungsten						
0003	PM	1750	6.37	700	610		109	1.395	0.750	1.88
0004	PM	1800	6.41	690	665		107	1.384	0.750	23.30
0031	PM	1700	3.31	550	465		119	1.700	0.740	12.25
0193	PM	1650	3.78	660	650	1.5	143	1.706	0.750	21.00
0194	PM	1650	3.30	620	600	2.0	134	1.711	0.750	21.75
0195	PM	1650	3.78	520	540	2.2	117	1.730	0.750	16.75
0196	PM	1650	3.78	520	520	2.5	113	1.738	0.750	13.25
0260	PM	1760	5.04	635	580	8.5	113	1.508	0.750	31.00
0624[b]	AC	1750	4.99	845	600	1.07	90	2.200	1.325	27.50
0625[b]	AC	1750	4.11	695	580	24.5	84	2.319	1.325	27.50
				W–5% Re						
0477	AC	1750	3.65	520	400	6.0	122	1.724	0.750	9.50
				W–25 or 26% Re						
0261	AC	2160	3.78	570	525	1.6	123	1.721	0.750	16.50
0420	PM	1850	3.30	640	540	8.2	155	1.797	0.750	15.25
0430	AC	1885	3.78	700	640	11.0	152	1.700	0.750	8.70
0443	AC	1800	6.90					1.800	1.000	31.00
0546	AC	1870	3.78	635	605	9.5	142	1.700	0.51	7.12

Table 10.1 (continued)

Extrusion Number	Consolidation Method[a]	Extrusion Conditions: Preheat Billet Temperature (°C)	Reduction Ratio	Ram Force (tons): Maximum	Ram Force (tons): Minimum	Speed (ips)	Extrusion Constant (psi)	Tube-Shell Dimensions, in.: Diameter: Outside	Diameter: Inside	Length
							$\times 10^3$			
				W–25, 26, or 30% Re–30% Mo						
0034	PM	2200	4.00	695				1.693		
0421	PM	1850	3.34	560	480	11.0	134	1.789	0.750	15.50
0423	PM	1850	3.28	640	500	12.5	155	1.802	0.750	16.00
0424	PM	1850	4.26	680	500	14.0	135	1.621	0.750	20.88
0541	AC	1870	3.89	420	410	15.6	94	1.775	1.000	15.50
0542	AC	1870	3.97	430	395	14.2	94	1.762	1.000	16.00

[a]AC – arc cast; PM – powder metallurgy.

[b]4-in.-diam billet; all other billets were 3 in. in diameter.

Table 10.2. Tungsten-Alloy Duplex Tube-Shell Extrusion

Extrusion Number	Consolidation Method[a]	Extrusion Conditions: Preheat Billet Temperature (°C)	Reduction Ratio	Ram Force (tons): Maximum	Ram Force (tons): Minimum	Speed (ips)	Extrusion Constant (psi)	Tube-Shell Dimensions, in.: Diameter: Outside	Diameter: Inside	Length
							$\times 10^3$			
				Unalloyed Tungsten						
0325	AC	1760	8.67	880	680		117	1.335	0.750	37.50
0327	AC	1700	8.82	880	680		116	1.240	0.750	41.50
				W–5% Re						
0560	AC	1850	8.80	700	560	2.2	93	1.250	0.750	44.00
0567	AC	1850	9.58	530	375	12.0	67	1.217	0.750	49.00
				W–25 or 26% Re						
0453	PM	1750	5.79	700	600	9.2	118	1.500	0.875	29.00
0472	AC	1750	5.22	670	500	15.1	117	1.500	0.750	24.75
0473	AC	1750	5.22	640	425	10.2	112	1.500	0.750	24.75
0489	PM	1700	4.74	660	560	11.5	128	1.556	0.750	23.50
0539	AC	1870	8.80	545	420	20.0	72	1.250	0.750	41.00
0540	AC	1860	9.02	575	450	20.0	75	1.240	0.750	45.00
0582	AC	1840	7.01	590	450	15.0	87	1.348	0.750	31.25

Table 10.2 (continued)

Extrusion Number	Consolidation Method[a]	Extrusion Conditions: Preheat Billet Temperature (°C)	Reduction Ratio	Ram Force (tons): Maximum	Ram Force (tons): Minimum	Speed (ips)	Extrusion Constant (psi)	Tube-Shell Dimensions, in.: Diameter: Outside	Diameter: Inside	Length
							$\times 10^3$			
			W-25, 26, or 30% Re-30% Mo							
0487	PM	1700	4.93	655	550	10.0	118	1.533	0.750	24.50
0488	PM	1700	4.79	510	480	11.5	94	1.552	0.750	24.00
0583[b]	AC	1840	8.89	550	430	15.0	72	1.246	0.750	40.00
0584	AC	1840	6.76	690	315	11.5	109	1.496	1.000	28.00
0585[b]	AC	1840	6.47	525	385	15.0	85	1.514	1.000	33.75
0586[b]	AC	1840	6.67	495	430	17.1	79	1.501	1.000	35.50
0587	AC	1840	6.47	670	280	1.7	110	1.514	1.000	27.00
0588[b]	AC	1850	5.09	515	370	21.4	91	1.514	0.750	35.00
0589	AC	1840	8.74	475	375	20.0	63	1.254	0.752	38.50
0590	AC	1850	7.99	505	570	20.0	70	1.290	0.750	42.50
0591	AC	1850	8.01	570	485	23.0	79	1.289	0.750	42.00
0592	AC	1850	8.65	515	430	20.0	69	1.258	0.752	43.00

[a] AC — arc cast; PM — powder metallurgy.

[b] Supplied to GE-NMPO.

Table 10.3. Tungsten-Alloy Primary and Duplex Rod Extrusions

Extrusion Number	Consolidation Method[a]	Extrusion Conditions: Preheat Billet Temperature (°C)	Reduction Ratio	Ram Force (tons): Maximum	Ram Force (tons): Minimum	Speed (ips)	Extrusion Constant (psi)	Dimensions of Extruded Rod, in.: Outside Diameter	Dimensions of Extruded Rod, in.: Length
							$\times 10^3$		
Primary Extrusions									
Unalloyed Tungsten									
0353	AC	1800	5.92	590	500	12.7	90	1.236	31.75
0532	PM		5.6	540	455	15.9	86	1.303	
0547	PM	1840	5.92	700	695		106	1.250	
0647	AC	1650	4.15	535	425	3.0	102	1.500	17.5
W–5% Re									
0451	AC	1800	5.99	640	560	7.6	97	1.250	10.12
W–26% Re									
0419	AC	1850	3.34	680	640	8.5	153	1.675	7.25
W–25% Re–30% Mo									
0449	AC	1850	5.99	670	600	8.8	101	1.250	24.00
0450	AC	1850	5.99	560	544	9.6	85	1.250	14.25

Table 10.3 (continued)

Extrusion Number	Consolidation Method[a]	Extrusion Conditions: Preheat Billet Temperature (°C)	Reduction Ratio	Ram Force (tons): Maximum	Ram Force (tons): Minimum	Speed (ips)	Extrusion Constant (psi)	Dimensions of Extruded Rod, in.: Outside Diameter	Length
			Duplex Extrusions						
Unalloyed Tungsten									
0500	PM	1800						1.512	28.125
0538	CVD	1870	5.2	420	345	20.0	63	1.252	
W–5% Re									
0561	PM	1800	4.26	380	325	14.0	71	1.483	26.50
0638	AC	1780	8.88	545	395	12.5	72	1.271	37.5
W–26% Re									
0429	AC	1850	9.36	700	680	5.7	85	1.000	46.75
0452	AC	1770	5.99	600	540	10.1	91	1.250	19.50

[a]AC – arc cast; PM – powder metallurgy; CVD – chemical vapor deposition.

Table 10.4. Tungsten-Alloy Sheet Bar Extrusions

Extrusion Number[a]	Extrusion Conditions: Preheat Billet Temperature (°C)	Reduction Ratio	Ram Force (tons) Maximum	Ram Force (tons) Minimum	Speed (ips)	Extrusion Constant (psi)	Dimensions of Extruded Sheet Bar, in. Width	Thickness	Length
						$\times 10^3$			
				Unalloyed Tungsten					
0354	1800	5.33	580	465	12.0	94	1.822	0.700	32.75
				W–5% Re					
0484	1550	4.51	560	480	7.0	101	2.030	0.803	8.25
				W–26% Re					
0485	1675	4.51	700	680		126	2.030	0.803	13.75
				W–25% Re–30% Mo					
0488	1850	5.60	640	600	12.7	100	1.750	0.750	22.00

[a]Arc cast.

Hot-Plug Drawing of Tungsten and Tungsten Alloys (G. A. Reimann)

Production of satisfactory tungsten and tungsten-alloy tubing by "conventional" techniques is difficult because of the elevated temperatures required to achieve significant deformations. At the drawing temperatures normally used for these alloys, about 200°C, the deformation per pass is very small, and many passes are required to produce tubing. To increase the amount of deformation per pass, one approach is to increase the drawing temperature to 700°C or above where tungsten can be more easily deformed without failure. The mandrel drawing approach is not suitable for temperatures above 700°C because no mandrel material has been found that will retain its properties at or above this temperature. However, plug drawing with ceramic-coated plugs has potential use in this temperature range.

The feasibility of plug drawing for tungsten tubing was demonstrated previously,[4] as was the apparent superiority of this approach to mandrel drawing. The W–30% Re–30% Mo tubing, duplex-extruded to a 1.030-in. outside diameter and 0.100-in. wall thickness, was drawn 30% in three passes at 1050°C without intermediate anneals. As expected, the tungsten-alloy tubing is considerably more difficult to draw than the molybdenum-alloy tubing investigated earlier, although were it not for the elevated temperature, attempts at drawing would have met with complete failure. No defects were evident in the tungsten-alloy tube, and, since each pass required about one-third of the bench capacity, the capability exists for considerably heavier reductions per pass.

Work has continued on developing plug drawing techniques suitable for reducing primary- and duplex-extruded tungsten tubing. Temperature, lubricants, tooling, and other drawing parameters are being investigated.

Lubricating the tubing during drawing is a major problem. Fiske 604, a proprietary compound intended for use as a hot-die lubricant, worked well when drawing molybdenum-alloy tubing at 750°C and below but is not recommended for use at temperatures of 1000°C and above. In an effort

---

[4]G. A. Reimann, Metals and Ceramics Div. Ann. Progr. Rept. June 30, 1967, ORNL-4170, p. 81.

to overcome lubrication problems above 1000°C, a number of glass compounds were investigated; however, formation of a tungsten oxide film prevented satisfactory adherence of the glass coatings. Also, thin-walled tubing (about 0.030-in. wall thickness) does not retain sufficient heat between the cooler die and plug to maintain glass fluidity so that the die, tube, and plug become cemented together by the solidifying glass. This problem could be eliminated if a glass were developed that remained fluid in the 350 to 425°C range of the tooling and if a satisfactory method were devised to apply it to the tube as it emerges from the furnace. Fiske 604 has so far been the best lubricant, even though the 1100 to 1200°C temperatures are above those recommended by the manufacturer.

The dies with zirconia inserts are working well, even at temperatures above 1200°C, but because of the lack of a suitable lubricant the life of the dies is short at high temperatures. Breakage of the zirconia-coated drawing plugs is a major problem, and additional drawing plugs have been ordered from a different supplier.

Chemical Vapor Deposition of Tungsten Alloys

J. I. Federer

Deposition of Tungsten-Rhenium Sheet for Mechanical Properties Evaluation

Tungsten-rhenium alloy sheet for metallurgical and mechanical properties evaluation is being deposited by the hydrogen reduction of WF_6 and ReF_6. Alloys are deposited on the external surface of substrates contained within a relatively large cold-wall chamber, which is shown schematically in Fig. 10.1. The water-cooled chamber is 4 in. in inside diameter by 24 in. long. The gases flow along the axes of the substrates, which are heated by direct resistance. The substrates are loaded in tension to maintain straightness. Deposition temperatures were varied from 600 to 950°C at about 10 torr. The $H_2/(WF_6+ReF_6)$ ratio was maintained constant at 15; the WF_6/ReF_6 ratio was adjusted to deposit nominal 5 to 25% Re alloys.

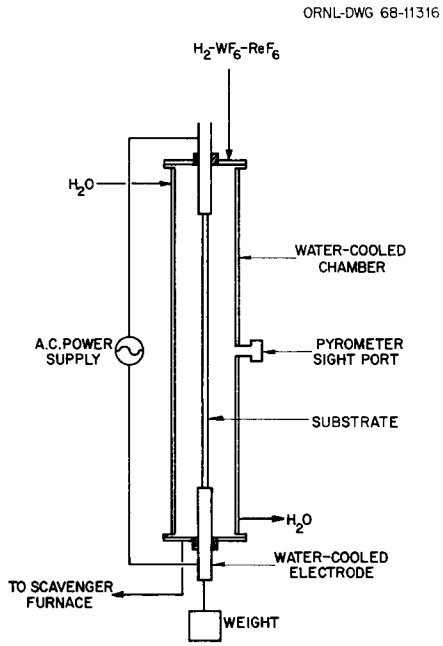

Fig. 10.1. Apparatus for Deposition on the External Surface of Tubular and Sheet Substrates.

The results of typical experiments, shown in Table 10.5, may be summarized as follows. (1) Nominal 5% Re alloys were generally uniform in composition along the length, and the composition was not particularly sensitive to temperature. Nominal 25% Re alloys were more uniform in composition when deposited at 750°C than at 600 or 950°C. (2) Nominal 5% Re alloys had smooth surfaces. Nominal 25% Re alloys deposited on sheet substrates had smooth surfaces, but they were nodular when deposited on 1/4-in.-OD substrates. (3) The thickness of the deposits gradually decreased from the gas-inlet end of the apparatus toward the outlet end as the WF_6 and ReF_6 became depleted. In deposits that were uniform in composition the WF_6/ReF_6 ratio apparently remained approximately constant along the deposition surface. The periodically reversed gas flow has improved the thickness uniformity of the deposits. Thus, the external coating arrangement is better than the internal coating technique previously used[5] both with respect to composition and thickness uniformity when the reversed gas flow technique is used.

---

[5]J. I. Federer, "Deposition of Tungsten-Rhenium Alloys," Metals and Ceramics Div. Ann. Progr. Rept. June 30, 1968, ORNL-4370, Chap. 16.

Table 10.5. Compositional Uniformity and Morphology of Tungsten-Rhenium Deposits

Temperature (°C)	Substrate[a]	Rhenium Content (%) at Intervals Along the Deposits				Morphology
		2 in.	6 in.	10 in.	14 in.	
850	A	6.6	3.9	3.7	3.3	Smooth
850	A					Smooth
800	A					Smooth
800	A					Smooth
800	A	3.3	3.2	3.4	3.5	Smooth
800	B	3.3	3.7	3.9	3.9	Smooth, a few nodules
600	B	4.4	3.6	3.4	3.3	Smooth
600	B	4.6	3.2	3.5	3.6	Smooth
600	B					Smooth
950	A	17.3	18.7	21.2	21.5	Smooth
750	B	22.1	24.6	24.8	21.9	Smooth, a few nodules
600	B		44.7	20.8	20.8	Smooth, a few nodules
750	C	25.9	25.5	25.2	24.8	Nodular
600	C	30.1	27.9	25.6	23.0	Nodular
600	C					Nodular
600	C					Nodular

[a]Substrate dimensions: A – 5/8- × 0.032- × 18-in. stainless steel plate; B – 1 1/2- × 0.02- × 18-in. stainless steel or molybdenum plate; C – 1/4-in.-OD × 18-in.-long stainless steel or molybdenum tube.

Based upon the results presented in Table 10.5, sheet deposits nominally containing 5% Re were prepared at 600°C, 10 torr, and 3000, 190, and 10 cfm of H_2, WF_6, and ReF_6, respectively. The substrate was 1 1/2-in.-wide by 0.020-in.-thick by 18-in.-long molybdenum sheet. The surface of the deposit was smooth on both sides except for a few isolated nodules. The reduction efficiency was about 75%. The rhenium content and thickness on both sides of the substrate are shown in Table 10.6. Although the rhenium content was less than the intended 5%, the deposit provides about 42 in.^{2} of flat stock with a thickness of at least 0.045 in. The deposit was machined into 50 bend specimens 1.5 in. long by 0.375 in. wide. Most of the specimens cracked during grinding to final thickness, which was intended to be 0.040 in. The deposit had a slight twist that imparted a small curvature to each specimen. This

Table 10.6. Rhenium Content and Thickness of Nominal 5% Re Sheet Deposit

Length (in.)	Rhenium (%)	Thickness, in.	
		Side A	Side B
2	3.2	0.051	0.045
6	2.2	0.069	0.056
10	2.5	0.079	0.063
14	3.2	0.077	0.061
16	4.9	0.056	0.049

curvature, unrelieved stress resulting from deposition, and restraint during grinding probably caused the cracking. The deposit was not stress relieved after deposition so that bend testing could be conducted in the as-deposited and several heat-treated conditions. At least part of future deposits to be machined into specimens should first be stress relieved.

Investigation of Methods for Producing Fine-Grained Deposits

A possible technique for obtaining fine-grained W–25% Re alloys by vapor deposition is to deposit layers of tungsten and rhenium or alloy, then homogenize by diffusion. We prepared deposits with 0.002- to 0.003-in.-thick layers of tungsten and rhenium, layers of tungsten and W–50% Re, and layers of W–25% Re by interrupted deposition. The nominal composition of these deposits was 25% Re. The rhenium layers in the first deposit were nodular and porous, while the other two deposits had no nodules and had smooth surface textures. The grain structure of the deposits was columnar within the layers.

The deposits were heat-treated at 2000°C in vacuum for 100 hr. The layers of tungsten and rhenium were not completely homogenized by this treatment. Although the other deposits appeared to be homogeneous, the original layer lines were still visible. The columnar grains within the layers grew into an approximately equiaxed structure with a grain size of about 100 μm. Different grain sizes can probably be obtained by using different heat treatments.

The technique of depositing layers of tungsten and W–50% Re or layers of W–25% Re may have the advantage of minimizing nodular growths that are a problem with thick W–25% Re deposits. Nodules usually nucleate after the deposit attains a thickness greater than the thickness of layers obtained in the deposits mentioned above.

Parametric Studies of the Tungsten-Rhenium Codeposition Process

A thermodynamic analysis of the tungsten-rhenium codeposition process indicated that the deposit composition will be identical to the metal content of the WF_6-ReF_6 mixture at specific temperatures and pressures.[6] Under these conditions, the WF_6/ReF_6 ratio in the gas mixture remains constant during deposition. Temperature or pressure variations would result in either rhenium-rich or rhenium-poor deposits. In order to confirm the results predicted by the analysis, we prepared a series of deposits to identify composition trends related to temperature and pressure variations. The conditions and results of these experiments are shown in Table 10.7.

Table 10.7. Conditions and Results of Parametric Study for Tungsten-Rhenium Codeposition Process

Temperature (°C)	Pressure (torr)	Rhenium Content, %		ΔRe (%)
		WF_6-ReF_6 Mixture	Deposit	
800	10	3.26	2.40	0.86
1000	10	4.00	3.14	0.86
1200	10	4.01	1.70	2.31
800	25	3.62	1.52	2.10
1000	25	3.79	2.20	1.59
1200	25	3.41	0.40	3.01

[6]W. C. Robinson and J. I. Federer, "Thermodynamic Considerations of the Chemical Vapor Deposition Process," paper presented at the 97th Annual Meeting of the American Institute of Mining, Metallurgical, and Petroleum Engineers, New York City, February 18–22, 1968.

The ΔRe values, representing the difference between the rhenium content of the WF_6 and ReF_6 mixture and the deposit, show no obvious trend with temperature at either pressure investigated. The rhenium content of the mixture was based on actual weights of WF_6 and ReF_6 used under steady flow and is accurate within ±0.05% Re. The colorimetric method used for rhenium analysis of the deposits is accurate within ±4% of the rhenium content. Thus, there is no ready explanation for the ΔRe values. Additional deposits are being prepared at 600, 800, and 1000°C (5 torr) and at 600°C (10 and 25 torr). This extension of deposition parameters may aid in finding composition trends related to temperature and pressure variations.

Metallurgical Properties of Tungsten Alloys

A. C. Schaffhauser K. Farrell

We are studying the deformation, recrystallization, and ductile-to-brittle transition temperature (DBTT) behavior of wrought CVD tungsten, since the CVD process offers advantages in supplying feed material for secondary working operations, particularly in the production of thin-walled tubing.[7] Previously, we have shown that fluorine impurities and the associated formation of gas bubbles that occurs on annealing prevent grain growth in undeformed CVD tungsten.[8,9] The present studies on rolled CVD tungsten sheet show that recrystallization and grain growth

---

[7]W. R. Martin et al., "Application of Chemical Vapor Deposition to the Production of Tungsten Tubing," pp. 303–314 in Proceedings of the Conference on Chemical Vapor Deposition of Refractory Metals, Alloys, and Compounds, Gatlinburg, Tennessee, September 12–14, 1967, ed. by A. C. Schaffhauser, American Nuclear Society, Hinsdale, Illinois.

[8]A. C. Schaffhauser and R. L. Heestand, "Effect of Fluorine Impurities on the Grain Stability of Thermochemically Deposited Tungsten," p. 222 in 1966 IEEE Conference Record of the Thermionic Conversion Specialist Conference, Institute of Electrical and Electronic Engineers, New York.

[9]A. C. Schaffhauser and R. L. Heestand, Metals and Ceramics Div. Ann. Progr. Rept. June 30, 1967, ORNL-4170, p. 88.

are also retarded by gas bubbles. Due to retention of the wrought structure after annealing between 1400 and 2000°C, the CVD sheet has a lower DBTT than tungsten sheet produced conventionally.

The starting material for the rolling studies was 1/8-in.-thick, 1-in.-wide CVD tungsten plate obtained by depositing on the inside of a 16-in.-long hexagonal mandrel. The deposition conditions and fabrication procedures were similar to those previously described.[10] A typical columnar grain structure was produced during deposition. The fluorine impurity concentration varied between 28 and 22 ppm from the inlet to outlet end of the deposit, and the concentration of all other impurities was less than 20 ppm. The sheet was rolled in molybdenum picture frames with stainless steel cover plates at 10% reduction per pass with no intermediate anneals.

Total reductions in thickness of 80% were attempted at temperatures from 1000 down to 200°C, and reductions between 40 and 95% were investigated at 600°C. The rolling conditions and results are given in Table 10.8. Sheet of excellent quality was obtained by rolling 80% at 1000 and 800°C. At 600°C a few edge cracks developed at low reductions, but the number and depth of the cracks did not increase for the heavier

[10] J. E. Spruiell, B. F. Shuler, and F. H. Patterson, Trans. Met. Soc. AIME 239(11), 1763–1767 (November 1967).

Table 10.8. Effect of Rolling Conditions on the Properties of CVD Tungsten Sheet

Rolling Temperature (°C)	Reduction (%)	Microstructure	Hardness (DPH)	Recrystallization Temperature, °C, for 1-hr Anneals	
				Start	Complete
1000	80	Wrought	493	1800	2200
800	80	Wrought	517	1800	2200
600	80	Wrought	517	1800	2200
400	80	Cracks	501	1200	2200
600	40	Columnar	502	2200	> 2500
600	60	Partially wrought	517	2000	2500
600	80	Wrought	517	1800	2200
600	95	Wrought	530	1600	2200

reductions. On rolling at 400°C, extensive edge and surface cracking on the original, coarse-grained surface was observed.

The microstructures of samples deformed 80% at 400 to 1000°C were similar with the exception of the cracks observed at the lower temperatures. Hardness data on the as-rolled specimens show recovery during rolling at 1000°C.

The effect of the reduction in thickness on the microstructures of samples rolled at 600°C is shown in Fig. 10.2. At 40% reduction, the columnar grains were merely squashed, which increased the width of the grains. As the reduction increased, the grains reoriented and were strung out in the rolling direction. Greater than 80% reduction is necessary to break up the original columnar grain structure completely in both the longitudinal and transverse directions.

The hardness of samples rolled at 600°C (Table 10.8) increases from approximately 460 DPH as-deposited to 530 DPH at 95% reduction in thickness. This increase in hardness is significantly less than the 380 to 520 DPH increase observed on rolling tungsten sheet derived by powder metallurgy techniques.[11] We believe this lower work hardening of the CVD material is a result of the greater hardness of the as-deposited material due to fluorine impurities.[9]

The recrystallization temperatures for samples rolled under different conditions are also listed in Table 10.8. Recrystallization in this material is very sluggish, occurring between 1800 and 2500°C. This contrasts with the very rapid recrystallization observed between 1200 and 1400°C in conventionally produced tungsten sheet that has similar fabrication history and higher impurity concentrations. Rolling temperature has no apparent effect on the recrystallization temperature of samples rolled 80% with the exception of a few areas of recrystallization associated with inhomogeneous deformation around cracks in the samples rolled at 400°C. The hardness drop occurring on recrystallization is typified by the top curve in Fig. 10.3. The microstructures of partially recrystallized samples after annealing at 1800 and 2100°C are shown in the top

---

[11]F. F. Schmidt and A. R. Ogden, The Engineering Properties of Tungsten and Tungsten Alloys, DMIC Report 191 (Sept. 27, 1963), p. A-40.

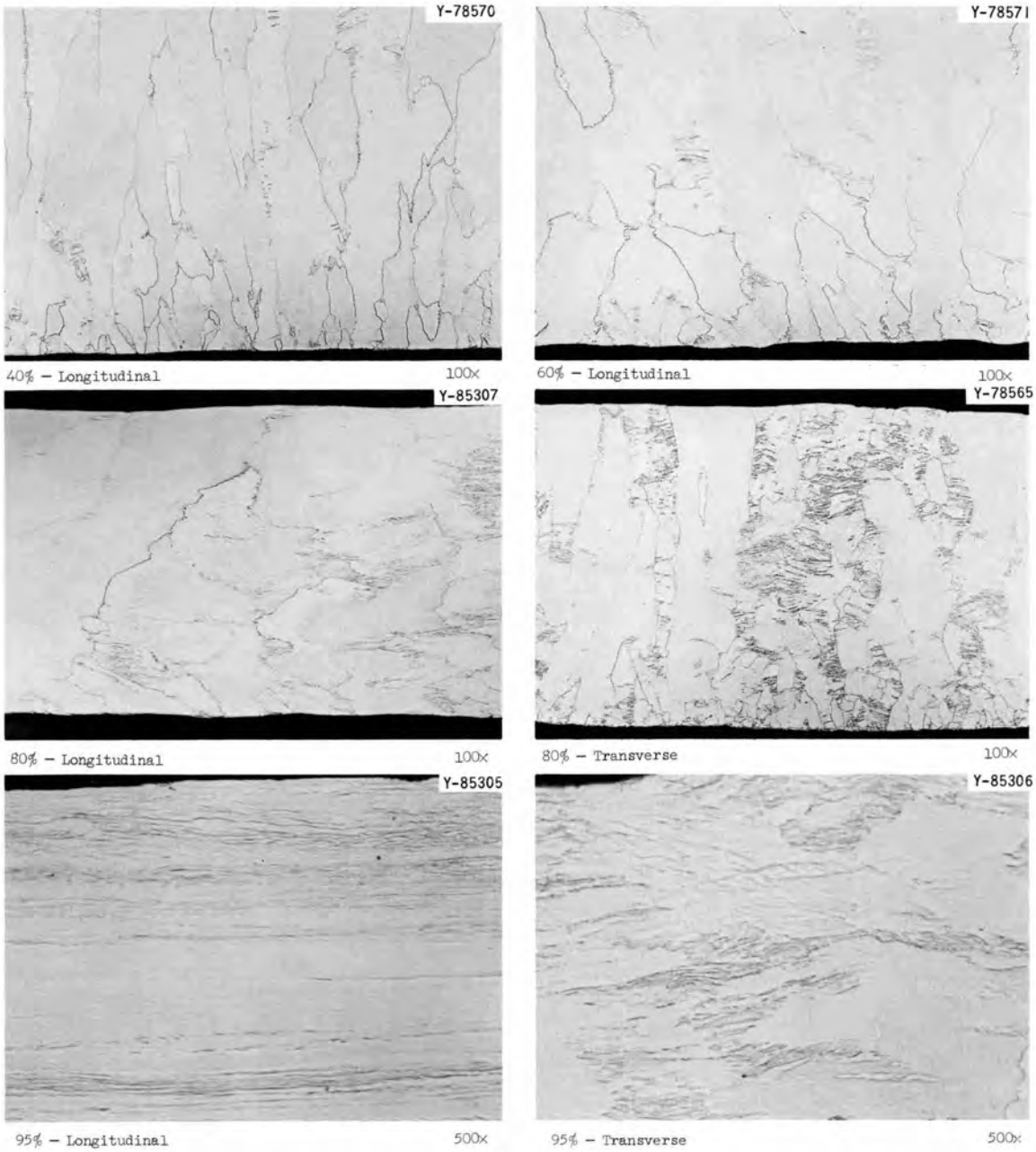

Fig. 10.2. Effect of Reduction in Thickness on Microstructure of Samples Rolled at 600°C.

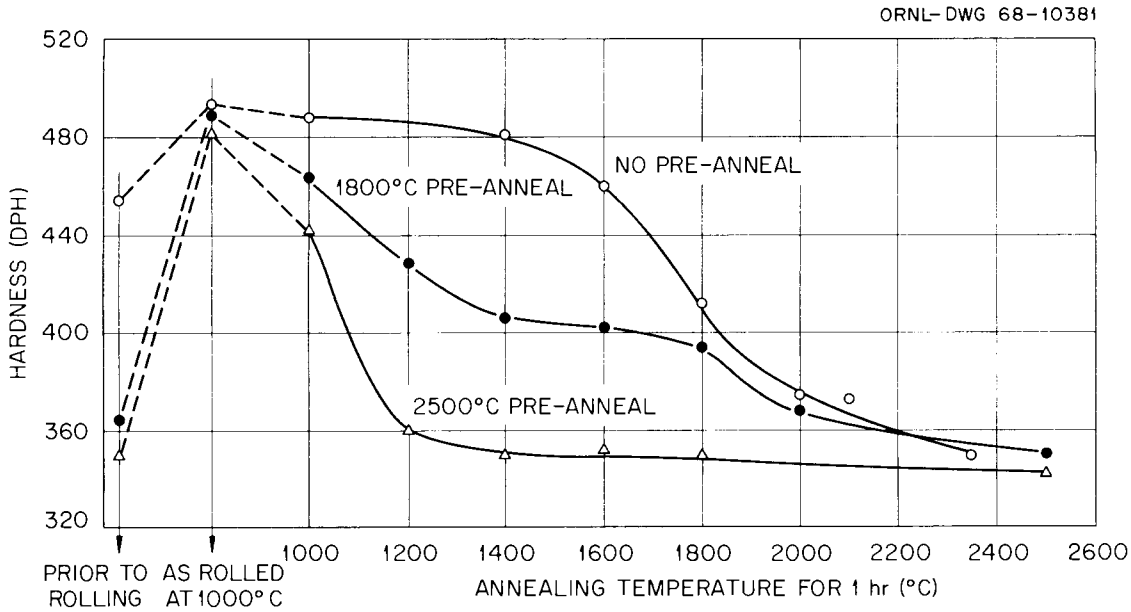

Fig. 10.3. Effect of Annealing Temperature on the Hardness of As-Deposited and Preannealed CVD Tungsten Sheet Rolled 80% at 1000°C.

pictures in Fig. 10.4. Recrystallization of material reduced less than 80% occurs at temperatures above 2000°C. We are determining the kinetics of recrystallization from measurements of the volume percentage of recrystallized material.

Transmission electron microscopy has shown that small bubbles less than 400 A in diameter are present on dislocations and subgrains in unrecrystallized material annealed at 1400 to 1800°C (Fig. 10.5). To assess the effect of these gas bubbles in retarding recrystallization, we annealed samples at 1800 and 2500°C before rolling to precipitate larger bubbles.[12] The effect of these preannealing treatments on the recrystallization behavior of material rolled 80% at 1000°C is seen in the hardness data in Fig. 10.3 and microstructures in Fig. 10.4. These data show that gas bubbles less than 400 A and/or unprecipitated fluorine impurities are effective in preventing recrystallization in this material.

---

[12] K. Farrell, J. T. Houston, and A. C. Schaffhauser, "The Growth of Grain Boundary Gas Bubbles in Chemically Vapor Deposited Tungsten," pp. 363–390 in Proceedings of the Conference on Chemical Vapor Deposition of Refractory Metals, Alloys, and Compounds, Gatlinburg, Tennessee, September 12–14, 1967, ed. by A. C. Schaffhauser, American Nuclear Society, Hinsdale, Illinois.

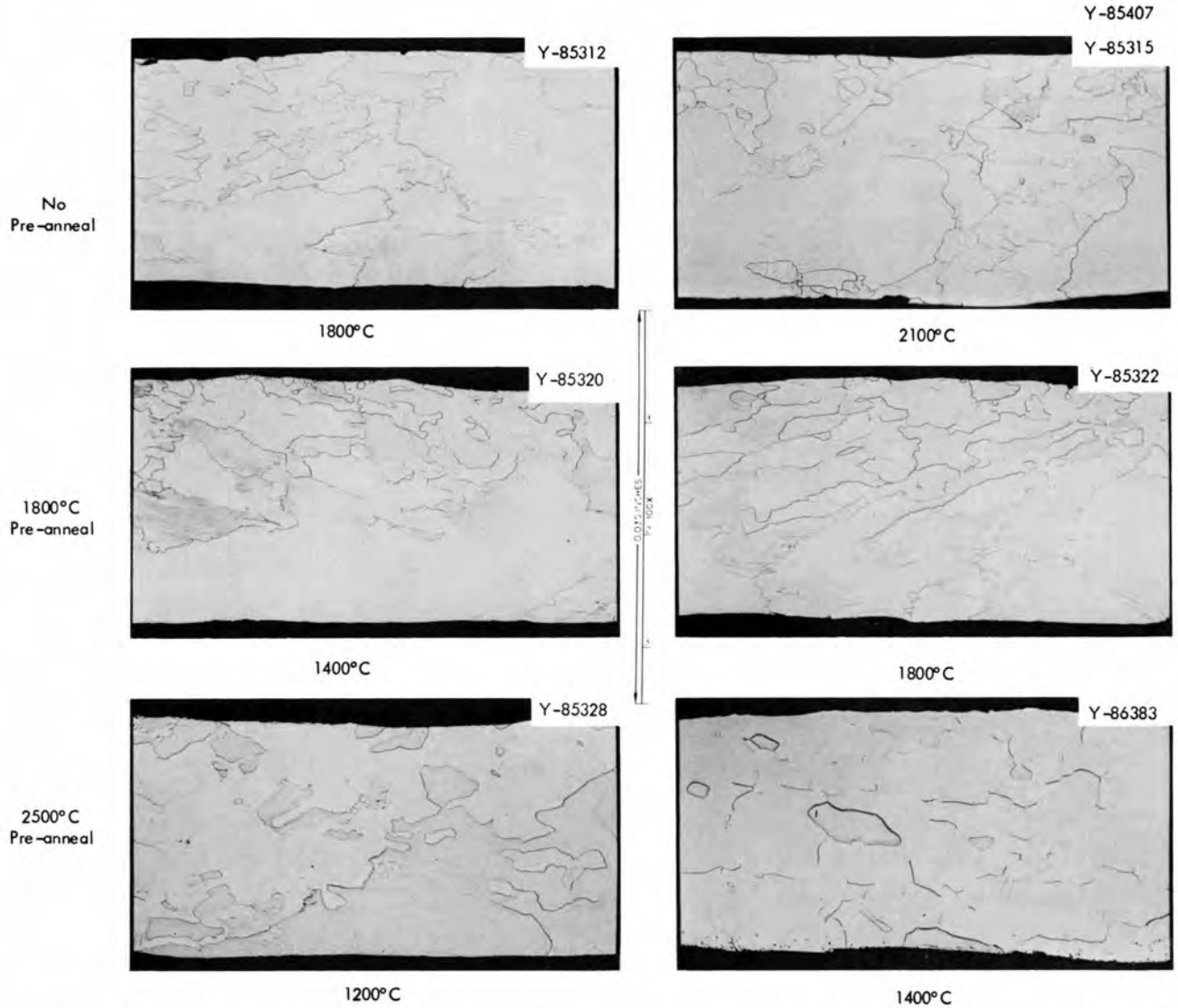

Fig. 10.4. Effect of Annealing Before Rolling on the Recrystallization Behavior of CVD Tungsten.

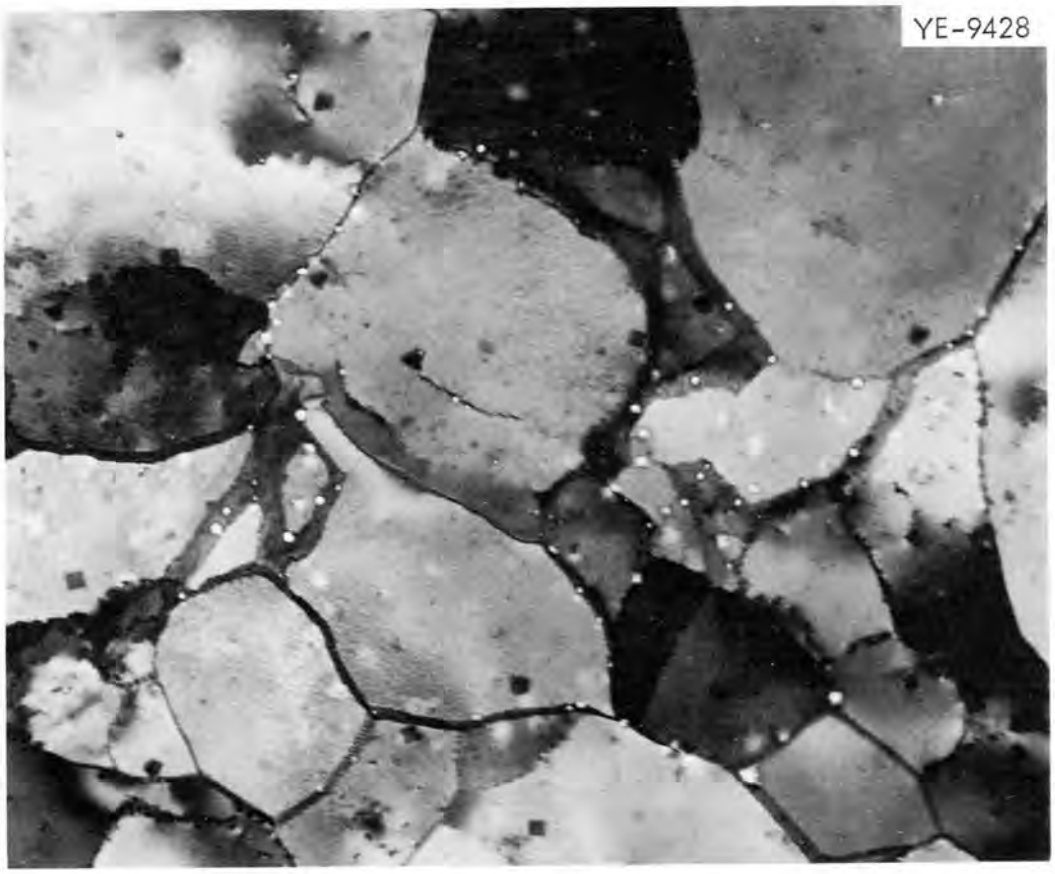

Fig. 10.5. Gas Bubbles in Substructure of CVD Tungsten Rolled 80% at 600°C and Annealed 1 hr at 1800°C. 30,000×.

The ductile-to-brittle transition behavior and low-temperature yield strength of sheet reduced 80% in thickness were evaluated by three-point bend tests. The data are shown in Fig. 10.6. Material rolled 80% at 600°C had a higher yield strength than material rolled at 1000°C, but the ductilities were similar. A 1-hr anneal at 1200°C produced no appreciable change in strength, but significantly lowered the temperature at which fracture occurred during bending. The transition temperature was increased by annealing at higher temperatures, particularly at 2100°C, where the sample was recrystallized.

A comparison of the effect of annealing treatment on the DBTT of as-deposited and rolled CVD tungsten sheet with rolled powder-metallurgy, arc-cast, and electron-beam-melted tungsten sheet is presented in Table 10.9. After annealing, the DBTT of as-deposited and rolled CVD tunsten is very similar. The DBTT of rolled powder-metallurgy, arc-cast,

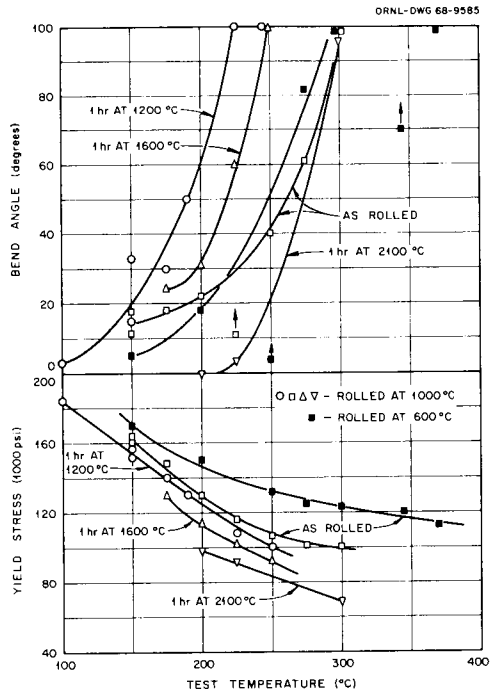

Fig. 10.6. Low-Temperature Bend Ductility and Yield Strength of Rolled and Annealed CVD Tungsten Sheet.

Table 10.9. Effect of 1-hr Annealing Treatments on the DBTT of Tungsten Sheet Produced by Various Methods

Method of Consolidation	Reduction in Thickness (%)	DBTT,[a] °C			
		As-Rolled	1200	1600	2100
CVD[b]	0	400[b]	200	200	275
CVD	80	225	175	200	260[c]
Powder metallurgy[d]	95		100	260[c]	280[c]
Arc cast[e]	85	95	120	280[c]	345[c]
Electron-beam melted[e]	85	140	275[c]	340[c]	375[c]

[a]Defined as the median temperature between the highest temperature at which the material was brittle and the lowest temperature at which it was ductile. The bending radius was four times the sheet thickness.

[b]As-deposited CVD sheet (PR 44), 25 ppm F.

[c]Recrystallized.

[d]K. Farrell, A. C. Schaffhauser, and J. O. Stiegler, J. Less-Common Metals 13, 141 (1967).

[e]W. D. Klopp and W. R. Witzke, Mechanical Properties and Recrystallization Behavior of Electron-Beam-Melted Tungsten Compared with Arc-Melted Tungsten, NASA TN D-3232 (January 1966).

and electron-beam-melted sheet is lower than that of the CVD sheet after annealing at temperatures below their recrystallization temperature. At the higher annealing temperatures, the CVD material has a lower DBTT because of its resistance to recrystallization and grain growth.

Long-Time Creep-Rupture Properties of Tungsten Alloys

R. L. Stephenson

We are continuing our evaluation of the long-time creep-rupture properties of tungsten alloys. Comparison of the creep-rupture properties of powder-metallurgy and arc-cast W–25% Re was completed,[13] and we are now evaluating arc-cast unalloyed tungsten, W–5% Re, W–26% Re, and W–25% Re–30% Mo.

The stress-rupture and secondary creep-rate data obtained to date are shown in Figs. 10.7 and 10.8. It appears that the addition of 5% Re

[13]R. R. Lowery and G. Asai, An Evaluation of W–25% Re Produced by Both Arc Melting and Powder Metallurgy, USBM-RC-1274 (Feb. 19, 1968).

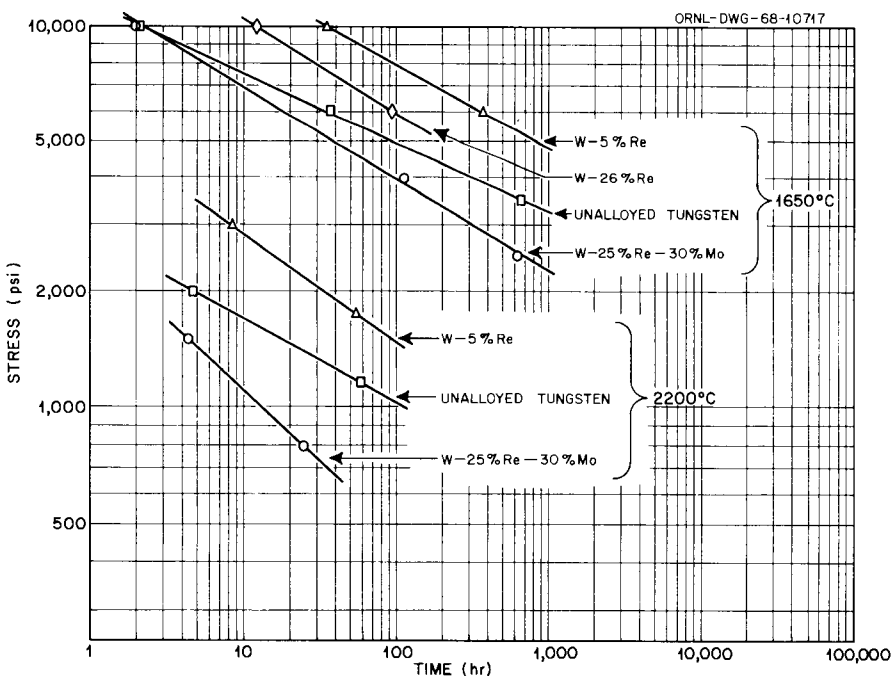

Fig. 10.7. Stress-Rupture Properties of Selected Tungsten-Base Alloys.

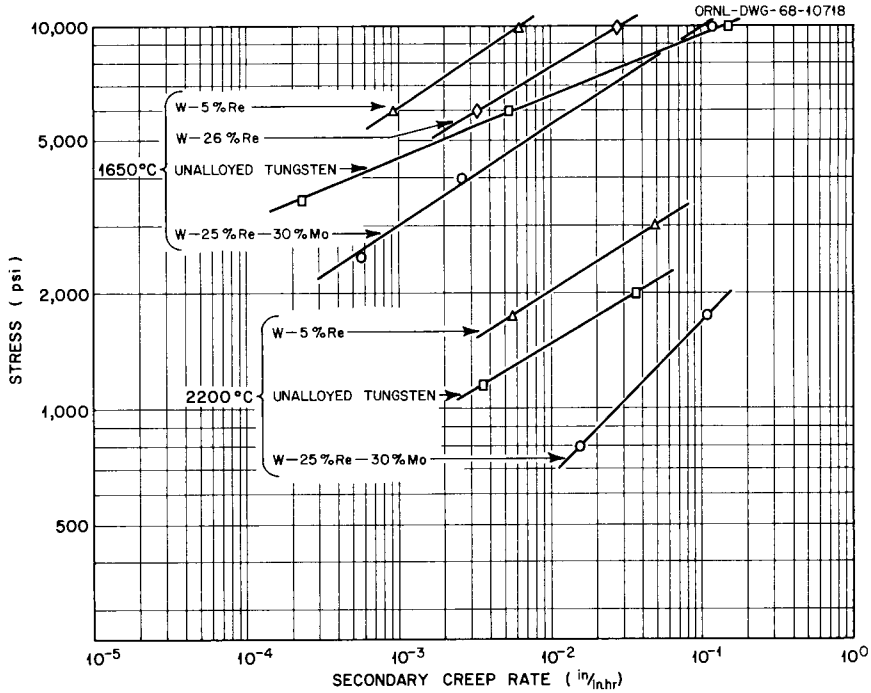

Fig. 10.8. Secondary Creep Rate Versus Stress for Selected Tungsten-Base Materials.

produces significant solution strengthening at the higher stresses and shorter rupture times. The addition of larger amounts of elements with lower melting points (rhenium and molybdenum) reduces the creep strengths at long times and high temperature.

Evaluation of Welds and Brazes in Tungsten Alloys

Nancy C. Cole

Since tungsten and its alloys are becoming more in demand in space and nuclear industries, weldability considerations are of utmost importance. In our program, we are studying the effects of welding on the properties of tungsten and tungsten-rhenium alloys produced by powder-metallurgy, arc-casting, and chemical vapor deposition.

Tungsten, like all refractory metals, must be welded in a high-purity atmosphere, whether it be inert gas (tungsten-arc process) or vacuum (electron-beam process).[14] We have found in tungsten-arc welding

[14]R. G. Gilliland, Joining of Tungsten, ORNL-TM-1606 (October 1966).

of unalloyed sheet (in thicknesses of 1/16 in.) that we must preheat the workpiece (Fig. 10.9 shows a schematic diagram of the preheating fixture). We investigated workpiece temperatures from room temperature to 540°C and found that a minimum workpiece preheat of 150°C is necessary to produce one-pass butt welds consistently free from cracking in specimens this thick. Higher preheats did not appear to be beneficial; however, configurations involving more severe stress concentrations or more massive parts may require higher preheat temperatures.

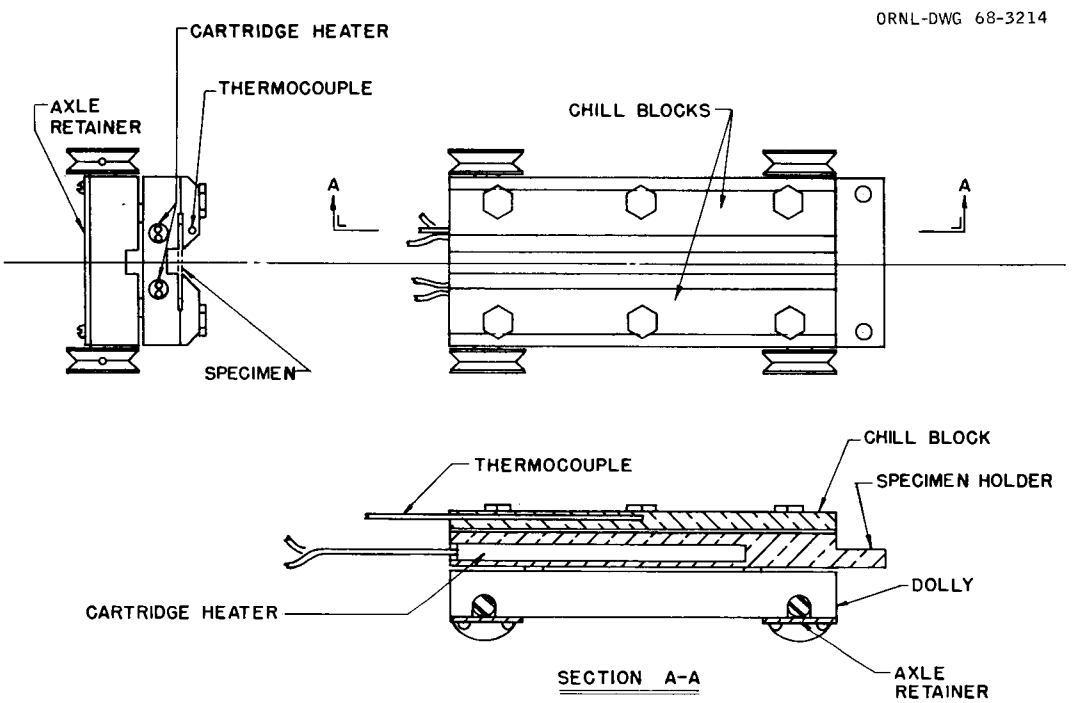

Fig. 10.9. Preheating Fixture Designed for Welding Tungsten.

The quality of a weldment depends greatly upon the methods and procedures used in fabricating the base metals. Welds in arc-cast and electron-beam-melted base metals are essentially free from porosity; welds in powder-metallurgy tungsten are characterized by gross porosity, particularly along the fusion line. The amount of this porosity is considerably reduced in welds in GE-15 (ref. 15) (Fig. 10.10). The

[15]Proprietary powder-metallurgy tungsten produced by General Electric, Cleveland, Ohio.

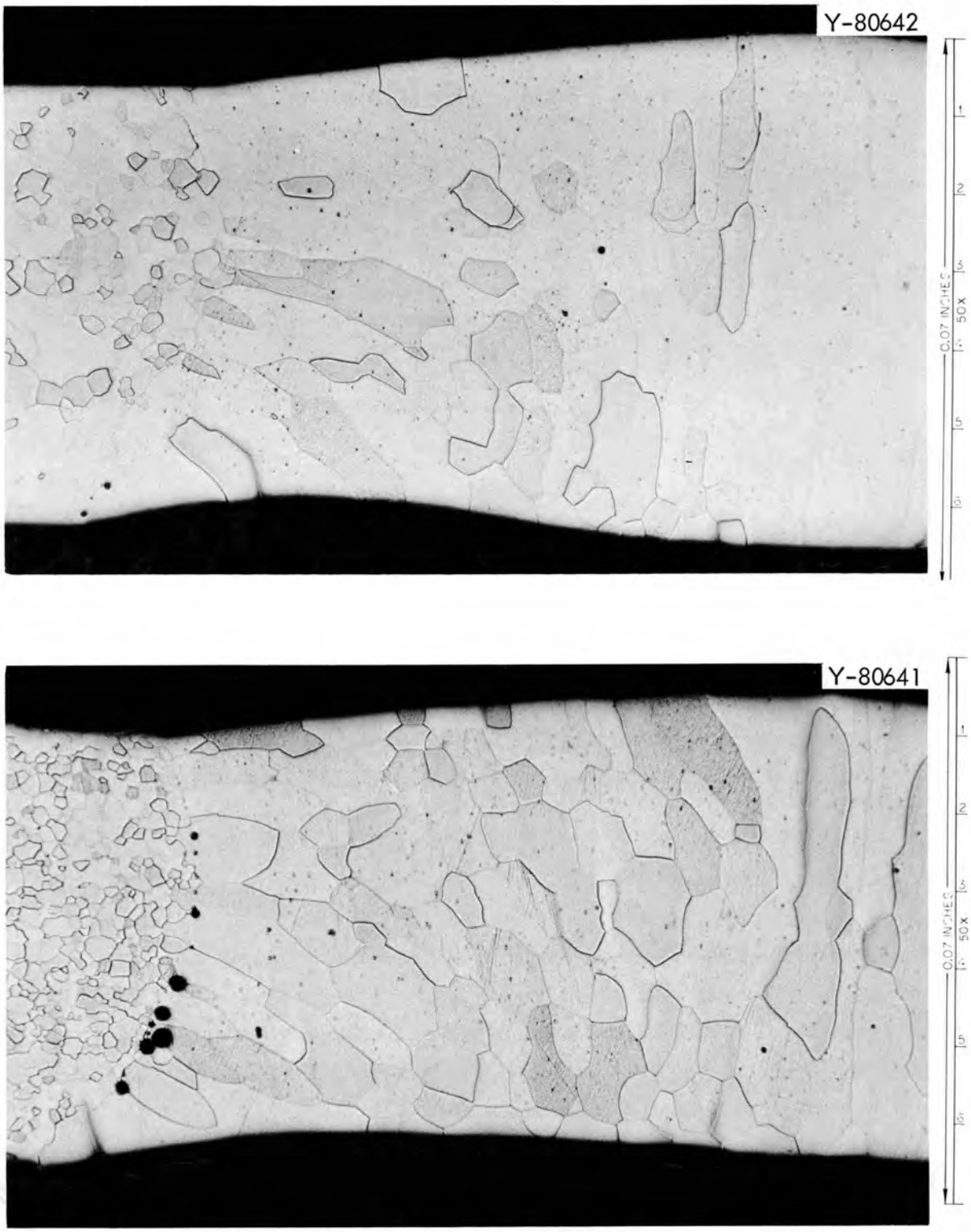

Fig. 10.10. Welds in Powder-Metallurgy Tungsten Showing the Lack of Porosity in Proprietary GE-15 Material (top) as Compared with a Typical Commercial Tungsten Product (bottom).

ductile-to-brittle transition temperature of these two materials is shown in Fig. 10.11. The DBTT of both unwelded materials was 150°C. Upon welding, the values increased to at least 325°C for the typical powder-metallurgy metal and 385°C for GE-15. We attribute much of this embrittling effect to the large grain size of the welds and the adjacent recrystallized heat-affected zone.

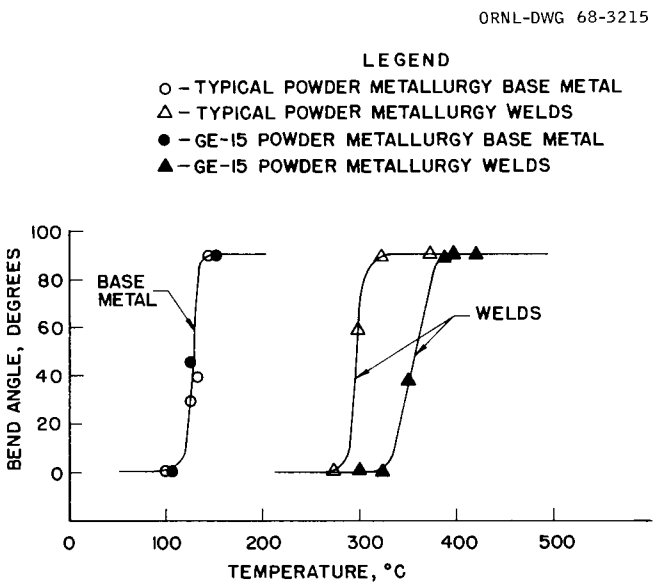

Fig. 10.11. Ductile-to-Brittle Transition Curves for Powder-Metallurgy Tungsten.

As documented elsewhere,[16] as-deposited tungsten has an unusual heat-affected zone due to its base-metal grain structure. Figure 10.12 shows the surface and corresponding cross section of a tungsten-arc butt weld in CVD tungsten. Note how the original fine grains at the substrate surface have grown due to the heat of welding. Also evident is the lack of growth of the large columnar grains. Cracking is found in the grain boundaries of these columnar grains when the residual fluorine content is greater than 10 to 20 ppm. However, we have not seen any cracking in the equiaxed grains.

---

[16]N. C. Cole and G. M. Slaughter, "Tungsten Welding Development," Metals and Ceramics Div. Ann. Progr. Rept. June 30, 1968, ORNL-4370, Chap. 16.

Fig. 10.12. Gas Tungsten-Arc Butt Weld in CVD Tungsten. (a) Top view, 8×, (b) cross section, 20×.

To increase our understanding of the welding metallurgy of tungsten and tungsten-rhenium alloys, we have made a study of bead-on-plate welds using unalloyed tungsten-base material and W–26% Re filler metal. The bead-on-plate welds were made manually on GE-15 and commercial-grade powder-metallurgy products. The specimens were examined metallographically, and hardness traverses were taken across the weld, heat-affected zone, and base metal in the as-welded and heat-treated conditions. Each type of weld was aged at 900, 1200, 1600, and 2000°C for 1, 10, 100, and 1000 hr.

The effects of time and temperature on the hardness of powder-metallurgy unalloyed tungsten welded with powder-metallurgy W–26% Re filler wire are shown in Fig. 10.13(a) and (b). Figure 10.13(a) shows the effect of time on specimens aged at 1200°C. The hardness is plotted as a function of distance from the weld center line. It can be seen that the hardness drops abruptly at the weld fusion line, the as-deposited W–26% Re weld metal being harder than the unalloyed tungsten-base metal. The resultant deposit is actually a braze weld with very little dissolution of the base metal. The porosity present is typical of powder-metallurgy products.

There is a gradual softening of the tungsten-rhenium weld metal as a function of time. Aging for 1 hr has very little effect on the hardness, whereas a 10-hr treatment softens it considerably. The hardness continues to decrease with increasing time, although the subsequent changes are not as great. After 1000 hr the tungsten-rhenium weld metal is still slightly harder than the unalloyed tungsten-base metal.

Figure 10.13(b) shows the effect of aging temperature on the hardness of specimens aged for 100 hr. The as-welded hardness is shown as before for comparison. One can see that the hardness of the weld decreases as temperature increases. In fact, after aging at 1600°C for 100 hr, the weld and base metals have the same hardness.

ORNL-DWG 68-10423

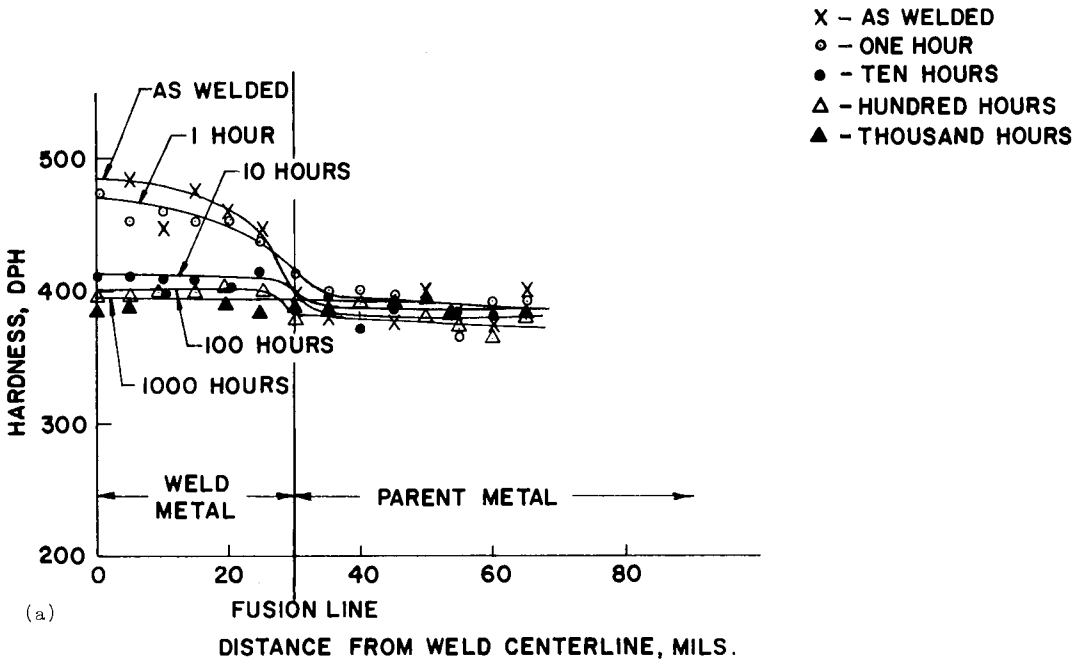

ORNL-DWG 68-10424

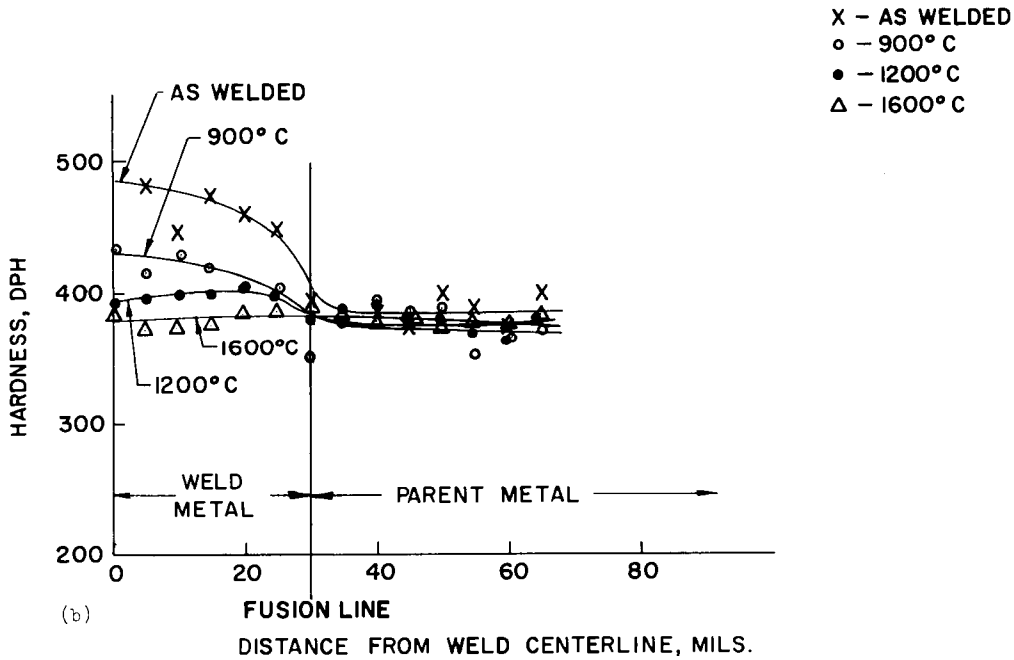

Fig. 10.13. Hardness of Powder Metallurgy Tungsten Welded and W–26% Re Filler Wire. (a) Effect of Time at 1200°C. (b) Effect of Temperature for 100 hr.

11. NONDESTRUCTIVE TEST DEVELOPMENT

R. W. McClung

This program is intended to develop new and improved methods of nondestructively evaluating reactor materials and components. To achieve this we are studying various physical phenomena, developing instrumentation and other equipment, devising application techniques, and designing and fabricating reference standards. Among the methods actively being pursued are electromagnetics (with major emphasis on eddy currents), ultrasonics, penetrating radiation, and holography. These and other methods are being evaluated for both normal and remote inspection.

Electromagnetic Studies

C. V. Dodd

We continued both analytical and empirical research and development. In our analytical research we are continuing to derive integral equations for problems of interest, and we are using our computer programs to find numerical solutions directly applicable to actual eddy-current tests.

We have determined that the signal due to a small spheroidal defect can be expressed as the product of a "defect sensitivity factor" multiplied by both a "shape-and-orientation factor" and the volume of the spheroid. Figure 11.1 contains contours of the "defect sensitivity" for a coil above a conducting plane. Figure 11.2 shows how the shape-and-orientation factor varies with the ratio of the axis of the spheroid. The volume of the spheroid is equal to $\frac{4}{3}\pi ab^2$. For the special case when the shape of the spheroid approaches that of a thin disk, the product of the shape-and-orientation factor multiplied by the volume is $\frac{16}{9} b^3 \cos^2\phi$.

We have also written computer programs to calculate the coil impedance for a coil encircling a conducting rod with a uniform layer of another conductor clad upon it. Figure 11.3 is a plot of the normalized coil impedance as a function of frequency and conductivity.

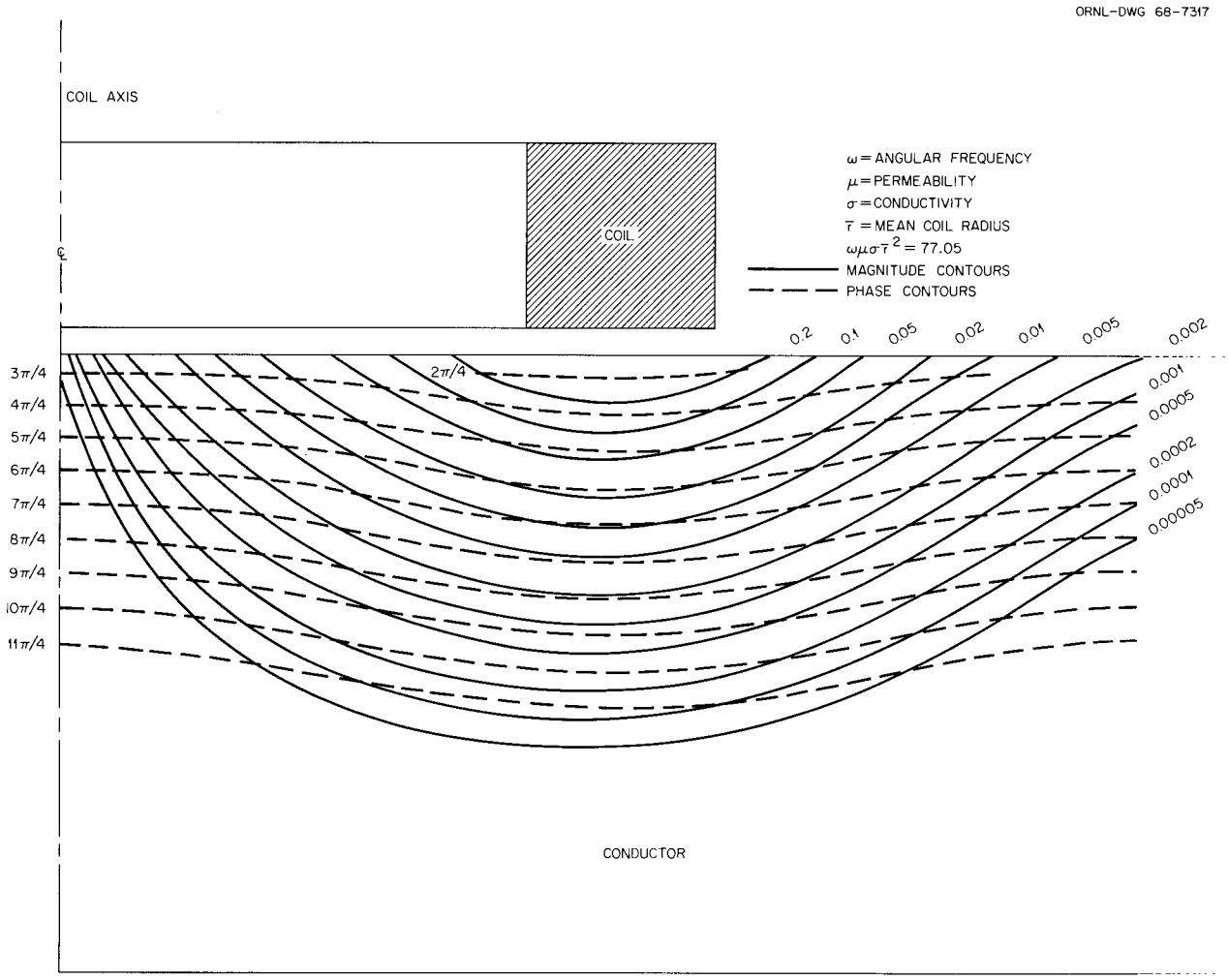

Fig. 11.1. Phase and Magnitude Contours of the "Defect Sensitivity" for a Coil Above a Conducting Plane.

We are experimentally investigating the focusing effects of reflection eddy-current coils for use with the phase-sensitive eddy-current instrument. The size of the focus or effective diameter of the eddy currents within the specimen is important because of its relation to the ability to detect small discontinuities and to resolve the response from a small discontinuity near other discontinuities. To measure the focus, we scan a coil across a metal plate that has a step change in thickness on the reverse side. The length of scan required to change the instrument response from within 1% of the value on the initial thickness to within 1% of the value on the final thickness is the "focal diameter" of the coil. This focal diameter depends on the shielding effect of the

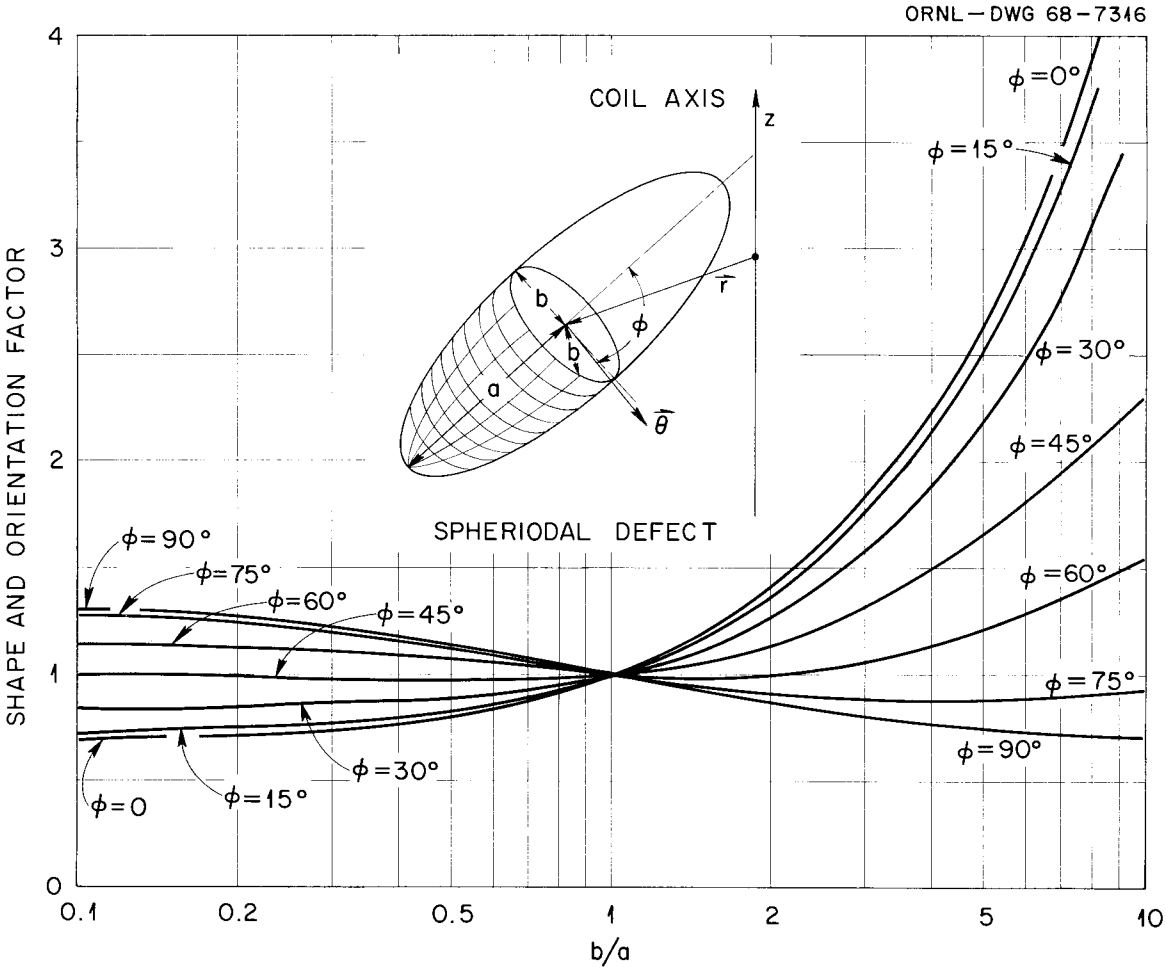

Fig. 11.2. Shape and Orientation Factor for a Spheroidal Defect.

metal housing of the probe surrounding the coil and the diameter of the coil. This focal diameter appears to be independent of the thickness being measured. The smallest focal diameter achieved thus far is 0.114 in. for a coil with a 0.036-in. OD in a 0.063-in.-ID aluminum cylinder. We will attempt to reduce the focal diameter by building smaller coils and using different shielding materials.

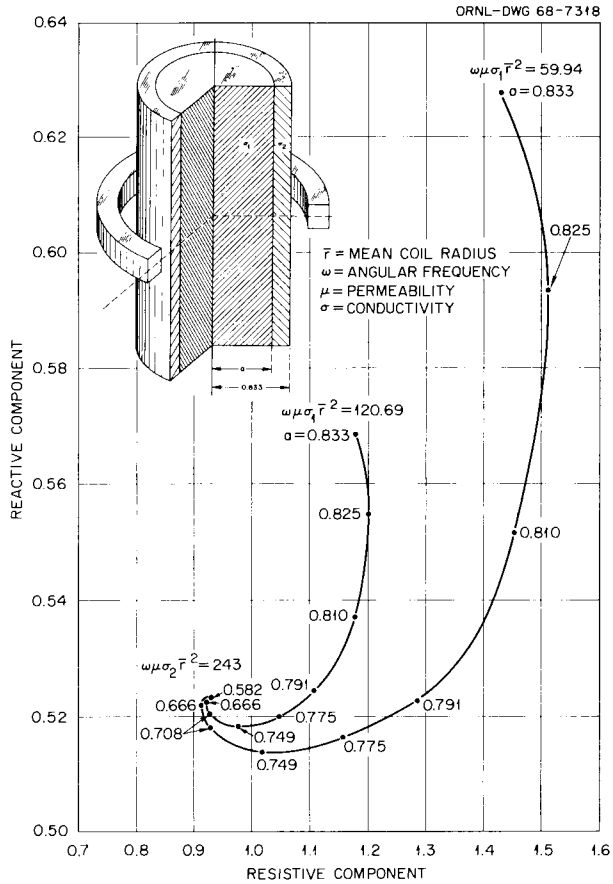

Fig. 11.3. Normalized Coil Impedance as a Function of Radius of the Inner Conductor.

Ultrasonic Test Methods

K. V. Cook H. L. Whaley

Optical Visualization of Ultrasound

We extensively modified our schlieren system to allow use of parabolic mirrors to produce the collimated light field. The chief reason for changing from lenses to mirrors was to obtain an increase (9×) in the viewing area. Since the mirrors have a long (48 in.) focal length and collimate light much better than the 2-in. lenses formerly used, the mirror system is also much more sensitive than the lens system, despite the fact that the light is spread over the much larger viewing area (e.g., thermal convection currents in room air are visible with the new system).

At the same time that necessary new mechanical fixtures were installed, the entire system was modified where necessary to provide for better stability and ease of operation.

Frequency Analysis

We have drawn a set of calibration curves to allow quantitative determination of the amplitude of each portion of a frequency spectrum. Spectra displayed at widely different system sensitivities can now be compared meaningfully. We are designing experiments for applying the system to a variety of interesting problems to gain a better understanding of the influence of the frequency spectra on specific ultrasonic techniques.

Holography

B. E. Foster

We continued studies on making reflection holograms of high quality for evaluation of surface as well as subsurface discontinuities in metals and ceramics.

The work surface consists of an aluminum block 45 in. long by 29 in. wide by 3 in. thick. To provide an area relatively free of building vibrations, this is mounted on four sections of rubber vacuum hose about 7 in. long by 3 in. in diameter with 1-in. wall thickness.

The use of a light meter with a photosensitive field effect transistor as a detector has enabled us to monitor and thus maintain efficient ratios of intensity between the reference and object beams. The reflected intensity from some objects can be only 1/30 of the intensity of the reference beam if a hologram of good quality is to be achieved. We are categorizing the reflectivity of various objects.

We are studying the depth-of-field limitations of our present equipment and are comparing single- and multiple-beam systems that use diverging light beams. The maximum depth of field we have seen so far is about 9 in. Better resolution is being achieved with the single-beam system, but this could be due to inferior optics in the multiple-beam experiment. Additional optics have been ordered.

12. JOINING RESEARCH ON NUCLEAR MATERIALS

G. M. Slaughter

We have a program under way to determine the influence of minor elements on the weldability of nickel-bearing alloys such as Inconel 600 and Incoloy 800. This has involved preparing a number of special heats of material and subsequently testing and evaluating the results.

During the past quarter, we have extended the investigation to include the combined effects of phosphorus and sulfur on Inconel 600.

Weldability Studies

D. A. Canonico W. J. Werner

Table 12.1 contains the chemical analysis of the alloys recently studied. For comparative purposes, we have included the analysis of the ternary and nominal experimental Inconel 600 alloys. These are identified, respectively, as 600-1 and 600-2. Alloys 600-6, 600-7, and 600-8 contain increasing amounts of phosphorus up to 0.015%. Alloys 600-9 and 600-10 include both phosphorus and sulfur. The Duffer's Gleeble[1] was used to determine the hot ductility of the alloys. We have investigated their properties upon heating and have established their individual zero ductility temperatures (ZDT). Figure 12.1 contains the complete ductility versus temperature results for these materials as heated. We have also included the curve obtained for the ternary (600-1) alloy. It is evident that the presence of phosphorus up to 0.015% did not appreciably affect the ZDT. All of the alloys exhibited ZDT's of 1345°C or greater. However, if the loss of ductility (rather than the ZDT) is compared, it can be seen that the alloy containing the most phosphorus (600-8) was least reduced in area at elevated temperatures. To illustrate this difference, we have compared the reduction in area of the experimental

[1]Duffer's Associates, Troy, New York.

Table 12.1. Chemical Analyses of Experimental Inconel 600 Alloys

Alloy Identification	Chemical Composition, wt %							
	C	Ni	Cr	Fe	H_2	N_2	S	P
600-6	0.027	70.9	15.9	12.1	0.0008	0.0013	< 0.002	0.006
600-7	0.026	73.7	15.8	9.3	0.0029	0.0018	< 0.002	0.011
600-8	0.023	72.6	15.9	10.4	0.0025	0.0028	< 0.002	0.015
600-9	0.034	72.6	16.2	11.4	0.0021	0.0016	0.003	0.004
600-10	0.026	72.3	16.2	11.5	0.0029	0.0011	0.003	0.006
600-1	0.004	75.2	15.9	8.13	0.0011	0.0004	0.003	0.001
600-2	0.028	75.6	16.1	8.55	0.0002	0.0010	0.002	0.002

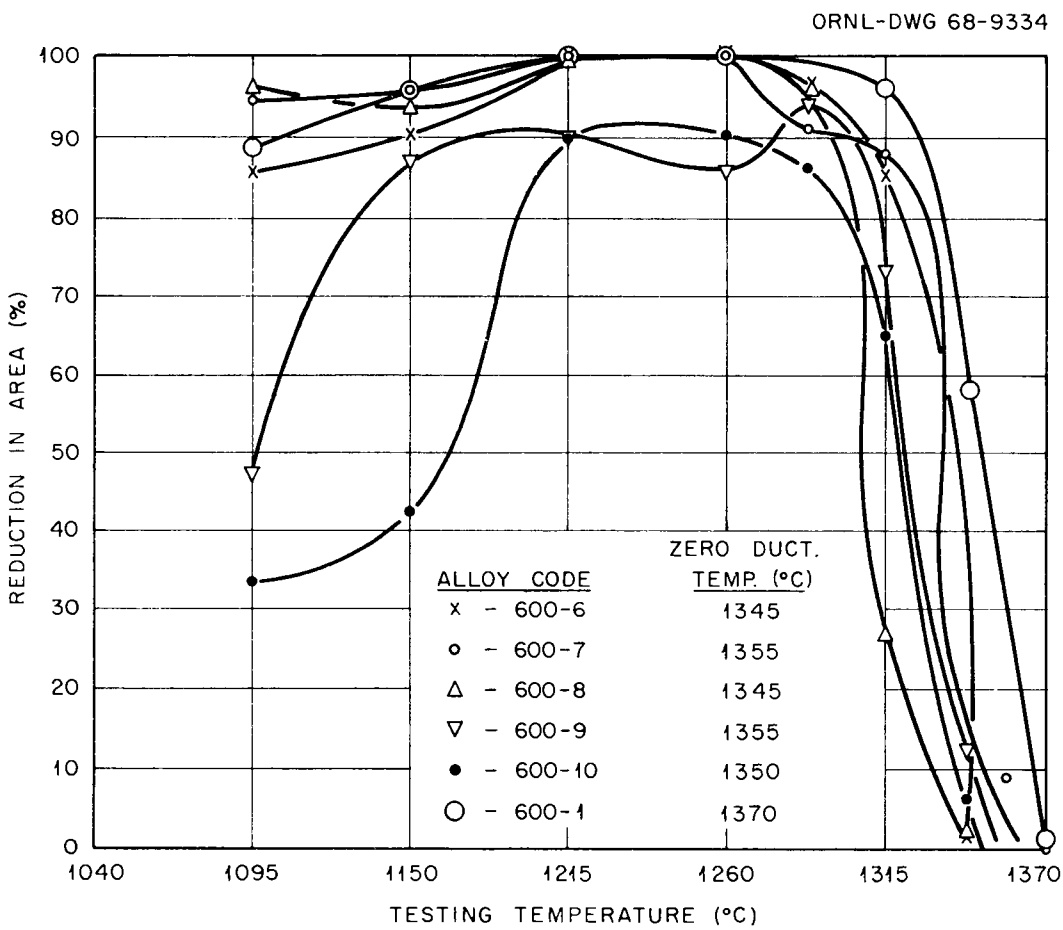

Fig. 12.1. Hot Ductility Results Obtained for the Experimental Inconel 600 Alloys.

alloys at 1315°C. These data as well as the ZDT's are given in Table 12.2. Alloy 600-8 was considerably less ductile (about 27%) than the other phosphorus-bearing alloys (all of which exceed 65%).

Figure 12.1 illustrates another phenomenon of interest. The two alloys that contained both phosphorus and moderate sulfur (600-9 and 600-10) have lower ductilities at 1095°C than the alloys with lower sulfur contents. This lack of ductility in the lower temperature range might indicate a propensity toward weld cracking and is under investigation.

Table 12.2. The Zero Ductility Temperature and Ductility at 1315°C for the Experimental Inconel 600 Alloys

Alloy Identification	Zero Ductility Temperature (°C)	Reduction in Area at 1315°C
600-6	1345	84.4
600-7	1355	87.4
600-8	1345	27.4
600-9	1355	73.5
600-10	1350	65.0
600-1	1370	96.0
600-2	1350	92.5

13. FUEL ELEMENT FABRICATION DEVELOPMENT

G. M. Adamson, Jr.

This section includes a brief presentation of the work on aluminum technology at Oak Ridge National Laboratory. The report incorporates work being done on the following AEC programs: Fuel Materials Development, HFIR Development, and Transuranium Element Processing. The report is divided into three general sections: fuel element procurement, dispersion development, and irradiation testing.

The various programs are aimed at improving the performance of research reactors. Major emphasis has been placed upon upgrading the fuel elements, but work on the structural components is also included. The studies include factors affecting both fabrication and irradiation performance. The fuel element studies should lead to the fabrication of fuel plates with increased fuel loadings, permit the use of cheaper fuels, provide assurance that a given fabrication practice will produce satisfactory plates, permit prediction of the effects on plate quality of changes in production equipment and processes, and provide data that will improve the quality of specifications and permit rapid solutions to the problems that continually arise in the shops of the industrial fabricators. Other studies will improve the reliability and reduce the cost of nondestructive inspection techniques and investigate the causes and provide solutions for the irradiation damage of aluminum structural materials.

Irradiation Studies of Dispersion Plates

M. M. Martin A. E. Richt
W. R. Martin

Exposure of ORNL's miniature test plates in the G-12 loop of the ETR was stopped prematurely during cycle 96 because of a fission break in a test sample that did not belong to ORNL. The ORNL miniature plates were also irradiated in cycles 93A, 93E, and 94A to greater than 5000 Mwd.

They will be returned to ORNL for postirradiation evaluation as soon as the radioactivity level becomes suitable for shipping.

We have begun fabricating test specimens scheduled to be inserted in the G-12 loop in cycle 100. We are preparing and characterizing the fuel compounds.

Fuel Plate Fabrication

Examination of Arc-Melting Techniques for Preparing UAl_x (J. T. Venard)

The principal method commercially used to prepare UAl_x intermetallic fuel is arc melting. The presence of free uranium within the rolled core has been a problem. We are investigating the possible origin of such unalloyed uranium. We melted uranium-aluminum compounds with approximately 75 wt % U in a water-cooled copper hearth and allowed them to solidify into 2-in.-diam buttons. For proper mixing, we turn the buttons over and remelt them up to six times. Buttons cast at ORNL have never shown any free uranium in the as-cast microstructure, but there are gross variations in microstructure within each button. Preliminary microprobe analysis indicates that UAl_3, UAl_4, and free aluminum are present. The multiplicity of types of microstructures within a given button may be influencing subsequent fabrication steps, such as grinding and crushing of the buttons to produce powder. We are examining alternate melting techniques that would reduce the segregation and nonuniform mixing during melting.

UAl_x Particle Preparation (M. M. Martin and W. R. Martin)

A significant increase in lifetime for the HFIR fuel assembly will undoubtedly require regions of the uranium-bearing portion of the fuel plates to perform adequately at burnups in the range of 3 to 4×10^{21} fissions/cm^3. One of the fuel compounds under consideration for this high loading and long life is arc-cast UAl_x.

Although hypostoichiometric UAl_3 was brittle and shattered when struck a sharp blow, arc-cast buttons of hyperstoichiometric UAl_3 resisted initial breakup to -4 mesh particles. The malleable nature of

this material caused severe wear of the screens in the hammer mill. To effect initial breakup to −4 mesh particles, we crushed the arc-cast buttons between steel platens with a press. In contrast, we milled 7 kg of hypostoichiometric UAl_3 with little evidence of screen wear.

To produce a sufficient quantity of UAl_x particles of the desired size, we used a 2.5-liter stainless steel rod mill to further crush the materials. After being crushed in the rod mill, the powders were sieved twice on a Ro-Tap shaker for 30 min; the results are shown in Table 13.1. About 40% of the particles were within the desired size range. Fines (−325 mesh) from −140 mesh hypostoichiometric and −100 mesh hyperstoichiometric UAl_3 compounds accounted, respectively, for 43.9 and 34.8% of the distribution. A heat treatment for 2 hr at 1000°C in an atmosphere of argon appeared to increase the production of fines to 50.6% during rod milling of 3.2 kg of hypostoichiometric UAl_3. Of course, fines and oversize materials can be recycled, respectively, in the rod mill and by remelting.

The range indicated in Table 13.1 for milling rate depends upon the quantity of material in the rod mill. With similar loadings, hypostoichiometric UAl_3 crushes about twice as fast as hyperstoichiometric UAl_3. The latter material also increased fourfold in losses.

We conclude that the yield of acceptable UAl_x particles from rod milling is comparable to that obtained from a diamond mortar and pestle, a rotating-disk pulverizer, or a hammer mill. Rod milling, however, gave the smallest production rate. To lower the production of fines, all particles of the desired size should be removed from the rod mill immediately after comminution of every oversize lump. We plan to study soon the effect of lower crushing temperatures and other crushing devices to minimize fines.

Determination of Powder Particle-Size Distribution of Research Reactor Fuels (M. M. Martin and W. R. Martin)

The particle size of the uranium-bearing phase may affect irradiation performance, evaluation of uranium homogeneity, and fabricability of aluminum-base dispersion fuel plates. The characterization of the

Table 13.1. Results from Crushing Various Arc-Melted UAl_x Materials

Crushing Results	Material			
	A[a]	B[b]	C[c]	D[d]
Desired size range, mesh	−140 to +325	−140 to +325	−140 to +325	−100 to +325
Separated distribution, wt %				
Within desired size range				
−100 +140 mesh				14.4
−140 +170 mesh	2.0	14.5	11.8	7.4
−170 +200 mesh	2.6	13.4	14.4	5.9
−200 +230 mesh	1.2	6.5	5.6	3.6
−230 +270 mesh	1.2	5.9	5.5	3.7
−270 +325 mesh	2.2	6.6	8.6	3.3
Total usable material	9.2	46.9	45.9	38.3
Material suitable for recycle				
Oversize, +100 or +140 mesh	74.5	3.3	0.4	5.3
Fines, −325 mesh	11.3	43.9	50.6	34.8
Total recycle material	85.8	47.2	51.0	40.1
Losses				
Crushing	5.0	5.4	2.9	21.4
Screening and handling		0.5	0.2	0.2
Total losses	5.0	5.9	3.1	21.6

[a]Material A, containing 4274 g of 74 wt % U, was crushed by Muller to < 0.5-in.-diam feed material and hammer milled at > 1000 g/hr to give the results reported.

[b]Material B, resulting from the hammer milling of 3476 g of material A to < 0.19-in.-diam feed material, was rod milled at 12 to 20 g/hr to give the results reported.

[c]Material C, resulting from the hammer milling of 3226 g of material A to < 0.19-in.-diam feed material, was given a 2-hr heat treatment in argon at 1000°C and then rod milled at 12 to 20 g/hr to give the results reported.

[d]Material D, containing 5003 g of 69 wt % U, was crushed by Muller and press to < 0.19-in.-diam feed material and rod milled at 7 to 12 g/hr to give the results reported.

starting fuel powder is important to any detailed research on fuel plates based on powder metallurgy products.

We are trying to circumvent the difficulty of characterizing the particle-size distribution of research reactor fuels with the accuracy desired for developmental work. For example, we desired three U_3O_8 blends from HFIR-grade oxide in which the distributions would be (1) 100% 88 to 74 μm; (2) evenly divided between 88 to 74, 74 to 63, 63 to 53, and 53 to 44 μm; and (3) 100% less than 44 μm. To prepare the experimental blends, we first separated the hi-fired (enriched) U_3O_8 particles that were supplied to us into known mesh fractions by sieving them twice on a Ro-Tap shaker. Then we recombined them in the desired weight proportions by blending them obliquely for 2 hr inside a glass bottle that contained about 75% mixing void volume. Analyses of the three prepared blends and the as-supplied U_3O_8, reported in Table 13.2, indicate that the actual distribution was grossly different from that we desired.

Table 13.2 illustrates the problem of interpreting particle size distributions encountered in the characterization of experimental U_3O_8 blends. The values for each technique are reproducible within approximately ±3 wt %, which is adequate for production operations; however, the values for the various techniques are not comparable. The distribution depends significantly upon the methods of analysis. The Coulter Counter and photographic techniques, which are considered to be the most accurate methods, measure the volume and major cross-sectional area of each particle, respectively. The distribution shown by the Ro-Tap sieve shaker and U.S. Standard Sieves represents essentially the minor area of the particles. When comparing the results in Table 13.2 for A, B, and C methods of analyses, one should therefore expect the distribution to shift successively to indicate more material at the larger sizes. Surface area measurements indicated little, if any, differences in particle size for the three blends and as-supplied material.

The distribution of the as-supplied U_3O_8 as determined by a Cenco-Meizer shaker and U.S. Standard Sieves should represent the major cross-sectional area of the particles. Although these devices use screens, they impart only a circular motion to the particles, so the possibility

Table 13.2. Distribution of Particle Sizes in U_3O_8 Blends

Powder Blend Designation	Method of Analysis[a]	Weight Percent of Particles of Indicated Maximum Sizes, μm						Surface Area (m^2/g)
		44	53	63	74	88	105	
As-supplied	A	9	33	51	78	100	100	0.054
	B	2	14	36	72	96	100	
	C	1	3	12	33	61	92	
	D	1	13	40	70	98	100	
Blend 1	A	0	0	0	12	100	100	0.053
	B	0	0	0	37	87	100	
	C	0	0	0	4	32	87	
Blend 2	A	2	33	60	78	100	100	0.057
	B	1	6	34	73	93	100	
	C	1	2	11	37	66	94	
Blend 3	A	100	100	100	100	100	100	0.060
	B	19	71	94	100	100	100	
	C	5	28	68	94	100	100	

[a]A: Ro-Tap sieve shaker; 100-g sample, 15 min. B: Coulter Counter; sample dispersed in 1 wt % aqueous NaCl solution. C: Photomicrograph using Ziess particle counter; 95×. D: Cenco-Meizer sieve shaker; 100-g sample, 30 min at setting 5.

of a long, narrow particle standing on end is not great. The photomicrographic and Cenco techniques should, therefore, give comparable results. Surprisingly, the results from the Coulter Counter, which measures particle volume, and the Cenco shaker agree well. To explain this discrepancy, we observed that particle-size determinations with shaking devices depend primarily upon the duration of agitation. For example, 5 hr of screening on the Cenco is equivalent to 45 min on the Ro-Tap.

The four methods for determining particle-size distribution should give identical results only on ideally spherical particles. Figure 13.1 illustrates the particle shape of the as-supplied U_3O_8 used to prepare the blends. Although the larger particles are nearly spherical, the smaller ones are more irregular. We conclude that the four methods examined will give reproducible results when properly controlled and will be comparable if the particles are spherical. However, for irregularly shaped particles, distribution depends on the method of analysis.

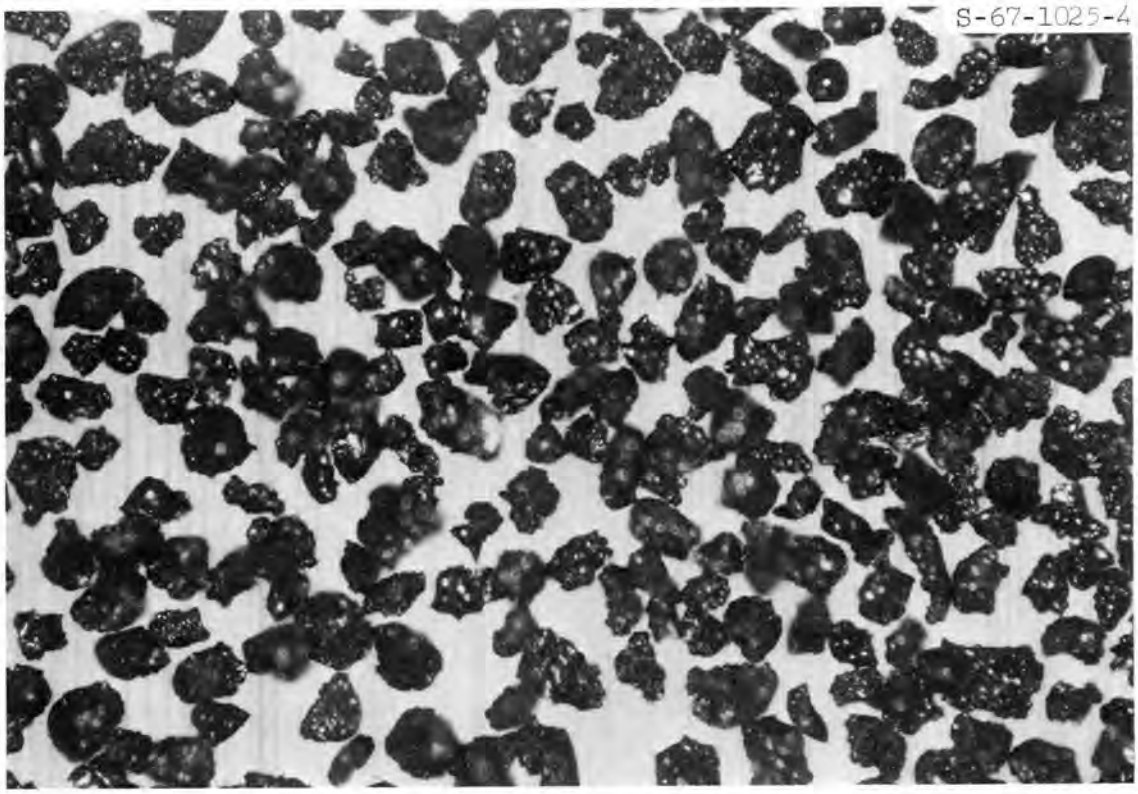

Fig. 13.1. Photomicrograph of Hi-Fired U_3O_8. As polished. 100×.

Consistency of shape for a given preparation process will, therefore, be very important in order to show similar distributions of particle sizes from batch to batch.

The Effect of Fuel Concentration on the Swelling of Fuel-Aluminum Compacts
(M. M. Martin and W. R. Martin)

At ORNL, we heat treat the fuel-aluminum compacts before we assemble the picture-frame billet for rolling. The heat treatment removes gases and lubricant from the compact and lessens the frequency of blisters in the rolled plate. This treatment, generally given at about 590°C a few years ago, has now been reduced to 500°C. When the heat-treating temperature for intermetallic fuels is above 500°C, fuel compacts containing UAl_x swell significantly more than U_3O_8-Al compacts. Such swelling can cause difficulty in assembling the billets and in extreme cases can cause warping of the rolled plates. To gain information on the degree of swelling of compacts heat treated at 500°C, we examined

the density change of compacts during degassing for 1 hr as a function of the amount of fuel for both hypostoichiometric UAl_x and U_3O_8. The results are given in Fig. 13.2. For compacts containing up to 35 vol % fuel, the swelling upon degassing is a function of the volume percent of fuel and not of the type of fuel. Density changes range from 0.5% for less than 10 vol % fuel to approximately 2% at 35 vol % fuel. Above 35 vol %, UAl_x-Al compacts swell much more than compacts containing U_3O_8. For fuel loadings up to 35 vol %, it appears that gas release is the principal cause of swelling. For higher fuel loadings, we think the transformation of UAl_3 to UAl_4 in compacts containing UAl_x is perhaps the cause of additional swelling (see next section). Because the U_3O_8 compound has a higher uranium concentration than the UAl_3 compound, swelling is always higher in UAl_3-Al compacts than in U_3O_8 compacts regardless of the level of fuel loading.

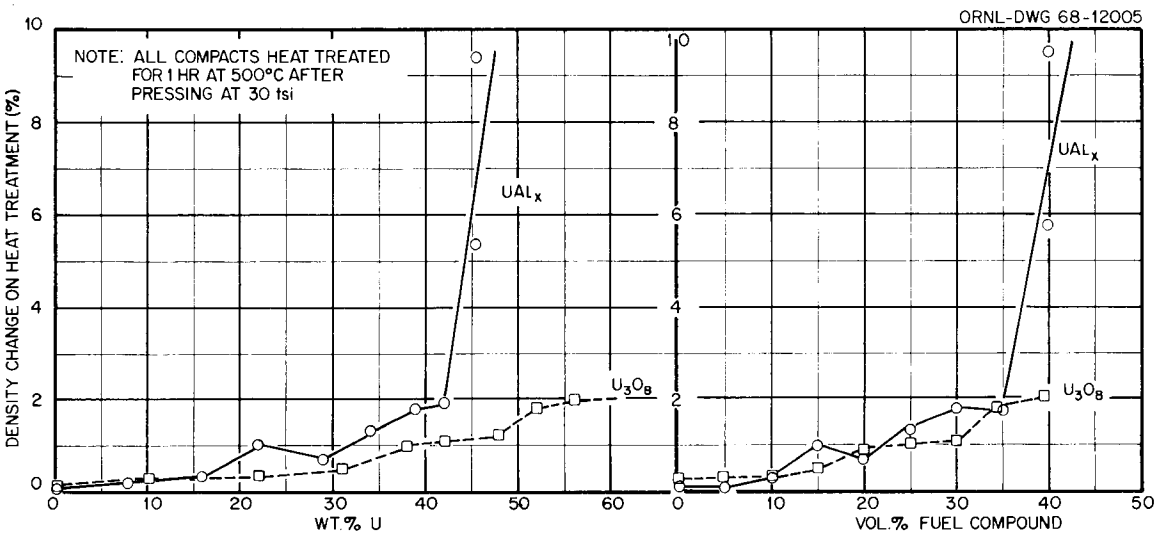

Fig. 13.2. Decrease in Density of Fuel-Aluminum Compacts During Degassing at 500°C.

Mechanisms of Swelling in UAl_x-Al Compacts (A. K. Chakraborty)

With the help of dilatometer, electrical resistance, and pressure change measurements, we studied the mechanism of swelling of UAl_x dispersed in 60 wt % Al. We made these measurements at 600°C so that the

extent of the reaction would be great enough to allow direct observations of structural transformations. Arc-cast and hot-pressed uranium-aluminum compounds containing UAl_3 + UAl_2 of different particle sizes were dispersed in 60 wt % Al (22 vol %) and pressed with 22.5 tsi to form pellets 1/2 in. high and 1/2 in. in diameter. We cleaned these pellets to remove all lubricant from the surface.

We measured changes in length and pressure during degassing at 600°C with a closed-volume dilatometer (Figs. 13.3 and 13.4). These two figures are marked with a broken line that indicates the time at which pellets reached a temperature of 600°C. These figures show that initially the increases in both pressure and length are very rapid. Afterwards, although the pressure changes slowly, there is no further change in length. There is no correlation between the particle sizes, change of pressure, and change in length; but it is evident that the curves are similar, and probably the cause for the changes is the same. Figure 13.4 also shows that the intermetallics with larger particle sizes initially show a slow change in length compared to the intermetallic with fines.

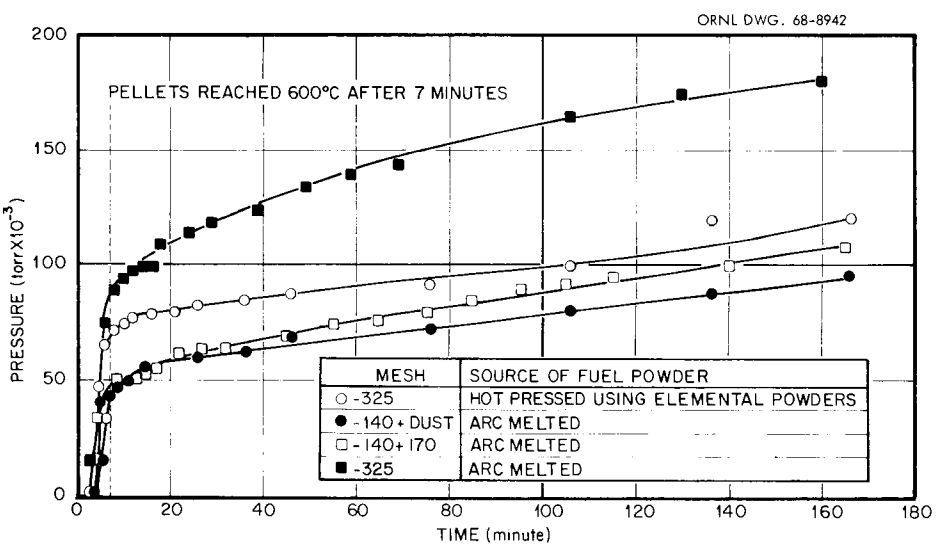

Fig. 13.3. Pressure Charge of Aluminum Pellets Containing Dispersion of UAl_3 of Different Particle Sizes During Degassing at 600°C.

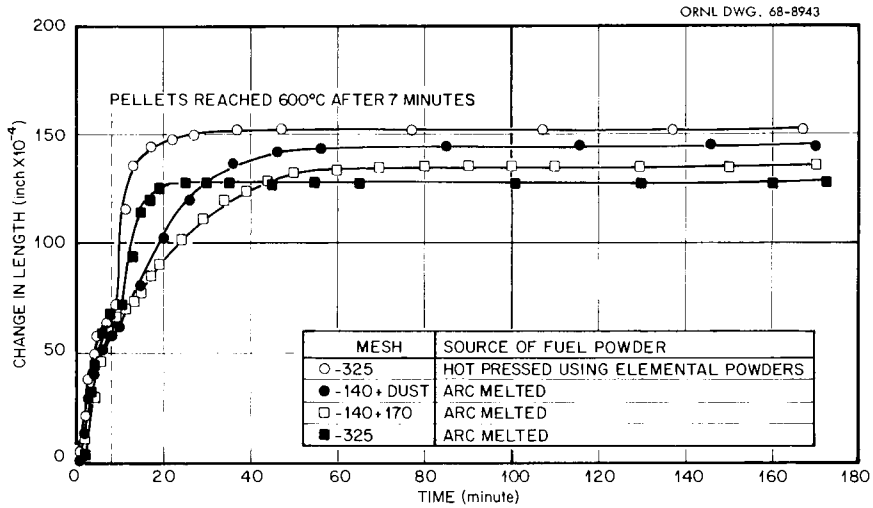

Fig. 13.4. Change in Length of Pellets of Aluminum Containing Dispersion of UAl_3 of Different Particle Sizes During Degassing at 600°C.

Figure 13.5 shows the change of resistance related to initial resistance as a function of degassing time at 600°C. Here, also, the changes resemble those of other curves of Figs. 13.3 and 13.4.

Figure 13.5 also shows that change of resistance is proportional to the particle sizes. The finer the particle size and the larger the surface area, the higher is the change of resistance. This measurement of resistance is probably a most sensitive measure of the volumetric changes that occur during the 600°C heat treatment.

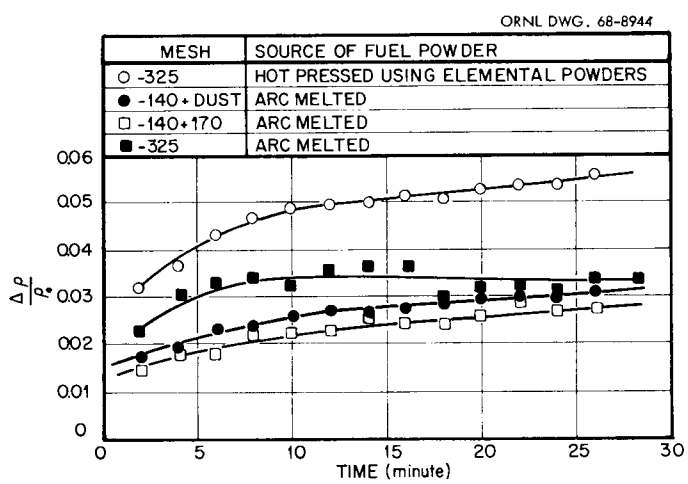

Fig. 13.5. Change in Electrical Resistance Related to Initial Resistance During Degassing at 600°C.

It is assumed that swelling of the compacts is caused by two important factors. The first is that evolution of adsorbed gases causes separations at grain boundaries and powder surfaces. Gregg, Crouse, and Werner[1] found that cracks developed in the microstructure of compacts from the second factor, preferred growth during diffusion-induced transformation of UAl_3 to UAl_4. This is accentuated by the fact that the aluminum diffuses more rapidly than the UAl_3, thus leaving pores in the matrix.

Microscope observations at 600°C indicated that transformation occurs after some incubation time. This incubation time appears to vary, depending upon the variation of composition of the UAl_x powder. Transformation of UAl_3 to UAl_4 takes place in successive layers. Layers start growing at the boundary of the dispersed particles and advance more slowly toward the interior of the particle. Stress developed because of the growth causes recrystallization in the aluminum matrix.

Compressive Strengths of U_3O_8- and UAl_3-Al Composites (J. H. Erwin and W. R. Martin)

Considering the problems of dogboning that have been encountered with hot rolling of dispersion fuel plates, it would appear quite likely that differences in compressive strength between the various billet components must exist at the rolling temperature, 500°C. To find how much difference in strength there is between the fuel mixtures at rolling temperatures, we investigated the compressive strength of mixtures of U_3O_8 and UAl_3 in 101 aluminum powder between 0 and 40 vol % and from 25 to 550°C.

The mixture of fuel and aluminum powder was processed by normal powder metallurgy procedures to produce 0.5-in.-diam by 0.5-in.-long compacts pressed at 22.5 tsi. The compacts were degassed 2 hr at 500°C and less than 5×10^{-2} torr. Each compression test required three compacts of the same fuel composition stacked end on end to produce a smooth test cylinder 0.5 in. in diameter by 1.5 in. long. The compression tests were conducted on an Instron Universal Testing machine

[1]J. L. Gregg, R. S. Crouse, and W. J. Werner, Swelling of UAl_3-Al Compacts, ORNL-4056 (1967).

operating at a crosshead speed of 0.002 in./min. Each test was continued to about 5% deformation.

The compressive strength corresponding to 5% plastic strain in the U_3O_8 and UAl_x fuel-aluminum powder mixtures at 0 to 40 vol % are compared in Fig. 13.6 at 25, 350, 400, and 550°C. For the lower volume percentages of fuel, the properties of the compacts are similar. However, for all temperatures above a certain volume percentage, which increases with temperature, the curves cross and the UAl_3 compacts show much higher compressive stresses. The U_3O_8 compacts show decreasing strengths with the higher fuel concentrations.

The large differences between the compressive strengths of the UAl_3-Al and U_3O_8-Al compacts with high fuel concentrations must be a significant cause of dogboning.

Effect of Billet Feed Angle on the Curl of Rolled Plate (J. H. Erwin and W. R. Martin)

"Curl" describes the shape of a plate issuing from a rolling mill in other than a flat plane due to nonuniform plastic deformation of the entering billet thickness. "Curl" of fuel plate billets is produced during the initial reduction passes. It obscures the details to be studied in other rolling studies by affecting the relationships between fuel core and cladding, and it extends the core beyond the desired lengths in normal roll cladding operations. The mechanism of uneven metal flow depends upon frictional forces both within and without the rolling billet and may be ascribed to a number of interrelated factors. Since the predominant external factor is roll friction, we began an investigation relating curl to unbalanced friction on the billet surface.

By feeding the billet from an elevated angle, we can increase the roll friction on the top roll to shift deformation and make the issuing plate curl downward. As shown in Fig. 13.7, we determined the relationship between feed angle and plate curl from five sample plates rolled at each of seven billet feed angles. The simulated billets were 1/4-in.-thick by 4-in.-wide by 9 1/2-in.-long X8001 aluminum. These were hot rolled (500°C) on a 12- by 14-in. mill at 20% reduction. The deflection was measured at 1-in. intervals along the length of the rolled plate to

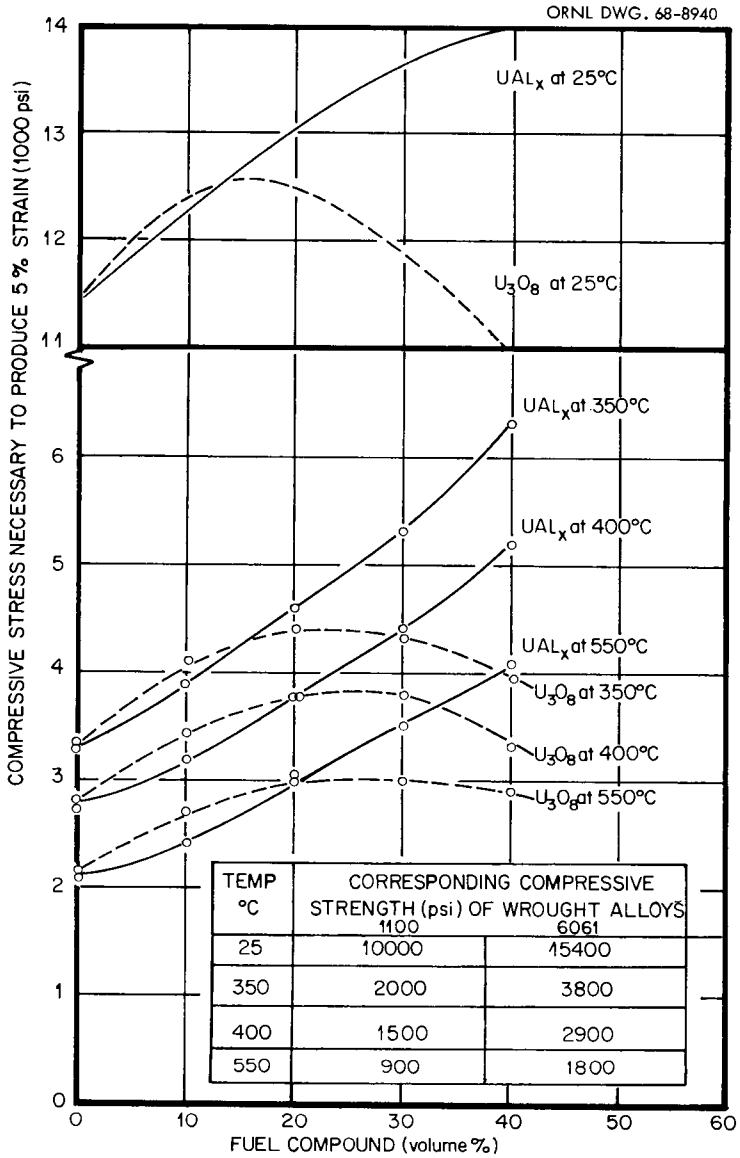

TEMP °C	CORRESPONDING COMPRESSIVE STRENGTH (psi) OF WROUGHT ALLOYS 1100	6061
25	10000	15400
350	2000	3800
400	1500	2900
550	900	1800

Fig. 13.6. Compressive Yield Stress of Fuel-Aluminum Compacts as a Function of Type and Amount of Fuel Compound in the Dispersion.

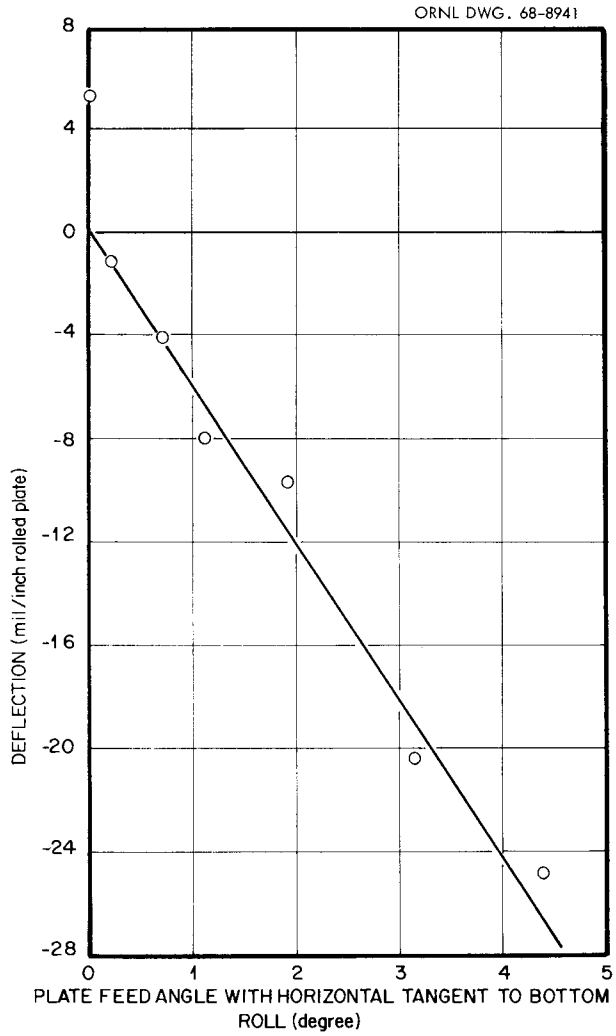

Fig. 13.7. Effect of Feed Angle on Curl Produced in Rolled Plate (1/4-in.-Thick X8001 Aluminum Reduced 20% at 500°C with a 12- by 14-in. Mill).

determine the curl produced. From these data it is obvious that close control of the feed angle is required if curl is to be avoided in commercial fabrication operations.

Investigations of Nonuniform Deformation in Simulated Fuel Plates
(J. H. Erwin and W. R. Martin)

Differences in the compressive mechanical properties of core, cover plate, and frame materials at the rolling temperature may be the primary cause of nonuniform deformation of a composite fuel plate. The shape of the nonuniformity of deformation in the core often looks like a "dogbone."

In our initial studies we have used wrought materials with different elevated-temperature mechanical properties to study the development of dogbone or inhomogeneous reduction in simulated fuel plates. At 500°C, the compressive yield strength of 1100 aluminum is slightly lower than that of X8001, but that of 6061 is higher. Rolling billets were constructed from 4-in.-wide by 9 1/2-in.-long frames and cover plates of X8001 aluminum. Each frame contained two 1 3/4-in.-wide by 1-in.-long tandem cavities separated by 2 1/2 in. The frames, 1/4 in. thick, were assembled with 1/8-, 1/4-, and 1/2-in.-thick cover plates to make 1/2-, 3/4-, and 1 1/4-in.-thick billets. Simulated cores, one of the 1100 and one of the 6061 aluminum alloy, 0.002 in. smaller than the cavities in all dimensions, were placed in each frame. The billets were heated to 500°C and rolled in multiples of 20% reduction per mill pass with a 12- by 14-in. mill. Multiple mill reductions were all made in the same billet feeding direction. After each reduction, we opened the billets and measured thickness contours describing the frame and core reductions.

A comparison of the relative thicknesses of the rolled frame and core shows that the components are reduced almost symmetrically at the ends of the cores; the frame is thicker adjacent to the 1100 aluminum core and thinner adjacent to the 6061 aluminum core; the 1100 aluminum core at both ends is thinner than the frame; and the 6061 aluminum core at both ends is considerably thicker than the frame. The nonuniformity of reduction of the core in these billets through five 20% mill passes is shown in Fig. 13.8.

In the case of the core being stronger than either the frame or the cover plate, the deformation of the frame, cover plates, and cores is nonuniform in the area near the end of the core. The effect is exaggerated in the schematic shown in Fig. 13.9. We stripped the cover plates from the frames and removed the cores. Photographs of the inside surfaces of the cover plate and frame with cores in place are shown in Fig. 13.10. After the simulated cores were removed from the frames, the nonuniform deformation at the end of the core was revealed as shown in Fig. 13.11. We made detailed measurements of the core thickness along the length of the core for both edges and the middle

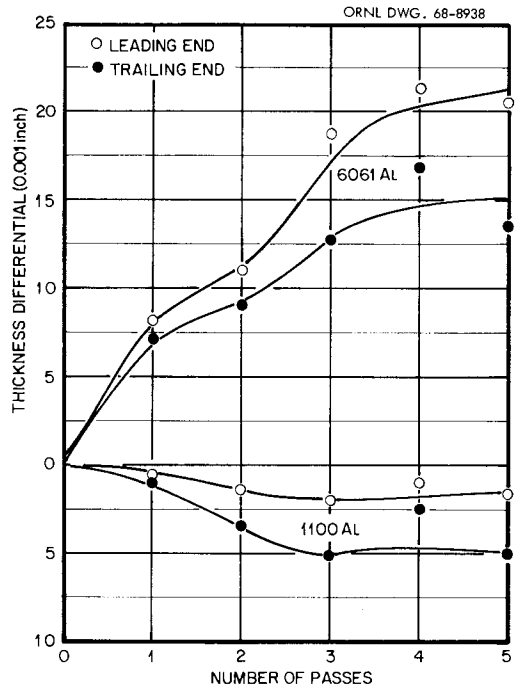

Fig. 13.8. Dogboning of 1100 and 6061 Aluminum Cores Within X8001 Aluminum Frames and Cover Plates During Rolling of Simulated Fuel Plate at 500°C.

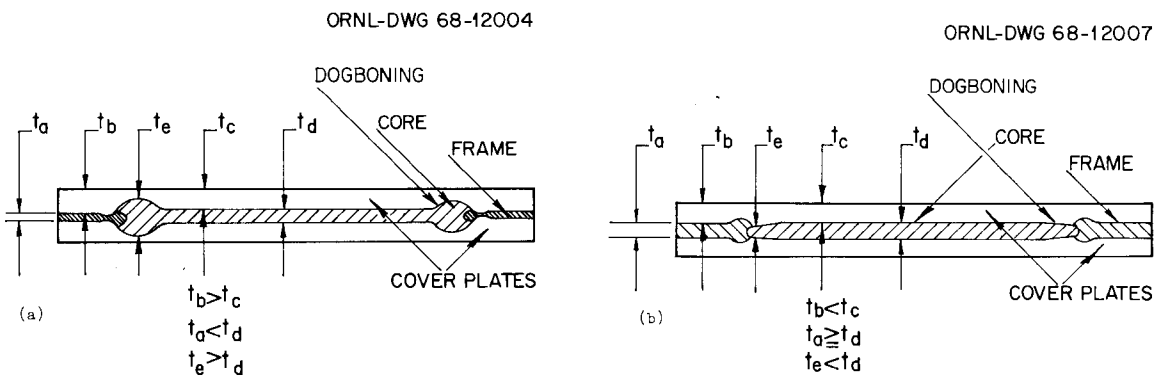

Fig. 13.9. Schematics of Nonuniform Deformation of Simulated Composite Fuel Plates During Rolling. (a) For core stronger than frame and cover plates and (b) for core weaker than frame and cover plates.

Fig. 13.10. Photograph of Inside Surface of Cover Plate and Frame-Core Surface After Stripping the Cover Plate from the Frame. Composite plate rolled six passes at 20% each pass at 500°C. Note the deep impressions on the cover plate made by the hard 6061 aluminum core.

of the core; these are shown in Fig. 13.12. Note that there was less dogboning on the trailing edge than on the leading edge.

Billets assembled with 1/8- or 1/2-in.-thick cover plates in lieu of the 1/4-in. plates were also reduced 20% per mill pass with the 12- by 14-in. mill. With six 20% mill passes, the average dogbone in the 6061 aluminum cores was 110, 118, and 135% of the average core thickness in billets assembled with 1/8-, 1/4-, and 1/2-in.-thick cover plates, respectively. Dogboning with each respective pass for the three type billets is shown in Fig. 13.13. Note that the degree of dogboning increased at about the same magnitude per pass, but there were no further increases for any of the three billets when the billet thickness decreased to about 0.375 in. Hence, it took more passes to reduce the thicker billet (thicker cover plates) than the thinner billet (thinner cover plates). One can make the general conclusion that dogboning is a function of billet size and/or ratio of cover plate thickness to frame thickness. But perhaps a more detailed study of these results could lead to understanding of the mechanism of dogboning. That study is now in progress.

ORNL-PHOTO 93277

Radiographic Views of Core Outline

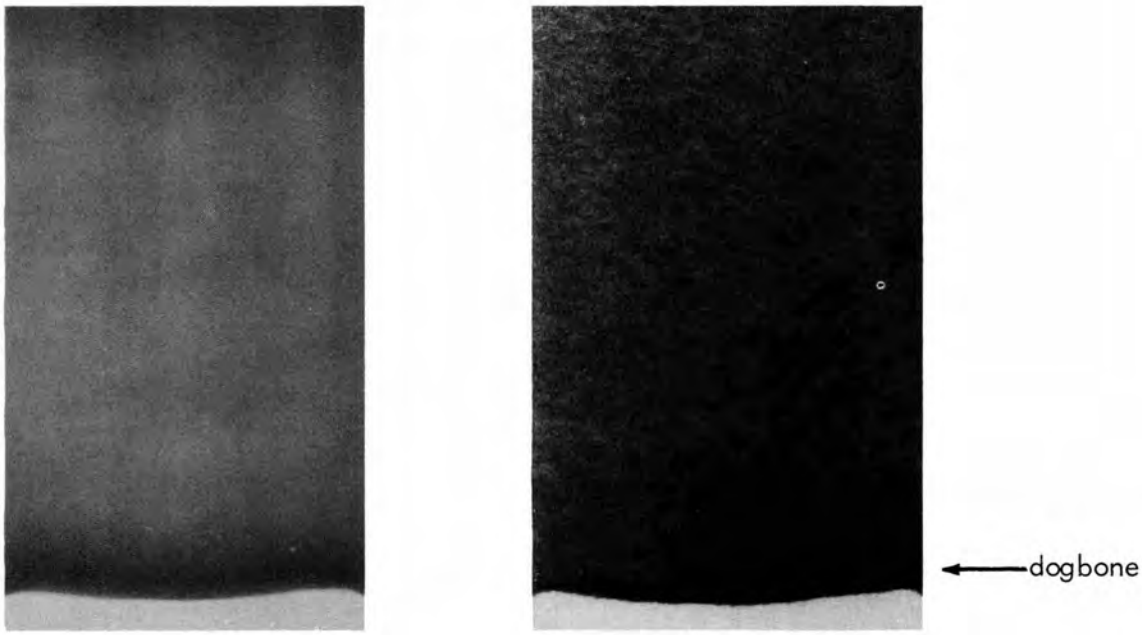

Simulated Core

ATR Plate 19 Core

Photograph of Cores Removed from Picture-Frame Composite

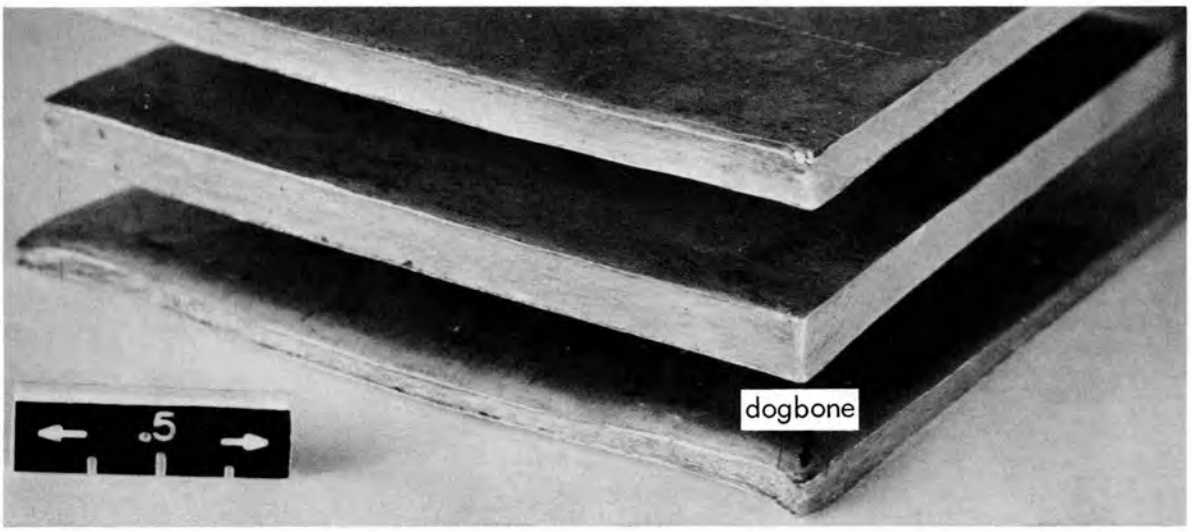

Fig. 13.11. Photograph and Radiographs of Nonuniform Deformation in Cores of Composite Plates.

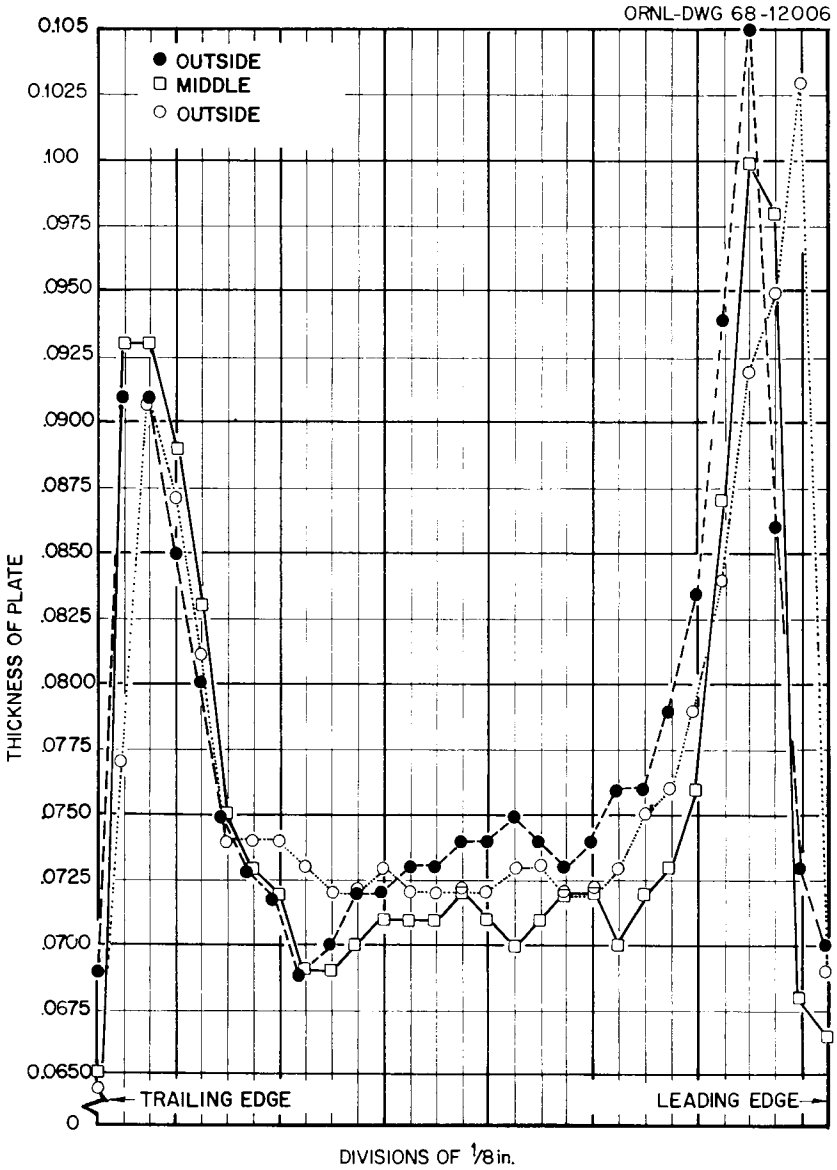

Fig. 13.12. Thickness Profile of 6061 Aluminum Core Rolled in X8001 Aluminum Frames Showing Dogbone.

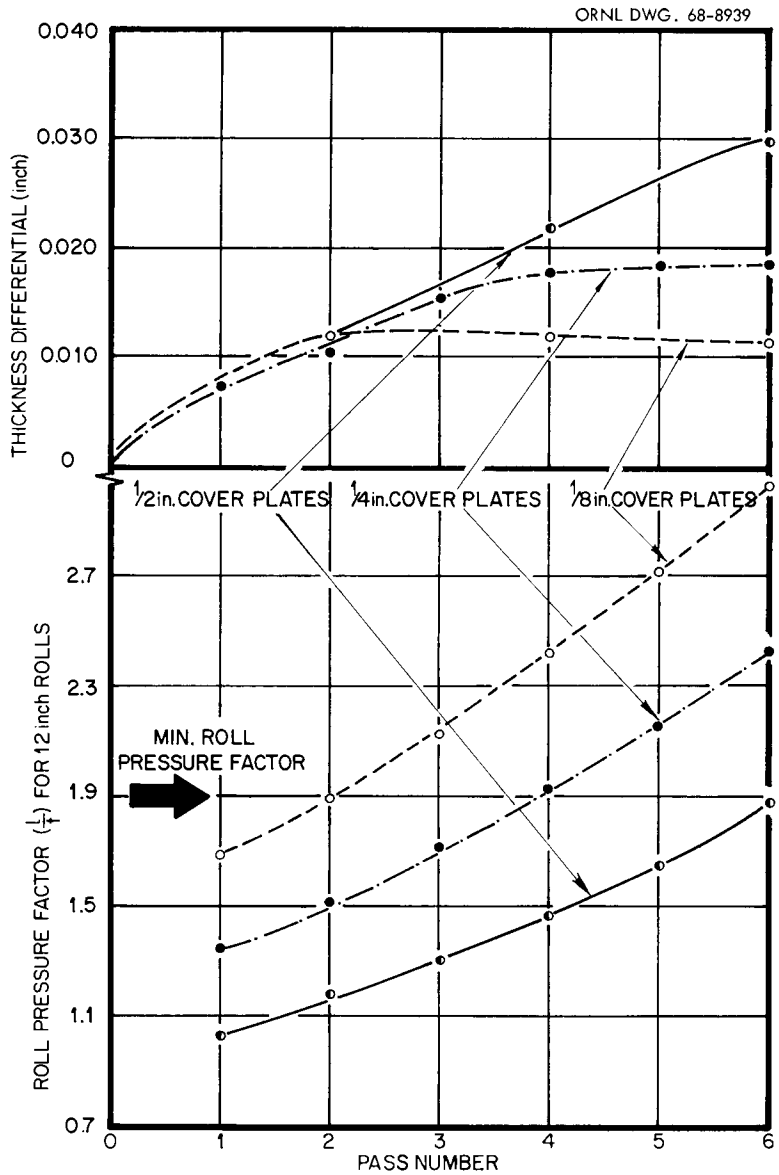

Fig. 13.13. Relationship of Roll Pressure to the Point at Which Dogboning Stabilizes During a 20% Reduction per Pass at 500°C.

Development of Ductile Dispersion-Strengthened Aluminum (G. L. Copeland)

The objective of this work is to improve the high-temperature ductility of sintered aluminum products through alloy modifications. The Illinois Institute of Technology Research Institute has successfully completed the subcontract atomization study. We have received from them the atomizing nozzle and operating procedures which should enable us to atomize alloy powders of a fine size distribution if we set up the required

equipment. They encountered no problems in producing aluminum-magnesium alloys in batches up to 30 lb. Atomization of the 30-lb melt of Al–4 Mo–2 Zr was interrupted when the tundish orifice became plugged with a piece of unalloyed molybdenum. This problem can be corrected by the use of master alloys and additional remelts before atomization. The atomized powders have been ball-milled at ORNL and consolidated by the process developed for HWOCR sintered aluminum products.

The alloys listed in Table 13.3 have been extruded and are presently being evaluated for microstructure, chemistry, and tensile properties. Some of the stronger alloys could not be extruded at 30:1 reduction in area under the maximum load available. These were extruded at 10:1 or 20:1 and hot-swaged to the total 30:1 reduction.

Table 13.3. Nominal Compositions and Milling Times Used for Dispersion-Strengthened Aluminum Alloys

Alloy Designation	Nominal Alloy Content, wt %							Milling Times for Batches of Alloy Powders (hr)
	Mg	Mo	Fe	Zr	Cr	Ti	V	
Standard								0, 8, 10, 12
M-2	2							0, 8, 10, 12
M-4	4							0, 8, 10, 12
M-5	5							8, 10, 12
M-6	6							0, 8, 10, 12
M-10	10							8, 10
A-602		6	0	2	0.2	0.2	0.2	0, 8, 12
A-204		2	0	4	0.2	0.2	0.2	0, 8, 10, 12
A-222		2	2	2	0.2	0.2	0.2	0, 8, 10, 12
A-620		6	2	0	0.2	0.2	0.2	0
A-440		4	4	0	0.2	0.2	0.2	0, 8, 10

Heat-Treatment Studies on Flame-Produced UO_2 Powders (J. I. Federer and W. R. Martin)

We have continued characterizing flame-produced UO_2 powder. The powder was prepared by reaction of UF_6 with hydrogen and oxygen in a flame reactor. The true particle size of as-prepared powder is typically less than 0.04 μm, but the apparent size range of UO_2 powder particles as determined by sieve analysis is much larger than the true particle size due to agglomeration.[2] As-prepared powder has size fractions in the usual mesh sizes common to powder metallurgy applications but also contains a large fraction of −325 mesh particles. A combination of defluorination, oxidation to U_3O_8, and reduction to UO_2 was used to determine whether the apparent particle size could be substantially increased. The following treatments were used:

1. A 50-g lot of as-prepared powder was sieve-analyzed on a Ro-Tap shaker for 15 min; afterwards, all fractions except the +60 mesh fraction were recombined and blended.

2. The powder was defluorinated at 1000°C in wet hydrogen for 16 hr and then sieve-analyzed.

3. The powder was oxidized to U_3O_8, part at 600°C and part at 1000°C, in a He–2.5 vol % O_2 mixture.

4. Both batches of U_3O_8 were reduced to UO_2 at 600°C in dry hydrogen (18 hr at 600°C) and then sieve-analyzed.

The sieve analyses shown in Table 13.4 indicate that the apparent particle size of as-prepared powder is larger than that of powder subjected to various heat treatments. After defluorination at 1000°C, the fractions retained on all screens except 140 mesh are smaller than are found for as-prepared powder, and the fraction of −325 mesh powder is correspondingly larger. We attribute this decrease in apparent particle size to a breaking up of agglomerates. Electron microscopic examination has previously shown that the true particle size actually increases but is still much smaller than 325 mesh (44 μm) (ref. 2). Oxidation to U_3O_8

---

[2] J. I. Federer, W. C. Robinson, Jr., and F. H. Patterson, "Conversion of UF_6 to UO_2 in a Flame Reactor," submitted to Nuclear Applications.

Table 13.4. Sieve Analysis of Flame-Produced Uranium Oxide Powder

Mesh Size	Distribution, wt %			
	As-Prepared	Defluorinated	Reduced to UO_2 at 600°C After Oxidation to U_3O_8 at[a]	
			600°C	1000°C
+60	4.9	0		
−60 +80	9.5	2.2		
−80 +100	7.3	2.5		
−100 +120	7.1	4.2		
−120 +140	7.3	7.9	1.6	0.6
−140 +170	8.7	5.0	1.1	0.6
−170 +200	8.0	6.5	3.3	1.2
−200 +230	4.6	3.4	9.1	1.1
−230 +270	11.2	6.1	11.7	3.2
−270 +325	9.6	11.3	13.7	6.3
−325	21.9	50.8	59.6	87.1

[a]Screens having mesh sizes 60 through 120 were not used for these analyses.

at 600 and 1000°C followed by reduction to UO_2 at 600°C further increases the fraction of fines, the powder oxidized at 1000°C being mostly −325 mesh after reduction. The conclusion to be derived from these results is that the thermal treatments used decrease the apparent particle size in the ranges normally used for powder metallurgy applications and increase the fraction of −325 mesh powder. Powder having a larger particle size could be obtained by crushing flame-produced powder that had been partially sintered. Also, as-prepared powder of larger particle size might be obtained by modifying the flame process.

We conducted a study to determine the effects of particle size, presintering heat treatment (defluorination), and sintering atmosphere on pellet density. A batch of powder was sieved to obtain −60, −60 +200, and −200 mesh powders. Each mesh size was separated into two portions. One portion of each size was uniaxially pressed into pellets at 10,000 psi with no binder and stearic acid as a die lubricant. The pellets were then isostatically pressed at 50,000 psi. The other portion of each mesh size was heat-treated at 1000°C for 20 hr in wet hydrogen

(0.03 g H_2O/liter H_2). This procedure consistently decreased the fluorine content to 50 ppm or less. The powder was then pressed into pellets as described above.

Pellets pressed from each size fraction of as-prepared powder and each size fraction of deflourinated powder were sintered at 1400°C in both dry and wet hydrogen. The densities of the sintered pellets are shown in Table 13.5. These and other observations may be summarized as follows:

1. As-prepared powder compacts sintered in dry hydrogen cracked and spalled badly. Densities were low, ranging from 56.2 to 81.5% of theoretical.

2. As-prepared powder compacts sintered in wet hydrogen cracked in several places. Four pellets broke into two pieces. Densities ranged from 89.0 to 92.4% of theoretical.

3. Defluorinated powder compacts sintered in either dry or wet hydrogen had no obvious defects. Smoothest surfaces occurred on pellets made from −200 mesh powder. Densities, which ranged from 85.2 to 91.7% of theoretical, were slightly higher for pellets sintered in dry hydrogen. Densities of pellets made from −60 +200 mesh powder were slightly higher for both sintering atmospheres.

Although this study was based on a small number of specimens, the following conclusions can be made:

1. Defluorination before sintering is necessary for structural integrity of the pellets. A slow heating rate in wet hydrogen might be suitable, provided fluorine were removed before much sintering began.

2. The particle sizes of the powder examined had only a small effect on sintered densities.

3. Defluorinated powder compacts had slightly higher densities when sintered in dry hydrogen than in wet hydrogen.

Table 13.5. Effect of Powder Size, Presintering Heat Treatment, and Sintering Atmosphere on the Density of UO_2 Pellets Sintered at 1400°C for 4 hr

Sintering Atmosphere[a] (H_2)	Density, percent of theoretical					
	As-Prepared Powder, Mesh Size[b]			Defluorinated Powder[c] Mesh Size[b]		
	−60	−60 +200	−200	−60	−60 +200	−200
Dry	57.5	75.5	79.3	91.0	91.7	90.7
Dry	56.2	80.0	81.5	85.2	91.1	90.0
Wet	89.6	92.0	91.8	85.2	89.9	88.8
Wet	89.0	91.9	92.4	90.1	90.3	88.4

[a]Hydrogen flow rate 0.75 liter/min; dry hydrogen less than 4 ppm H_2O; wet hydrogen 0.39 g H_2O/liter H_2.

[b]60 mesh = 50 μm; 200 mesh = 74 μm.

[c]1000°C, 20 hr, 0.03 g H_2O/liter H_2; hydrogen flow rate 2 liters/min.

Preparation of PuO_2 Powder from PuF_6 by Chemical Vapor Deposition
(W. C. Robinson, Jr., and W. R. Martin)

A document discussing the demonstrated feasibility of the direct conversion for PuF_6 to a pure PuO_2 powder product has been prepared for publication.

Plate Surface Studies

J. V. Cathcart

We have continued our efforts to develop a protective anodic oxide coating for aluminum alloys to be used as cladding for HFIR fuel elements. We have demonstrated the effectiveness for this purpose of anodic films formed in dilute oxalic acid solutions. Our research during the past quarter has been aimed at characterizing the oxalic acid films more fully, attempting to improve their protectiveness, and continuing both static and flowing loop tests of the films.

Structure of Anodic Films Formed in Oxalic Acid

The anodic films formed in oxalic acid solutions are of the so-called "porous" type. Such films typically[3] consist of a close-packed array of approximately hexagonal cells of oxide ranging in diameter from 1000 to 3000 A. A micropore a few hundred angstroms in diameter runs down the center of each cell and terminates at a "barrier layer" whose thickness is dependent on the anodizing voltage and other parameters. In our experiments we have used an anodizing voltage of 65 v. On the basis of electron microscope studies, we found that the films formed in a 1 wt % oxalic acid bath had a cell size of about 1500 A with a barrier layer thickness of about 300 A. We have not determined the pore size. As indicated below, this fine structure of the films appears to have an important effect on the degree of protectiveness of the films.

When these oxalic acid films are exposed to static, 200°C water, their outer surfaces are slowly converted to Boehmite. The result of this reaction is illustrated in Fig. 13.14, which is an electron micrograph of the surface of a 99.999% Al specimen exposed for 336 hr to water at 200°C. The surface was originally smooth and featureless; after attack, however, well-formed crystallites of Boehmite are plainly evident. The original pore structure of the anodic film was still intact below this reaction layer.

The anodic films eventually broke down at spots on the specimens. Once the aluminum substrate was exposed, the rate of corrosion accelerated greatly. Large stresses developed which visibly deformed the specimen and which contributed to the further breakdown of the anodic film in adjacent areas.

Effect of the Temperature of the Anodizing Bath

The anodizing characteristics of aluminum are sensitive to the temperature of the anodizing bath. We have investigated three temperatures: 3, 16, and 25°C. The change in current during anodization at these

---

[3]G. C. Wood, J. P. O'Sullivan, and B. Vaszko, J. Electrochem. Soc. 115, 618–620 (1968).

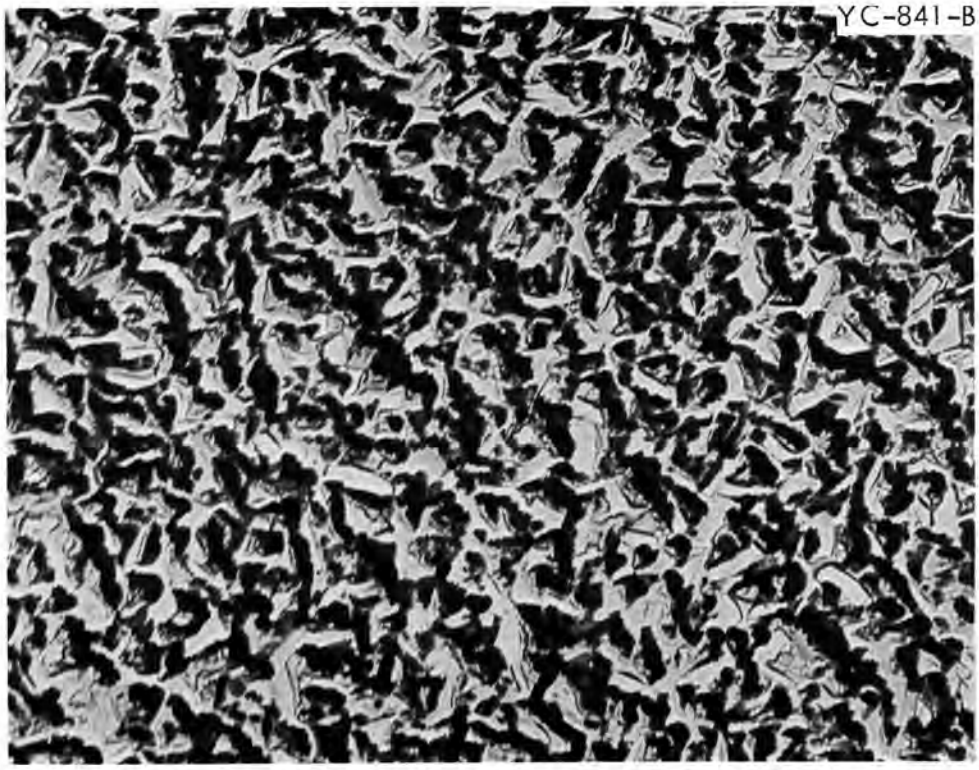

Fig. 13.14. Indirect Replica of the Surface of a 99.999% Al Specimen Anodized for 20 min at 65 v in a 1 wt % Oxalic Acid Solution at 25°C. Specimen exposed to 200°C water for 336 hr. 36,000×.

three temperatures is summarized in Fig. 13.15. The initial surge of current when voltage was first applied to the cell was followed by a sharp drop and a slower recovery to a steady state. This behavior is probably related to the initial formation of a relatively thick barrier layer and its subsequent thinning as the pore structure develops. Note that the limiting current density decreased with decreasing temperature, indicating the formation of a thicker barrier layer and/or an alteration of the pore structure of the films.

These changes in the character of the anodic films have an important and beneficial effect on the corrosion properties of the films. For example, a film formed at 16°C had a lifetime in 200°C water at least four times that of a comparable film formed at 25°C. An autoclave test of a film formed at 3°C has been running for 600 hr, 150 hr longer than the breakdown time for a 16°C film.

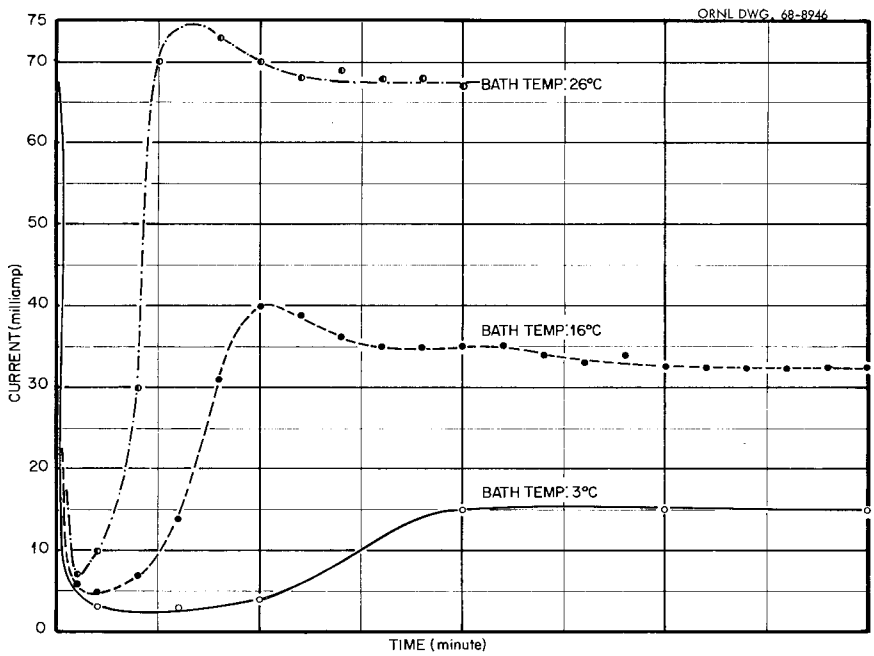

Fig. 13.15. Cell Current Versus Time for 1 wt % Oxalic Acid Bath at a Voltage of 65 v.

Flowing Loop Tests

A more definitive test of the protectiveness of anodic films on 6061 aluminum was provided by the flowing loop apparatus designed by J. C. Griess[4] of the Reactor Division. The crucial feature of this apparatus is the very large heat flux (about 10^6 Btu hr^{-1} ft^{-2}) across the water-aluminum interface in the loop that simulates reactor conditions.

The specimen is an integral part of the loop and takes the form of a rectangular slot 0.078 × 0.5 × 6 in. For our test purposes it is necessary that the interior of this narrow slot be anodized before the assembly of the loop.

The results of the first loop test were rather inconclusive. The failure of an electrical connection forced the premature shutdown of the test, and, more importantly, temperature measurements along the

[4]J. C. Griess, H. C. Savage, and J. L. English, Effect of Heat Flux on the Corrosion of Al by Water. Part IV. Tests Relative to the Advanced Test Reactor and Correlation with Previous Results, ORNL-3541 (February 1964).

surface of the test section were sufficiently similar to those from previous tests with unanodized specimens as to suggest that the anodic film was much thinner than we had predicted.

Before starting the second loop test, we revised our anodizing procedures. We replaced the wire that had served as the cathode with a thin stainless steel strip stretched down the center axis of the specimen. We pumped the anodizing solution through the specimen during anodization, thus sweeping out gas bubbles that formed. Furthermore, we held the specimen at 16°C during anodization to take advantage of the greater corrosion resistance of anodic films formed at low temperatures. While it was impossible to examine the interior of the test specimen itself after anodization, mockups of the loop specimens were anodized and cross-sectioned. Their interior surfaces were found to be completely and evenly coated with an anodic film.

The second loop test, for which the specimen had been prepared in the manner described above with an anodic oxide film 0.0002 in. thick, was stopped after 168 hr, again because of problems with the electrical leads. The indicated corrosion rate was about half that for an unanodized loop, and the test specimen is now undergoing metallographic examination.

This improvement in corrosion rate is not, however, completely unambiguous. Griess showed that the corrosion rate of aluminum alloys is a function of the heat flux across the specimen. The heat flux may be estimated two ways. If the inlet and outlet water temperatures are monitored, the heat input can be obtained from the temperature change of the water and a knowledge of the flow rate. Secondly, since the specimen is heated by resistance, the heat input can be calculated from the voltage drop across the specimen and the current. In this test the value of the heat flux (about 1.5×10^6 Btu hr^{-1} ft^{-2}) obtained from the water temperature was normal, but that calculated from the electrical data was about 20% low. The cause of this discrepancy is not known, and, while we regard the results of this test as encouraging, it is clear that additional runs will be required.

14. SINTERED ALUMINUM PRODUCTS DEVELOPMENT

W. R. Martin

The sintered aluminum products program has been terminated as a separate activity. All experimental objectives have been completed on the development of a billet process specification. Details of the findings have been reported.[1] A minimal effort on the development of a ductile SAP-type alloy by alloying the aluminum is in progress and will be continued and reported as a portion of the Fuel Element Fabrication Development Program. (See, for example, Chapter 13, this report.)

---

[1]G. L. Copeland *et al.*, *Effect of Powder and Process Variables on the Properties of Sintered Aluminum Products*, ORNL-TM-2215 (May 1968).

PART V.

ENGINEERING PROPERTIES OF REACTOR MATERIALS

15. PHYSICAL AND MECHANICAL METALLURGY OF REFRACTORY ALLOYS

W. O. Harms

The purpose of this program is to provide a broad, base-technology evaluation of high-temperature alloys for use in high-performance nuclear reactors and isotopic heat sources for advanced space, terrestrial, and civilian power applications. Principal emphasis is placed on materials problems involving tantalum-, niobium-, molybdenum-, and vanadium-base alloys for systems that use alkali metals as thermodynamic working fluids and heat-transfer media. Some work on superalloys is included because of the more immediate need for these materials in thermoelectric power devices.

Basic Physical Metallurgy Studies

H. Inouye

Solubility, Diffusivity, and Permeability of Interstitials in Refractory Metals (R. L. Wagner)

The aim of this task is to assess the ability of candidate refractory alloy fuel cladding to contain and not interact deleteriously with the decomposition products, such as oxygen, carbon, and nitrogen, of ceramic fuels. The interactions of refractory metals with active gases at low pressures between 600 and 2000°C result in their contamination, decarburization, and sublimation. The factors governing the extent and kinetics of these reactions in terms of the temperature, pressure, reaction time, alloying effects, and specimen geometry were recently discussed.[1,2]

---

[1]H. Inouye, Interactions of Refractory Metals with Active Gases in Vacua and Inert Gas Environments, ORNL-4312 (in press).

[2]H. Inouye, "High Temperature Sorption of Nitrogen by Nb–1% Zr in Ultrahigh Vacuum," submitted for publication to Transactions of the American Society for Metals.

Our current efforts are concerned with measuring the degassing rate of nitrogen from tungsten. From this, we can calculate the solubility and diffusivity of nitrogen in tungsten. At 1800°K the diffusivity of nitrogen was determined to be 2.8×10^{-8} cm^2/sec. This is lower than the published value by about an order of magnitude.[3] At 1800°K and 760 torr of nitrogen, we calculated the nitrogen solubility in tungsten to be 28 ppm compared to literature values[4] of 3.0 and 0.17 ppm. The disagreement between our data and the published values is due in part to the difficulty of measuring the small quantities of nitrogen in tungsten. The radiated heat from our wire sample causes some degassing of the high-vacuum apparatus and contributes to some degree of uncertainty regarding our measurements. The apparatus is being modified to minimize this source of gas.

Interaction of Stress and Vacuum on Properties of Superalloys at Elevated Temperatures (D. T. Bourgette)

Several conventional superalloys have high-temperature properties that meet many of the requirements of proposed isotope and reactor power systems for space, but in high-vacuum environments the selective loss of the higher vapor pressure components by vaporization causes significant structural changes in the alloys.[5,6] The objective of this task is to determine for these alloys the effects of evaporation on creep behavior and the effects of stress on evaporation kinetics. A study of Haynes alloy No. 25 is summarized below.

Haynes alloy No. 25 was creep tested 1000 hr in high vacuum at 785°C and stress levels of 2100 to 14,500 psi to correlate evaporation losses and microstructural characteristics with the observed creep

---

[3]R. Frauenfelder, Permeation, Diffusion, and Solution of Nitrogen in Tungsten and Molybdenum, WERL-2823-28 (June 30, 1967), p. 31.

[4]Ibid., p. 33.

[5]D. T. Bourgette, Vaporization Phenomena of Haynes Alloy No. 25 to 1150°C, ORNL-TM-1786 (May 1967).

[6]D. T. Bourgette, Evaporation of Iron-, Nickel-, and Cobalt-Base Alloys at 760 to 980°C in High Vacuum, ORNL-3677 (November 1964).

behavior and stress. Evaporation losses increased with stress:

Stress (psi)	Weight Loss (mg/cm^2)
0	0.06
2100	0.15
4500	0.19
6900	0.20
9500	0.22
14,500	0.04 (specimen ruptured at 246 hr)

Microstructural examinations showed that the amount of Laves phase precipitated in 1000 hr also increased with stress.

Evaporation also affected the creep properties of Haynes alloy No. 25. For example, a 0.012-in.-thick specimen tested at 10^{-8} torr and 14,500 psi ruptured in 246 hr at 785°C, but a control specimen tested in argon at 1 atm ruptured in 540 hr. These results contrast with a rupture life of 2500 hr at 816°C for specimens tested in air.[7] The times to 1% plastic strain for the samples tested in vacuum were one-eighth to one-fifteenth of those for samples comparably stressed in air.

Section thickness is an important test parameter for creep in vacuums because of the preferential evaporation of the elements with high vapor pressures.[5] Initial results showed that at 785°C and 15,000 psi a 0.012-in. specimen ruptured in 246 hr, while a 0.030-in. specimen failed in 741 hr. Since the evaporation losses per unit area were nearly the same, the change in composition of the thinner specimen was more severe.

Development of Age-Hardening Refractory Alloys (C. T. Liu)

The purpose of this task is to investigate the feasibility of improving the high-temperature strength of refractory alloys through controlled precipitation of stable second phases, such as intermetallic compounds, products of spinodal decomposition, and products of ordering reactions. Binary alloy systems whose phase diagrams show the existence

[7] R. Widmer, J. M. Dhosi, A. Mullendore, and N. J. Grant, Mechanisms Associated with Long Time Creep Phenomena, AFML-TR-65-181 (June 1965).

of miscibility gaps below their solidus temperatures favor conditions required for spinodal decomposition. Eventually this mode of phase transformation leads to the precipitation of fine particles uniformly throughout the grains. Listed in Table 15.1 are the characteristic temperatures of two niobium-base and two tantalum-base binary alloy systems of current interest relative to the transformation of the high-temperature solid solutions into two new phases. Coherent strains arising from differences in the atomic sizes of each component depress the transformation temperatures from T_c to T_s. An estimate of the amount of undercooling $(T_c - T_s)$ was calculated[8] by

$$T_c - T_s = n^2 \, E/2 \, (1 - \nu) k N_v \, , \qquad (15.1)$$

where

$T_c - T_s$ = difference in temperature between the chemical miscibility gap and coherent miscibility gap,

n = the lattice expansion of lattice/unit composition change,

E = Young's modulus,

ν = Poisson's ratio,

k = Boltzman's constant,

N_v = number of atoms per unit volume.

The alloys Nb–40% Hf, Nb–53% Hf, Ta–50% Hf, and Ta–65% Hf were prepared, homogenized 50°C above T_c, quenched in oil, and then aged between 600 and 1500°C. Debye-Scherrer x-ray diffraction patterns of quenched specimens from both alloy systems show small-angle scattering and strong, diffuse streaks associated with the main Bragg reflections of the high-temperature solid solution that suggest the formation of Guinier-Preston (G-P) zones.

The studies to date indicate that these alloys do not undergo spinodal decomposition on aging, for the Bragg reflections have not been flanked by the characteristic side bands. The morphology of the precipitates typical of aged specimens is shown in Fig. 15.1. Precipitates that are initially spherical and gradually become needlelike with aging time

[8] J. W. Cahn, Acta Met. 9, 795 (1961).

Table 15.1. Characteristic Temperatures and Properties of Four Binary Refractory Alloy Systems in Which Spinodal Decompositions are Possible

Alloy System	Solidus Temperature at Symmetrical Composition (°C)	Critical Temperature, °C		Temperature Depression Due to Coherent Strain $T_c - T_s$ (°C)	Eutectoid Temperature (°C)	Lattice Misfit (%)
		Chemical Spinodal[a] T_c	Coherent Spinodal[b] T_s			
Ta-Hf	2160	1660	1110	550	1020	5.9
Nb-Hf	2050	1800	1380	420	830	5.7
Ta-Zr	2040	1780	750	1030	800	8.5
Nb-Zr	1860	970	230	740	610	8.2

[a]Chemical spinodal: locus of points where second derivative of the free energy with respect to composition is zero.

[b]Coherent spinodal: locus of points defining a region within the miscibility gap where coherent precipitation occurs.

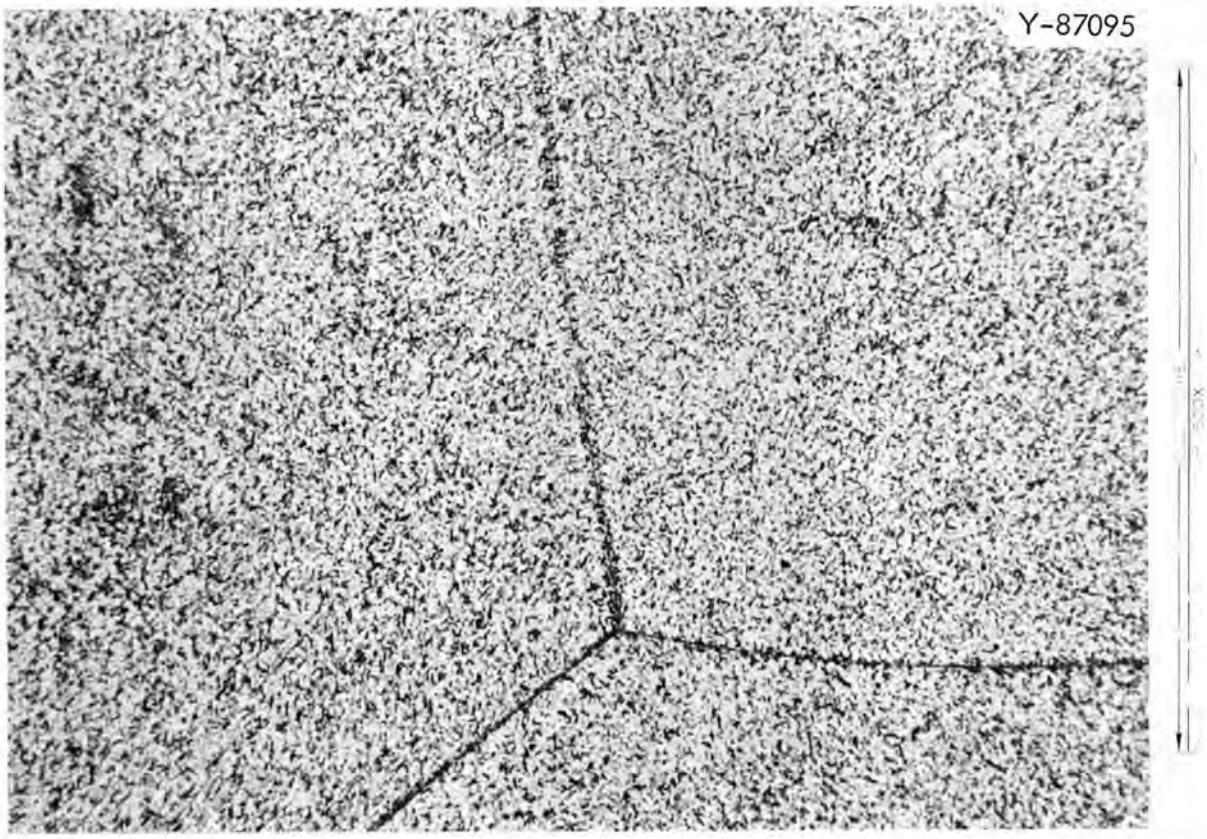

Fig. 15.1. Photomicrograph of Ta–50 wt % Hf Aged 6 hr at 1100°C. 500×.

are uniformly distributed throughout the grain structure. This change in shape is more prominent in the Ta-Hf alloys than in the Nb-Hf alloys where the atomic mismatch is less (see Table 15.1).

Data for the hardness as a function of the aging temperature for Nb–53% Hf and for Ta–50% Hf and Ta–65% Hf are shown in Figs. 15.2 and 15.3, respectively. The highest rate of coarsening, corresponding to the valley of the hardness plot, is at 1050°C in the Nb–53% Hf alloy and at about 1200°C for the two Ta-Hf alloys. The high hardness values for the quenched specimens agree with the x-ray diffraction observations.

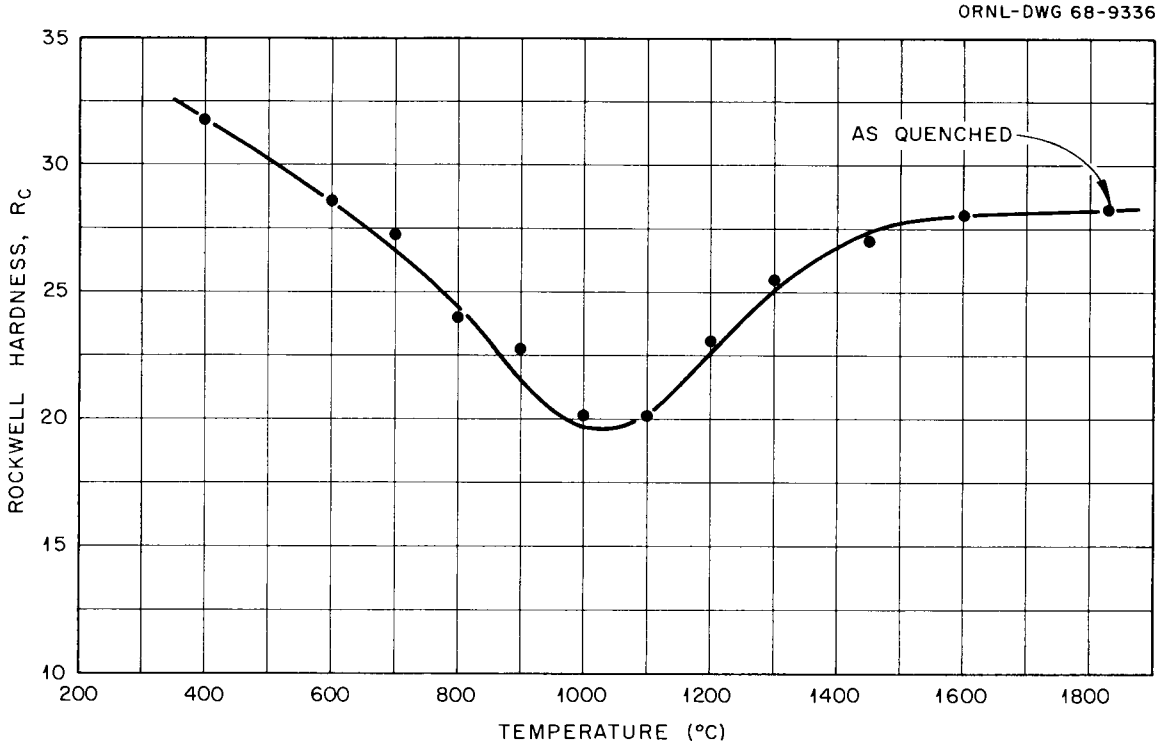

Fig. 15.2. Hardness as a Function of Aging Temperature for Nb–53% Hf Alloy Aged 3 hr.

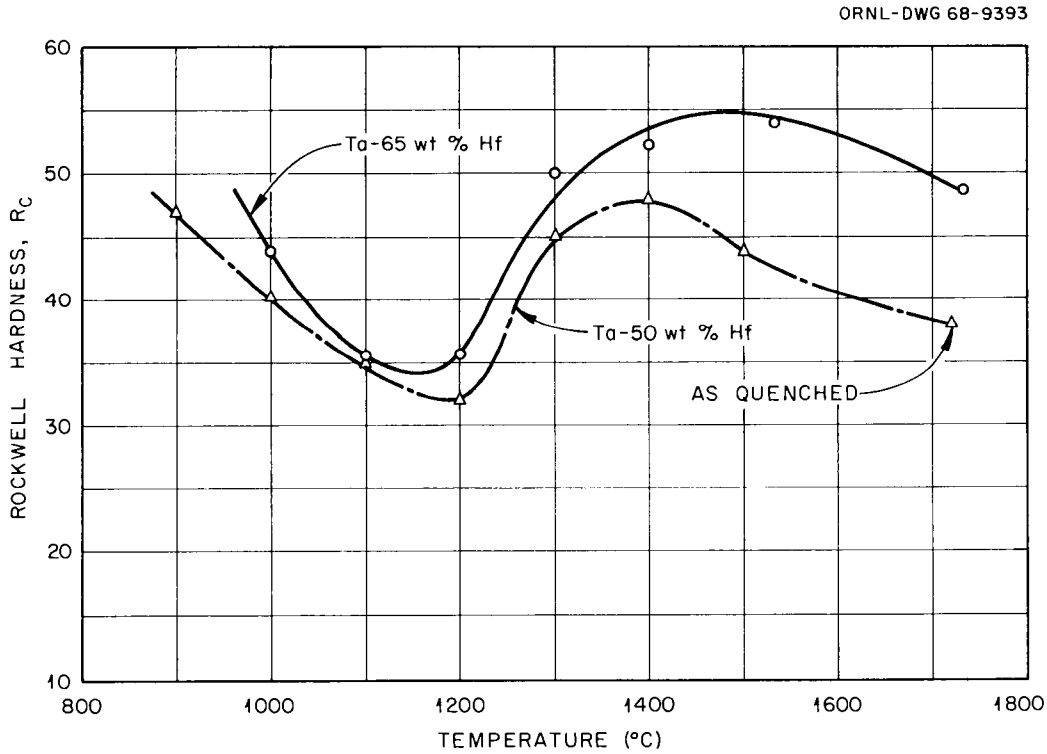

Fig. 15.3. Hardness as a Function of Aging Temperature for Tantalum-Hafnium Alloys Aged 6 hr.

Long-Time, High-Temperature Mechanical Properties of Commercial Refractory Alloys

J. R. Weir, Jr.

The object of this program is to evaluate the creep-rupture properties of promising refractory-metal alloys at high temperatures. Stress-rupture curves are determined from 10 to 1000 hr at several temperatures from 1000 to 1650°C. In addition, we study the effects of annealing treatment and fabrication variables in an effort to better understand and improve the most promising alloys. Recent results on niobium- and tantalum-base alloys are being published.[9]

Molybdenum Alloys (R. L. Stephenson)

We are studying the effect of fabrication variables on the creep-rupture properties of molybdenum alloys. Quantities of TZM in the stress-relieved and recrystallized conditions, fabricated according to current mill practice, have been tested as controls. Quantities of TZM, Cb-TZM (columbium-modified TZM), and TZC were fabricated according to one of two experimental fabrication schedules.

Figure 15.4 shows the 1000-hr rupture stress plotted against temperature for each of these materials. Several conclusions can be drawn from these data: fabrication variables have a substantial effect on the long-time creep-rupture properties of TZM and Cb-TZM; strengths of all three alloys compare very favorably with those of other refractory alloys in the temperature range studied; at 982°C, 1000-hr rupture stresses of 90,000 to 100,000 psi are attainable for some alloys; and the processing history can be adjusted to optimize the alloy for the anticipated service temperature.

---

[9]R. L. Stephenson, J. Less-Common Metals 15(4), 395–424 (1968).

ORNL-DWG 68-9335

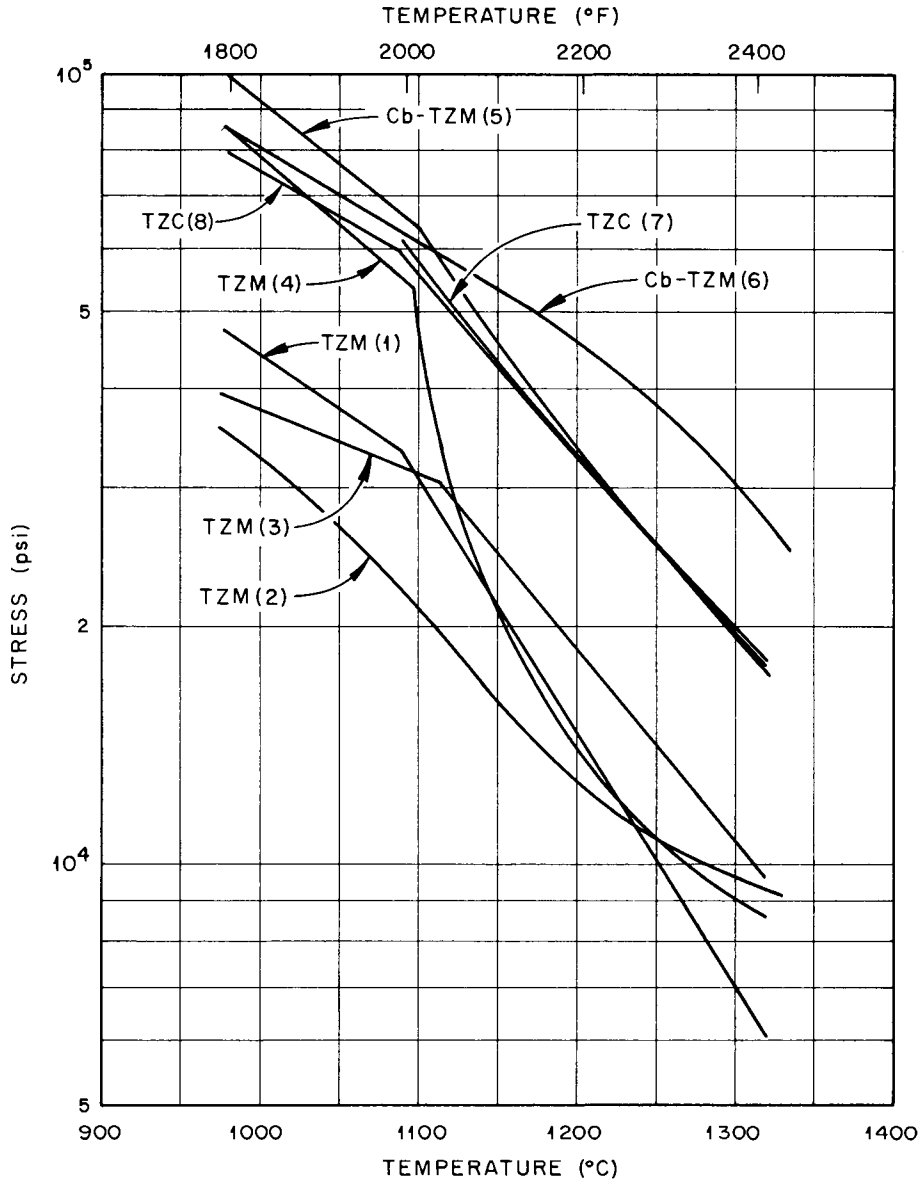

Fig. 15.4. Effect of Fabrication Variables on 1000-hr Rupture Stress of four Molybdenum-Base Alloys. TZM(1), stress-relieved at 1230°C, TZM(2), recrystallized at 1540°C, TZM(3), 1540°C, warm worked at 1040°C and stress-relieved at 1230°C, TZM(4), annealed 2095°C, re-extruded and warm worked at 1315°C, Cb-TZM(5), annealed 2095°C, re-extruded and warm worked at 1315°C, Cb-TZM(6), annealed 1925°C and warm worked at 1370°C, TZC(7), annealed 2095°C, re-extruded and warm worked at 1315°C, TZC(8), annealed 1925°C and warm worked at 1370°C.

Welding and Brazing Development

G. M. Slaughter

Brazing Alloy Development (D. A. Canonico and Nancy C. Cole)

Previously,[10] we have discussed a number of ternary systems for high-temperature brazing alloys and, in particular, certain specific compositions within those systems. Recently, we have concentrated on the Ti-Zr-Ge system. Figure 15.5 shows the appropriate equilibrium binary diagrams and the ternary compositions under evaluation as brazing

[10] D. A. Canonico and N. C. Cole, Metals and Ceramics Div. Ann. Progr. Rept. June 30, 1967, ORNL-4170, pp. 73–74.

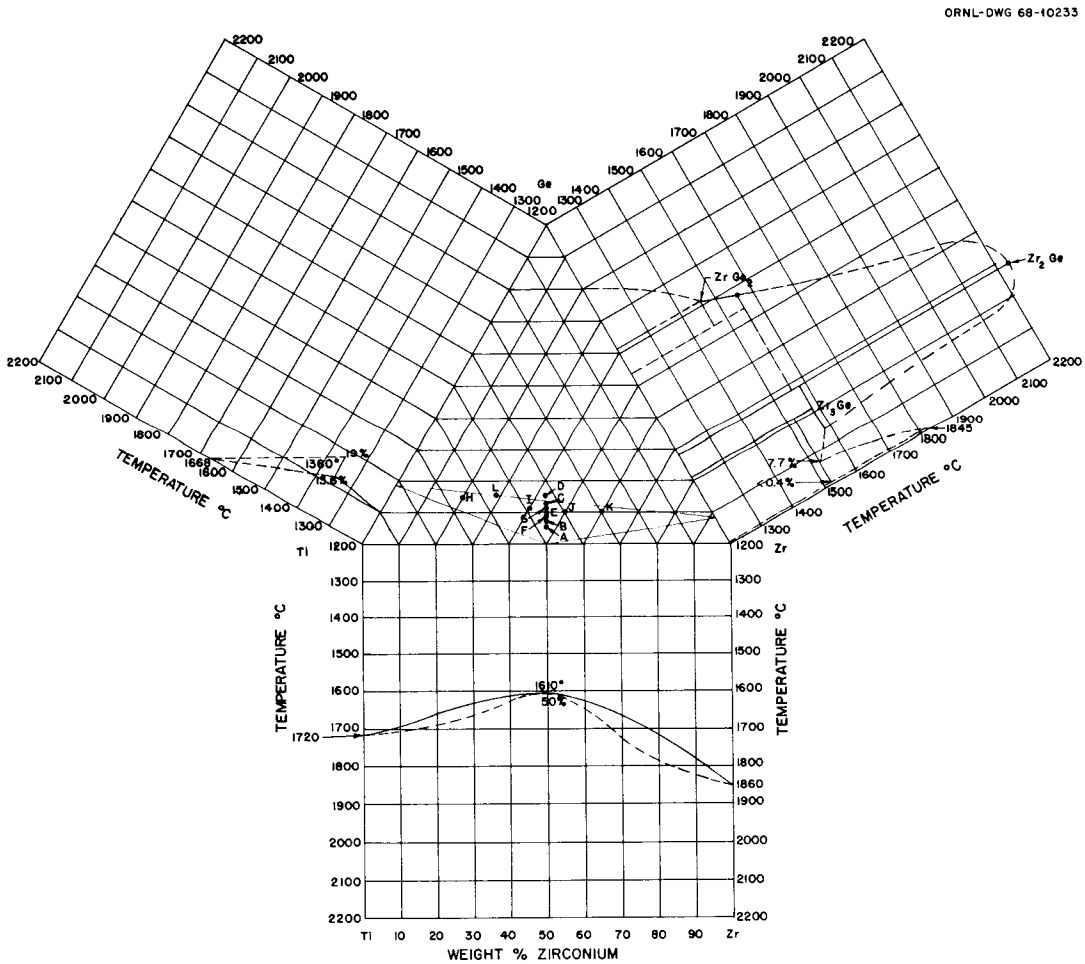

Fig. 15.5. Equilibrium Binary Diagrams that Comprise the Ti-Zr-Ge System.

alloys. As can be noted, the titanium- and zirconium-rich eutectics both occur with germanium additions of less than 20%; therefore, our studies for alloy development have been concentrated in that compositional region. The chemical compositions and brazing temperatures for this series of alloys are given in Table 15.2.

Table 15.2. Brazing Alloys Developed Within the Ti-Zr-Ge System

Alloy Number	Composition, wt %			Brazing Temperature (°C)
	Ti	Zr	Ge	
8A	48	48	4	760
8B	46	46	8	735
8C	44	44	12	760
8D	42	42	16	760
8E	45	45	10	705
8F	45.5	45.5	9	760
8G	44.5	44.5	11	735
8H	65	20	15	735
8I	49	40	11	760
8J	40	50	10	725
8K	30	60	10	725
8L	55	29	16	760

All of the alloys wet refractory metals, but some are superior to others. The refractory metals we have been investigating are Ta, Ta–10% W, W, and TZM. Figure 15.6 shows photomicrographs of two brazed joints made with alloy 8B (Ti–46% Zr–8% Ge). The filleting is excellent, and the joints are sound.

Among those alloys studied, 8H (Ti–20% Zr–15% Ge) is outstanding for joining graphite.[11] Figure 15.7 is a photomacrograph of high-density graphite brazed to itself with this alloy. The exceptionally good wettability is evidenced by the flow of the filler metal both into the capillary of the braze joint and up the sides of the vertical leg of the T-joint.

Studies are continuing on the alloys in this ternary system as well as in other alloy systems.

[11]D. A. Canonico and N. C. Cole, Metals and Ceramics Div. Ann. Progr. Rept. June 30, 1968, ORNL-4370, Chap. 15.

PHOTO 87637R

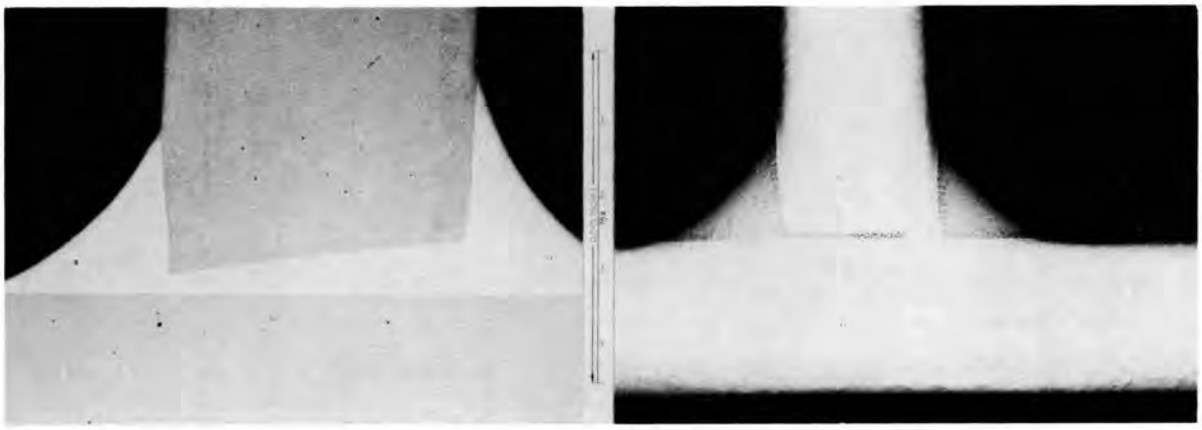

Ta TO Ta Mo TO Mo

Fig. 15.6. T-Joints Using Brazing Alloy, Ti–46% Zr–8% Ge.

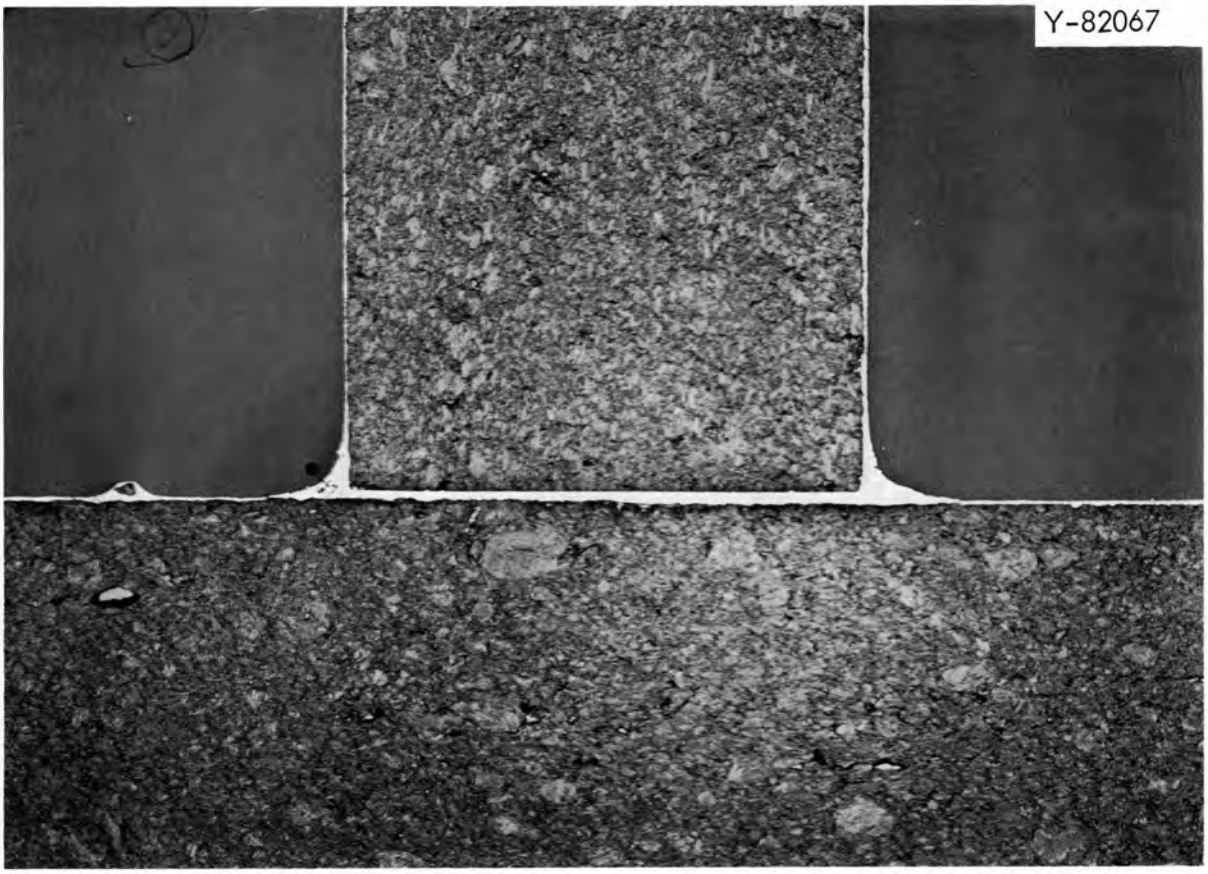

Fig. 15.7. High-Density Graphite Brazed with Ti–20% Zr–15% Ge Alloy. 22×.

Physical Properties of Refractory Materials

D. L. McElroy

We are measuring, correlating, and attempting to understand the high-temperature physical properties of refractory materials. Their characteristics are sought by accurate measurements of thermal conductivity, electrical resistivity, thermoelectric power, specific heat, and total hemispherical emittance.

Physical Properties of Molybdenum (R. K. Williams and J. P. Moore)

We measured the electrical resistivity and thermoelectric power of 99.97%-pure molybdenum from 100 to 1700°K and determined the thermal conductivity of the material from 100 to 1250°K. The material was obtained from Climax Molybdenum Company (CMX-WB-LB-1 grade) after being arc-cast, hot-rolled, and given a recrystallization anneal. We found the electrical resistivity ratio ($\rho_{273}/\rho_{4.2}$) of the material to be 142, indicating that impurity effects should be negligible over most of the temperature range. Smoothed values for the physical properties are shown in Table 15.3, and thermal conductivity data from another recent study are included for comparison. Our data for thermal conductivity, λ, and electrical resistivity, ρ, can be correlated from 100 to 1250°K by the equation

$$\lambda = 2.67 \times 10^{-8}[1 - \exp(-\frac{T}{\theta} + 0.214)]\,\frac{T}{\rho} + \frac{7}{T}\,,$$

to ±0.5%, when θ is chosen to be 90°K. The constants obtained from this fit indicate that the Lorenz number of molybdenum exceeds the Sommerfeld value (2.443×10^{-8} V^2/K^2), where V is volts, at high temperatures and is similar to the Lorenz number we found for tungsten. Feith[12] found the Lorenz number to be less than the Sommerfeld value because his thermal conductivity values are 27 to 29% less than ours in the range of overlap. This illustrates the need for accurate thermal conductivity values for the determination of the behavior of the Lorenz value at high

[12]Thermal conductivity data from A. D. Feith, Measurements of the Thermal Conductivity and Electrical Resistivity of Molybdenum, USAEC GE-TM-65-10-1 (1965).

Table 15.3. Physical Properties of Recrystallized Molybdenum[a]

Temperature (°K)	Thermal Conductivity (w/cm°K)	Electrical Resistivity (μΩcm)	Absolute Seebeck Coefficient (μv/K)	Thermal Conductivity[b] (w/cm°K)
100	1.752	0.930	+0.20	
200	1.477	3.235	+2.93	
300	1.401	5.561	+5.80	
400	1.337	7.960	8.07	
500	1.277	10.451	10.48	
600	1.231	13.021	12.85	
700	1.195	15.649	14.79	
800	1.167	18.333	16.03	
900	1.143	21.051	16.87	
1000	1.123	23.815	17.35	
1100	1.106	26.613	17.56	
1200	1.094	29.432	17.47	0.863
1300	1.08[c]	32.301	17.15	0.849
1400	1.07[c]	35.209	16.64	0.835
1500	1.05[c]	38.183	15.91	0.821
1600	1.04[c]	41.201	14.78	0.807
1700	1.03[c]	44.305	13.16	0.794

[a]Corrected for thermal expansion.

[b]Thermal conductivity data from A. D. Feith, Measurements of the Thermal Conductivity and Electrical Resistivity of Molybdenum, USAEC GE-TM-65-10-1 (1965).

[c]Extrapolated from $K = \frac{2.67 \times 10^{-8}\ T}{\rho} + \frac{7}{T}$.

temperatures. The 7/T term represents the lattice contribution, which is smaller than we found for tungsten.

Nondestructive Testing

R. W. McClung

Ultrasonic Inspection of Tubing (K. V. Cook)

Because of increased interest in wall thickness and eccentricity measurements and the desire for permanent records, we have adapted our ultrasonic resonance equipment to produce strip-chart recordings of wall thickness as a function of rotation and translation along the tube. The immersed resonance technique measures to an accuracy of ±0.0001 in.

ORNL-4330
UC-25 — Metals, Ceramics, and Materials

INTERNAL DISTRIBUTION

1–3. Central Research Library
4–5. ORNL — Y-12 Technical Library
Document Reference Section
6–20. Laboratory Records Department
21. Laboratory Records, ORNL R.C.
22. ORNL Patent Office
23. G. M. Adamson, Jr.
24. T. E. Banks
25. J. H. Barrett
26. S. E. Beall
27. R. L. Beatty
28. R. J. Beaver
29. M. Bender
30. R. G. Berggren
31. D. S. Billington
32. E. E. Bloom
33. A. L. Boch
34. E. S. Bomar
35. B. S. Borie
36. D. T. Bourgette
37. G. E. Boyd
38. R. A. Bradley
39. R. J. Breeding
40. R. B. Briggs
41. R. E. Brooksbank
42. W. E. Brundage
43. D. A. Canonico
44. R. M. Carroll
45. J. V. Cathcart
46. A. K. Chakraborty
47. Ji Young Chang
48. D. L. Clark
49. G. W. Clark
50. N. C. Cole
51. K. V. Cook
52. W. H. Cook
53. G. L. Copeland
54. W. B. Cottrell
55. C. M. Cox
56. F. L. Culler
57. C. W. Cunningham
58. J. E. Cunningham
59. H. L. Davis
60. V. A. DeCarlo
61. J. H. DeVan
62. J. R. DiStefano
63. C. V. Dodd
64. R. G. Donnelly
65. D. A. Dyslin
66. W. S. Ernst
67. J. H. Erwin
68. K. Farrell
69. J. S. Faulkner
70. J. I. Federer
71. D. E. Ferguson
72. R. B. Fitts
73. B. Fleischer
74. B. E. Foster
75. A. P. Fraas
76. J. H Frye, Jr.
77. W. Fulkerson
78. L. C. Fuller
79. T. G. Godfrey, Jr.
80. J. M. Googan (Y-12)
81. R. J. Gray
82. W. R. Grimes
83. A. G. Grindell
84. H. D. Guberman
85. D. G. Harman
86. W. O. Harms
87–89. M. R. Hill
90. N. E. Hinkle
91. D. O. Hobson
92. H. W. Hoffman
93. R. W. Horton
94. W. R. Huntley
95. H. Inouye
96. D. H. Jansen
97. J. D. Jenkins
98. W. H. Jordan
99. G. W. Keilholtz
100. R. T. King
101. R. L. Klueh
102. J. Komatsu
103. J. A. Lane
104. J. M. Leitnaker
105. B. C. Leslie
106. T. B. Lindemer
107. A. P. Litman
108. C. T. Liu

109. H. R. Livesey
110. A. L. Lotts
111. R. N. Lyon
112. H. G. MacPherson
113. R. E. MacPherson
114. M. M. Martin
115. W. R. Martin
116. R. W. McClung
117. H. E. McCoy, Jr.
118. H. C. McCurdy
119. R. E. McDonald
120. W. T. McDuffie
121. D. L. McElroy
122. C. J. McHargue
123. F. R. McQuilkin
124. A. J. Miller
125. E. C. Miller
126. J. P. Moore
127. R. E. Moore
128. W. L. Moore
129. C. S. Morgan
130. J. G. Morgan
131. F. H. Neill
132. G. T. Newman
133. T. M. Nilsson
134. T. A. Nolan (K-25)
135. K. Notz
136. S. M. Ohr
137. A. R. Olsen
138. M. F. Osborne
139. P. Patriarca
140. W. H. Pechin
141. A. M. Perry
142. S. Peterson
143. R. A. Potter
144. R. B. Pratt
145. M. K. Preston
146. R. E. Reed
147. C. R. Reese
148. D. K. Reimann
149. G. A. Reimann
150. A. E. Richt
151. P. L. Rittenhouse
152. W. C. Robinson
153. M. W. Rosenthal
154. D. J. Rucker
155. C. F. Sanders
156. G. Samuels
157. A. W. Savolainen
158. J. E. Savolainen
159. A. C. Schaffhauser
160. J. L. Scott
161. J. D. Sease
162. C. E. Sessions
163. O. Sisman
164. G. M. Slaughter
165. S. D. Snyder
166. K. E. Spear
167. I. Spiewak
168. P. Spindler
169. J. E. Spruiell
170. W. J. Stelzman
171. R. L. Stephenson
172. J. O. Stiegler
173. D. A. Sundberg
174. E. J. Tenckhoff
175. D. B. Trauger
176. R. P. Tucker
177. G. M. Watson
178. S. C. Weaver
179. M. S. Wechsler
180. A. M. Weinberg
181. J. R. Weir, Jr.
182. W. J. Werner
183. H. L. Whaley
184. G. D. Whitman
185. F. W. Wiffen
186. J. M. Williams
187. R. K. Williams
188. R. O. Williams
189. J. C. Wilson
190. R. G. Wymer
191. F. W. Young, Jr.
192. C. S. Yust
193. A. F. Zulliger
194. C. M. Adams, Jr. (Consultant)
195. Leo Brewer (Consultant)
196. L. S. Darken (Consultant)
197. J. A. Krumhansl (Consultant)

EXTERNAL DISTRIBTUION

AIR FORCE MATERIALS LABORATORY, Wright-Patterson Air Force Base

198. C. H. Armbruster
199. H. M. Burte
200. G. Glenn
201. Technical Director

AIR FORCE WEAPONS LABORATORY, Kirtland Air Force Base

202. D. Brooks

AMES LABORATORY

203. O. N. Carlson
204. W. L. Larsen
205. M. Smutz
206. F. H. Spedding

ARGONNE NATIONAL LABORATORY

207. L. Baker
208. J. H. Kittel
209. M. V. Nevitt
210. P. G. Shewmon
211. R. C. Vogel

LMFBR PROGRAM OFFICE, Argonne National Laboratory

212. A. Amorosi
213. L. Burris
214. L. Kelman
215. J. M. McKee

AEC-RDT SITE REPRESENTATIVES

216. M. E. Jackson, Argonne National Laboratory
217. D. J. Wille, Atomic Power Development Associates
218. R. L. Morgan, Atomics International
219. J. V. Levy, General Electric, Cincinnati
220. J. F. Weissenberg, General Electric, Cincinnati
221. R. H. Ball, Gulf General Atomic
222. J. E. Hebert, Idaho
223. D. A. Moss, Idaho
224. K. A. Trickett, Idaho
225. D. F. Cope, Oak Ridge National Laboratory
226. C. L. Matthews, Oak Ridge National Laboratory
227. P. G. Holsted, Pacific Northwest Laboratory
228. J. Sako, Pacific Northwest Laboratory
229. Atomic Energy Commission Library, Washington

DIVISION OF NAVAL REACTORS, AEC, Washington

230. R. H. Steele

DIVISION OF REACTOR DEVELOPMENT AND TECHNOLOGY, AEC, Washington

231. J. C. Crawford, Jr.
232. G. W. Cunningham
233. A. Giambusso
234. H. G. Hembree
235. J. R. Hunter
236. E. E. Kintner
237. W. H. Layman
238. W. H. McVey
239. J. J. Morabito
240. R. E. Pahler
241. A. J. Pressesky
242. M. A. Rosen
243. J. M. Simmons
244. E. E. Sinclair
245. A. Taboada
246. A. N. Tardiff
247. A. Van Echo
248. C. E. Weber
249. M. J. Whitman

DIVISION OF RESEARCH, AEC, Washington

250. P. W. McDaniel
251. D. K. Stevens

DIVISION OF SPACE NUCLEAR SYSTEMS, AEC, Washington

252. R. E. Anderson
253. D. Beard
254. J. F. Griffo
255. C. E. Johnson
256. J. A. Powers
257. F. C. Schwenk

OAK RIDGE OPERATIONS OFFICE

258. W. J. Larkin
259. Laboratory and University Division

ATOMIC POWER DEVELOPMENT ASSOCIATES

260. E. C. Kovacic
261. A. A. Shoudy

ATOMICS INTERNATIONAL

262. H. Pearlman

BABCOCK AND WILCOX COMPANY, Lynchburg, Virginia 24505

263. C. Baroch
264. S. P. Grant
265. C. Johnson
266. L. Weissert

BATTELLE MEMORIAL INSTITUTE, Columbus, Ohio

267. W. Berry
268. D. Keller
269. S. J. Paprocki
270. Defense Materials Information Center

BATTELLE MEMORIAL INSTITUTE, PNL, Richland, Washington

271. A. L. Bement
272. J. J. Cadwell
273. T. T. Claudson
274. D. L. Condotta
275. E. Evans
276. B. R. Hayward
277. W. E. Roake
278. J. C. Tobin
279. R. G. Wheeler
280. Technical Information File

FAST FLUX TEST FACILITY, Battelle-Northwest

281. E. R. Astley

BROOKHAVEN NATIONAL LABORATORY

282. D. H. Gurinsky
283. C. Klamut

BUREAU OF MINES

284. Haruo Kato, Albany Metallurgy Research Center, P. O. Box 70, Albany, Oregon 97321
285. T. Sullivan, Bureau of Mines, Boulder City, Nevada 89005

COMBUSTION ENGINEERING

286. W. P. Chernock
287. S. S. Christopher

GENERAL ELECTRIC, Cincinnati

288. D. H. Ahmann
289. H. C. Brassfield
290. V. P. Calkins
291. E. Hoffman
292. J. McGurty
293. J. Moteff

GENERAL ELECTRIC, Nuclear Systems Programs, Cincinnati

294. E. E. Hoffman

GENERAL ELECTRIC, San Jose

295. R. Duncan
296. H. Klepfer

GENERAL ELECTRIC, Pleasanton

297. H. W. Alter

GENERAL ELECTRIC, Sunnyvale

298. K. P. Cohen
299. F. Comprelli
300. R. Skavdahl
301. C. Spalaris
302. E. L. Zebroski

GULF GENERAL ATOMIC

303. D. B. Coburn
304. A. J. Goodjohn
305. J. P. Howe
306. S. Jaye
307. J. F. Watson

IDAHO NUCLEAR CORPORATION

308. W. C. Francis

ILLINOIS INSTITUTE OF TECHNOLOGY RESEARCH INSTITUTE

309. D. J. McPherson

JET PROPULSION LABORATORY (NASA)

310. J. Davis

KNOLLS ATOMIC POWER LABORATORY

311. R. F. Wojciescak
312. Document Library

LOS ALAMOS SCIENTIFIC LABORATORY

313. R. D. Baker
314. D. B. Hall
315. J. A. Leary
316. R. Perkins
317. R. E. Peterson
318. Reports Library

MOUND LABORATORY

319. R. G. Grove

NASA, LEWIS RESEARCH CENTER

320. M. Ault
321. J.W.R. Creagh
322. J. J. Lombardo
323. T. P. Moffitt
324. T. A. Moss
325. F. E. Rom
326. L. Rosenblum
327. N. D. Sanders
328. N. Saunders
329. H. Schwartz

NAVAL RESEARCH LABORATORY

330. J. R. Hawthorne
331. C. Serpan
332. L. E. Steele

NORTH CAROLINA UNIVERSITY, Raleigh, North Carolina 27607

333. J. Beeler
334. R. E. Dahl

NUCLEAR MATERIALS AND EQUIPMENT CORPORATION

335. C. Caldwell
336. K. Puechl

OHIO STATE UNIVERSITY, Columbus, Ohio 43212

337. M. G. Fontana
338. R. W. Staehle

RENSSELAER POLYTECHNIC INSTITUTE

339. C. B. Willingham, Jr.

SANDIA CORPORATION

340. J. Jacobs
341. D. R. Johnson
342. R. P. Stromberg

SAVANNAH RIVER LABORATORY

343. P. H. Permar
344. S. P. Rideout

TRW SYSTEMS (NASA), Redondo Beach, California 90278

345. H. Lurie

UNION CARBIDE CORPORATION, New York

346. J. A. Swartout

UNION CARBIDE CORPORATION, Materials Systems Division, Indianapolis

347. C. F. Leitten, Jr.

UNITED NUCLEAR CORPORATION

348. A. Strasser

UNIVERSITY OF CALIFORNIA, Lawrence Radiation Laboratory, Livermore

349. W. R. Holman
350. J. S. Kane
351. L. W. Roberts
352. A. J. Rothman
353. B. Rubin

U.S. NAVAL AIR SYSTEM COMMAND (AIR-52031B)

354. T. Kearns
355. I. Machlin

USAEC Scientific Representative, American Embassy, Box 40 FPO, N. Y. 09510

356. W.L.R. Rice

WESTINGHOUSE, Advanced Reactor Division, Waltz Mill Site

357. E. C. Bishop
358. J.C.R. Kelly
359. P. J. Levine
360. P. Murray
361. W. E. Ray
362. G. A. Whitlow

WESTINGHOUSE, Astronuclear Laboratory

363. R. T. Begley
364. D. C. Goldberg

WESTINGHOUSE, Atomic Power Division

365. T. Stern

WESTINGHOUSE, Bettis

366. R. H. Fillnow
367. P. N. Gustafson
368. Westinghouse Bettis Laboratory Library

369–590. Given distribution as shown in TID-4500 under Metals, Ceramics, and Materials category (25 copies – CFSTI)